Abstract

Toward the Quantum Control of the Motional State of Superfluid ^{4}He in a Optomechanical Resonator

Jiaxin Yu
2023

The ability to generate and manipulate non-Gaussian macroscopic quantum states and multi-body entanglement with light is foundational to achieving quantum-enhanced technologies, and furthuring our understanding on macroscopic quantum effects and decoherence mechanism. Optomechanical devices which coherently couple the optical and mechanical degrees of freedom have emerged as a prominent platform for them in the past two decades.

I will present in this thesis my work toward realizing full optical quantum control of the motional state of superfluid ^{4}He in a fiber Fabry-Perot cavity, where coherent coupling between the intensity of the optical field and the density fluctuation of ~ 1 ng of liquid helium is established via electrostrictive interaction. The characterization of the device and demonstration of standard optomechanical effects, such as sideband asymmetry and dynamical backaction, have been previously reported in the works [1] [2] via a heterodyne detection scheme. In this work, I will present the measurements done with a heralded single photon detection scheme, where the detection of a single photon heralds the creation or annihilation of a single phonon.

Photon and phonon statistics, such as the coherence function, reveal properties of the quasi-probability distribution of a state, which is widely used to verify the quantumness of a state. I will present measurements of the phonon coherence used to characterize our system. In particular, the coupling, damping and heating mechanism of the device is modeled by measurements of the first-order coherence. The acoustic state is characterized by its phonon coherences up to the fourth-order, and found to be consistent with a thermal state in equilibrium to its bath via a Markovian coupling. Through post-selection on photon detection events, a k-phonon-subtracted or -added out-of-equilibrium state is heralded and characterized by its phonon coherences (for $k \leq 3$).

These studies employ single-mode optomechanics, in which the optical mode couples to exactly one acoustic mode. Measurements on multimode coupling indicate that the system is well-approximated by the single-mode coupling assumption up to 99%, as a result of the orthogonality condition between spatial profiles of the coupled modes imposed by the geometry of our device.

Works presented in this thesis demonstrate the robust implementation of single photon counting for our system, providing access to the nonlinear quantum optomechanical effects induced by measurement backaction, and lays the foundation for implementing a full quantum protocol to generate, manipulate, store and read out an acoustic state on the single quantum level.

Toward the Quantum Control of the Motional State of Superfluid ^{4}He in a Optomechanical Resonator

A Dissertation
Presented to the Faculty of the Graduate School
of
Yale University
in Candidacy for the Degree of
Doctor of Philosophy

by
Jiaxin Yu

Dissertation Director: Jack Harris

2023

Contents

List of Figures

List of Tables

Chapter 1

Introduction

In the past two decades, the field of optomechanics have emerged rapidly as a platform to merge the optical and the mechanical domains, and to access quantum phenomena on a macroscopic scale. Fundamentally, while quantum mechanics is well-established in describing physical laws on a microscopic level, there remains a gap to bridge in the understanding of quantum effect and its decoherence mechanism on macroscopic objects. More tangibly, recent rapid development in quantum-enhanced technologies, such as sensing, memories, information processing and communication, has led to a growing demand for interfacing single photon with more robust and accessible platforms to be used as the building blocks of large-scale quantum network [3].

Quantum optomechanical devices harness the coherent coupling between the electromagnetic and mechanical degrees of freedom, in order to manipulate and probe the mechanics on the single quanta level using light. This makes such a system an ideal candidate for studying macroscopic quantum mechanics. Methods that are extensively studied and understood in the field of quantum optics can be implemented in an optomechanical system, while mechanical elements are more scalable and orders of magnitude more macroscopic than atomic and molecular ensembles. A full optical control over the mechanical motion will make the system promising for testing macroscopic quantum mechanics, studying decoherence mechanism of quantum effects, and exploring potential physics beyond the standard model [4] [5] [6] [7].

On the other hand, while there already exists a wide range of quantum optical devices interfacing with various elements (such as atoms [8], superconducting circuits [9], solids [10], quantum dots, cystal defects [11]), mechanical resonators have been drawing growing interests since they are generally more robust with simpler design and low dissipation, which could be used as solid-state quantum memory and sensing elements. Since mechanical motion can be easily coupled to any system and tunable in frequency, it can be used to build hybrid quantum devices [9] [12] to establish coupling between otherwise incompatible systems.

Strong cooperativity is the regime where information gets transferred between the modes and read out faster than the decoherence of the system. Many interesting quantum effects have been demonstrated in the optomechanical domain, including sideband cooling to ground state [13] [14], enhanced precision measurement beyond the standard quantum limit [15] [16], and squeezed light [17] [18]; however, it remains a challenge to implement optomehchanical system in the strong single-photon cooperativity regime, due to limited coupling compared to the damping of the oscillators. While linear equations of motion suffice to formulate the intrinsic optomechanical coupling and interaction for existing optomechanical systems, nonlinearity is required to access mechanical states that are higher in the hierarchy of non-classical states, exhibiting stronger quantum effects such as negativity in Wigner function or violation of Bell-type inequalities. This will truly allow for a full optical control over the mechanical state on the single quantum level and offer quantum advantage in universal information processing and computing [19].

To access the nonlinear regime with weak intrinsic single-photon coupling, one method is to introduce nonlinearity in other stages of the experiment, such as the measurement backaction-induced nonlinearity at the detection stage with the use of single photon detectors [20]. This scheme has been widely implemented in the field of quantum optics and cavity-QED [21]. For optomechanics in particular, the detection of one photon scattered by the mechanics heralds the creation or annihilation of one phonon in the coupled mode. The strong projective measurement on the optical field alters and heralds the state of the mechanics, enabling quantum control over its preparation, manipulation, readout and verification. Moreover, conditional state preparation can be used to generate multi-body entanglement via postselection on detection events. It can be shown that postselection enables the state to carry more information, giving rise to a non-classical advantage [22].

This protocol has been demonstrated by several groups in the field of optomechanics. In particular, Painter group at Caltech has shown phonon counting and behaviors resembling a phonon laser using a photonic crystal made of silicon nanobeam (GHz) [23]. Gröblacher (Delft) and Aspelmeyer (Vienna) groups have demonstrated various non-classical effects in a similar device ($\sim$ 1 pg), where they verify the generation of non-classical entanglement between a photon-phonon pair, single phonon Fock state, entanglement between two remote nanomechanical resonators and quantum teleporation [24] [25] [26] [27]. Polzik group (Niels Bohr Insititute) has shown phonon counting and ground state cooling with a membrane resonator ($\sim$ 2 ng and 1 MHz) [28]. Vanner group (Oxford) shows a heralded multi-phonon-subtracted pre-cooled mechanical state which is non-Gaussian as verified by tomography in a Brillouin-optomechanical system [29] [30]. The single photon detection scheme and conditional state preparation are thus a prominent means in generating and manipulating non-Gaussian mechanical state and multi-body macroscopic entanglement in the presence of limited coupling.

It was first demonstrated in the 19th century that light carries momentum and exerts a radiation-pressure force when interacting with other matter [31]. Bilateral unitary coupling between the two can thus be established when the perturbation on the matter in turn imprints its motion on the electromagnetic field without loss of information. Since then, a wide range of optomechanical systems have been implemented which can be categorized by their various coupling forces (unitary forces such as radiation pressure force [32], electrostriction [1], and dipole forces [33]), type of resonators (such as Fabry-Perot cavities, microtoroids [34], whispering gallery mode of a superfluid He droplet [35]), operating frequency of the light (GHz to THz) and mechanics (Hz to GHz), type of mechanical elements and their effective mass (from nanoscale membrane [36] to suspended mirros of kilogram [37]).

In this work, we use a fiber Fabry-Perot cavity filled with ~ 1 ng of superfluid ^{4}He, where the motional state of ^{4}He density fluctuation is coupled to an optical cavity mode in the telecom range via electrostriction. Unique properties of superfluid He, such as low optical absorption, zero viscosity, and high thermal conductivity, make it ideal for building an optomechanical system toward stronger coupling and cooperativity. The simple geometry and coupling mechanism of the device give rise to a single-mode coupled system, which is rather unique in optomechanics, as it is often challenging to isolate mechanical coupling. An initial characterization of the device is presented in [2] [38] [39] [1], where they show the quantum fluctuations of the acoustic mode via power spectral density of the auto-correlation and cross-correlation of the Stokes and the anti-Stokes sideband under a heterodyne detection scheme.

I will proceed presenting our progress toward realizing optical quantum control of liquid He motion using a single photon heralding detection scheme. This work is motivated by (i) the necessity to introduce nonlinearity via strong projective measurements to access and manipulate the mechanics on the single quantum level; (ii) developing a potential new platform for quantum information technologies, which has a simple design and is scalable in size and number, operating in the telecom range compatible with fiber communication; (iii) demonstration of macroscopic quantum effects on nanogram (rather straightforward to scale up for our system) of liquid helium, and test for macroscopic quantum theory.

The thesis is structured as follows:

- **Chpater 2** I will provide a formulation of the dynamics of an optomechanical system, and some well-known results arising from optomechanical interaction. I will highlight the importance of achieving a nonlinear regime in quantum optomechanics, and the motivation for using a single photon counting scheme. I will also describe the working principle of our system with superfluid He.

- **Chpater 3** I introduce the definition of photon coherences and the use of photon statistics in characterizing quantum states. I will highlight its relevance in verification of non-classicality. I will discuss the hierarchy for non-classicality, as some states exhibit behaviors that are ”more quantum” and cannot be explained by the formulation of those states from a lower tier.

- **Chpater 4** describes the experiemntal setup and procedure, which is mainly to implement a photon counting scheme and protocol.

- **Chpater 5** gives the characterization of our device and demonstration of standard optomechanical effects such as sideband asymmetry and backaction via single photon counting.

- **Chpater 6** shows measurements on phonon coherences of the thermal state of superfluid He up to the fourth-order. I will also discuss our measurements on phonon-subtracted and -added thermal states, which is prepared and probed via postselection.

- **Chpater 7** shows the characterization of multimode coupling, and the model to account for its deviation from the assumed single mode coupling regime imposed by the orthogonality condition in our system.
- **Chpater 8** I will summarize the work presented in this thesis and discuss the outlook for future work related to this experiment.

Chapter 2

Quantum optomechanics

In this chapter I will provide the formulation of the canonical optomechanical system and some relevant signature effects arising from optomechanical interaction. I will then provide an overview of the field of optomechanics, in particular, the implementation of nonlinear optomechanics in the quantum regime. I will then discuss the motivation for implementing the single photon counting scheme to access the nonlinear regime. Finally I will give a description of our optomechanical system, including its implementation with superfluid helium and its coupling mechanism.

2.1 Canonical optomechanical system

An optomechanical system is implemented by coupling light to some mechanical degree of freedom. An optical cavity is often used to enhance the coupling to a mechanical resonator involving any arbitrary forms of mechanical excitations. Figure 2.1 shows the schematic of a canonical optomechanical system, where a Fabry-Perot cavity with one movable end-mirror is attached to a spring. The cavity optical field exerts a radiation pressure force on the mechanical motion of the mirror. The change in the mirror position in turn changes the cavity resonant frequency, thus establishing the coupling between the optical and the mechanical degree of freedom.

2.1.1 Fabry-Perot cavity

We first formulate the dynamics of the optical mode. A single optical mode $\hat{a}$ in a lossless system is described by the simple harmonic oscillator Hamiltonian,

$$\hat{H}_\mathrm{c} = \hbar\omega_\mathrm{c}(\hat{a}^\dagger\hat{a} + \frac{1}{2}) \tag{2.1}$$

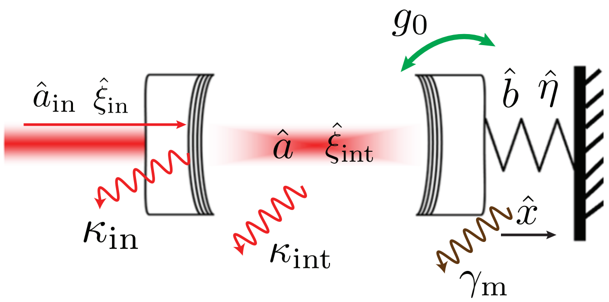

Figure 2.1: Schematic of a canonical optomechanical system, where a Fabry-Perot cavity with one movable end-mirror is attached to a spring. Wiggly arrows describe the various dissipation associated to each port that couples the optical mode to the environment.

where ω_{c} is the optical mode frequency and $\hat{a}$ the annihilation operator. The Heisenberg equation of motion of the mode is given by

$$\dot{\hat{a}} = -\frac{i}{\hbar}[\hat{a}, \hat{H}_{\text{c}}] = -i\omega_{\text{c}}\hat{a} \tag{2.2}$$

To include the couplings of mode $\hat{a}$ to the environment, we apply the input-output theory [40] [41] to model the various quantum fluctuations or drive coupled to the system via each of its ports. Each port is associated to an input mode and corresponding dissipation. In the canonical system, we have two ports, the internal ("int") loss port whose input is the vacuum noise $\hat{\xi}_{\text{int}}$ with a damping rate κ_{int}; and the input port ("in") whose input is $\hat{\xi}_{\text{in}} + \hat{a}_{\text{d}}(t)$ with a damping rate κ_{in}. $\hat{a}_{\text{d}}(t)$ is the drive applied to the cavity. The equation of motion in equation 2.2 is thus modified to

$$\dot{\hat{a}} = -i\omega_{\text{c}}\hat{a} - \frac{\kappa_{\text{c}}}{2}\hat{a} + \sqrt{\kappa_{\text{int}}}\hat{\xi}_{\text{int}} + \sqrt{\kappa_{\text{in}}}\hat{\xi}_{\text{in}} + \sqrt{\kappa_{\text{in}}}\hat{a}_{\text{d}}(t) \tag{2.3}$$

where $\kappa_{\text{c}} = \kappa_{\text{int}} + \kappa_{\text{in}}$ is the total damping rate of the cavity. Here we assume the input mirror is the lower reflectivity side, hence most of the external loss occurs through the input mirror with κ_{in}. In the rotating frame of the cavity frequency ω_{c}, we have $\hat{a} \to \hat{a}e^{-i\omega_{\text{c}}t}$ such that

$$\dot{\hat{a}} = -\frac{\kappa_{\text{c}}}{2}\hat{a} + \sqrt{\kappa_{\text{int}}}\hat{\xi}_{\text{int}} + \sqrt{\kappa_{\text{in}}}\hat{\xi}_{\text{in}} + \sqrt{\kappa_{\text{in}}}a_{\text{d}}e^{-i\Delta t} \tag{2.4}$$

under a classical coherent drive $\hat{a}_{\text{d}}(t) \to a_{\text{d}}e^{-i\omega_{\text{d}}t}$. The drive has a steady amplitude of a_{d}, frequency ω_{d}, and drive detuning $\Delta = \omega_{\text{d}} - \omega_{\text{c}}$. For a drive power of P_{d}, the rate of photons sent to the optical cavity is $\langle a_{\text{d}}^* a_{\text{d}} \rangle = P_{\text{d}}/(\hbar\omega_{\text{d}})$.

It is helpful to identify the intracavity field as the sum of a classical field $\bar{a}e^{-i\Delta t}$ and a quantum fluctuation field $\delta\hat{a}$, such that $\hat{a} = (\bar{a} + \delta\hat{a})e^{-i\Delta t}$. It follows that the optical fluctuation is described by

$$\delta\hat{a} = -\frac{\kappa_{\mathrm{c}}}{2}\delta\hat{a} + \sqrt{\kappa_{\mathrm{int}}}\hat{\xi}_{\mathrm{int}} + \sqrt{\kappa_{\mathrm{in}}}\hat{\xi}_{\mathrm{in}} \tag{2.5}$$

Meanwhile, the cavity has a steady state amplitude

$$\bar{a} = \frac{1}{\kappa_{\mathrm{c}}/2 - i\Delta}\sqrt{\kappa_{\mathrm{in}}}a_{\mathrm{d}} \equiv \chi_{\mathrm{c}}[\Delta]\sqrt{\kappa_{\mathrm{in}}}a_{\mathrm{d}} \tag{2.6}$$

where $\chi_{\mathrm{c}}[\omega]$ is the cavity susceptibility. The intracavity photon number is thus given by

$$n_{\mathrm{c}} = \langle \bar{a}^* \bar{a} \rangle = \frac{\kappa_{\mathrm{in}} P_{\mathrm{d}}/(\hbar\omega_{\mathrm{d}})}{\kappa_{\mathrm{c}}^2/4 + \Delta^2} \tag{2.7}$$

Finally, we note that the vacuum noise operators $\hat{\xi}_i$ have the following important correlation relations that characterize the field properties, including

$$\langle \hat{\xi}_i(t)\hat{\xi}_j(t') \rangle = \langle \hat{\xi}_i^\dagger(t)\hat{\xi}_j^\dagger(t') \rangle = 0 \tag{2.8}$$

$$\langle \hat{\xi}_i^\dagger(t)\hat{\xi}_j(t') \rangle = 0 \tag{2.9}$$

$$\langle \hat{\xi}_i(t)\hat{\xi}_j^\dagger(t') \rangle = \langle \hat{\xi}_i^\dagger(t)\hat{\xi}_j(t') \rangle + [\hat{\xi}_i(t), \hat{\xi}_j^\dagger(t')] = \delta_{ij}\delta(t - t') \tag{2.10}$$

which follow the commutation relations obeyed by any operators associated to the independent Markovian bath coupled to each port [39],

$$[\hat{\xi}_i(t), \hat{\xi}_j^\dagger(t')] = \delta_{ij}\delta(t - t') \tag{2.11}$$

$$[\hat{\xi}_i^\dagger(t), \hat{\xi}_j(t')] = 0 \tag{2.12}$$

2.1.2 Mechanical resonators

For the canonical mechanical resonator, we consider the mechanical mode $\hat{b}$ to be coupled to a thermal bath with no external mechanical drive. There is thus only one coupled port whose input is the thermal noise $\hat{\eta}$ with a total mechanical damping γ_{m}. The equation of motion of $\hat{b}$ is thus given by

$$\begin{aligned}\dot{\hat{b}} &= -\frac{i}{\hbar}[\hat{a}, \hat{H}_{\mathrm{m}}] - \frac{\gamma_{\mathrm{m}}}{2}\hat{b} + \sqrt{\gamma_{\mathrm{m}}}\hat{\eta} \\ &= -(i\omega_{\mathrm{m}} + \frac{\gamma_{\mathrm{m}}}{2})\hat{b} + \sqrt{\gamma_{\mathrm{m}}}\hat{\eta} \end{aligned} \tag{2.13}$$

where ω_{m} is the mechanical frequency, and the bare mechanical oscillator Hamiltonian is given by

$$\hat{H}_{\mathrm{m}} = \hbar\omega_{\mathrm{m}}(\hat{b}^\dagger\hat{b} + \frac{1}{2}) \tag{2.14}$$

By Fourier transforming equation 2.13, we have

$$i\omega\hat{b}[\omega] = -(i\omega_\mathrm{m} + \frac{\gamma_\mathrm{m}}{2})\hat{b}[\omega] + \sqrt{\gamma_\mathrm{m}}\hat{\eta} \tag{2.15}$$

The mechanical mode is thus described by

$$\hat{b}[\omega] = \frac{1}{\gamma_\mathrm{m}/2 - i(\omega - \omega_\mathrm{m})}\sqrt{\gamma_\mathrm{m}}\hat{\eta} \equiv \chi_\mathrm{m}[\omega]\sqrt{\gamma_\mathrm{m}}\hat{\eta} \tag{2.16}$$

where $\chi_\mathrm{m}[\omega]$ is the susceptibility of a bare mechanical resonator.

Note that the creation and annihilation operators are related to the position and momentum of the mechanical motion by $\hat{x} = x_\mathrm{ZPF}(\hat{b} + \hat{b})$ and $\hat{p} = im_\mathrm{eff}\omega_\mathrm{m}x_\mathrm{ZPF}(\hat{b} - \hat{b})$, where the effective mass of the mechanics is m_eff, and the zero-point fluctuation of the mechanical motion is given by

$$x_\mathrm{ZPF} = \sqrt{\frac{\hbar}{2m_\mathrm{eff}\omega_\mathrm{m}}} \tag{2.17}$$

Note that the mechanical displacement in the ground state is thus $\langle 0|\hat{x}^2|0\rangle = x_\mathrm{ZPF}^2$.

The correlations of the thermal noise operator $\hat{\eta}$ associated with any Markovian bath at temperature T are given by

$$\langle\hat{\eta}_i^\dagger(t)\hat{\eta}_j(t')\rangle = n_\mathrm{th}\delta_{ij}\delta(t-t') \tag{2.18}$$

$$\langle\hat{\eta}_i(t)\hat{\eta}_j^\dagger(t')\rangle = \langle\hat{\eta}_i^\dagger(t)\hat{\eta}_j(t')\rangle + [\hat{\eta}_i(t), \hat{\eta}_j^\dagger(t')] = (n_\mathrm{th}+1)\delta_{ij}\delta(t-t') \tag{2.19}$$

where we apply the general Markovian commutation relation in equation 2.12, and $n_\mathrm{th} = 1/(e^{\hbar\omega_\mathrm{m}/(k_\mathrm{B}T)}-1)$ is the occupation number following Bose-Einstein statistics[1]. The power spectral density (PSD) of $\hat{b}^\dagger$ and $\hat{b}$ can thus be computed using equation 2.16 such that

$$\langle\hat{b}^\dagger[\omega]\hat{b}[-\omega]\rangle = \frac{\gamma_\mathrm{m}}{(\gamma_\mathrm{m}/2)^2 + (\omega+\omega_\mathrm{m})^2}\langle\hat{\eta}^\dagger[\omega]\hat{\eta}[-\omega]\rangle \propto n_\mathrm{th} \tag{2.20}$$

$$\langle\hat{b}[\omega]\hat{b}^\dagger[-\omega]\rangle = \frac{\gamma_\mathrm{m}}{(\gamma_\mathrm{m}/2)^2 + (\omega-\omega_\mathrm{m})^2}\langle\hat{\eta}[\omega]\hat{\eta}^\dagger[-\omega]\rangle \propto n_\mathrm{th}+1 \tag{2.21}$$

The difference of a single phonon in the mechanical PSDs is the well-known phenomenon of sideband asymmetry, originating from the correlation relation of the quantum noise operator in equations 2.18 and 2.19.

---

[1] Note that the correlation relation in equation 2.18 is generic for all noise operators associated with a weakly coupled Markovian bath. For $\hat{\xi}$ in equation 2.10, the optical radiation's occupation of the thermal bath is negligible at room temperature (optical frequency usually $\omega_\mathrm{c} \gg (k_\mathrm{B}T_\mathrm{room}/\hbar)$). $\hat{\xi}$ is thus effectively a vacuum noise operator for $n_\mathrm{th} \to 0$.

2.1.3 Optomechanical coupling

We can thus write the total Hamiltonian of the coupled system as

$$\hat{H}_{\text{OM}} = \hbar\omega_{\text{c,eff}}\hat{a}^\dagger\hat{a} + \hbar\omega_{\text{m}}\hat{b}^\dagger\hat{b} \tag{2.22}$$

In the canonical system, the mechanical motion modulates the cavity length, which is related to the bare cavity frequency by $\omega_{\text{c}} = \pi c q / L_{\text{cav}}$. c is the speed of light and q some integer representing the longituidinal mode number. The effective optical resonant frequency is thus given by

$$\begin{aligned}\hat{\omega}_{\text{c,eff}} &= \frac{\pi c q}{L_{\text{cav}} + \hat{x}} = \omega_{\text{c}}(1 + \frac{\hat{x}}{L_{\text{cav}}})^{-1} \\ &= \omega_{\text{c}} + \frac{\partial\hat{\omega}_{\text{c,eff}}}{\partial x}\hat{x} + \mathcal{O}(\hat{x}^2) \approx \omega_{\text{c}} + (\frac{\partial\hat{\omega}_{\text{c,eff}}}{\partial x}x_{\text{ZPF}})(\hat{b} + \hat{b}^\dagger) \end{aligned} \tag{2.23}$$

where the coupling is linearized under the expansion of $\hat{\omega}_{\text{c,eff}}$ to the first order of $\hat{x}$ given that $\hat{x} \ll L_{\text{cav}}$. We define the single photon optomechanical coupling as

$$g_0 \equiv \frac{\partial\hat{\omega}_{\text{c,eff}}}{\partial x}x_{\text{ZPF}} \tag{2.24}$$

which characterizes the coupling strength between a single photon and a single phonon. Equation 2.22 thus becomes

$$\hat{H}_{\text{OM}} = \hbar\omega_{\text{c}}\hat{a}^\dagger\hat{a} + \hbar\omega_{\text{m}}\hat{b}^\dagger\hat{b} + \hbar g_0\hat{a}^\dagger\hat{a}(\hat{b}^\dagger + \hat{b}) \tag{2.25}$$

Equations of motion of the coupled modes, $\hat{a}$ and $\hat{b}$, are thus described by

$$\dot{\hat{a}} = -\frac{\kappa_{\text{c}}}{2}\hat{a} - ig_0(\hat{b} + \hat{b}^\dagger)\hat{a} + \sqrt{\kappa_{\text{int}}}\hat{\xi}_{\text{int}} + \sqrt{\kappa_{\text{in}}}\hat{\xi}_{\text{in}} + \sqrt{\kappa_{\text{in}}}a_{\text{d}}e^{-i\Delta t} \tag{2.26}$$

$$\dot{\hat{b}} = -(i\omega_{\text{m}} + \frac{\gamma_{\text{m}}}{2})\hat{b} - ig_0\hat{a}^\dagger\hat{a} + \sqrt{\gamma_{\text{m}}}\hat{\eta} \tag{2.27}$$

The last term in the Hamiltonian 2.25 can be understood as the interaction term where the radiation pressure force $\hat{F}_{\text{RP}} = \hbar g_0\hat{a}^\dagger\hat{a}/x_{\text{ZPF}}$ acts on the mechanical displacement $\hat{x}$. We linearize the interaction term $\hat{H}_{\text{int}} = \hbar g_0\hat{a}^\dagger\hat{a}(\hat{b}^\dagger + \hat{b})$ with $\hat{a} = \bar{a} + \delta\hat{a}$, such that

$$\begin{aligned}\hat{H}_{\text{int}} &= \hbar g_0\bar{a}^2(\hat{b}^\dagger + \hat{b}) + \hbar g_0\bar{a}(\hat{b}\delta\hat{a}^\dagger + \hat{b}^\dagger\delta\hat{a}) + \hbar g_0\bar{a}(\hat{b}^\dagger\delta\hat{a}^\dagger + \hat{b}\delta\hat{a}) \\ &= \hat{H}_{\text{ss}} + \hat{H}_{\text{bs}} + \hat{H}_{\text{pdc}} \end{aligned} \tag{2.28}$$

The linearization is valid under the criteria that $|g_0(\hat{b} + \hat{b}^\dagger)| \ll \kappa_{\text{c}}$, or the less strict criteria $g_0 \ll \kappa_{\text{c}}$, under which single photon decaying with τ cannot be resolved by the mechanics [42]. This allows us to drop the terms in the equations of motion that are quadratic in optical fluctuation $\delta\hat{a}$ and mechanical fluctuation $\delta\hat{b}$. The first term describes the average radiation pressure force inducing a steady state mechanical displacement, while the latter two terms resemble a beam splitter-like interaction (create one quanta as one quanta is

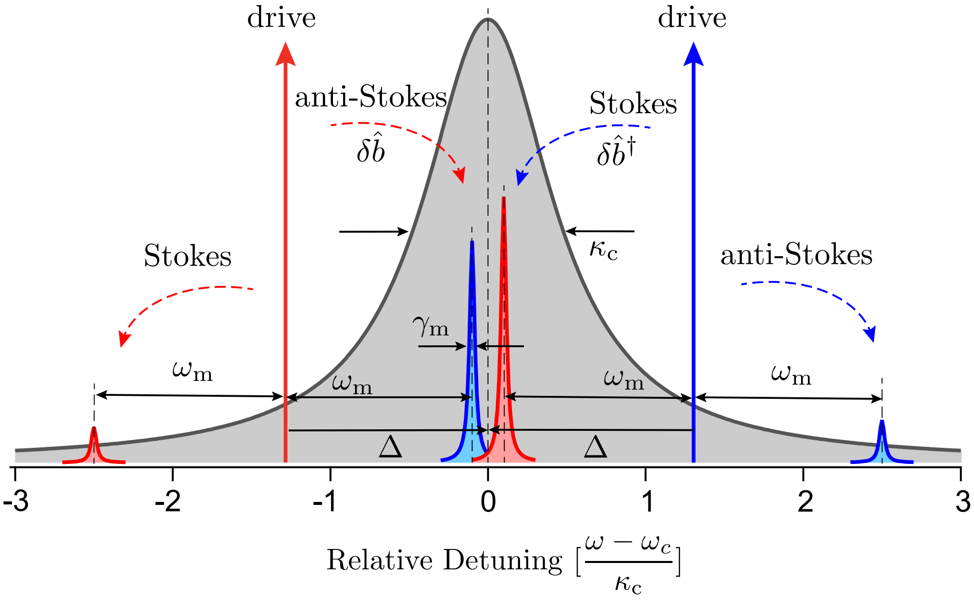

Figure 2.2: Schematic showing the drive tone and mechanical sidebands under optical cavity filtering in the sideband-resolved regime. The anti-Stokes sideband of the red drive (corresponding to the annihilation of one phonon and a beam splitter-like interaction) and the Stokes sideband of the blue drive (corresponding to the creation of one phonon and a parametric down conversion-like interaction) are resonant with the optical cavity.

destroyed) and a parametric down conversion-like interaction (create or destroy a pair of quanta simultaneously) respectively.

By solving the linearized equations of motion of the coupled optical and mechanical modes given by,

$$\delta\dot{\hat{a}} = -(\frac{\kappa_c}{2} - i\Delta)\delta\hat{a} - ig_0\bar{a}(\delta\hat{b} + \delta\hat{b}^\dagger) + \sqrt{\kappa_{int}}\hat{\xi}_{int} + \sqrt{\kappa_{in}}\hat{\xi}_{in} \tag{2.29}$$

$$\delta\dot{\hat{b}} = -(i\omega_m + \frac{\gamma_m}{2})\delta\hat{b} - ig_0(\bar{a}\delta\hat{a}^\dagger + \bar{a}^*\delta\hat{a}) + \sqrt{\gamma_m}\hat{\eta} \tag{2.30}$$

it can be shown that the optical fluctuation $\delta\hat{a}$ can be written as the sum of a mechanical motion-dependent part and a vacuum noise part, $\delta\hat{a} = \delta\hat{a}^\dagger_{\hat{x}}[\omega] + \delta\hat{a}_{\hat{\xi}}[\omega]$, where [39]

$$\delta\hat{a}^\dagger_{\hat{x}}[\omega] = -ig_0\bar{a}\chi_c[\omega + \Delta](\delta\hat{b}[\omega] + \delta\hat{b}^\dagger[\omega]) \tag{2.31}$$

$$\delta\hat{a}_{\hat{\xi}}[\omega] = \chi_c[\omega + \Delta](\sqrt{\kappa_{int}}\hat{\xi}_{int} + \sqrt{\kappa_{in}}\hat{\xi}_{in}) \tag{2.32}$$

where we expand $\hat{b}$ around the steady state solution to be $\bar{b} + \delta\hat{b}$. Note that $\delta\hat{a}^\dagger_{\hat{x}}[\omega]$ is the sum of two parts, $\delta\hat{a}_{\delta\hat{b}}[\omega]$ and $\delta\hat{a}_{\delta\hat{b}^\dagger}[\omega]$.

For $\delta\hat{a}_{\delta\hat{b}}[\omega] \propto \chi_c[\omega + \Delta]\delta\hat{b}[\omega]$, we note that $\delta\hat{b}[\omega]$ is centered around $+\omega_m$ (equation 2.21). $\delta\hat{a}_{\delta\hat{b}}[\omega]$ is thus known as the anti-Stokes scattered sideband that is only resonant with the cavity under a red-detuned drive ($\Delta = \omega_d - \omega_c \approx -\omega_m$) due to the optical cavity filtering characterized by $\chi_{\mathrm{c}}[\omega + \Delta]$. It corresponds to the operator $\hat{H}_{\mathrm{bs}}$.

Similarly, we have $\delta\hat{b}^{\dagger}[\omega]$ centering around $-\omega_{\mathrm{m}}$ (equation 2.20), $\delta\hat{a}_{\delta\hat{b}^{\dagger}}[\omega]$ is thus known as the Stokes sideband, which is only resonant with a blue-detuned drive ($\Delta \approx +\omega_{\mathrm{m}}$). It corresponds to the operator $\hat{H}_{\mathrm{pdc}}$. A schematic of the two resonant sidebands are shown in figure 2.2 in the resolved-sideband regime ($\omega_{\mathrm{m}} \gg \kappa_{\mathrm{c}}$).

2.2 Applications of the optomechanical interaction

The formulation of a canonical optomechanical system presented in the preceding section are universal for any optomechanical system which couples one optical mode to one mechanical mode. I will give a brief overview of some of the important phenomena explored and observed in the field of optomechanics as a result of the optomechanical interaction.

2.2.1 Optomechanical cooling

To realize quantum control of a mechanical oscillator, the mechanical state needs to be near ground state. It can be optomechanically cooled via the interaction $\hat{H}_{\mathrm{bs}} = \hbar g_0 \bar{a}(\hat{b}\delta\hat{a}^{\dagger} + \hat{b}^{\dagger}\delta\hat{a})$. A red-detuned drive photon is scattered into the anti-Stokes sideband gaining an energy of $\hbar\omega_{\mathrm{m}}$ while one phonon is absorbed. In the resolved-sideband regime, the cooling process is strongly enhanced by the optical cavity filtering. Similarly, on the blue-detuned side, the drive photon scattered into the Stokes sideband loses an energy of $\hbar\omega_{\mathrm{m}}$ while one phonon is created in the process, resulting in optomechanical amplification in effect.

To derive this backaction effect, we examine the coupled linearized equations of motion (Fourier transformed from equations 2.26 and 2.26),

$$\begin{aligned}
\delta\hat{a}[\omega] &= \delta\hat{a}^{\dagger}_{\hat{x}}[\omega] + \delta\hat{a}_{\hat{\xi}}[\omega] \\
&= -ig_0\bar{a}\chi_{\mathrm{c}}[\omega+\Delta](\delta\hat{b}[\omega] + \delta\hat{b}^{\dagger}[\omega]) + \chi_{\mathrm{c}}[\omega+\Delta](\sqrt{\kappa_{\mathrm{int}}}\hat{\xi}_{\mathrm{int}} + \sqrt{\kappa_{\mathrm{in}}}\hat{\xi}_{\mathrm{in}}) &\quad (2.33)\\
\delta\hat{b}[\omega] &= -ig_0\chi_{\mathrm{m}}[\omega](\bar{a}\delta\hat{a}^{\dagger}[\omega] + \bar{a}^{*}\delta\hat{a}[\omega]) + \chi_{\mathrm{m}}[\omega]\sqrt{\gamma_{\mathrm{m}}}\hat{\eta}[\omega] &\quad (2.34)
\end{aligned}$$

Plugging equation 2.33 into equation 2.34, we have

$$\begin{aligned}
\delta\hat{b}[\omega] &= -g_0^2 n_{\mathrm{c}}(\chi_{\mathrm{c}}[\omega+\Delta] - \chi_{\mathrm{c}}[\omega-\Delta])\chi_{\mathrm{m}}[\omega](\delta\hat{b}[\omega] + \delta\hat{b}^{\dagger}[\omega]) \\
&\qquad - ig_0\chi_{\mathrm{m}}[\omega](\bar{a}\delta\hat{a}^{\dagger}_{\xi}[\omega] + \bar{a}^{*}\delta\hat{a}_{\xi}[\omega]) + \chi_{\mathrm{m}}[\omega]\sqrt{\gamma_{\mathrm{m}}}\hat{\eta}[\omega] \\
&= -i\Sigma[\omega]\chi_{\mathrm{m}}[\omega](\delta\hat{b}[\omega] + \delta\hat{b}^{\dagger}[\omega]) - i\chi_{\mathrm{m}}[\omega]\hat{F}_{\mathrm{RPSN}}[\omega] + \chi_{\mathrm{m}}[\omega]\hat{F}_{\mathrm{th}}[\omega] &\quad (2.35)
\end{aligned}$$

where we define the radiation pressure shot noise as $\hat{F}_{\mathrm{RPSN}}[\omega] = g_0(\bar{a}\delta\hat{a}^{\dagger}_{\xi}[\omega] + \bar{a}^{*}\delta\hat{a}_{\xi}[\omega])$ arising from the vacuum fluctuations of the optical field. And the thermal noise force is defined as $\hat{F}_{\mathrm{th}}[\omega] = \sqrt{\gamma_{\mathrm{m}}}\hat{\eta}[\omega]$. We also have

$$\Sigma[\omega] = -ig_0^2 n_{\mathrm{c}}(\chi_{\mathrm{c}}[\omega+\Delta] - \chi_{\mathrm{c}}[\omega-\Delta]) \qquad (2.36)$$

as the optomechanical self-energy. It acts as an extra force exerted on the mechanics by the optomechanical interaction[39], which is proportional to the mechanical displacement.

Note that the term $\Sigma[\omega]\chi_{\mathrm{m}}[\omega]\delta\hat{b}^{\dagger}[\omega]$ in equation 2.35 is negligible as $\chi_{\mathrm{m}}[\omega]$ centers around $+\omega_{\mathrm{m}}$ while $\delta\hat{b}^{\dagger}[\omega]$ centers around $-\omega_{\mathrm{m}}$. We thus rewrite equation 2.35 as

$$\delta\hat{b}[\omega] = (\hat{F}_{\mathrm{th}}[\omega] - i\hat{F}_{\mathrm{RPSN}}[\omega])\chi_{\mathrm{m,\,eff}}[\omega] \tag{2.37}$$

where we define a modified acoustic susceptibility in response to the extra optical force as

$$\chi_{\mathrm{m,\,eff}}[\omega]^{-1} = \chi_{\mathrm{m}}[\omega]^{-1} + i\Sigma[\omega] \tag{2.38}$$

We can write $\Sigma[\omega] = -i\gamma_{\mathrm{opt}}/2 + \delta\omega_{\mathrm{m}}$ such that $\chi_{\mathrm{m,\,eff}}[\omega]$ can be written in the familiar form

$$\chi_{\mathrm{m,\,eff}}[\omega] = \frac{1}{\frac{\gamma_{\mathrm{m}}+\gamma_{\mathrm{opt}}}{2} - i(\omega - (\omega_{\mathrm{m}} + \delta\omega_{\mathrm{m}}))} \tag{2.39}$$

where we can identify the modified mechanical frequency and damping as

$$\omega_{\mathrm{m,eff}} = \omega_{\mathrm{m}} + \Re(\Sigma[\omega_{\mathrm{m,eff}}]) \tag{2.40}$$

$$\gamma_{\mathrm{m,eff}} = \gamma_{\mathrm{m}} - 2\Im(\Sigma[\omega_{\mathrm{m,eff}}]) \tag{2.41}$$

The change in frequency is known as the optical spring effect, and the change in damping rate is known as the optomechanical damping (positive change) or anti-damping (negative change) effect. Note that $\Sigma[\omega]$ is evaluated at $\omega_{\mathrm{m,eff}}$, leading to a nonlinear equation. Under the weak coupling regime where $|g_0\bar{a}| \ll \kappa$, we approximate the solution by evaluating at ω_{m}[2] such that

$$\Sigma[\omega_{\mathrm{m}}] = g_0^2 n_{\mathrm{c}}\left(\frac{1}{(\Delta + \omega_{\mathrm{m}}) + i\kappa_{\mathrm{c}}/2} + \frac{1}{(\Delta - \omega_{\mathrm{m}}) - i\kappa_{\mathrm{c}}/2}\right) \tag{2.42}$$

It follows that

$$\gamma_{\mathrm{opt}} = -2\Im(\Sigma[\omega_{\mathrm{m,eff}}]) = \frac{4g_0^2 n_{\mathrm{c}}\kappa_{\mathrm{c}}}{4(\Delta + \omega_{\mathrm{m}})^2 + \kappa_{\mathrm{c}}/4} - \frac{4g_0^2 n_{\mathrm{c}}\kappa_{\mathrm{c}}}{4(\Delta - \omega_{\mathrm{m}})^2 + \kappa_{\mathrm{c}}/4} \tag{2.43}$$

Under a red-detuned drive where $\Delta = -\omega_{\mathrm{m}}$, the optomechanical damping is $\gamma_{\mathrm{opt}} = +4n_{\mathrm{c}}g_0^2/\kappa_{\mathrm{c}}$, resulting in an increase in the effective mechanical damping. Under a blue-detuned drive where $\Delta = +\omega_{\mathrm{m}}$, we instead have $\gamma_{\mathrm{opt}} = -4n_{\mathrm{c}}g_0^2/\kappa_{\mathrm{c}}$, resulting in a reduced effective mechanical damping. The dynamical backaction of optomechanical damping thus allows for optomechanical cooling. The complete theory of sideband cooling can be found in works [42] and [43].

In the weak coupling regime, it is shown that the minimum phonon number can be achieved in the absence of couplings to the external thermal bath (intrinsic $\gamma_{\mathrm{m}} = 0$) is

---

[2] Since $\kappa_{\mathrm{c}} \gg \gamma_{\mathrm{m,eff}}$, we can assume $\omega_{\mathrm{m}} \approx \omega_{\mathrm{m,eff}}$ is a constant across $\gamma_{\mathrm{m,eff}}$.

given by

$$n_{\text{min,0}} = (\frac{\kappa_{\text{c}}}{4\omega_{\text{m}}})^2 < 1 \tag{2.44}$$

in the resolved-sideband regime. Taking into account of the coupling to the thermal environment with n_{th} at a rate of γ_{m}, we have

$$n_{\text{min}} = \frac{\gamma_{\text{opt}} n_{\text{min,0}} + \gamma_{\text{m}} n_{\text{th}}}{\gamma_{\text{opt}} + \gamma_{\text{m}}} \tag{2.45}$$

setting the lower limit for optomechanical cooling. We thus define the dimensionless constant,

$$C = \frac{\gamma_{\text{opt}}}{\gamma_{\text{m}}} = \frac{4n_{\text{c}} g_0^2}{\kappa_{\text{c}} \gamma_{\text{m}}} \tag{2.46}$$

known as the multi-photon cooperativity, which is an important parameter that characterizes the strength of optomechanical coupling with respect to the decoherence of the system. The thermal decoherence time of the system is $1/(n_{\text{th}}\gamma_{\text{m}})$, which is the time it takes for one quanta of the mechanical motion to decohere from the ground state. A cooperativity of

$$C = \frac{\gamma_{\text{opt}}}{\gamma_{\text{m}}} > n_{\text{th}} \tag{2.47}$$

thus indicates that the optomechanical coupling, or the entanglement or state transfer between a photon and a phonon, is faster than the thermal decoherence. This sets the coherence threshold of quantum information transfer between the optical and the mechanical mode. A larger C allows for sideband cooling to the lowest occupancy limit in equation 2.44. This quantum coherence limit further leads to the definition of the quantum cooperativity

$$C_{\text{qu}} = \frac{C}{n_{\text{th}}} = \frac{\gamma_{\text{opt}}}{\gamma_{\text{m}} n_{\text{th}}} \tag{2.48}$$

which takes into account of the thermal bath.

While one can lower the bath temperature n_{th} to reach near mechanical ground state, the lowest temperature the dilution fridge could continuously cool down to is around 20 mK. It thus requires a mechanical resonator of ω_{m} on the GHz scale to reach near ground state via cryogenic cooling [24]. To allow for a wider range of mechanical platform, pre-cooling via the optomechanical cooling is more efficient and desirable. Large cooperativity past the quantum coherence threshold ($C > 1$) has been realized by implementing mechanical resonators of ultra-high mechanical quality factor, such as a silicon nitride membrane which is cooled to the lowest mechanical mode temperature reported in the μK range [44]. Other micro-/nano-mechanical oscillators that are optomechanically cooled to the quantum ground state ($n_{\text{m}} < 1$) include works in [14] [13].

2.2.2 Quantum state transfer

Note that under $\hat{H}_{\text{int}}$, the optomechanical interaction is unitary, which preserves information transfer between the optical and the mechanical modes, and enables its application in quantum communication and information processing. The beam-splitter interaction $\hat{H}_{\text{bs}} = \hbar g_0 \bar{a}(\hat{b}\delta\hat{a}^\dagger + \hat{b}^\dagger\delta\hat{a})$ describes the quantum state transfer between light and mechanics. As proposed in [45], a pulsed drive is used to enable a full state swap between the $\delta\hat{a}$ excitation and the $\hat{b}$ excitation.

This protocol has been implemented in experiments extensively. For instance, the state of a travelling microwave field is transferred into and readout coherently from a mechanical oscillator at the single quantum level [46]. Under a strong microwave excitation, the interaction is enhanced by the multi-photon coupling to the strong coupling regime ($g_0\sqrt{n_\text{c}} > \kappa_\text{c}$) with a $C \gg 1$, which simultaneously swaps the states of the microwave resonator and the mechanical oscillator, at a rate faster than its decoherence. Via the same interaction, a measurement pulse is applied after sometime to read out the state of the mechanics, showing the ability of such a system to store information. Bidirectional coherent conversion between microwave and optical light has also been demonstrated [47] [48] [49], where a low frequency mode and a high frequency mode can be coupled to a mechanical mode mediating the conversion between the two fields. It demonstrates the potential of an optomechanical system in enabling large-scale quantum information network [50] [3] [51].

2.2.3 Squeezed light and mechanics

Optomechanical interaction has also been proposed and demonstrated to generate and manipulate non-classical states of light and mechanics. One prominent example is a squeezed mechanical state, which is of great importance in high precision measurement, such as the detection of gravitational waves [52]. A squeezed optical drive can be used to directly transfer the squeezing from the optical field to the mechanics [53]. In general, to generate quadrature squeezing, a parametric coupling for $\hat{b}$ is introduced and the mechanical hamiltonian is in the form of $(\hat{b}^2+\hat{b}^{\dagger 2})$. A modulating laser can be applied to parametrically drive the mechanical oscillator as proposed in [54], which compensates the optomechanically induced frequency shift. The squeezing Hamiltonian is given by

$$\hat{H}_{\text{sq,m}} = \frac{\hbar\delta\omega_\text{m}/\cos{(2\omega_\text{m}t)}}{2}(\hat{b}^2 + \hat{b}^{\dagger 2}) \tag{2.49}$$

in the rotating frame of ω_m, where $\delta\omega_\text{m}$ is the optical spring, or change in mechanical frequency given by equation 2.40. The drive is thus modulated at $\delta\omega_\text{d}(t) = \delta\omega_\text{m}/\cos{(2\omega_\text{m}t)}$, which results in the quadrature-squeezed mechanical mode

$$\hat{b}(t) = \cosh{(\delta\omega_\text{d}t)}\hat{b}(0) - i\sinh{(\delta\omega_\text{d}t)}\hat{b}^\dagger(0) \tag{2.50}$$

displaying exponential squeezing in the mechanical quadrature operator as time increases ($\propto e^{-\delta\omega_\text{m}t}$).

On the other hand, schemes for generating squeezed noise in the optical field are proposed in [55] [56] which play an important role in quantum enhanced metrology and optical communication. An optical cavity with an intensity-dependent length acts as a nonlinear Kerr medium inside the cavity, which induces a squeezing effect. While the magnitude of squeezing is limited by the thermal decohrence of the mechanics, sub-shot-noise optical squeezing has been demonstrated in the implementation of cavity optomechanics with ultracold atoms [12]. The atoms' center of mass alters cavity resonant frequency linearly, which is thus coupled to the quantum fluctuation of radiation pressure analogous the the mirror displacement. The strongly multi-photon-coupled system acts as a high-gain, nonlinear parametric amplifier for the quantum fluctuation of the intensity [57]. Similarly, it has also been demonstrated in a silicon micromechanical resonator coupled to a photonic cavity, where steady-state squeezing below the vacuum noise level is shown in the reflected light that is sent in to the cavity for continuous position measurement [17].

The generation of squeezed state is also closely related to the realization of a backaction-evading or quantum non-demolition (QND) measurement on the optical amplitude quadrature or the photon number statistics [58] [59]. When measuring the two quadratures of motion simultaneously, the precision of the pair of noncommuting observables is limited by the Heisenberg uncertainty principle. However, since the optomechanical system commutes with the observable, measurement on a single observable can be up to an arbitrary precision and achieve quantum nondemolition [60] [61]. In general, a QND measurement for the energy requires the coupling of the probe to be proportional to the squared generalized coordinate of the system [60] [62]. A QND measurement of the mechanical position using a pulsed scheme is demonstrated in [63] [64]. Since the pulse is applied over duration much shorter than the period of the mechanical motion, a measurement on the position is backaction-evading and only perturbs the momentum and leaves the position unchanged, such that

$$\begin{aligned} X_{\mathrm{c}}^{\mathrm{out}} &= X_{\mathrm{c}}^{\mathrm{in}}, \qquad & P_{\mathrm{c}}^{\mathrm{out}} &= P_{\mathrm{c}}^{\mathrm{in}} + \chi X_{\mathrm{m}}^{\mathrm{in}} \\ X_{\mathrm{m}}^{\mathrm{out}} &= X_{\mathrm{m}}^{\mathrm{in}}, \qquad & P_{\mathrm{m}}^{\mathrm{out}} &= P_{\mathrm{m}}^{\mathrm{in}} + \chi X_{\mathrm{c}}^{\mathrm{in}} + \Omega_{\mathrm{p}} \end{aligned} \tag{2.51}$$

where X and P are the dimensionless amplitude and phase quadrature, χ characterizes the strength of the position measurement, and Ω_{p} describes the classical momentum transfer from the measurement. The precision is thus only limited by the optical phase noise [65], as the position measurement suppresses the position variance ($\sigma_{\mathrm{X_M}} \propto 1/\chi^2$) while the momentum variance increases ($\sigma_{\mathrm{P_M}} \propto \chi^2$). A subsequent pulse is sent after 1/4 of the mechanical period to measure initial momentum and reduces phonon occupancy ($n_{\mathrm{eff}} = (\sigma_{\mathrm{X_M}}\sigma_{\mathrm{P_M}})^{1/2}$). The QND protocol gives rise to cooling and quantum state preparation that is based on quantum measurement and feedback [66] [7] [4].

2.2.4 Quantum entanglement

Entanglement between the optical and the mechanical modes can be used to demonstrate quantum interference among quantum states in a macroscopic system. Consider a state initiated in

$$|\Psi(0)\rangle = |\alpha\rangle_{\mathrm{c}} \otimes |\beta\rangle_{\mathrm{m}} \tag{2.52}$$

where $|\alpha\rangle_{\mathrm{c}}$ and $|\beta\rangle_{\mathrm{m}}$ are the initial coherent states of the optical field and the mechanics. It can be shown that under time evolution in the interaction picture, at time t the state is evolved to an entangled state in the form of

$$|\Psi(t)\rangle = \sum_{n=0}^{\infty} c_n e^{i\phi_n(t)} |n\rangle_{\mathrm{c}} \otimes |\phi_n(t)\rangle_m \tag{2.53}$$

where $c_{\mathrm{n}}|n\rangle_{\mathrm{c}}$ is the coherent state of the cavity field in the basis of Fock states, $\phi_n(t)$ is the phase shift acquired from the optomechanical coupling, and $|\phi_n(t)\rangle_m = |\beta e^{-it}\rangle_{\mathrm{m}}$ the time evolved mechanical coherence state [67] [68]. At $t = 2\pi$, depending on the value of g_0-dependent $\phi_n(0)$, non-classical state of the cavity field can be acquired in the form of multi-component Schrodinger cat state, such as

$$|\Psi_{\mathrm{cat}}\rangle_{\mathrm{c}} = e^{-|\alpha|^2/2} \Big[(\frac{1+i}{2}) | + \alpha\rangle_{\mathrm{c}} + (\frac{1-i}{2}) | - \alpha\rangle_{\mathrm{c}} \Big] \tag{2.54}$$

Furthermore, through the entanglement, non-classical states of the mechanics can be generated via conditional measurements on the field [68]. For instance, it can be shown that a measurement of the x-quadrature of the field at time projects the mechanical state into

$$|\Psi(x)\rangle_{\mathrm{m}} = \sum_{n=0}^{\infty} c_n e^{i\phi_n(\pi)} \langle x|n\rangle |\phi_n(\pi)\rangle_m \tag{2.55}$$

derived from equation 2.53, which is a non-classical state of superposition of spatially separated coherent states, resembling a Schrodinger cat state with different values of coherent components. Generation of such non-classical optical and mechanical state are advantageous in optical communication application and in the study of quantum mascroscopic coherence.

The proposal for continuous-variable entanglement stems from the Einstein-Podolsky-Rosen (EPR) paper [69], even preceding the notion of quantum entanglement, where they consider a two-particle state correlated in their positions and momenta,

$$\int dx_1 dx_2 \psi(x_1, x_2) |x_1, x_2\rangle \propto \int dx |x, x-u\rangle \tag{2.56}$$

where the two-particle wave function is given by $\psi(x_1, x_2) \propto \delta(x_1 - x_2 - u)$. The two particles are perfectly correlated in their positions and momenta ($x_1 - x_2 = u$, $p_1 + p_2 = 0$), such that the measurement on one state allows one to predetermine that of the other state with certainty [70]. The origin of such correlations must originate from a quantum theory which cannot be explained by any classical theory. Quantum entanglement thus has the potential in enabling information processing beyond classical bounds [71], sensing beyond standard quantum limit [72] [73] and also test for fundamental quantum theory on massive objects [5].

Experimentally, continuous wave schemes have been proposed to demonstrate genuine multipartite entanglement in the steady state [74] [75] [76] [77]. With a continuous-wave light field, the system is in a stationary state, and the entanglement is verified via quadrature measurement on the continuous-variable of the output light field. The entanglement with the mechanical state thus can only be inferred from the correlations between the optical modes, which often raises ambiguity, as it is shown that separable states can distribute entanglement as well [78].

Alternatively, a pulsed scheme has been proposed and widely used to generate entanglement [79], which is first implemented with atomic ensembles [80]. The quantum control protocol begins with the mechanics optomechanically cooled via the $\hat{H}_{\text{bs}}$. A blue-detuned pulse ("write" drive) is then applied to entangle the states between the mechanics and the optical field via the parametric-down-conversion Hamiltonian $\hat{H}_{\text{pdc}} = \hbar g_0 \bar{a}(\hat{b}^\dagger \delta\hat{a}^\dagger + \hat{b}\delta\hat{a})$, which generates photon-phonon pairs. A two-mode squeezing or entangled state is generated when the optical and the mechanical modes are initiated near ground state. The system is in the multi-photon strong coupling regime during the pulse in order to generate entangled pairs faster than the decoherence of the system. After storing the entangled mechanical state in the system for some time delay, the state is read out with a red-detuned pulse ("read" drive) via $\hat{H}_{\text{bs}}$ mapping the entangled mechanical state to the emerging output field. Variances of the quadrature amplitudes of both the write and read pulses are used to determine the inseparability, or the quantum entanglement criteria of the photon-phonon pair. An EPR-type of entanglement between the mechanics and a microwave field is demonstrated in [81]. Remote entanglement between two micromechanical oscillators is verified in [26]. Furthermore, the pulsed scheme is used to realize quantum teleportation [79] [82] [27], where an input photonic state is transferred to the joint vibrational state of a pair of mechanical resonators. The long memory time and low loss transfer operating on-chip make such a system a desirable candidate as the quantum memory or repeater in a quantum network [3] [83].

The pulsed scheme has the advantage that the system is not limited by more restrictive stability requirements compared to that of a continuous wave scheme. Furthermore, the time sequence of the pulse guarantees a direct and unambiguous verification of correlation that is originated from quantum entanglement [80].

2.3 Nonlinear quantum optomechanics

In the formulation presented in the last section, the optomehcanical interaction is linearized such that

$$\hat{H}_{\text{int}} = \hbar g_0 \hat{a}^\dagger \hat{a}(\hat{b}^\dagger + \hat{b}) \rightarrow \hbar g_0 (\delta\hat{a}^\dagger + \delta\hat{a})(\hat{b}^\dagger + \hat{b}) \tag{2.57}$$

in the assumption of small single-photon optomechanical coupling $g_0 \ll \kappa_{\text{c}}$ which holds true for all of the existing optomechanical systems. As shown in section 2.2 where I give an overview of some of the important results of the optomechanical interaction in the linearized picture, this linearized quadratic Hamiltonian ($\hat{H}_{\mathrm{bs}} + \hat{H}_{\mathrm{pdc}}$) is sufficient in describing these quantum phenomena of interest.

Note that a strong single-photon coupling regime where

$$C_0 = \frac{4g_0^2}{\kappa_{\mathrm{c}}\gamma_{\mathrm{m}}} \gg n_{\mathrm{th}} \tag{2.58}$$

allows us to access the system at the single quantum level, but puts a very strict restriction on the system parameters, including high quality factors of the optical and the mechanical oscillators and the single photon coupling (which scales with $1/L_{\mathrm{cav}}$ and $1/\sqrt{m_{\mathrm{eff}}}$ in the canonical system, thus becoming weaker with more massive objects). While the single-photon strong cooperativity has been achieved with microwave qubits [84] [85] [86] and microwave photons [87], and has also been demonstrated with optical photons in [88], it remains challenging to build systems satisfying the requirement which limits the available platforms suitable for quantum technologies and tests.

In this section, I will give an overview of the experimental methods proposed and implemented to circumvent the single-photon strong coupling restriction, in order to access and manipulate the system on the single quantum level, and generate states exhibiting more exotic quantum nature, such as non-Gaussian states and states with Wigner-function negativity.

2.3.1 Multi-photon strong coupling regime

By the linearized interaction description, optomechanical coupling strength scales with the field amplitude as $g = g_0\sqrt{n_{\mathrm{c}}}$. It is thus a convenient method to circumvent the restriction of a weak g_0 by using a stronger drive such that

$$C = \frac{4n_{\mathrm{c}}g_0^2}{\kappa_{\mathrm{c}}\gamma_{\mathrm{m}}} > n_{\mathrm{th}} \tag{2.59}$$

The system thus operates in the strong multi-photon coupling regime where information is transferred or readout between a single photon and a single phonon at a rate faster than the decoherence, which gives access to the discrete nature of the light and the mechanics.

As discussed in section 2.2, a few interesting results have been demonstrated under this regime, such as optomehcanically cooling the mechanics into its quantum ground state (2.2.1). Non-classical states such as the squeezed optical and mechanical state below shot noise have been generated in this regime as well (2.2.3). While the coupling conveniently scales with the strength of the drive, it also inadverdently introduces unwanted heating to the device and increases thermal decoherence.

2.3.2 Nonlinearity in quantum optomechanics

Here we refer to non-classical states as any state that cannot be described as a statistical mixture of the coherent states. They have highly irregular Glauber-Sudarshan P-function

[89] [90], which exhibits negativity and singular behavior. A more detailed classification and criteria for non-classical states are described in chapter 3. While some states with negative P-function are accessible in the multi-photon strong cooperativity regime, we cannot access the more "quantum" states such as the non-Gaussian (states cannot be describes by a statistical mixture of Gaussian states) or the negative Wigner-function states with a classical drive. Under the linearized interaction, the resulting equations of motions are also linear as shown in equations 2.29 and 2.30. The output state thus remains a Gaussian state (or a state with positive Wigner function) with a Gaussian or a positive-Wigner function state input [42] [19]. The dynamics is intrinsically nonlinear in their equations of motions only under the full cubic interaction in equation 2.57.

While any protocol relying on a single-quadrature measurement can be described in the linearized picture in general [91], nonlinearity needs to be introduced into the formulation of the system to generate non-Gaussian or more exotic states of the quantum nature. For instance, for the Schrodinger cat state describe in equation 2.54, it is stems directly from the time evolution of a coherent state following the cubic interaction Hamiltonian in equation 2.57 [68].

Another prominent example where nonlinearity is required to describe the interaction is the detection of discrete phonon number [92]. As the phonon number operator is given by $\hat{n} = \hat{b}^\dagger \hat{b}$, measurement of the discrete number state of the mechanics is equivalent to a measurement to it energy, or the quadratic $\hat{x}^2$. This requires the optomechanical system to establish a coupling between the light field and the square of its displacement $\hat{x}^2$, instead of $\hat{x}$ in the canonical system, such that the interaction term is in the form of

$$\hat{H}_{\text{int}} = \hbar g_0 \hat{a}^\dagger \hat{a} (\hat{b}^\dagger + \hat{b})^2 \tag{2.60}$$

where the coupling is in the form

$$g_0 \propto \frac{\partial^2 \hat{\omega}_{\text{c}}}{\partial x^2} x_{\text{ZPF}}^2 \tag{2.61}$$

One way to introduce such nonlinearity intrinsic to an optomechanical system is by placing some dielectric object near a node or anti-node of the optical mode inside a cavity, which creates a coupling proportional to $\hat{x}^2$ (at extrema, $\omega_{\text{c}}(x) \propto \hat{x}^2$ to the lowest order for small oscillation amplitude), known as the membrane-in-the-middle setup demonstrated in works [93] [94] [95] [36] [96]). For such systems where the cavity detuning is periodic in the displacement of the dieletric object (partially transparent), the optomechanical system and coupling are said to be dispersive, allowing for a direct measurement on the phonon number or the quantum nature of its energy [97] [98] [99] [100].

Note that with the quadratic coupling, it is still challenging to build an optomechanical system operating in the single-photon strong cooperativity regime. Intrinsic nonlinearity has been more accessible to implement in coupled qubit (in the GHz range)-oscillator systems [101] or coupled atom-cavity system [102], which allows for the manipulation of the mechanical state at the single quantum level, and for the generation and storage of non-Gaussian mechanical states [103]. Regarding its application in information processing with quantum advantage, such full quantum control is desirable with an optomechanical system as well, as it allows for direct coupling to photons of telecom-wavelength travelling in standard telecom optical fibers. In the following section, I will describe a single photon counting scheme that is used to circumvent the restriction due to a weaker coupling.

2.4 Single photon counting scheme

In this work, we adopt the method widely implemented in quantum optics to introduce nonlinearity external to the optomechanical system at various other stages of the experiment [20], such as using a single photon source at the input, which can be transferred and mapped onto the mechanics to generate a single phonon Fock state via the linearized optomechanical interaction. Alternatively, single-photon detection at the measurement stage can be used to generate nonlinearity directly via the measurement backaction. Instead of manipulating the system Hamiltonian or manufacturing specific device parameters, this method introduces nonlinearity through the external fields that interact with the system in the controlling and probing stages. It can be shown that such nonlinearity lifts the strict requirement on a strong or nonlinear coupling [104], and the backaction from single photon detectors is robust against detection efficiency and errors from damping of these system [20].

The scheme of generating a non-Gaussian mechanical such as a Fock state by using a single photon source is formulated in [105]. State transfers of a pair of quantum-correlated light fields to a pair of macroscopic oscillators has also been proposed in [45], where an EPR state in position and momentum of macroscopic objects can be realized. It is also proposed to be used for the generation of quantum superposition of a mirror in a single-photon Michelson interferometer setup, which can be made feasible for gravitational wave detection [106] [107] [108]. Each arm of the interferometer contains a Fabry-Perot cavity, with one of them has a moving mirror at one end. The system is initiated in a mechanical ground state with the moving mirror in arm A as $|0\rangle_{\mathrm{m}}$, and the photon is in a superposition of being in either arm A or B as $|0\rangle_{\mathrm{A}}|1\rangle_{\mathrm{B}} + |1\rangle_{\mathrm{A}}|0\rangle_{\mathrm{B}}$, such that

$$|\psi(0)\rangle = \frac{1}{\sqrt{2}}(|0\rangle_{\mathrm{A}}|1\rangle_{\mathrm{B}} + |1\rangle_{\mathrm{A}}|0\rangle_{\mathrm{B}})|0\rangle_{\mathrm{m}} \tag{2.62}$$

The state at time t is then given by

$$|\psi(t)\rangle \propto |0\rangle_{\mathrm{A}}|1\rangle_{\mathrm{B}}|0\rangle_{\mathrm{m}} + e^{i(g/\omega_{\mathrm{m}})^2(\omega_{\mathrm{m}}t - \sin\omega_{\mathrm{m}}t)}|1\rangle_{\mathrm{A}}|0\rangle_{\mathrm{B}}|g/\omega_{\mathrm{m}}(1 - e^{-i\omega_{\mathrm{m}}t})\rangle_{\mathrm{m}} \tag{2.63}$$

where in the second term, the mechanics is oscillating in a coherent state with amplitude, $g/\omega_{\mathrm{m}}(1 - e^{-i\omega_{\mathrm{m}}t})$, under the influence of the radiation pressure force exerted by the single photon in arm A [109]. The mechanical state thus gets entangled and disentangled from the photon every $t = 2\pi/\omega_{\mathrm{m}}$ periodically, indicated by the visibility of the photon interference. It is further shown that arbitrary mechanical quantum states can be prepared in the single photon interferometer setup via the postselection of the time of arrival of the output single photon [110] [68].

Note that such schemes still in general require the system to operate in the single

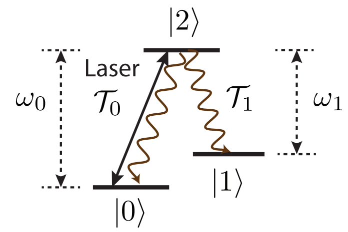

Figure 2.3: Structure of a three-level atom, which is used to produce entangled atomic states under a weak laser pulse and projective measurement protocol.

photon strong coupling regime, where the zero point fluctuation of the mechanics is at least larger than the linewidth of the cavity, in order to produce the nonlinear effects. As for the qubit-mechanics coupled systems [101] [85] [111] [112], where a measurement on the discrete state of the qubit directly projects the mechanical state onto highly non-classical states, we can introduce nonlinearity effectively in an optomechanical system via a strong projective measurement on the optical field enabled by the single photon detector [20] [113].

Conditional state preparation

The probabilistic measurement protocol for preparation of a heralded non-Gaussian state, such as an entangled state, is pioneered in quantum optics with atomic states, where non-linearity is induced by state projection measurement [114].

Consider two three-level atoms A and B with a Lambda configuration with $|0\rangle$ and $|1\rangle$ being the ground state and $|2\rangle$ the excited state, as shown in figure 2.3. The atoms are prepared in the ground state $|0\rangle_\mathrm{A}|0\rangle_\mathrm{B}$. A weak laser pulse at ω_0 is sent to the atoms on resonance with the $|0\rangle \leftrightarrow |2\rangle$ transition. Suppose a detector is placed in the middle of the two atoms and is sensitive to only the frequency $\sim \omega_1$, corresponding to the spontaneous emission $|2\rangle \rightarrow |1\rangle$ occurring at a rate $\mathcal{T}_1$ for the atom in the excited state $|2\rangle$. The detection of a photon thus indicates that the pulse prepares a superposition of states $|0\rangle_\mathrm{A}|2\rangle_\mathrm{B}$ and $|2\rangle_\mathrm{A}|0\rangle_\mathrm{B}$ just before the detection. Since the detector cannot distinguish where the detected photon is emitted from, an entangled state in the form of

$$|\Psi\rangle = \frac{1}{\sqrt{2}}(|0\rangle_\mathrm{A}|1\rangle_\mathrm{B} + e^{i\phi}|1\rangle_\mathrm{A}|0\rangle_\mathrm{B}) \tag{2.64}$$

is heralded upon detection.

Note that in such a probabilistic measurement, there is no requirement on a strong interaction, or a high probability of exciting the atom under the initial drive. In fact, the drive is required to be sufficiently weak, such that the probability of exciting both atoms ϵ^2 is much smaller than exciting one ϵ. Suppose the detector cannot resolve photon arrivals in very close proximity, a detection actually heralds the state $|1\rangle_\mathrm{A}|1\rangle_\mathrm{B}$ instead if both atoms are excited, decreasing the fidelity of the entangled state. Thus, an excitation probability of $\epsilon \ll 1$ by the weak pulse is required.

Entanglement is effectively produced by the storng projective measurement on the photon state, or equivalently induced by the backaction of the measurement. Such a detector can be formulated as a collection of atoms, among which one atom C is coupled to the pair of atoms A and B. Upon the detection of a photon, atom C is left in the excited state $|e\rangle$. The density operator of atoms A and B conditioned on a detection event is thus governed by the master equation

$$\frac{d}{dt}\rho = \Big[\mathcal{L}^C + \sum_{i=A,B} (\mathcal{L}^i + \mathcal{S}^{i,C} + \mathcal{J}^{i,C})\Big]\rho \tag{2.65}$$

where $\mathcal{L}^j$ is the Liouvillian action on some atom [115]. For instance, we have

$$\mathcal{L}^C\rho = -\frac{\gamma}{2}(\sigma^C_{ee}\rho + \rho\sigma^C_{ee}) + \gamma\sigma^C_{gg}\rho\sigma^C_{eg} \tag{2.66}$$

acting on the detector atom C, where γ is the detector bandwidth and $\sigma_{ij} = |i\rangle\langle j|$. $\mathcal{S}^{i,C}$ and $\mathcal{J}^{i,C}$ account for the dipole-dipole and re-absorption interaction between atom i and C. A full model describing the system using this master equation method is shown in [114] [115] [116].

A strong projective measurement is made possible for our experiment with the development of single photo detectors in the last few decades. In particular, fiber-coupled superconducting nanowire single photon detectors (SNSPD) are particularly useful for experiments in the near-infrared regime (as compared to single-photon avalanche diodes which is much more efficient for visible photons) [117] [118] [119]. SNSPD is made of a narrow superconducting wire which is biased with a current just below its critical current. The absoprtion of an incident photon breaks its superconductivity locally, where the current flows through causing the current density to increase in adjacent regions as well. A normal resistance region is thus formed across the wire, yielding a voltage spike to be detected. For near-infrared detection, sub-50 picosecond dead time (inactive time after a photon detection event to restore superconductivity, mostly sub-100 nanosecond) [120], sub-50 picosecond jitter time (variation in the delay time between optical input and electric signal output) [121], sub-1 Hz dark count rate (output in the absence of any incident photons), and $> 90\%$ detection efficiency has been demonstrated in experiments [122].

DLCZ protocol

To enable robust quantum communication between massive particles (such as atomic ensembles) over distant lossy channels, Duan, Lukin, Cirac and Zoller propose the DLCZ protocol which generates strong entanglement, stores the state and transfer the state with high fidelity via conditional measurement [123] [21] [124]. The DLCZ protocol originates from the scheme entangling single atom through single-photon interference as discussed in the last section 2.4, which does not require a non-classical input light and super high finesse resonator for the light and mechanics. Entangled states of atomic ensembles [125] [126] [127] [10], spin of the ions or qubits, and macroscopic solid bodies (bulk vibration mode in diamonds [10]) have been demonstrated via a DLCZ protocol.

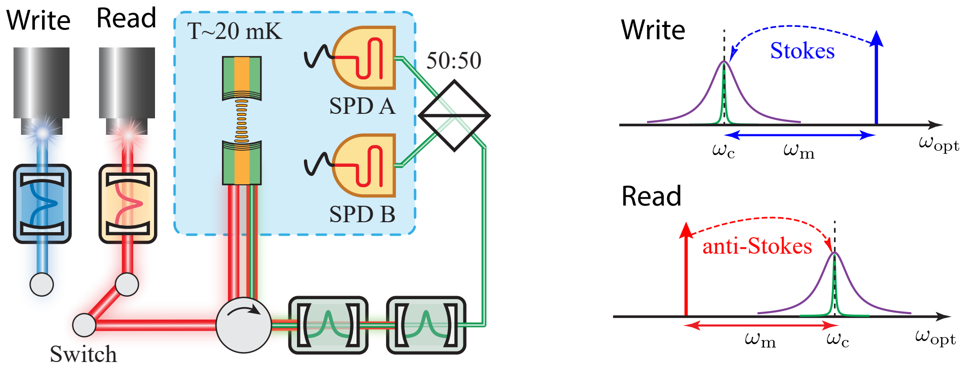

Figure 2.4: Schematic for the DLCZ protocol to generate, store, and read out an entangled state of the optomechanical system.

For a coupled light-mechanical system, a DLCZ protocol to generate entangled states between a single photon and phonon is shown in figure 2.4. The optomechanical device and a pair of SNSPDs are placed in a dilution fridge. The mechanical mode can be either cryogenically cooled by the fridge, or further optomechanically cooled via sideband cooling to near its ground state $n_{\mathrm{th}} \ll 1$. The system is thus initiated approximately in $|\Psi_{\mathrm{OM}}\rangle = |0\rangle_{\mathrm{c}}|0\rangle_{\mathrm{m}}$.

At time $t = 0$, a blue-detuned pulse at $\Delta = +\omega_{\mathrm{m}}$ is applied, denoted as ”write”, creating two-mode squeezing via the interaction $\hat{H}_{\mathrm{pdc}} = \hbar g_0 \bar{a}(\hat{b}^\dagger \delta\hat{a}^\dagger + \hat{b}\delta\hat{a})$, driving the state into

$$|\Psi_{\mathrm{OM}}\rangle = |0\rangle_{\mathrm{c}}|0\rangle_{\mathrm{m}} + \sqrt{p_{\mathrm{b}}}|1\rangle_{\mathrm{c}}|1\rangle_{\mathrm{m}} + p_{\mathrm{b}}|2\rangle_{\mathrm{c}}|2\rangle_{\mathrm{m}} \tag{2.67}$$

where the excitation probability $p_{\mathrm{b}} \ll 1$ and higher order terms can be neglected. The detection of a single Stokes-scattered photon following the write pulse thus heralds an entangled state of $|1\rangle_{\mathrm{c}}|1\rangle_{\mathrm{m}}$.

After some time τ, a second pulse, which is red-detuned by $\Delta = -\omega_{\mathrm{m}}$, acts on the system by $\hat{H}_{\mathrm{bs}} = \hbar g_0 \bar{a}(\hat{b}^\dagger \delta\hat{a} + \hat{b}\delta\hat{a}^\dagger)$. We denote it as the ”read” pulse as it reads out the mechanical state through a state swap. A subsequent detection of a single anti-Stokes scattered photon thus heralds a successful state transfer from the mechanics. The arrival time of each write and read pair of photons are recorded by the SNSPDs. The pulse sequence is repeated to collect sufficient photon counts for calculating their statistics. After post-selecting on the pulse sequences where a single photon is emitted following each pulse, the auto-coherences and cross-coherences of these photon pairs can be used to verify the non-classical nature of the heralded entangled photon-phonon state.

Photon statistics and their correspondence with non-classicality, and the fidelity of the heralded state are discussed further in chapter 3. Note that compared to a homodyne or heterodyne measurement, where the continuous-quadrature variable is measured, we can directly access the discrete energy levels or phonon numbers of the mechanical motion made possible by the projective measurement via single photon detection. Phonon

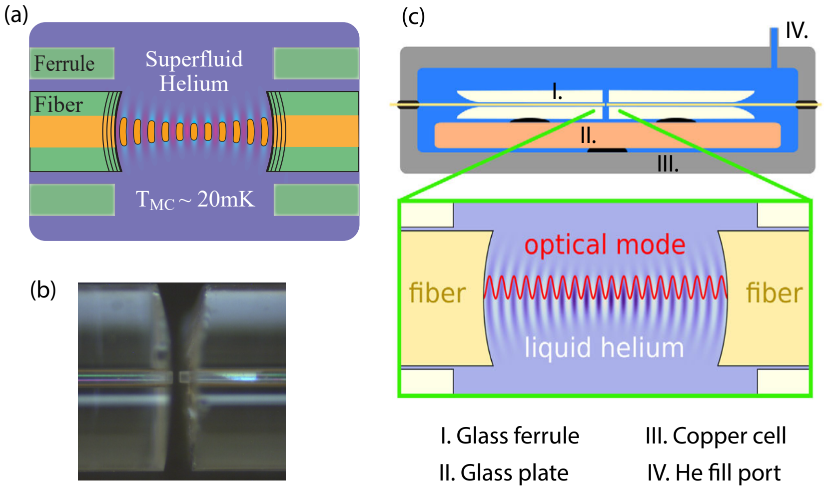

Figure 2.5: Device schematic: A fiber Fabry-Perot cavity filled with superfluid ^{4}He.

counting [23] [28], single phonon Fock state [25], entangled photon-phonon pair [24], entangled remote mechanical oscillators, quantum teleportation and Bell test [26] [128] have been demonstrated with various nanomechanical oscillators using the DLCZ scheme. A characterization of the non-classical state of a single phonon-added or -subtracted thermal mechanical state has also been shown in [29] [30]. Single photon detection thus provides access to the non-Gaussian and negative Wigner function regime in optomechanics despite that the systems cannot achieve single-photon strong coupling yet, enabling further studies in quantum communication technology and macroscopic quantum effects.

2.5 Optomechanics with superfluid He

In this section, I will explain the design and coupling mechanism of our optomechanical device, which is made a fiber Fabry Perot cavity filled with superfluid ^{4}He as shown in figure 2.5.

The Fiber Perot cavity is formed by a pair of single-mode telecom (1550 nm) optical fibers[3]. The fibers are ablated by a CO_2 laser by the Jakob Reichel Lab (Paris) [129] [130] [38] to produce a concave indentation at the fiber ends. Optical Distributed Bragg Reflector (DBR) made of layers of silica and tantala is then deposited onto the indentations to form highly reflective mirrors. A more detailed documentation of the building of the cavity is presented in [38].

It is formed by a pair of optical fibers coated with dbr mirrors with high reflectivity to form a fabry perot cavity. They are aligned by a pair of glass ferrules, and housed in a copper cell. Since the glass ferrules are very narrow confining the position of the fibers, the cavity does not require any in situ alignment. The device is placed inside a dilution fridge below 20mK. The cavity is filled with superfluid helium via the capillary

---

[3] IVG fiber: Cu 1300 and Cu 1300/200. SMF-28 fiber with a 125 μm diameter.

$n_{\mathrm{He}}\lambda_{\mathrm{c}}$	$\omega_{\mathrm{c}}/2\pi$	L_{cav}	$\kappa_{\mathrm{c}}/2\pi$	η_{κ}	$\Delta\omega_{\mathrm{FSR}}/2\pi$	$\mathcal{F}_{\mathrm{c}}$	Q_{c}
1548.3 nm	193.63 THz	70.3 μm	47.2 MHz	0.29	2.08 THz	4.4×10^{4}	4.1×10^{6}

λ_{ac}	$\omega_{\mathrm{ac}}/2\pi$	$\gamma_{\mathrm{ac}}/2\pi$	$\Delta\omega_{\mathrm{FSR}}/2\pi$	$\mathcal{F}_{\mathrm{ac}}$	Q_{ac}
754.5 nm	315.4 MHz	3250 Hz	1.7 MHz	500	9.7×10^{4}

V_{mode}	m_{eff}	$g_0/2\pi$	n_{th}	C_0	$C_{\mathrm{qu,0}}$
5000 $\mu\mathrm{m}^3$	$\sim$ 1 ng	4600 Hz	1.4	5.5×10^{-4}	3.9×10^{-4}

Table 2.1: Parameters of the superfluid He-filled optomechanical device.

line into the fill port. The mechanical element consists of $\approx$ 1 ng of superfluid He. Table 2.1 shows important parameters of the device. Characterization of some of the important parameters is shown in chapter 5, and measurement of standard optomechanical effects such as quantum sideband asymmetry and optomechanical backaction are shown in section 5.3.

2.5.1 Coupling mechanism

The ”mechanical” element in our device is the acoustic excitation, in particular, the density fluctuations of superfluid He, which is indicated by the blue wave in the schematic in figure 2.5.

In the canonical system, the coupling arises from the radiation pressure force. Here we make use of the electrostrictive force instead. As the electromagentic field inside the He-filled cavity polarizes the He atom, causing the atoms to move along the electric field gradient. The change in the density profile of He inside the cavity thus changes the dielectric constant (the index of refraction locally), in turn changing the detuning of the cavity. The electrostriction-induced interaction is fully described by the formulation of the canonical system as discussed in section 2.1, as they are both unitary and bi-directional and fully captured by the interaction term in the Hamiltonian.

Spatial profile of the electric field inside the cavity can be written as

$$\nabla^2 E(\vec{r}) + \frac{\omega^2 n_{\mathrm{He}}^2(\vec{r})}{c^2} E(\vec{r}) = 0 \tag{2.68}$$

where n_{He} is the spatial profile of the index of refraction of He inside the cavity. Assume the interaction introduces small perturbation to ω, $E(\vec{r})$ and n_{He}, we write the perturbed terms as

$$n_{\mathrm{He}}^2(\vec{r}) = \bar{n}_{\mathrm{He}}^2 + 2\bar{n}_{\mathrm{He}}\delta n_{\mathrm{He}}(\vec{r}) \tag{2.69}$$

$$\omega^2 = \bar{\omega}^2 + 2\bar{\omega}\delta\omega \tag{2.70}$$

where $\bar{n}_{\mathrm{He}} = 1.0261$ for superfluid ^{4}He. By applying the proper boundary condition [38], we can find that the detuned frequency by the interaction is given by

$$\delta\omega = -\omega\frac{\int_V \delta n_{\mathrm{He}}(\vec{r})I(\vec{r})d^3\vec{r}}{\int_V n_{\mathrm{He}}(\vec{r})I(\vec{r})d^3\vec{r}} \tag{2.71}$$

Local change in index of refraction can be related to the change in density profile by the Clausius-Mossotti relation, such that $\rho_{\mathrm{He}} \propto (n_{\mathrm{He}} - 1)$ [131]. The optomechanical coupling is thus proportional to the overlap integral between the intensity of the field and the density fluctuation of the helium. Note that electrostriction gives rise to an elastic force, such that the energy stored in the acoustic excitation can be written as

$$U_{\mathrm{ac}} = \frac{1}{2}\int_V \mathcal{K}_{\mathrm{He}}\Big(\frac{\delta\rho_{\mathrm{He}}(\vec{r})}{\rho_{\mathrm{He}}}\Big)^2 d^3\vec{r} = \hbar\omega_{\mathrm{ac}}\hat{b}^\dagger\hat{b} \tag{2.72}$$

where $\mathcal{K} = v_{\mathrm{He}}^2\rho_{\mathrm{He}}$ is the Young modulus of helium. Re-writing optomechanical coupling defined in section 2.1, we have

$$\begin{aligned} g_0 &= \frac{\partial\hat{\omega}_{\mathrm{c,eff}}}{\hat{b}+\hat{b}^\dagger} = \partial\hat{\omega}_{\mathrm{c}}\sqrt{\frac{\hbar\omega_{\mathrm{ac}}}{4U_{\mathrm{ac}}}} \\ &= \omega_{\mathrm{c}}\sqrt{\frac{\hbar\omega_{\mathrm{ac}}}{4\mathcal{K}}}\Big(\frac{n_{\mathrm{He}}^2-1}{2n_{\mathrm{He}}^2}\Big)\frac{\int_V \delta\rho_{\mathrm{He}}(\vec{r})I(\vec{r})d^3\vec{r}}{(\int_V I(\vec{r})d^3\vec{r})\sqrt{\int_V(\delta\rho_{\mathrm{He}}(\vec{r}))^2 d^3\vec{r}}} \end{aligned} \tag{2.73}$$

Note that we thus have

$$g_0 \propto \omega_{\mathrm{c}}\sqrt{\frac{\omega_{\mathrm{ac}}}{V_{\mathrm{mode}}}} \tag{2.74}$$

where the acoustic mode volume $V_{\mathrm{mode}} \sim L_{\mathrm{cav}}w_0^2 \sim 5000\mu\mathrm{m}^3$ with w_0 being the beam waist of the cavity. As the transverse mode size $\sim w_0^2 \propto L_{\mathrm{cav}}$, we have $V_{\mathrm{mode}} \propto\sim L_{\mathrm{cav}}^2$. The single-photon optomechanical coupling thus approximately scales with $1/L_{\mathrm{cav}}$.

Wavelength matching

One important advantage of the simple geometry of our device is that wave equations for the optical mode and the acoustic mode share the same boundary conditions, set by the mirror ends of the fiber cavity. While the optical mode is confined by the highly reflective optical DBR, the acoustic wave is confined by the large acoustic impedance mismatch at the He-fiber boundary ($v_{\mathrm{SiO2}} \gg v_{\mathrm{He}}$). Note that the wave equation for helium also shares the same form of that of the optical mode as shown in equation 2.68, such that

$$\nabla^2\phi_{\mathrm{He}}(\vec{r}) + \frac{\omega^2}{v_{\mathrm{He}}^2}\phi_{\mathrm{He}}(\vec{r}) = 0 \tag{2.75}$$

where $\phi_{\mathrm{He}} \propto \delta\rho_{\mathrm{He}}(\vec{r})/\rho_{\mathrm{He}}$ is the velocity potential of He, derived from the continuity equation [39].

It can be shown that solutions to these wave equations can be written as the orthonormal set of Hermite-Gaussian modes (see chapter 7 for more details). Note that the coupling is proportional to the overlap integral between the three-dimensional Gaussian modes of $|E(\vec{r})|^2$ and $\delta\rho_{\text{He}}(\vec{r})$. For simplicity, we will consider the 1D plane wave case here which closely corresponds to the longituidinal profile of the waves as illustrated in figure 2.5(c). For the optical mode which has a node at the boundary, we have

$$I(z) \propto |E(z)|^2 \propto \sin^2\left(\pi q^{\text{opt}}_{\lambda/2} z/L_{\text{cav}}\right) \tag{2.76}$$

And for the acoustic wave which is confined by the impedance mismatch, it has an anti-node at the boundary, following

$$\delta\rho(z) \propto \cos\left(\pi q^{\text{ac}}_{\lambda/2} z/L_{\text{cav}}\right) \tag{2.77}$$

where $q^{\text{opt}}_{\lambda/2}$ and $q^{\text{ac}}_{\lambda/2}$ are the number of half-wavelength inside the cavity.

Optomechanical coupling between modes of different mode number is thus given by

$$\begin{aligned} g_0^{q^{\text{opt}},q^{\text{ac}}} \propto \int_0^{L_{\text{cav}}} I(z)\delta\rho(z)dz &\propto \int_0^{L_{\text{cav}}} \sin^2\left(\pi q^{\text{opt}}_{\lambda/2} z/L_{\text{cav}}\right)\cos\left(\pi q^{\text{ac}}_{\lambda/2} z/L_{\text{cav}}\right) \\ &= \int_0^{L_{\text{cav}}} \left(1-\cos\left(2\pi q^{\text{opt}}_{\lambda/2} z/L_{\text{cav}}\right)\right)\cos\left(\pi q^{\text{ac}}_{\lambda/2} z/L_{\text{cav}}\right) \\ &\propto \delta_{2q^{\text{opt}}_{\lambda/2},q^{\text{ac}}_{\lambda/2}} \end{aligned} \tag{2.78}$$

By the orthogonality of the Gaussian modes, the coupling is only nonzero if

$$q^{\text{ac}}_{\lambda/2} = 2q^{\text{opt}}_{\lambda/2} \tag{2.79}$$

or in terms of wavelength of the mode, $\lambda_{\text{ac}} = \lambda_{\text{c}}/2$, where λ_{c} is the wavelength in He.

The geometry of the device thus guarantees an efficient single mode coupling, where one optical mode only interacts with the motion of one acoustic mode and vice versa. This is rather unique for an optomechanical system where it is usually challenging to isolate the optical mode from the motions of various mechanical modes [132] [42]. While multimode optomechanics give rise to various interesting results (such as enhanced nonlinear dynamics [133] [134], phonon lasing based on population inversion [135], non-reciprocal couplings in phononic device [136]), in quantum applications where we want to implement full quantum control over the system with high fidelity, the single mode condition allows for more convenient data taking and analysis without the need to distinguish the source of photons. We assume the exact same boundary conditions in a one-dimensional model in deriving the wavelength matching condition. In chapter 7 we measure to what extent this approximation holds for our system.

2.5.2 Superfluid He

Liquid helium was first found to exhibit abnormal behavior below 2.2 Kelvin in 1938 [137], such as diminishing viscosity, resembling a superfluid. Several theories have been proposed to formulate its transition [138] [139], and its properties have been extensively studied in experiments in the past few decades, which can be found in [140] [141]. Several properties of superfluid ^{4}He make it an ideal candidate for implementing an optomechanical system (as opposed to the fermion ^{3}He which transitions into superfluid at a much lower temperature $<$ 2.5 mK).

First, superfluid is predicted to have a very low optical absorption of infrared photons under low temperature ($<$ 300 mK) of less than 10^{-12} mm^{-1}, due to its large bandgap ($<$ 20 eV [142]). There also exists no chemical impurities under its low transition temperature ($\sim$ 500 mK), and no structural defects in a liquid. It also does not have any viscosity, such that the dominant damping in He is the three-phonon process scaling as T^4 [143]. A superfluid system thus could acheive ultra-low optical and acoustic loss.

A combination of low optical absorption and high thermal conductivity [140] makes it an ideal mechanical element to be able to handle a large optical drive (or the drive-induced thermal phonons) without excessive heating, as it can be thermalized by the bath (dilution fridge) effectively.

Superfluid He is thus ideal for implementing an optomehcanial system toward higher cooperativity, which requires high finesse optical cavity and mechanical resonator, handling of large optical power and low thermal phonons. Furthermore, fluid He which conformally fills the cavity allow for the simple geometry of the system, which does not require in situ alignment and leads to the single-mode wavelength matching condition.

There are several existing optomechanical experiments with superfluid helium, including the Schwab (CalTech) group where ultra-high Q ($> 10^8$) acoustic resonators in bulk ^{4}He has been built to study macroscopic quantized motion [144] [145]. The Bowen group [146] demonstrated sideband cooling of excitations in superfluid He film coupled to a microtoroid. There are systems studying the He ripplon [147] or He droplets [148] [35]. However, no stronger quantum effects have been shown to date.

Chapter 3

Nonclassicality Criteria

As proposed in section 2.4, photon counting statistics is used to characterize and verify the quantum feature of a state. I will start this chapter by describing the temporal coherences of a thermal state in both the classical and quantum picture. I will then discuss how coherence is used to classify the nature of the distribution function, which exhibits quantum features of the state and verify its non-classicality.

3.1 Temporal coherences of a thermal state

3.1.1 Classical theory of optical coherence

While the fluctuations in optical fields are too rapid to be observed directly, interferometric experiments allow for the measurements of the correlations between these fluctuations at different space-time points, which reveal the statistical properties and classification of the associated field. Although interferometry first emerged in astronomy to measure the spatial coherences of the light emitted by visible stars and to determine their stellar angular diameters [149] [150], some of the resulting observations of unexpected correlation properties also sparked debate on the nature of light, suggesting the need of a complete quantum mechanical theory to describe electromagnetic radiation [151] [152]. We will first examine the coherence functions with the classical theory of light, where the electric field is a classical variable.

Two types of interferometry are shown in Figure 3.1. The Mach-Zehnder Interferometer shown on the left measures the electric field correlations. It is equivalent to the Michelson interferometer where the light paths are recombined before detection [149]. The intensity of the light time averaged over some measurement period at the output port is $\langle I_{\text{out}}(t)\rangle \propto \langle |E_{\text{out}}(t)|^2\rangle$, where $E_{\text{out}}(t) = \frac{1}{2}E(t_1) + \frac{1}{2}E(t_2)$ and $t - t_i$ is the time it takes to travel from the input port to the output port via path i, assuming 50/50 lossless

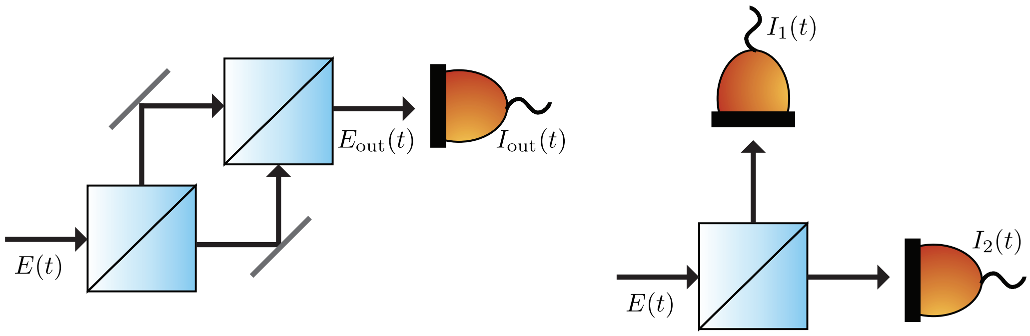

(a) Field Interferometer (b) Intensity Interferometer

Figure 3.1: Schematic of a Michelson-type field interferometer (a) and a Hanbury Brown and Twiss-type intensity interferometer (b).

beamsplitters. We thus have

$$\begin{aligned}\langle I_{\text{out}}(t)\rangle \propto \langle |E_{\text{out}}(t)|^2\rangle &= \frac{1}{4}\Big\langle |E(t_1)|^2 + |E(t_2)|^2 + \Re[E^*(t_1)E(t_2)] + \Re[E(t_1)E^*(t_2)]\Big\rangle \\ &= \frac{1}{4}\left(\Big\langle |E(t_1)|^2\Big\rangle + \Big\langle |E(t_2)|^2\Big\rangle + 2\Re\Big[\Big\langle E^*(t_1)E(t_2)\Big\rangle\Big]\right) \qquad (3.1)\end{aligned}$$

where the last term gives rise to the interference effect. It includes the first-order time correlator of the electric fields $\langle E^*(t)E(t+\tau)\rangle$, evaluating the time average of the product of the electric fields travelling through the two paths with a time delay of τ in between[1]. It follows that the normalized first-order temporal coherence function is defined as

$$g^{(1)}(\tau) \equiv \frac{\langle E^*(t)E(t+\tau)\rangle}{\langle E^*(t)E(t)\rangle} \qquad (3.2)$$

Figure 3.1(b) shows an intensity interferometer instead. This was first demonstrated in the Hanbury Brown and Twiss (HBT) experiment, where the correlation between the photocurrents generated by two spatially separated photomultipliers were measured, demonstrating high-order interference (i.e., correlations between the intensities instead of the first-order interference between fields) [154]. The correlation between the two intensities detected at the output ports is $\langle I_1(t)I_2(t+\tau)\rangle$. By the classical description of light, the intensities detected at the output ports are simply $I_1(t) = I_2(t) = \frac{1}{2}I(t)$ (intensity measured by averaging over a cycle of oscillation), the normalized measured correlation is thus related to the second-order temporal coherence function such that

$$\frac{\langle I_1(t)I_2(t+\tau)\rangle}{\langle I_1(t)\rangle\langle I_2(t)\rangle} = \frac{\langle I(t)I(t+\tau)\rangle}{\langle I(t)\rangle^2} = \frac{\langle E^*(t)E^*(t+\tau)E(t+\tau)E(t)\rangle}{\langle E^*(t)E(t)\rangle^2} \equiv g^{(2)}(\tau) \qquad (3.3)$$

---

[1] $\langle E^*(t_1)E(t_2)\rangle$ is equivalent to $\langle E^*(t)E(t+\tau)\rangle$ with the assumption that the field is ergodic, which means the statistical properties of the field fluctuation do not change with time. Hence, the correlation only depends on delay $\tau = t_2 - t_1$ instead of t_i [153].

For a classical stationary wave with fixed amplitude and phase $E(t) = e^{-i\omega_0 t + i\phi}$, $g^{(2)}(\tau) = 1$ for all τ showing that its intensity is temporally uncorrelated. We can consider a realistic picture of a classical field corresponding to the emission from some atoms (for instance, a conventional gas lamp light source) and its detection corresponding to the absorption of radiation by the atoms (for instance, via photoionization). Although the field is associated with the process of atomic transition, which requires quantum mechanical theory to describe fully [155], it is shown that such light fields, and in general, any thermal radiation[2] can be satisfactorily modeled by a classical collision-broadening theory, where the radiation is emitted from excited atoms undergoing random collision [153]. Such a field produced by N excited radiating atoms is modeled by the sum $E(t) = E_0 e^{-i\omega_0 t}\{\sum_i^N e^{i\phi_i(t)}\}$, where $\phi_i(t)$ describes the random change in the phase of the radiation when a collision occurs.

The field correlator is directly computed as $\langle E^*(t)E(t+\tau) = NE_0^2 e^{-\gamma|\tau|}$, where γ is the mean rate of collision[3]. It follows that

$$g^{(1)}(\tau) = e^{-\gamma|\tau|} \tag{3.4}$$

The second-order coherence is computed similarly as[4]

$$g^{(2)}(\tau) = 1 + |g^{(1)}(\tau)|^2 = 1 + e^{-2\gamma|\tau|} \tag{3.5}$$

We see that $g^{(2)}(0) = 2$ at zero delay for a thermal source, indicating that the average of the joint intensity differentiates from the product of the average intensity measured at the two detectors individually ($\langle I_1(t)I_2(t)\rangle \neq \langle I_1(t)\rangle\langle I_2(t)\rangle$), due to the thermally-induced intensity fluctuation. In particular, the joint detection at zero delay is twice as that at a large delay, at which point they become uncorrelated like a classical stationary wave. More generally, it can be directly computed using the same classical model for a thermal source that

$$\begin{aligned} &\langle I(t)^{\mathrm{l}}\rangle = l!\langle I(t)\rangle^l \\ \text{or}\quad &g^{(l)}(0,\cdots,0) = l! \end{aligned} \tag{3.6}$$

---

[2] Thermal light, also known as chaotic light, is emitted from sources in thermal equilibrium and can be described by blackbody radiation passing through some linear filter such as a cavity [156].

[3] To take the statistical average of the product of $E^*(t)$ and $E(t+\tau)$, we note that the phase change ϕ_i is random, hence the cross terms with different values of i vanishes on average. The field correlator is thus reduced to $\langle E^*(t)E(t+\tau)\rangle = N\langle E_i^*(t)E_i(t+\tau)\rangle \propto \langle e^{i(\phi_i(t+\tau)-\phi_i(t))}\rangle$. Again only the atoms that do not get collided before time τ contribute to the last term, and the probability of which is described by $\int_\tau^\infty p(\tau)d\tau = (1/\tau_\mathrm{c})e^{-\tau/\tau_\mathrm{c}}\mathrm{d}\tau$, where τ_c is the mean time between collision [153].

[4] Cross terms involving fields from different atoms i give an overall zero average. Assuming N is very large such that only the terms with a leading factor of N^2 dominate, we are left with only these two terms in the intensity correlator, $\sum_{i\neq j}^N \Big\langle E_i^*(t)E_j^*(t+\tau)E_j(t+\tau)E_i(t)\Big\rangle \rightarrow N^2\Big\langle E_i^*(t)E_i(t)\Big\rangle^2$, and $\sum_{i\neq j}^N \Big\langle E_i^*(t)E_j^*(t+\tau)E_i(t+\tau)E_j(t)\Big\rangle \rightarrow N^2\Big\langle E_i^*(t)E_i(t+\tau)\Big\rangle^2$. Upon normalization to $N^2\Big\langle E_i^*(t)E_i(t)\Big\rangle^2$ and comparing to the form of $g^{(1)}$ we have equation 3.5 [153].

3.1.2 Quantum optical coherence

We will now examine the coherences using the quantum description of light, where the field is quantized through associating each field mode to a quantum harmonic oscillator [157]. The classical electric field is replaced by the field operator $\hat{E}$, which is written as the sum of a positive and a negative frequency parts, analogous to the right- and left-propagating travelling wave in a free classical field. The photon annihilation and creation operators, $\hat{a}$ and $\hat{a}^\dagger$, can be understood as the process of absorbing one photon from or emitting one to the field mode they act upon, and are associated with the positive and negative frequency parts of the field operator respectively[5].

Photon detection in the quantum picture is described by the absorption of a photon where the field transits to a final state $|f\rangle$ via $\hat{a}|i\rangle$. The probability of photon detection using one single photon detector is thus the sum of the transitional probabilities to all final states (which form a complete basis), given by

$$\sum_f |\langle f|\hat{a}|i\rangle|^2 = \sum_f \langle i|\hat{a}^\dagger|f\rangle\langle f|\hat{a}|i\rangle = \langle i|\hat{a}^\dagger\hat{a}|i\rangle \tag{3.7}$$

Measurements with two single photon detectors are thus analogously described by the absorption of two photons with some time delay τ in between, $\hat{a}(t+\tau)\hat{a}(t)|i\rangle$,

$$\begin{aligned}\sum_f |\langle f|\hat{a}(t+\tau)\hat{a}(t)|i\rangle|^2 &= \sum_f \langle i|\hat{a}^\dagger(t)\hat{a}^\dagger(t+\tau)|f\rangle\langle f|\hat{a}(t+\tau)\hat{a}(t)|i\rangle \\ &= \langle i|\hat{a}^\dagger(t)\hat{a}^\dagger(t+\tau)\hat{a}(t+\tau)\hat{a}(t)|i\rangle \end{aligned} \tag{3.8}$$

For the discussions relevant to this work, we assume the detectors are superimposed in position as viewed by the field, and focus on the temporal correlation to characterize the state of the oscillator. The field is thus evaluated at the same space points. It follows that the l-fold time delayed detection is described by

$$\langle i|\hat{a}^\dagger(t)\hat{a}^\dagger(t+\tau_1)\cdots\hat{a}^\dagger(t+\tau_1+\cdots+\tau_{l-1})\hat{a}(t+\tau_1+\cdots+\tau_{l-1})\cdots\hat{a}(t+\tau_1)\hat{a}(t)|i\rangle \tag{3.9}$$

The l^{th}-order temporal coherence function defined using quantum operators is thus

$$g^{(l)}(\tau_1,\cdots,\tau_{l-1}) \equiv \frac{\langle \hat{a}_0^\dagger\hat{a}_1^\dagger\cdots\hat{a}_{l-1}^\dagger\hat{a}_{l-1}\cdots\hat{a}_1\hat{a}_0\rangle}{\langle\hat{a}_0^\dagger\hat{a}_0\rangle\cdots\langle\hat{a}_{l-1}^\dagger\hat{a}_{l-1}\rangle} \tag{3.10}$$

where $\hat{a}_i = \hat{a}(t+\tau_1+\cdots+\tau_i)$.

For the aforementioned thermal source discussed in section 3.1.1, where a large num-

---

[5] The electric field operator is expressed as $\hat{E}(\mathbf{r},t) = \hat{E}^+(\mathbf{r},t) + \hat{E}^-(\mathbf{r},t)$. The positive frequency part is given by $\hat{E}^+(z,t) \propto \int_0^\infty \sqrt{\hbar\omega}\hat{a}[\omega]e^{-i\omega t}e^{ikz}d\omega$, and the negative frequency part is $\hat{E}^-(z,t) \propto \int_{-\infty}^0 \sqrt{\hbar\omega}\hat{a}[\omega]e^{i\omega t}e^{-ikz}d\omega = \int_0^\infty \sqrt{\hbar\omega}\hat{a}^\dagger[\omega]e^{i\omega t}e^{-ikz}d\omega$, where we use $\hat{a}[-\omega] = \hat{a}^\dagger[\omega]$ [157]. For simplicity the field operator described here is projected onto a single polarized direction and quantized along the z-axis.

ber of modes are excited through some broadening process, the field acquires a continuous spectrum with some finite bandwidth. More generally, the power spectral density (PSD), or the mean energy per angular frequency of any stationary and stochastic process, where the radiative broadening process is homogeneous (i.e., atoms absorb and emit light at the same frequency), can be described by a Lorentzian lineshape[6], given by

$$f_{\mathrm{F}}[\omega] = \frac{N}{\pi}\frac{\gamma}{\gamma^2+\omega^2} \tag{3.11}$$

in the rotating frame of the field center frequency ω_0, and $N = \langle \hat{a}^\dagger(t)\hat{a}(t)\rangle$ is the total mean energy in the field. By the Wiener-Khintchine theorem [156], the autocorrelation of $\hat{a}(t)$ (describing a stationary random process), $\langle \hat{a}^\dagger(t)\hat{a}(t+\tau)\rangle$, forms a Fourier transform pair with its PSD, such that

$$\langle \hat{a}^\dagger(t)\hat{a}(t+\tau)\rangle = \int_{-\infty}^{\infty} f[\omega]e^{-i\omega\tau}d\omega = \frac{N}{\pi}\int_{-\infty}^{\infty}\frac{\gamma}{\gamma^2+\omega^2}e^{-i\omega\tau} = Ne^{-\gamma|\tau|} \tag{3.12}$$

The corresponding first-order temporal coherence for a thermal state is thus

$$g^{(1)}(\tau) = \frac{\langle \hat{a}^\dagger(t)\hat{a}(t+\tau)\rangle}{\langle \hat{a}^\dagger(t)\hat{a}(t)\rangle} = e^{-\gamma|\tau|} \tag{3.13}$$

We can also examine the frequency correlation of the thermal state via the continuous mode operator in frequency, defined as the inverse Fourier transform of $\hat{a}(t)$, $\hat{a}[\omega] = \frac{1}{\sqrt{2\pi}}\int_{-\infty}^{\infty}\hat{a}(t)e^{i\omega t}dt$. It follows that

$$\begin{aligned}\langle \hat{a}^\dagger[\omega]\hat{a}[\omega']\rangle &= \Big\langle \frac{1}{2\pi}\int_{-\infty}^{\infty}dt\int_{-\infty}^{\infty}dt'\ \hat{a}^\dagger(t)e^{-i\omega t}\hat{a}(t')e^{i\omega' t'}\Big\rangle \\ &= \frac{1}{2\pi}\int_{-\infty}^{\infty}dt\ e^{i(\omega'-\omega)t}\int_{-\infty}^{\infty}d\tau\ \langle \hat{a}^\dagger(t)\hat{a}(t+\tau)\rangle e^{i\omega'\tau} \\ &= \frac{1}{2\pi}\delta(\omega-\omega')\int_{-\infty}^{\infty}d\tau\ \langle \hat{a}^\dagger(t)\hat{a}(t+\tau)\rangle e^{i\omega\tau} = \delta(\omega-\omega')f[\omega]\end{aligned} \tag{3.14}$$

where we apply the Wiener-Khintchine theorem again in the last step by the inverse of equation 3.12, such that

$$f[\omega] = \frac{1}{2\pi}\int_{-\infty}^{\infty}d\tau\ \langle \hat{a}^\dagger(t)\hat{a}(t+\tau)\rangle e^{i\omega^\tau} \tag{3.15}$$

---

[6] $F(t)$ is said to be a random or stochastic process of t when F does not depend on t deterministically. $F(t)$ can thus only be described by its ensemble average or expectation value $\langle F(t)\rangle = \int Fp(F,t)dF$, associated to some probability density. The autocorrelation function is thus given by $\langle F(t_1)F(t_2)\rangle = \int F_1F_2p_2(F_2,t_2;F_1,t_1)dF_1dF_2$, where p_2 is the two-fold joint probability density. And such a process is then considered as statistically stationary if the properties of its fluctuations do not change with t. Its autocorrelation is thus invariant under a translation of the origin of time and only depends on the delay in between, and is Hermitian, equivalent to $\langle F^*(t)F(t+\tau)\rangle = \langle x^*(t)x(t-\tau)\rangle^*$ [156].

To compute the higher-order correlation, it is useful to apply Wick's theorem which reduces arbitrary products of the operators to sums of the products of operator pairs [158][159]. For any Gaussian state, we can express the second-order correlation function as

$$\begin{aligned}\langle \hat{a}^\dagger(t)\hat{a}^\dagger(t+\tau)\hat{a}(t+\tau)\hat{a}(t)\rangle = \langle \hat{a}^\dagger(t)\hat{a}(t)\rangle\langle \hat{a}^\dagger(t+\tau)\hat{a}(t+\tau)\rangle + \\ \langle \hat{a}^\dagger(t)\hat{a}(t+\tau)\rangle\langle \hat{a}^\dagger(t+\tau)\hat{a}(t)\rangle\end{aligned} \tag{3.16}$$

and in frequency domain as

$$\begin{aligned}\langle \hat{a}^\dagger[\omega]\hat{a}^\dagger[\omega^{'}]\hat{a}[\omega^{'}]\hat{a}[\omega]\rangle = \langle \hat{a}^\dagger[\omega]\hat{a}[\omega]\rangle\langle \hat{a}^\dagger[\omega^{'}]\hat{a}[\omega^{'}]\rangle + \\ \langle \hat{a}^\dagger[\omega]\hat{a}[\omega^{'}]\rangle\langle \hat{a}^\dagger[\omega^{'}]\hat{a}[\omega]\rangle\end{aligned} \tag{3.17}$$

Using equation 3.12, we thus compute the second-order correlation and coherence function as

$$\langle \hat{a}^\dagger(t)\hat{a}^\dagger(t+\tau)\hat{a}(t+\tau)\hat{a}(t)\rangle = N^2(1+e^{-2\gamma|\tau|}) \tag{3.18}$$

$$g^{(2)}(\tau) = \frac{\langle \hat{a}^\dagger(t)\hat{a}^\dagger(t+\tau)\hat{a}(t+\tau)\hat{a}(t)\rangle}{\langle \hat{a}^\dagger(t)\hat{a}(t)\rangle\langle \hat{a}^\dagger(t+\tau)\hat{a}(t+\tau)\rangle} = 1+e^{-2\gamma|\tau|} \tag{3.19}$$

Similarly, the third-order correlation function can be written as

$$\begin{aligned}\langle \hat{a}_0^\dagger\hat{a}_1^\dagger\hat{a}_2^\dagger\hat{a}_2\hat{a}_1\hat{a}_0\rangle = \langle \hat{a}_0^\dagger\hat{a}_0\rangle\langle \hat{a}_1^\dagger\hat{a}_1\rangle\langle \hat{a}_2^\dagger\hat{a}_2\rangle + \langle \hat{a}_0^\dagger\hat{a}_0\rangle\langle \hat{a}_1^\dagger\hat{a}_2\rangle\langle \hat{a}_2^\dagger\hat{a}_1\rangle + \langle \hat{a}_2^\dagger\hat{a}_2\rangle\langle \hat{a}_0^\dagger\hat{a}_1\rangle\langle \hat{a}_1^\dagger\hat{a}_0\rangle \\ + \langle \hat{a}_0^\dagger\hat{a}_2\rangle\langle \hat{a}_1^\dagger\hat{a}_1\rangle\langle \hat{a}_2^\dagger\hat{a}_0\rangle + \langle \hat{a}_0^\dagger\hat{a}_1\rangle\langle \hat{a}_1^\dagger\hat{a}_2\rangle\langle \hat{a}_2^\dagger\hat{a}_0\rangle \\ + \langle \hat{a}_0^\dagger\hat{a}_2\rangle\langle \hat{a}_1^\dagger\hat{a}_0\rangle\langle \hat{a}_2^\dagger\hat{a}_1\rangle\end{aligned} \tag{3.20}$$

where $\hat{a}_i = \hat{a}(t+\tau_1+\cdots+\tau_i)$. Plugging 3.20 into the third-order coherence functions

$$g^{(3)}(\tau) = \frac{\langle \hat{a}_0^\dagger\hat{a}_1^\dagger\hat{a}_2^\dagger\hat{a}_2\hat{a}_1\hat{a}_0\rangle}{\langle \hat{a}_0^\dagger\hat{a}_0\rangle\langle \hat{a}_1^\dagger\hat{a}_1\rangle\langle \hat{a}_2^\dagger\hat{a}_2\rangle} \tag{3.21}$$

with the relation in equation 3.18 such that $\langle \hat{a}_i^\dagger\hat{a}_j\rangle\langle \hat{a}_j^\dagger\hat{a}_i\rangle = \langle \hat{a}_i^\dagger\hat{a}_j^\dagger\hat{a}_j\hat{a}_i\rangle - \langle \hat{a}^\dagger\hat{a}\rangle^2$, it is easy to show that the first three terms in expanded $g^{(3)}(\tau)$ is $1+e^{-2\gamma|\tau_2|}+e^{-2\gamma|\tau_1|}+e^{-2\gamma(|\tau_1+\tau_2|)}$. Furthermore, we have the remaining terms such as

$$\frac{\langle \hat{a}_0^\dagger\hat{a}_1\rangle\langle \hat{a}_1^\dagger\hat{a}_2\rangle\langle \hat{a}_2^\dagger\hat{a}_0\rangle}{\langle \hat{a}^\dagger\hat{a}\rangle^3} = e^{-2\gamma(|\tau_1+\tau_2|)} \tag{3.22}$$

All higher order coherences can be calculated via the Wick's therorem as such, and we have

$$\begin{aligned} g^{(3)}(\tau) =& \frac{\langle \hat{a}_0^\dagger \hat{a}_1^\dagger \hat{a}_2^\dagger \hat{a}_2 \hat{a}_1 \hat{a}_0 \rangle}{\langle \hat{a}_0^\dagger \hat{a}_0 \rangle \langle \hat{a}_1^\dagger \hat{a}_1 \rangle \langle \hat{a}_2^\dagger \hat{a}_2 \rangle} \\ &= 1 + e^{-2\gamma|\tau_2|} + e^{-2\gamma|\tau_1|} + 3e^{-2\gamma(|\tau_1+\tau_2|)} \end{aligned} \tag{3.23}$$

$$\begin{aligned} g^{(4)}(\tau) =& \frac{\langle \hat{a}_0^\dagger \hat{a}_1^\dagger \hat{a}_2^\dagger \hat{a}_3^\dagger \hat{a}_3 \hat{a}_2 \hat{a}_1 \hat{a}_0 \rangle}{\langle \hat{a}_0^\dagger \hat{a}_0 \rangle \langle \hat{a}_1^\dagger \hat{a}_1 \rangle \langle \hat{a}_2^\dagger \hat{a}_2 \rangle \langle \hat{a}_3^\dagger \hat{a}_3 \rangle} \\ &= 1 + e^{-2\gamma|\tau_1|} + e^{-2\gamma|\tau_2|} + e^{-2\gamma|\tau_2|} + e^{-2\gamma(|\tau_1+\tau_3|)} \\ &+ 3e^{-2\gamma(|\tau_1+\tau_2|)} + 3e^{-2\gamma(|\tau_2+\tau_3|)} \\ &+ 9e^{-2\gamma(|\tau_1+\tau_2+\tau_3|)} + 4e^{-2\gamma(|\tau_1+2\tau_2+\tau_3|)} \end{aligned} \tag{3.24}$$

It is thus obvious that for a thermal state, the join detection at zero delay is $g^{(l)}(0, \cdots, 0) = l!$, agreeing with the derivation in section 3.1.1.

A thermal state can also be described by a statistical mixture described by a density operator $\hat{\rho}$, in place for the correlation function in the continuum frequency space. For a thermal state in thermal equilibrium with a bath at temperature T, the state is represented by $\hat{\rho}_{\text{th}} = \sum_0^\infty p(n)|n\rangle\langle n|$, where $p(n)$ is the probability that the field mode contains n photons, given by the Bose-Einstein distribution

$$p(n) = \frac{e^{-E_n/k_{\text{b}}T}}{\sum_n e^{-E_n/k_{\text{b}}T}} = (1-P)P^n = \langle n\rangle^n/(1+\langle n\rangle)^{n+1} \tag{3.25}$$

We take $P = e^{-\hbar\omega/k_{\text{b}}T}$ and the mean photon number of the state is $\langle n\rangle = 1/(P^{-1}-1)$. Replacing the state vector $|i\rangle$ in equation 3.9 by $\hat{\rho}$, we calculate the expectation value of the l-fold time-delayed joint detection as

$$\langle \hat{a}_0^\dagger \hat{a}_1^\dagger \cdots \hat{a}_{l-1}^\dagger \hat{a}_{l-1} \cdots \hat{a}_1 \hat{a}_0 \rangle = Tr\{\hat{\rho} \hat{a}_0^\dagger \hat{a}_1^\dagger \cdots \hat{a}_{l-1}^\dagger \hat{a}_{l-1} \cdots \hat{a}_1 \hat{a}_0\} \tag{3.26}$$

As shown with the semi-classical theory in equation 3.6, there exhibits higher order correlations with a thermal state at zero delay which decays with some functions of γ. We again compute $g^{(l)}(0, \cdots, 0)$ with the thermal state ρ_{th}[7] such that

$$g^{(l)}(0, \cdots, 0) = \frac{\langle (\hat{a}^\dagger)^l \hat{a}^l \rangle}{\langle \hat{a}^\dagger \hat{a} \rangle^l} = \frac{Tr\{\hat{\rho}_{\text{th}} (\hat{a}^\dagger)^l \hat{a}^l\}}{n^l} \tag{3.27}$$

Note that the numerator of $g^{(2)}(0)$ can be written as

$$\langle \hat{a}^\dagger \hat{a}^\dagger \hat{a} \hat{a} \rangle = \langle \hat{a}^\dagger (\hat{a}\hat{a}^\dagger - 1))\hat{a} \rangle = \langle \hat{n}(\hat{n}-1) \rangle \tag{3.28}$$

---

[7] Note that we have $\hat{\rho}_{\text{th}} = (1-P)\sum_0^\infty P^n|n\rangle\langle n| = (1-P)P^{\hat{n}} = (1-P)P^{\hat{a}^\dagger\hat{a}}$. For Hermitian operator $\hat{n} = \hat{a}^\dagger\hat{a}$ and $\hat{n} = \sum_{n=0}^\infty n|n\rangle\langle n|$, we can use the power-series expansion to write $e^{\hat{n}} = \sum_{l=0}^\infty \hat{n}^l/l! = \sum_{n=0}^\infty \sum_{l=0}^\infty (\frac{n^l}{l!})|n\rangle\langle n| = \sum_{n=0}^\infty e^n|n\rangle\langle n|$, thus $P^{\hat{n}} = e^{\hat{n}\ln P} = \sum_{n=0}^\infty P^n|n\rangle\langle n|$.

It follows that the numerator of $g^{(l)}(0, \cdots, 0)$ can be written as

$$\langle (\hat{a}^\dagger)^l \hat{a}^l \rangle = \langle \hat{n}(\hat{n}-1)(\hat{n}-2)\cdots(\hat{n}-l+1)\rangle \tag{3.29}$$

Note that $\langle n(n-1)(n-2)\cdots(n-l+1)\rangle$ is the l-th factorial moment of the probability distribution $p(n)$ such that

$$\begin{aligned}\langle n(n-1)(n-2)\cdots(n-l+1)\rangle &= \sum_{n=0}^{\infty} n(n-1)(n-2)\cdots(n-l+1)(1-P)P^n \\ &= \sum_{n=0}^{\infty} \frac{n!P^n}{(n-l)!}(1-P) \\ &= l!P^l(1-P)\sum_{n=l}^{\infty} \frac{(n-l)!P^{n-l}}{(n-l)!} \\ &= l!P^l(1-P)\sum_{n=0}^{\infty} P^n \end{aligned} \tag{3.30}$$

Substituting $\langle n\rangle = 1/(P^{-1}-1)$, we have

$$\langle n(n-1)(n-2)\cdots(n-l+1)\rangle = l!\langle n\rangle^l \tag{3.31}$$

We again have that

$$g^{(l)}(0, \cdots, 0) = \frac{l!\langle n\rangle^l}{\langle n\rangle^l} = l! \tag{3.32}$$

Assume in an actual experiment with a measurement efficiency η, the photon number distribution of the state, or the probability to measure n photons for a system characterized by ρ, given by

$$P_n = Tr\hat{\rho}|n\rangle\langle n| = \sum_n p(n) \tag{3.33}$$

for the thermal state, is obviously compromised by η. The actual detected distribution for the state with an expected value of n photons is

$$P_m = \sum_n P_m^{(n)} p(n) = \sum_n \Big(\binom{n}{m} \eta^m (1-\eta)^{n-m} \Big) p(n) \tag{3.34}$$

where $P_m^{(n)}$ is the probability of detecting m photons for an expectation value of n photons. However, by the definition of photon coherences in equation 3.10, the dependence on mean photon flux is removed by the normalization, which is thus a photon statistics of a state independent of detection efficiency.

3.2 Coherences for various states

We can now examine the photon coherence $g^{(l)}(\boldsymbol{\tau})$ at zero delay as well as its time dependence as defined in 3.10 for some other states. In particular, for the second-order coherence at zero time delay $g^{(2)}(0)$, we can re-write equation 3.19 as

$$g^{(2)}(0) = \frac{\langle \hat{a}^\dagger \hat{a}^\dagger \hat{a} \hat{a} \rangle}{\langle \hat{a}^\dagger \hat{a} \rangle^2} = \frac{\langle n^2 \rangle - \langle n \rangle}{\langle n \rangle^2} = \frac{\sigma_n^2 - \langle n \rangle}{\langle n \rangle^2} + 1 \tag{3.35}$$

where $\sigma_n^2 = \langle n^2 \rangle - \langle n \rangle^2$ is the fluctuations in photon number.

A coherent state is a pure state given by

$$|\alpha\rangle = \mathcal{D}(\alpha)|0\rangle = e^{-|\alpha|^2/2} \sum_{n=0}^{\infty} \frac{\alpha^n}{\sqrt{n!}} |n\rangle \tag{3.36}$$

where the probability of detecting n photons is given by

$$\begin{aligned} P_n = Tr\{\hat{\rho}|n\rangle\langle n|\} = |\langle n|\alpha\rangle|^2 &= e^{-|\alpha|^2} \frac{\alpha^{2n}}{n!} \\ &= \frac{\langle n \rangle^n e^{-\langle n \rangle}}{n!} \end{aligned} \tag{3.37}$$

where we use $\langle n \rangle = \langle \hat{a}^\dagger \hat{a} \rangle = |\alpha|^2$. Note that this is a Poissonian distribution where the expectation value and variance are both given by $\sigma_n^2 = \langle n \rangle = |\alpha|^2$. Plugging into equation 3.35, we thus have

$$g^{(2)}(0) = 1 \tag{3.38}$$

for a coherent state, or any state with a Poissonian number distribution with $\sigma_n^2 = \langle n \rangle$. High-order coherence for a Gaussian state can be calculated via the Wick's Theorem as done in section 3.1.2.

For a Fock state $|n\rangle$, we simply have $\sigma_n^2 = \langle n^2 \rangle - \langle n \rangle^2 = 0$, such that

$$g^{(2)}(0) = 1 - \frac{1}{\langle n \rangle} \tag{3.39}$$

We therefore note that there exists a correspondence between the probability distribution of the state in the Fock state basis and the classical or quantum nature of the state. Assume a constant mean photon emission rate is λ, the probability of detecting one photon in time dt is thus λdt. And assume all the detection events are all independent and occur at separate time, the probability of detecting n photons in time interval Δt is thus given by the binomial distribution,

$$P(n, \Delta t) = \lim_{\Delta t/dt \to \infty} \left(\binom{\Delta t/dt}{n} (\lambda dt)^n (1 - \lambda dt)^{(\Delta t/dt - n)} = \frac{e^{-\lambda dt} (\lambda dt)^n}{n!} \right. \tag{3.40}$$

In the limiting case where $\Delta t/dt \to \infty$, it is reduced to the Poissonian distribution. We thus classify the number distribution of a given state by

$$\text{Poissonian}, \sigma_n^2 = \langle n \rangle : \quad g^{(2)}(0) = 1, \quad \text{random} \tag{3.41}$$

$$\text{Sub-Poissonian}, \sigma_n^2 < \langle n \rangle : \quad g^{(2)}(0) < 1, \quad \text{anti-bunching} \tag{3.42}$$

$$\text{Super-Poissonian}, \sigma_n^2 > \langle n \rangle : \quad g^{(2)}(0) > 1, \quad \text{bunching} \tag{3.43}$$

Note that since for any arbitrary state $g^{(2)}(\infty) \to 1$ as photon emission events are all uncorrelated at large time delay. We thus describe the behavior of $g^{(2)}(\tau_1) > g^{(2)}(\tau_2)$ for $\tau_1 < \tau_2$ for a super-Poissonian distribution as bunching, where the photons tend to arrive together. Similarly for a sub-Poissonian distribution where $g^{(2)}(\tau_1) < g^{(2)}(\tau_2)$ for $\tau_1 < \tau_2$, we describe the photons as anti-bunching which are less likely to arrive together than those of a Possionian distribution. Here I assume that the dynamics of coherence is monotonic over some time interval Δt where we define whether the state is Poissonian [160].

3.3 Criteria for non-classicality

Quantum states can be fully described by functions of quasi-probability distribution, analogous to the classical probability distribution. However, unlike a classical distribution which is always positive and definite, behaviors of the quasi-probability distribution of a non-classical state exhibit features which cannot originate from a classical theory.

The Glauber-Sudarshan P-function is an example of the quasi-probability distribution. Since observables are expressed in normal order in a P-function, it is a natural choice used to describe light in phase space, where operators such as $\hat{n}$ are in normal order. It is formulated in [161] [162] by Sudarshan and Glauber, where the density operator is written in terms of coherent state projection $|\alpha\rangle\langle\alpha|$ as

$$\hat{\rho} = \int P(\alpha)|\alpha\rangle\langle\alpha| d^2\alpha \tag{3.44}$$

known as the P-representation of state $\hat{\rho}$. Here we have $d^2\alpha = d\Re\{\alpha\})d\Im\{\alpha\})$ and $P(\alpha)$ being the Glauber-Sudarshan P-function. To determine $P(\alpha)$, we have

$$\begin{aligned}\langle\beta|\hat{\rho}|\beta\rangle &= \int P(\alpha)\langle\beta|\alpha\rangle\langle\alpha|\beta\rangle d^2\alpha \\ &= e^{-|\beta|^2}\int P(\alpha)e^{-|\alpha|^2}e^{\beta\alpha^*-\beta^*\alpha}d^2\alpha\end{aligned} \tag{3.45}$$

Inverting the Fourier integral, We thus have

$$P(\alpha) = \frac{e^{|\alpha|^2}}{\pi^2}\int\langle\beta|\hat{\rho}|\beta\rangle e^{|\beta|^2}e^{-\beta\alpha^*+\beta^*\alpha}d^2\beta \tag{3.46}$$

And $P(\alpha)$ is normalized such that $\int P(\alpha)d^2\alpha = 1$ [156].

For a coherent state, we have

$$\langle\beta|\hat{\rho}|\beta\rangle = e^{-|\beta|^2-|\alpha'|^2}e^{\beta\alpha'^{*}+\beta^*\alpha'} \tag{3.47}$$

It follows that

$$P(\alpha) = \frac{e^{|\alpha|^2}}{\pi^2}\int e^{-|\alpha'|^2}e^{\beta(\alpha'^{*}-\alpha^*)-\beta^*(\alpha'-\alpha)}d^2\beta = \delta^2(\alpha-\alpha') \tag{3.48}$$

which should be intuitive for coherent state in the $|\alpha\rangle$ basis. It shows that for a coherent state, the P-function is indeed positive and definite, and the coherent state has the same phase space function as in the classical integral representation

$$\int \delta(x-x_0, p-p_0)dxdp \tag{3.49}$$

for a classical oscillator at (x_0, p_0). For a thermal state, it can be shown that

$$P(\alpha) = \frac{e^{-|\alpha|^2/\langle n\rangle}}{\pi\langle n\rangle} \tag{3.50}$$

which is positive everywhere as well.

For a non-classical state such as the Fock state [156], we have

$$\langle\beta|\hat{\rho}|\beta\rangle = \frac{e^{-|\beta|^2}(-|\beta|^2)^n}{n!} \tag{3.51}$$

where $\hat{\rho} = |n\rangle\langle n|$. This yields

$$\begin{aligned} P(\alpha) &= \frac{e^{|\alpha|^2}}{n!\pi^2}\int -|\beta|^{2n}e^{-\beta\alpha'^{*}+\beta^*\alpha}d^2\beta \\ &= \frac{e^{|\alpha|^2}}{n!}\frac{\partial^{2n}}{\partial\alpha^{*n}\partial\alpha^n}\delta^2(\alpha) \end{aligned} \tag{3.52}$$

which involves the second derivative of the delta function, exhibiting singularity that classical probability distribution does not have.

3.3.1 Non-classical bound

In the field of quantum optics, non-classical states are generally defined as any states with a P-function that has negativity somewhere which cannot be described by a mixture of coherent states. And we can see that written in terms of photon coherence, when $P(\alpha)$ is non-negative everywhere, this statement results in

$$\int d^2\alpha P(\alpha)(|\alpha|^2-\langle\hat{a}^\dagger\hat{a}\rangle)^2 \geq 0 \tag{3.53}$$

which is equivalent to

$$g^{(2)}(0) = \langle \hat{a}^\dagger \hat{a}^\dagger \hat{a} \hat{a} \rangle - \langle \hat{a}^\dagger \hat{a} \rangle^2 - \langle \hat{a}^\dagger \hat{a} \rangle \geq 1 \tag{3.54}$$

We thus have the classical bound $g^{(2)}(0) \geq 1$ where a violation to it is sufficient to prove the state is non-classical and its P-function has some negativity.

3.3.2 Cauchy-Schwarz inequality

While the phonon coherence $g^{(l)}$ as we so far has discussed evaluates the auto-correlation of photons from the same state, in order to verify correlations between different modes we need to access their cross-correlations to examine their joint probability distribution.

The Cauchy-Schwarz inequality states that for any classical probability distribution,

$$|\langle u, v \rangle|^2 \leq \langle u, u \rangle \cdot \langle v, v \rangle \tag{3.55}$$

where $\langle \cdot, \cdot \rangle$ is the expectation value of the inner product [153].

We denote the cross-coherence between mode a and b as $g^{(l)}_{a,b}$, such that

$$g^{(2)}_{a,b} = \frac{\langle \hat{a}^\dagger \hat{b}^\dagger \hat{b} \hat{a} \rangle}{\langle \hat{a}^\dagger \hat{a} \rangle \langle \hat{b}^\dagger \hat{b} \rangle} \tag{3.56}$$

for the second-order coherence. Comparing it with the auto-coherences where

$$g^{(2)}_{o,o} = \frac{\langle \hat{o}^\dagger \hat{o}^\dagger \hat{o} \hat{o} \rangle}{\langle \hat{o}^\dagger \hat{o} \rangle \langle \hat{o}^\dagger \hat{o} \rangle}, \qquad \hat{o} = \hat{a} \text{ or } \hat{b} \tag{3.57}$$

it is straightforward to see that

$$g^{(2)}_{a,b}(\tau)^2 \leq g^{(2)}_{a,a}(\tau) g^{(2)}_{b,b}(\tau) \tag{3.58}$$

since we have

$$\langle \hat{a}^\dagger \hat{b}^\dagger \hat{b} \hat{a} \rangle^2 \leq \langle \hat{a}^\dagger \hat{a}^\dagger \hat{a} \hat{a} \rangle \langle \hat{b}^\dagger \hat{b}^\dagger \hat{b} \hat{b} \rangle \tag{3.59}$$

by the Cauchy-Schwarz inequality for any classical joint probability distribution. A violation of equation 3.58 thus directly verifies the non-classicality of the joint state. This is a standard criteria in quantum optics to verify the fidelity of entanglement, for instance for photon-phonon entanglement [24], phonon-phonon [26], or Hanbury-Brown-Twiss experiment for a single phonon state [25] in a silicon microbeam optomechanical system.

3.4 Hierarchy of non-classical effects

There exists a hierarchy of non-classical effects, each is associated to stronger quantum effects which the states in the lower non-classicality tier do not have [89] [163] [164]

[165].

We discuss the non-classical bound in the previous section, which is the lowest tier of hierarchy. Negativity in P-function distinguishes it from arbitrary mixtures of coherent states, which are considered as the most classical quantum states, setting the boundary between classicality and non-classicality.

The next tier is categorized to be the non-Gaussian quantum states, which cannot be described by the statistical mixture of any pure Gaussian states. We can consider a general Gaussian state given by

$$\hat{\rho}_{\alpha,\xi,\langle n\rangle} \equiv \hat{\mathcal{D}}(\alpha)\hat{\rho}_{\xi,\langle n\rangle}\hat{\mathcal{D}}^{\dagger}(\alpha) = \hat{\mathcal{D}}(\alpha)\hat{\mathcal{S}}(\xi)\hat{\rho}_{\langle n\rangle}\hat{\mathcal{S}}^{\dagger}(\xi)\hat{\mathcal{D}}^{\dagger}(\alpha) \tag{3.60}$$

which is a thermal state squeezed by ξ and displaced by α, with $\hat{\mathcal{D}}(\alpha)$ and $\hat{\mathcal{S}}(\xi)$ being the displacement and squeezing operators respectively, and $\hat{\rho}_{\langle n\rangle}$ is the density matrix of a thermal state with occupancy $\langle n\rangle$. At maximum amplitude squeezing, it is shown [166] that

$$g^{(2)}(0) = 1 + \frac{2|\alpha|^2(d-s) + s^2 + d^2}{(|\alpha|^2 + d)^2} \tag{3.61}$$

where

$$\langle n\rangle_{\text{tot}} = |\alpha|^2 + d \tag{3.62}$$

$$d = Tr[\hat{\rho}_{\xi,\langle n\rangle}\hat{a}^{\dagger}\hat{a}] \tag{3.63}$$

$$s = Tr[\hat{\rho}_{\xi,\langle n\rangle}\hat{a}\hat{a}^{\dagger}] \tag{3.64}$$

Conditions on displacement (thermal occupancy) and squeezing can reduce $g^{(2)}(0) < 1$, below the classical threshold set by the coherent state $g^{(2)}(0) = 1$. Gaussian states can thus be non-classical, while the non-Gaussian states are a subset of non-classical states which exhibit more quantum features.

Furthermore, since Wigner function of any Gaussian state is positive anywhere, a violation of the Wigner-function positivity is considered as the highest tier in non-classicality. An example of a non-Gaussian state that has a positive Wigner function is a single-photon state in the presence of large optical loss, destroying its robustness [167] [168]. It is shown that any quantum circuits that can be described by postitive Wigner function can be calssically efficently simulated [19], indicating that a non-negative Wigner function is essential to achieve true quantum advantage in quantum computing.

Chapter 4

Measurement Setup

The purpose of this chapter is to give a detailed description of the measurement setup of the experiment. I will describe the optical paths and electrical circuits configured to realize the single photon counting experimental scheme introduced in Chapter 2.4. Then I will describe the measurement and data acquisition procedure used to record single photon scattered by the acoustic mode.

4.1 Optical setup

The optical schematic is illustrated in Figure 4.1, as well as in the frequency domain in Figure 4.2. The optical beam paths are divided into two configurations: the lock configuration depicted in green, and the drive configuration in orange. We alternate between the two during the experiment. During the lock period, a lock tone is prepared to lock all the optical components to the desired frequencies. During the drive period, most of the optical components are free-running without active feedback, while a drive tone is sent to the optomechanical cavity (OMC) and the sideband photons scattered by the acoustic mode are collected for analysis. A series of MEMS optical switches[1] are used to alternate between the optical paths of the two configurations, and the time sequence is described in section 4.2.

The lock tone is produced by a diode tunable laser (TL)[2]. It is prepared in region (A) in Figure 4.1, and is described in detail in section 4.1.1. The lock tone enters an IQ modulator (MIQM)[3] operating in the single-sideband carrier-suppressed mode (SSBCS), such that the output contains only one tone that is downshifted in frequency from ω_{TL} to a frequency that will be locked to the OMC resonance at ω_{c}, via feedback to the MIQM (see section 4.1.1).

An Erbium-doped fiber amplifer (EDFA)[4] amplifies the lock tone exiting the MIQM

---

[1] Thorlabs 1×2 MEMS fiber-optic switches; Model: OSW12-1310-SM.

[2] ID Photonics CoBrite DX1; Model: PPCL200.

[3] EOspace QPSK modulator; Model: IQ-ODKS-25.

[4] Thorlabs Erbium-doped fiber amplifier; Model: EDFA100S

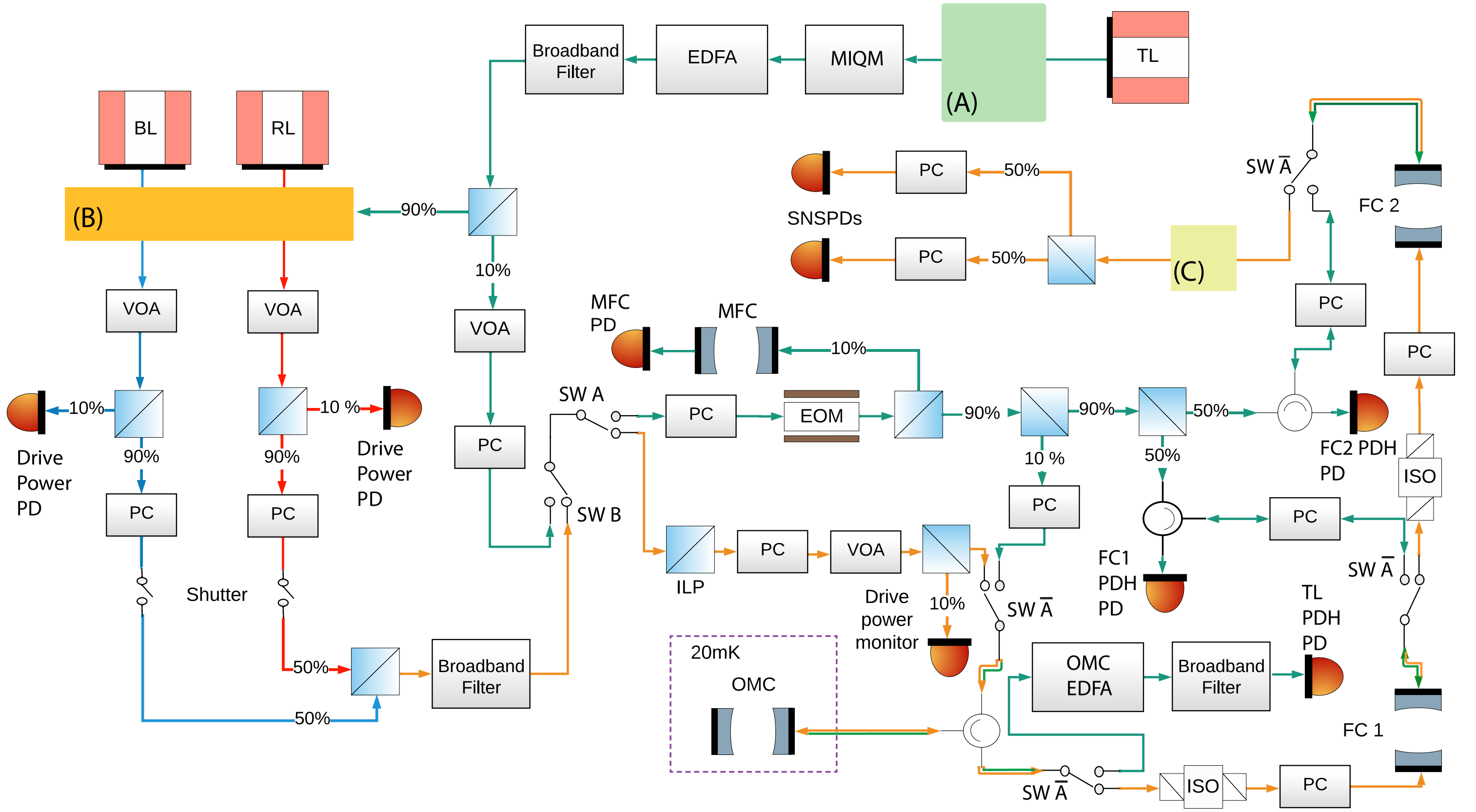

Figure 4.1: **Optical schematic** of the two configurations of the optical paths, “lock” (green) and “drive” (orange). The lock tone is a tunable laser (TL) prepared in region (A) (see section 4.1.1). Under the lock configuration, TL is locked to the optomechanical cavity (OMC) and signal filters (FC1, FC2) are locked to the TL. Drive lasers (BL, RL) are prepared in region (B) (see section 4.1.2). During the drive period, a drive tone is sent to the OMC, and sideband photons are collected by the superconducting nanowire single photon detectors (SNSPDs) at the end of the detection chain. Efficiency of the detection chain is optimized and calibrated by the setup in region (C) (see section 4.3). A series of MEMS optical switches (SW) are used to alternate the optical paths between the two configurations. PC: polarization controller. PD: photodiode. VOA: variable optical attenutator. EDFA: Erbium-doped fiber amplifier. EOM: electro-optic modulator. ILP: in-line polarizer. ISO: isolator. MFC: monitor filter cavity. MIQM: IQ modulator.

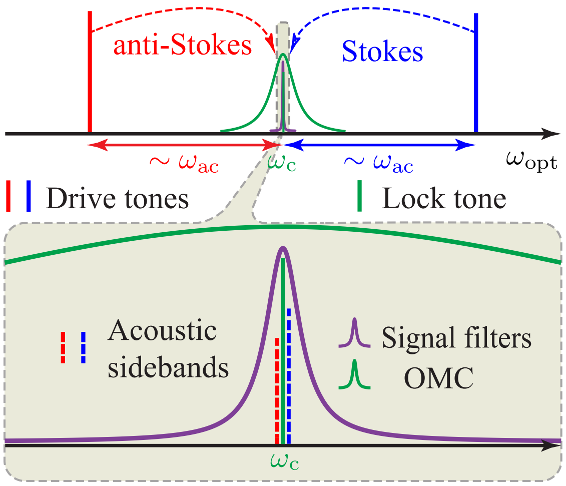

Figure 4.2: **Spectrum of optical tones and components** showing the frequencies of the drive tones (BL, RL), the lock tone (TL), the optomechanical cavity (OMC), the Stokes- and anti-Stokes-scattered acoustic sidebands, and the signal filters (FC1, FC2).

from 5 μW to 1.4 mW. The following broadband filter[5] suppresses the amplified spontaneous emission (ASE) noise produced by the EDFA. A total of $\sim$ 0.5 mW of lock tone power is then split[6] into a portion to be used for the locking of the drive tones (90%), and a portion used to lock the TL and the signal filters (FC1, FC2) (10%). The latter passes through an electro-optic modulator (EOM)[7] which produces a pair of sidebands on the lock tone for standard Pound-Drever-Hall (PDH) locking (see appendix A.1), and 10% of which is then sent to a monitor filter cavity (MFC)[8]. The transmission of the piezo-tuned MFC is detected on a photodetector (PD)[9] to monitor the spectrum of the lock tone exiting the MIQM and to tune its control voltages for its optimal operation in the SSBCS regime (see section 4.1.1).

The rest of the 90% is further split into three parts, which are sent to the OMC and the two signal filter cavities (FC1[10], FC2[11]). The TL gets locked to the OMC centering at ω_{c}, and the FCs are simultaneously locked to the TL, as illustrated in Figure 4.2. Even though the lock tone is switched off during data acquisition under the drive configuration, it is further attenuated to an optical power of $\sim$ 0.1 μW before being sent to the OMC to minimize residual heating on the acoustic resonator. Reflection from the OMC is obtained via a circulator[12] as the error signal for the PDH lock. It is detected after being amplified by an EDFA[13] by a factor of $\sim$ 20 in order to improve the SNR of the signal, which will

---

[5] OZ Optics tunable filter; Model: TF-100-11; linewidth $\Delta\lambda_{\mathrm{broadband}} \approx 0.3$ nm.

[6] All optical couplers/splitters used in our setup: Thorlabs' SM/PM 1×2 or 2×2 fiber couplers series.

[7] EO Space phase modulator; Model: PM-OKS-10.

[8] Made in-house; $\kappa_{\mathrm{MFC}}/2\pi \approx 200$ MHz; free spectral range $\Delta\omega_{\mathrm{MFC}}/2\pi \approx 1.5$ THz.

[9] All photodetectors used in our setup are from the Thorlabs' PDA10CS series unless otherwise specified.

[10] Micron Optics FFP-SI FF24U8; $\kappa_{\mathrm{FC1}}/2\pi = 1.71 \pm 0.02$ MHz; $\Delta\omega_{\mathrm{FC1}}/2\pi \approx 1$ GHz

[11] Micron Optics FFP-SI FF24U7; $\kappa_{\mathrm{FC2}}/2\pi = 1.21 \pm 0.05$ MHz; $\Delta\omega_{\mathrm{FC2}}/2\pi \approx 1$ GHz

[12] Thorlabs SM fiber optic circulator. Model: 6015-3-APC.

[13] NuPhoton EDFA; Model: EDFA-CW-LNF-RS-10-40-FCA.

otherwise be dominated by the amplifier noise on the PD output. The amplified reflected beam is filtered by a broadband filter[14] to suppress the ASE noise. FC1 and FC2 are similarly locked on reflection via PDH locks that operate by sending feedback to their piezos (see appendix A.1).

The drive tones are prepared in region (B) in Figure 4.1, and is described in detail in section 4.1.2. The two drive lasers, BL and RL[15], are used to produce the lock tone. They can be current-, temperature-, and piezo-tuned via their controller[16]. They are continuously frequency-offset locked by approximately $+\omega_{\mathrm{ac}}$ and $-\omega_{\mathrm{ac}}$ from the lock tone at ω_{c} as shown in Figure 4.2, such that only the scattered acoustic sideband photons can transmit through the signal filters centering at ω_{c}. The two drive tones are combined to the common drive optical path (depicted in orange) via a 50/50 fiber coupler to drive the OMC. The pair of shutters[17] are used to determine whether the BL or the RL drives the OMC. The shutter suppresses the input by 55 dB in its closed state, thus ensuring that only one drive tone can reach the OMC when one shutter is kept closed. The shutter have a fast response time of $\sim$ 100 ns and a repetition rate greater than 1 MHz, which are suitable to set the desired pulse sequence for pulsed measurements (see section 5.4).

During the drive configuration, sideband photons that are scattered by the acoustics are sent to the FCs, along with the unscattered drive photons that account for a dominating majority ($\sim$ 1 per 10^9 of the drive photons is scattered) of the photons exiting the OMC. The two FCs combined in series suppress those unscattered photons that are $\pm\omega_{\mathrm{ac}}$ away from their resonance at ω_{c} by a factor of 10^{-10}. An optical isolator (ISO)[18] is inserted to prevent a poor finesse cavity from forming in between the two FCs which would disturb the locking of the individual cavities.

The sideband photons exiting the FCs are collected by a pair of SNSPDs[19]. The setup in region (C) in Figure 4.1 is described in detail in section 4.3. It allows for the optimization of the polarization of photons entering the SNSPDs, as their quantum efficiency is polarization-dependent. It also calibrates the overall efficiency of the photon detection chain. We note that the SNSPDs have a dead time < 50 ns, which is much shorter than the coherence time of our acoustic resonator (10 - 100 μs). Multiple scattering events occurring during the coherence time are thus detectable by each of the SNSPDs individually. Therefore, the photon arrival times recorded by the two SNSPDs are combined into a single record for the analysis presented in this work.

Since the OMC and the FCs are highly birefringent, each input to the cavity is preceded by a manual polarization controller (PC)[20] to adjust the input polarization to one of the polarization eigenstate of the cavities. The EOM is polarization-sensitive as well which requires the polarization of the input light to be aligned to the optical axis of its

---

[14] OZ Optics tunable filter; Model: TF-100-11; linewidth $\Delta\lambda_{\mathrm{broadband}} \approx$ 0.6 nm.

[15] Toptica grating stabilized tunable single-mode diode laser; Model: DLPro.

[16] Toptica DLC pro laser controller.

[17] BATi Nanona ultra-fast optical switch; Model: FOS 3220.

[18] Thorlabs fiber isolator; Model: IO-F-1550APC.

[19] Quantum Opus 1550 nm superconducting nanowire single-photon detectors.

[20] Thorlabs 3-paddle polarization controllers; Model: FPC032.

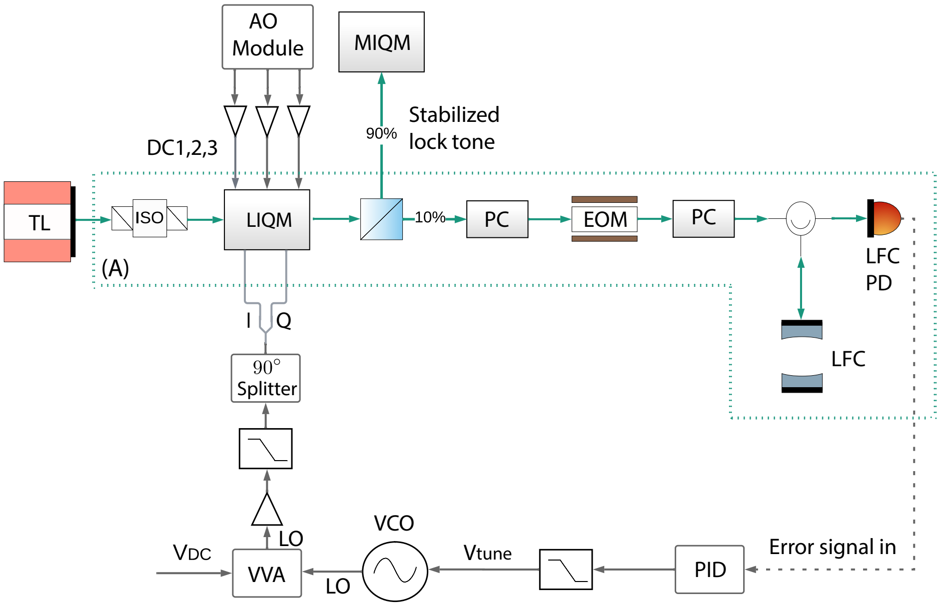

Figure 4.3: **Lock tone preparation** Green solid lines denote the optical fibers, and gray lines denote the electrical connections. The tunable laser (TL) is continuously locked to the reference filter cavity (LFC) to enhance frequency stability of the TL output. The lock is implemented via microwave feedback to an IQ modulator (LIQM) serving as a frequency shifter of the TL output. Control voltages (DC1, DC2, DC3) are adjusted such that the LIQM operates in the SSBCS regime. A voltage-controlled oscillator (VCO) serves as the LO that sets the frequency shift by converting the error correction in voltage generated by the PID module into a microwave output.

crystal. The variable optical attenuators (VOA)[21] are voltage controlled and located in various junctions of the optical path to set the desired power for monitoring, testing and measurement purposes. In particular, the power of the drive tones are continuously locked via feedback to the VOAs in their respective paths. The error signal is generated by the difference between the desired optical power setpoint and the power detected at the drive power PDs, while the feedback signal is generated by a proportional-integral-derivative (PID) module[22].

4.1.1 Lock tone preparation

A schematic for the preparation of a frequency-stabilized lock tone (region (A) in Figure 4.1) is shown in Figure 4.3. The output of the TL is continuously locked to a free-running (no feedback to its piezo) reference cavity (LFC)[23] before being sent to the OMC. The LFC is temperature stabilized (see appendix A.2) to stabilize its resonant frequency, allowing it to serve as a frequency stabilizer for the TL, which otherwise would wander over a few

---

[21] Thorlabs eletronic variable optical attenuator; Model: V1550A; Max attenuation 30 dB.

[22] Liquid Instruments Moku-Lab; Instrument: PID controller.

[23] Micron Optics FFP-SI FF24WZ; $\kappa_{\mathrm{LFC}}/2\pi \approx 2$ MHz, $\Delta\omega_{\mathrm{LFC}} \approx 1$ GHz.

GHz on the scale of a day due to thermal drift.

The optical path is shown by solid green lines in Figure 4.3. The TL passes an ISO to prevent back-reflection into the laser which impairs its frequency stability and causes damage to the diode. It then enters an IQM operating in the SSBCS regime (LIQM)[24]. The output is a single tone downshifted in frequency. It is split 90/10, where the 90% exits region (A) into the MIQM as the stabilized lock tone. The 10% path is sent to an EOM[25], which adds a pair of sidebands to generate the error signal for a PDH lock. The TL operates at a constant power around 15 mW. Upon entering the EDFA in Figure 4.1, the lock tone power reduces to 5 μW after tone preparation in region (A) and passing through the MIQM.

The electrical connections are shown by gray lines in Figure 4.3. To implement the lock via feedback to the IQ modulator, a PDH error signal is obtained from the reflection off the LFC of the phase-modulated lock tone (see appendix A.1). A feedback signal is then generated using a commercial PID controller[26]. The feedback voltage is converted to a correction in frequency with the use of a voltage-controlled oscillator (VCO)[27]. The low-pass filtered[28] feedback signal drives the VCO which outputs a microwave signal LO at ω_{VCO}. The fast response time and wide tuning range of the VCO are ideal for implementing locks with large bandwidth and allow for a large accumulated correction in laser frequency drift. The depth of modulation at the LIQM is determined by the amplitude of the LO, and is tuned by a voltage-controlled variable attenuator (VVA)[29] followed by a fixed-gain amplifier[30] and a low-pass filter[31] to eliminate higher order harmonics in the amplified output. Bias voltage to the VVA (V_{DC}) is manually tuned to eliminate higher order harmonics in the LIQM output.

To implement the lock where the IQM serves as a frequency shifter, it must operate in the SSBCS regime such that the output of the modulator contains strictly one frequency-shifted tone. An IQM consists of two Mach-Zehnder interferometers combined in parallel as illustrated in Figure 4.4. One arm of each of the interferometers has a tunable phase (ϕ_1, ϕ_2) set by a bias voltage (DC1, DC2), along with a small amplitude fast modulation set by $Q(t)$ and $I(t)$. The output of each interferometer is then recombined with one side gaining another tunable phase ϕ_3 set by DC3. It can be shown that to operate the IQM in an ideal SSBCS regime, $\phi_1 = \phi_2 = \pi$ and $\phi_3 = \pi/2$ need to be satisfied to suppress the carrier, and the output of the IQM is then described as

$$a_{\text{IQM}}(t) = a_{\text{TL}} e^{-i\omega_{\text{TL}} t}(I(t) + iQ(t)) \tag{4.1}$$

where $Q(t)$ and $I(t)$ are of small amplitude and known as the in-quadrature and in-phase signal, and $a_{\text{TL}} e^{-i\omega_{\text{TL}} t}$ is the input tone the IQM[39]. Bias voltages (DC1,2,3) are manually

---

[24] Photline Dual Parallel Mach Zehnder Modulator; Model: MXIQ-LN-40. $V_\pi = 7$V.

[25] Thorlabs 10GHz Lithium Niobate Phase Modulator; Model: LN65S-FC.

[26] New Focus PI controller; Model: LB1005.

[27] Mini-Circuits ZX95-1410-S+; Frequency tuning range: 850 - 1410 MHz.

[28] Stanford Research System low-pass filter; Model: SIM 965.

[29] Mini-Circuits variable voltage attenuator; Model: ZX73-2500-S+.

[30] Mini-Circuits ZHL-2-12; 15 dB gain.

[31] Mini Circuits VLF-1350+.

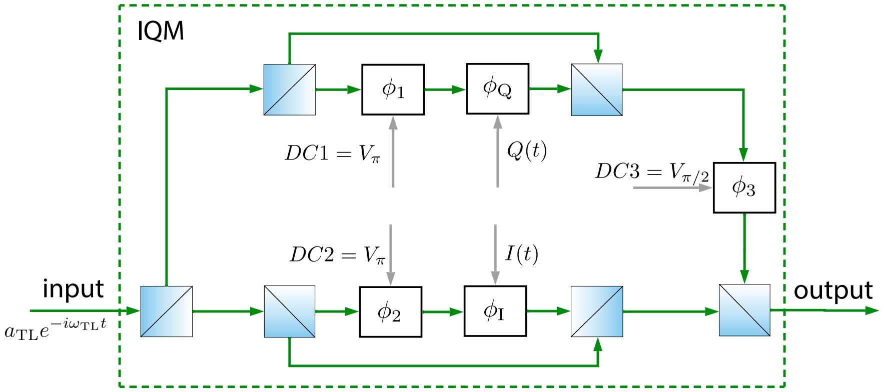

Figure 4.4: **IQM operating in the SSBCS regime** consisting of two Mach-Zehnder interferometers combined in parallel. Control signals into its ports, including DC1,2,3 (slow, large amplitude) and $Q(t)$ and $I(t)$ (fast, small amplitude), set the phase changes in their corresponding interferometer arms to produce the phase and amplitude modulation of interest.

set by an analog output module[32] which are then amplified by a home-built low noise amplifier, such that the tuning range is large enough to cover the V_π of the IQM, which is the voltage required to induce a π-phase shift.

In addition, for $Q(t)$ and $I(t)$ of equal amplitude and 90°out of phase, such that $Q(t) = \beta\sin(\omega_{\mathrm{VCO}}t)$ and $I(t) = \beta\cos(\omega_{\mathrm{VCO}}t)$, equation 4.1 becomes

$$a_{\mathrm{IQM}}(t) = a_{\mathrm{TL}}e^{-i\omega_{\mathrm{TL}}t}(\beta\cos(\omega_{\mathrm{VCO}}t) + i\beta\sin(\omega_{\mathrm{VCO}}t)) = a_{\mathrm{TL}}\beta e^{-i(\omega_{\mathrm{TL}}-\omega_{\mathrm{VCO}})t} \tag{4.2}$$

where the output of the VCO is split by a 90° splitter[33] as the I and Q inputs into the LIQM shown in Figure 4.3. The LIQM now outputs exactly one downshifted tone as the stabilized lock tone at frequency $\omega_{\mathrm{LFC}} = \omega_{\mathrm{TL}} - \omega_{\mathrm{VCO}}$ as set by the VCO.

To lock this stabilized lock tone to the OMC, another IQ modulator (MIQM) is used to downshift its frequency from ω_{LFC} to ω_c. The electrical setup on the MIQM (not shown in Figure 4.3) is identical to that of the LIQM.

Output of the two IQMs in series is monitored via its transmission through the MFC, in order to individually and manually tune the bias voltages to the IQMs to set the desired phases for them to operate in the SSBCS regime. A typical transmission of the piezo-swept MFC is given in Figure 4.5, showing the spectra of the lock tone when the IQMs operate in different regimes. The top spectrum contains the carriers and pairs of sidebands from both IQMs. By turning off the modulation depth on the MIQM, the LIQM is optimized individually first such that only a single sideband tone is visible. The middle of Figure 4.5 shows the spectrum after LIQM optimization and the modulation on MIQM is turned back on. The extra small peak indicates a non-negligible output in the higher order harmonics, and can be eliminated by reducing the modulation depth via the VVA. The right-hand figure shows an ideal spectrum of both IQMs operating in their ideal SSBCS regime.

---

[32] National Instrument static analog output device. Model: PXI-6704.

[33] Mini-Circuits power splitter; Model: ZX10Q-2-12-S+.

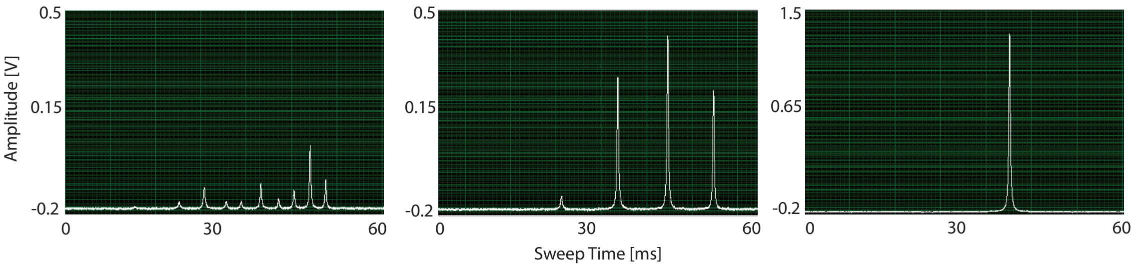

Figure 4.5: **Optimizing control voltages of the IQMs** The spectrum of the lock tone exiting the LIQM and subsequently MIQM is monitored via its transmission through the MFC. The plots show the regime where (left:) both IQMs are operating away from the SSBCS regime, (middle:) LIQM is optimized and its single sideband output acts as the carrier for the unoptimized MIQM, and (right:) both IQMs are operating in the ideal SSBCS regime with a single downshifted stabilized lock tone locked to the OMC.

The extra tones are suppressed by a factor of 45 dB via this method, which is limited by the amplifier noise on the MFC PD output, but sufficient to achieve stable locks for our measurement. Note that the IQMs are temperature stabilized such that the TL lock lasts at least 48 hours without active feedback to the IQM bias voltages. After this period, they could deviate significantly from the SSBCS regime and introduce extra tones that interrupt the locks.

4.1.2 Drive tone preparation

A schematic for the preparation of the drive tones (region (B) in Figure 4.1) is shown in Figure 4.6. The BL and RL are continuously locked to the lock tone at ω_c with a frequency offset of $\sim \pm\omega_{ac}$. 10% of each laser is used to implement the beat lock. Each combines with the lock tone via a 50/50 coupler and the detected beat note is used to generate the error signals for a beat lock [34]. The implementation of such a lock is described in detail in the following section 4.1.2. The BL and RL can be sent to the OMC directly via the monitor tap-off, and the reflection from the OMC is detected by sweeping the laser piezo to monitor the drive tone spectrum directly. This is particularly useful when the lasers experience mode-hopping and need to be tuned manually to operate in single mode.

Before reaching the OMC, each drive laser passes through a fiber-optic cavity (BFC, RFC)[35] to get rid of the broadband classical noise of the lasers. BFC and RFC are locked to BL and RL respectively on transmission via thermal tuning of the cavities. The error signal is generated by the difference between the setpoint ($\sim$80% of the max transmission through VFC and RFC on resonance) and the actual transmitted optical power detected on the photodetectos in the tap-off arms (BFC PD, RFC PF). The feedback loop is implemented digitally via LabView[36], and the feedback voltage is converted into a control

---

[34] Thorlabs photodetector DET 01CFC; Maximum bandwidth 1.2 GHz $\gg \omega_{ac}$, which is required to detect the beat note of frequency ω_{ac}.

[35] Micron Optics FFPI, $\kappa_{\mathrm{BFC,\,RFC}}/2\pi \approx$ 30 MHz, $\Delta\omega_{\mathrm{BFC,\,RFC}} \approx$ 12.5 GHz.

[36] National Instrument NIUSB6210.

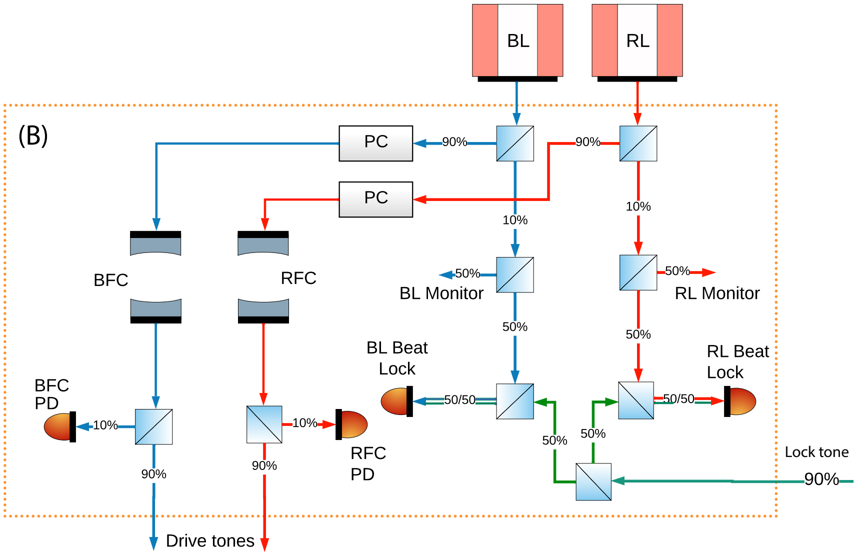

Figure 4.6: **Preparation of drive tones** The BL and RL are constantly locked to the lock tone at ω_c with a frequency offset via a beat lock. Each drive tone passes through a filter cavity (BFC, RFC) for boradband noise filtering before entering the OMC.

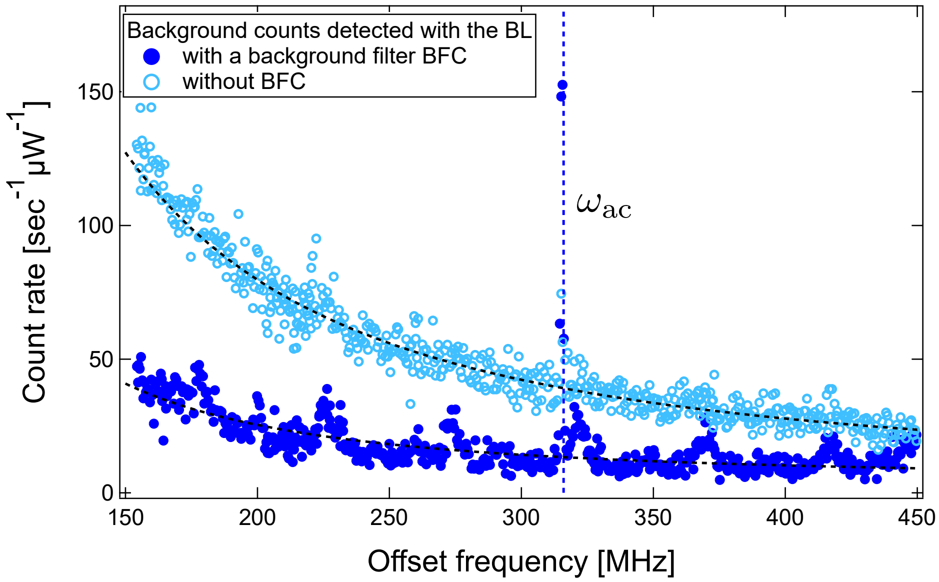

Figure 4.7: **Drive laser noise filtering** Count rate detected by the SNSPDs and normalized by drive power is plotted against the offset frequency of the BL from ω_c, which exhibits an overall frequency-dependent descending background counts. It decays following the tail of the filter cavity transfer function, and is significantly reduced with the addition of the broadband drive laser noise filter cavity BFC.

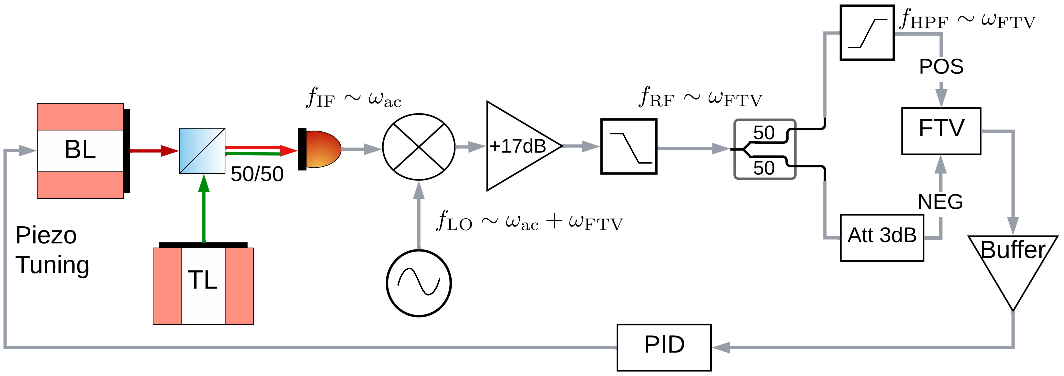

Figure 4.8: **Schematic of the drive laser beat lock** Gray lines show the electrical connections. The optical beat tone is detected by a PD and mixed down to generate a frequency dependent error signal via a frequency-to-voltage (FTV) converter, which makes use of the amplitude response of a high pass filter.

current to the cavities via a temperature controller[37].

To characterize the laser noise suppression, the BL is sent to drive the OMC either following or bypassing the BFC. The photon count rate detected by the SNSPDs is normalized by drive power and plotted in Figure 4.7, as a function of the offset frequency of the BL $\Delta\omega_{\mathrm{BL}}$ from ω_{c}. Here, the offset frequency is locked at discrete steps over a wide frequency range to examine the pattern in the overall background in particular. As illustrated in Figure 4.2, there exists a narrow acoustic sideband feature centered at $\omega_{\mathrm{ac}} \approx$ 315 MHz (denoted by the vertical line). A detailed description and characterization of the acoustic sideband as well as the other peaks exhibited in Figure 4.7 will be presented in section 5.1. These signatures appear on top of a frequency-dependent descending background, which corresponds to the tail of the transfer function of FC1 and FC2 in series in the detection chain, and either with or without the addition of the BFC. The background is fit to $\Delta\omega_{\mathrm{BL}}{}^{-\alpha}$. The addition of BFC increases the best-fit value of α from 2.1 to 2.4. At the frequency of interest ($\Delta\omega_{\mathrm{BL}} \approx \omega_{\mathrm{ac}}$), the background count rate is reduced from 39 to 13 $\mathrm{s}^{-1}\mu\mathrm{W}^{-1}$.

Drive tone beat lock

A schematic of the beat lock is shown in Figure 4.8, where the gray lines indicate electrical connections. As discussed before, the a beat lock PD detects a beat at $\sim \omega_{ac}$. The beat signal is mixed down[38] with a LO[39]. The mixed-down tone is amplified by 17 dB and then low-pass filtered to eliminate higher-order harmonics from the amplifier. In order to generate the error signal for a frequency offset lock, a frequency-to-voltage (FTV) converter is implemented to produce a frequency dependent error signal [169].

One way to achieve this goal is to utilize the amplitude response of an electronic high

---

[37] Stanford Research Systems programmable temperature controller PTC10.

[38] Mini-Circuits mixer. Model:ZX05-10L-S+.

[39] Vaunix RF signal generator. Model: LMS-451D.

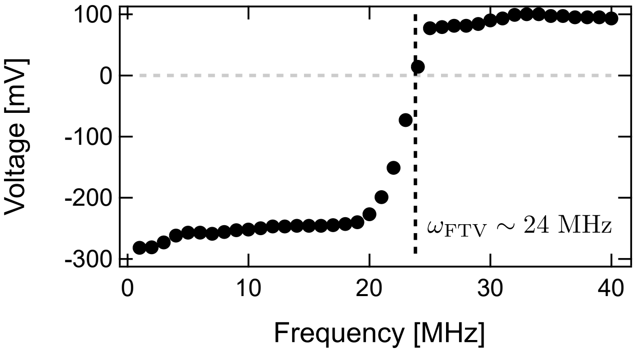

Figure 4.9: **Error signal obtained from the frequency-to-voltage (FTV) converter,** where the voltage output of the FTV circuit is plotted against the beat frequency sent into the FTV. The setpoint at zero-point voltage crossing is around 24 MHz for our circuit.

pass filter (HPF)[40] that has a sharp slope around its cutoff frequency f_{HPF} [170]. The LO is set to frequency $\omega_{\mathrm{ac}} + \omega_{\mathrm{FTV}}$ such that the mixed-down tone serves as the input to the FTV converter and has a frequency $\omega_{\mathrm{FTV}} \approx f_{\mathrm{HPF}}$. It is split 50/50 into two branches. One branch passes through the HPF, while the other is attenuated by 3 dB directly. The two branches are sent into the positive and negative input ports of the FTV respectively, which consist of diodes of opposite direction that produce a positive and negative DC signal respectively. The sum of these DC signals are used as the error signal. A detailed schematic of the home-built FTV circuit is described in appendix A.3. Figure 4.9 shows an example of the error signal produced by the FTV circuit as a function of the beat frequency input. The circuit produces a steep slope with near-linear dependence around the lock point at the zero voltage crossing, $\omega_{\mathrm{FTV}} \approx 25$ MHz, hence allowing for a feedback loop that keeps the drive tones frequency-offset locked to the TL. The error signal is sent to a commercial PID module[41] that generates the voltage correction sent to the drive laser piezo.

4.2 Measurement time sequence

During a continuous wave (CW) measurement, which is the main protocol for obtaining the results presented in this work, we alternate between the two configurations, lock and drive, as discussed in the previous section. A detailed time sequence regulating the switching of the optical paths, the locking and the data acquisition procedure is shown in Figure 4.10.

A master TTL (transistor-to-transistor logic) signal is used as the main trigger for regulating the time sequence of the experiment. It is a 5 Hz square wave with a 50% duty cycle. The drive configuration corresponds to the high state of the TTL in our experiment. The master TTL is used as the trigger for a field-programmable gate arrays-enabled input/output(I/O) device (FPGA)[42]. It is programmed to send out subsequent triggers and

---

[40] Mini-Circuits LC high pass filter. Model: BHP-25+.

[41] Liquid Instruments Moku-Lab; Instrument: PID controller.

[42] National Instrument PXI multifunction reconfigurable I/O module: PXI-7854R.

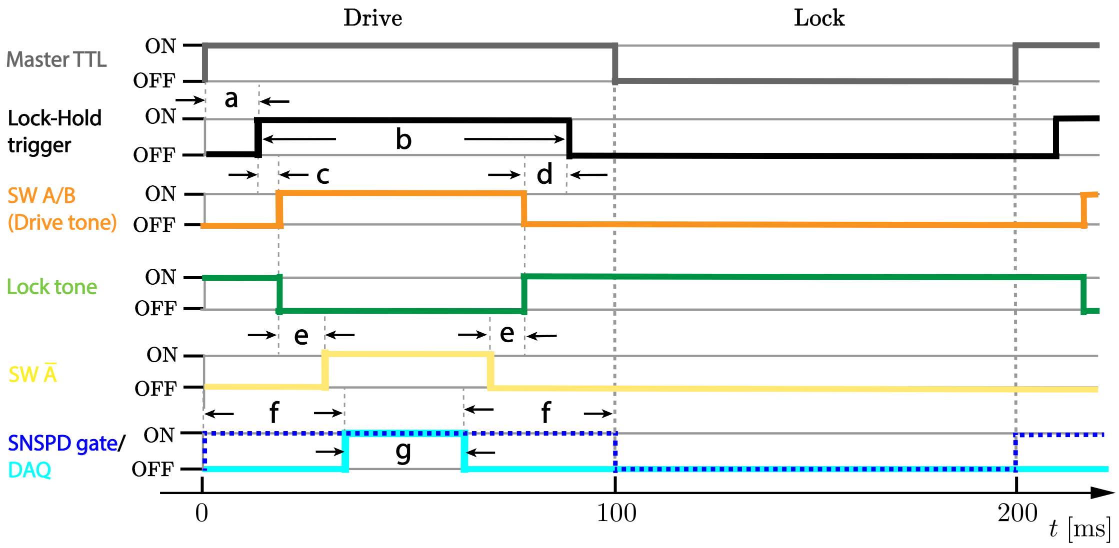

Figure 4.10: **Measurement time sequence** showing the master TTL regulating the drive and lock cycles, the lock-hold trigger controlling the lock feedback to the lock tone and signal filters, the control signal to the optical switches which set the optical paths under different configurations, and the triggering of the SNSPD and data acquisition (DAQ) window. See text for the exact time offsets between these control signals.

control signals, upon triggering from the master TTL, to various instruments with precise control on their timing and synchronization.

The first control signal is a lock-hold (LH) trigger sent to the PID controllers used for locking the lock tone and the signal filters. As the lock tone gets switched out of the optical path under the drive configuration, the PID controllers no longer receive information on the error signal. The LH trigger (high state) signals the PID controllers to stop performing error correction and hold their current states so that the lock is preserved when the lock tone is switched back on. The LH trigger lags t_a = 1 ms behind the master TTL. It remains in the high state for t_b = 97.6 ms, during which the feedback signals to the lock tone and the signal filters are held as they are free-running from the OMC.

The switching between sending either a lock tone or a drive tone into the OMC is controlled by optical switches SW A and SW B as illustrated in Figure 4.1. The TTL signal used to control them is shown in orange in Figure 4.10, where the switches are switched to the drive configuration path when the TTL is in the high state. The time during which the lock tone is sent to the OMC is shown in green as a mirror image of the drive tone control signal. The FPGA outputs the orange control signal, which lags t_c = 30 µs behind the LH trigger. This is to ensure that the locks do not lose the error signal produced by the lock tone before the PID controllers are set to the hold state. For the same reason, SW A and B are switched back to the lock configuration t_d = 1.1 ms before the LH trigger turns off to ensure that the switches have had enough time to switch back[43], such that only the lock tone is being sent to the cavities and the correct error signals have been generated

---

[43] The switches (Thorlabs OSW12-1310-SM) are measured to have a max switching time $<$ 1 ms.

when the PID controllers are turned back on. Note that the digital I/O ports of the FPGA cannot provide sufficient current for multiple switches, the control signal (orange) is thus sent to a function generator[44] as the trigger for it to output a 5V square wave (identical to the orange TTL) as the control signal to the optical switches.

The rest of the optical switches (denoted by SW $\bar{\mathrm{A}}$) are controlled via the same scheme. The control signal (yellow) lags $t_{\mathrm{e}} = 780$ µs behind that of SW A and B. This is to account for the switching time of SW A and B and ensure that the lock tone is completely switched out of the optical path so that it will not pass the signal filter FCs. Under the drive configuration, the output of the FCs in series is connected to the SNSPDs, and the huge photon flux of the lock tone on resonance with the FCs could damage the SNSPDs. TTL for SW $\bar{\mathrm{A}}$ also switches off $t_{\mathrm{e}} = 780$ µs before the SW A TTL. This is also to ensure that the optical path to the SNSPDs is cut out (by the switching of SW $\bar{\mathrm{A}}$) completely before SW A and B switch the lock tone back on.

Finally, a control signal is used to gate the SNSPDs (dark blue), such that the SNSPDs are only enabled during gate high state. The control signal is identical to the master TTL. The photon detected by the SNSPDs are time tagged by the time-correlated single photon counting (TCSPC) electronics[45]. With the gate signal, each photon's time tag of detection can be labeled by the relative time of arrival with respect to each master TTL trigger and the photon counts are histogrammed over a large number of drive-and-lock cycles. The triggering and histogramming of the photon counts allow for long averaging times, which improve the SNR. An example of the photon arrival histogram is shown in Figure 4.11. The detected counts are histogrammed by 0.5 ms of relative time window over 16000 drive and lock cycles, then normalized by the total time in each window to obtain the count rate. The erratic count rate shown in the first 5 ms and last 5 ms during the drive window are due to switching between the optical paths and lasers. Hence as shown by the data acquisition (DAQ) window (dashed blue line), only the photons arriving during the middle 90 ms of the drive period are kept for data analysis for the CW measurement presented in this work. This also ensures that only a steady flux of acoustic sideband photons of interest are analyzed when characterizing the acoustic resonator in thermal equilibrium to exclude transient behavior (due to heating and optomechanical backaction).

4.3 Detection efficiency calibration

The overall efficiency along the detection chain is routinely optimized and calibrated during the experiment via the setup illustrated in Figure 4.12 (region (c) in Figure 4.1).

Independent measurements of the signal FCs gives their maximum transmittivity as 17% and 40% individually, corresponding to an overall transmittivity in series of $\sim 7\%$. These values are highly polarization-dependent. As a result, the input polarization is adjusted by the two PCs preceding the FCs. The transmittivity is calibrated via the "Trans In PD" photodiode at the input of the detection chain and the "Trans PD"[46] at the out-

---

[44] Rigol arbitrary waveform generator DG1022

[45] PicoQuant TCSPC and MCS board with PCIe interface; Model: TimeHarp 260.

[46] Thorlabs fixed gain amplified detector; Model: PDF10C.

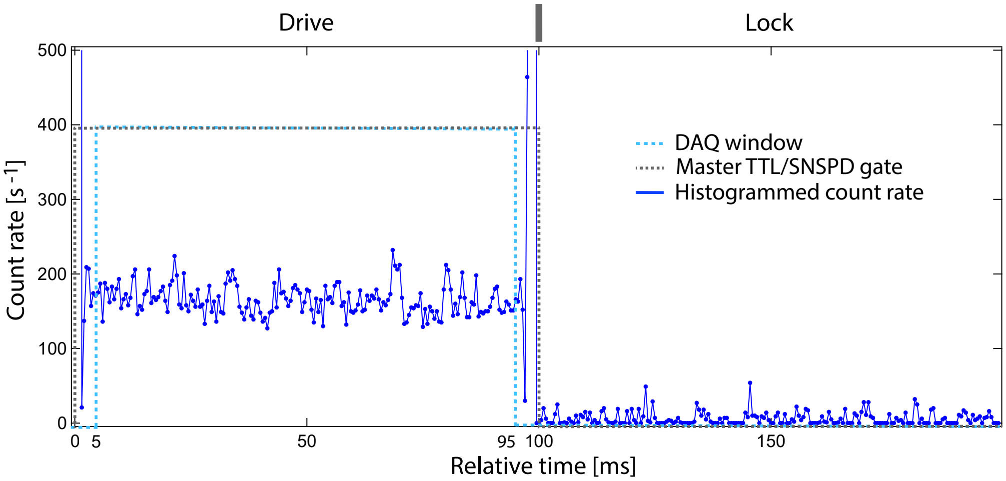

Figure 4.11: **Histogrammed count rate detected by the SNSPDs** is plotted as a function of the time of detection relative to the SNSPDs trigger. The detected counts are histogrammed by 0.5 ms of relative time window over drive and lock cycles. Dashed lines show the master TTL signal (also the SNSPDs gate) and the DAQ window.

put. Sideband photon signal is too weak to be measured on standard PDs, hence the on-resonance lock tone is routinely (usually every 1 to 5 minutes during an experiment) sent through the FCs to track any slow changes in their transmittivity (which is mainly due to temperature-induced changes in the polarization and lock quality). During the transmittivity calibration, the drive-and-lock timing sequence is identical to that of an actual experiment, only with SW B being kept continuously in the low state to allow the lock tone into the drive configuration path while the FCs are free-running in frequency, and the SNSPDs are disabled to avoid detecting the huge flux of lock photons. The overall transmittivity measured via this setup is typically $\sim 5\%$.

Other losses in the detection chain following the exit of sideband photons from the OMC originate from intermediate optical components along the path, including optical fibers, circulator, isolator, and splitters. The total efficiency of these components is independently calibrated to be ~ 0.55.

The quantum efficiencies of the SNSPDs are highly dependent on the input polarization of the photons, which is optimized prior to each experiment. A very weak lock tone from the 0.1% tap-off is sent to the SNSPDs after passing a PC, a polarization beam splitter (PBS)[47] followed by another PC. The PC and attenuators preceding the PBS ensure the lock tone does not saturate the SNSPDs during optimization. The PBS then splits orthogonal polarizations into two polarization-maintaining (PM) output ports, such that the input polarization to the SNSPDs is maintained by the output of the PBS, regardless of the source and polarization of the input photons. The “PBS PD” photodiode detects the amount of light in the other orthogonal polarization, which is minimized by adjusting the PC at the output of the FCs to allow maximum transmittivity via the PBS. The PCs following the PBS output are then adjusted to maximize detection efficiency of the SNSPDs,

---

[47] Thorlabs polarization beam splitter; Model: PBC1550SM-APC.

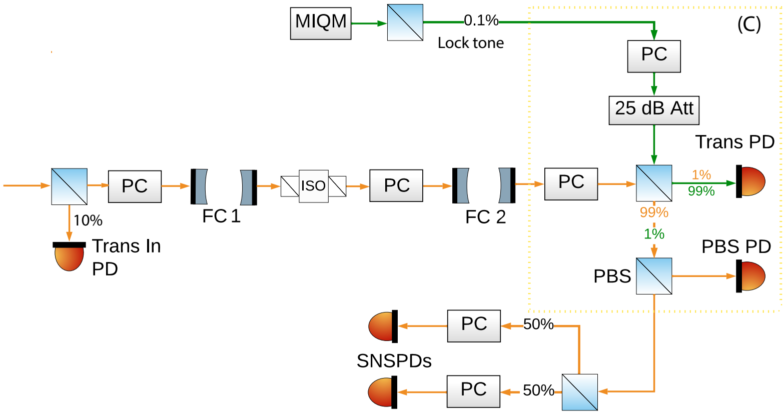

Figure 4.12: **Setup for the calibration and optimization of detection efficiency** (shown as region (c) in the full optical schematic 4.1). A polarization beam splitter is used to maintain and control the input polarization into the SNSPDs to maximze their quantum efficiency. Multiple tap-off and PDs are used to chracterize the efficiency of the detection chain.

which is ~ 0.9 according to the specification. The overall efficiency of the detection chain is thus estimated to be $\eta_{\text{det, est}} = 2.5\%$. The detection efficiency is alternatively inferred from sideband photon count rates and modeling of the effective phonon occupancy of the mechanical resonator, which will be discussed in more detail in the next chapter.

Chapter 5

Device Characterization

The purpose of this chapter is to give a detailed characterization of our optomechanical resonator. I will first describe how we probe the acoustic mode via photon counting spectra constructed from the sideband scattered photons. Then I will present our characterization of the device temperature via phonon thermometry. We model the effective mean phonon occupancy of the acoustics as a function of the superfluid helium bath temperature and the drive power incident on the device. Finally we employ a pulsed drive scheme to probe and model the transient behavior of the acoustics during a pulse, such as parametric instability and acoustic ringdown.

5.1 Photon counting spectrum

In this section I will describe the characterization of a photon counting spectrum, which measures the photon detection rate as a function of the drive frequency. We determine the optomechanical scattering rate via such a spectrum which provides information on the damping rate γ_{ac}, and the mean phonon occupancy n_{ac} of the acoustics, as well as the single photon optomechanical coupling rate g_0.

Figure 5.1 shows an example of a photon counting spectrum. The blue spectrum corresponds to the sideband photons Stokes-scattered by the acoustics with a blue-detuned drive laser ($\Delta \sim +\omega_{\text{ac}}$). The red spectrum corresponds to the anti-Stokes scattered photons from a red-detuned drive laser at $\Delta \sim -\omega_{\text{ac}}$. Photon detection events are registered by the SNSPDs as Δ is stepped and measured by the beat frequency between the drive tone and the lock tone (as described in section 4.1.2). The photon counting rates are thus measured by binning the recorded Δ and calculated as [total number of photon detection events registered]/[total time spent] in each bin of Δ. The measured rates are shown as solid circles with a bin size of (2π) 0.4 MHz in the example shown in Figure 5.1.

The fits (solide lines) of the photon counting spectrum will be described in detail in the rest of this section. It includes a frequency-independent background, consisting of dark counts of the SNSPDs (gray), stray photons leaking into the detection chain (purple) and photon leakage around the signal filters (orange). It also exhibits a broad signature (green) around $|\Delta/2\pi| \sim 322$ MHz, which is caused by the guided acoustic wave Brillouin

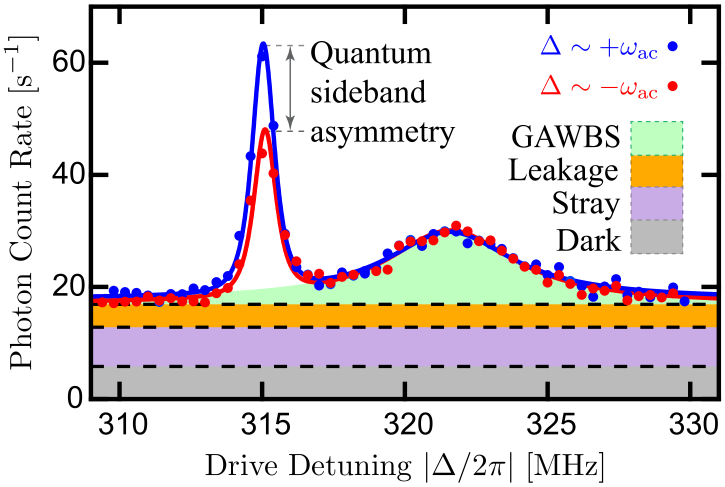

Figure 5.1: A typical photon count rate spectrum which shows the detected photon count rate (solid circles) as a function of the drive laser detuning frequency. Fits of the spectrum include contribution from a frequency-independent background (orange, purple and gray), a guided acoustic wave Brillouin scattering signature (green) and the narrow sidebands arising from photons Stokes (blue) and anti-Stokes (red) scattered by the acoustic mode.

scattering (GAWBS) of the drive photons in the optical fibers, and is described in detail in section 5.1.1. Finally it exhibits a narrow signature around $\Delta \approx \pm\,\omega_{\mathrm{ac}}$, which is the Stokes (anti-Stokes) sideband of the acoustic mode, and the amplitude of which is the rate of acoustically scattered photons of interest. Under low drive power ($P_{\mathrm{in}} \sim 400$ nW in Figure 5.1) where optomechanical backaction is negligible, the difference between the two sidebands is attributed to the quantum sideband asymmetry and is discussed in detail in section 5.2.

To characterize each of the aforementioned sources of detected photons in a photon counting spectrum, we acquire such spectrum at various values of the drive power P_{in}, ranging from 0.1 μW to 5 μW, with a blue-detuned and a red-detuned drive respectively as shown in Fig.5.2.

The broad signature around 322 MHz due to GAWBS can be described by a Lorentzian,

$$f_{\mathrm{G}}(\Delta) = \frac{1}{1 + 4\left(\frac{|\Delta| - \omega_{\mathrm{G}}}{\kappa_{\mathrm{G}}}\right)^2} \tag{5.1}$$

It centers at the GAWBS mode frequency ω_{G} with a linewidth κ_{G} independent of P_{in} (see section 5.1.1). Since GAWBS arises from the scattering of drive photons, the amplitude of the GAWBS signature R_{G} varies with P_{in} as shown in Figure 5.2. The contribution from GAWBS is thus described by $f_{\mathrm{G}}(\Delta) R_{\mathrm{G}}(P_{\mathrm{in}})$.

Photons scattered by the acoustic mode are detected after passing through the two cascaded signal filters (FC1, FC2) centering around ω_{c}. Since their linewidths κ_{FC1}, κ_{FC2} are much narrower than the linewidth of the optical mode of the device ($\kappa_{\mathrm{c}}/2\pi$ = 47.2 ± 0.5 MHz), the acoustic sideband signature can be characterized by the product of the

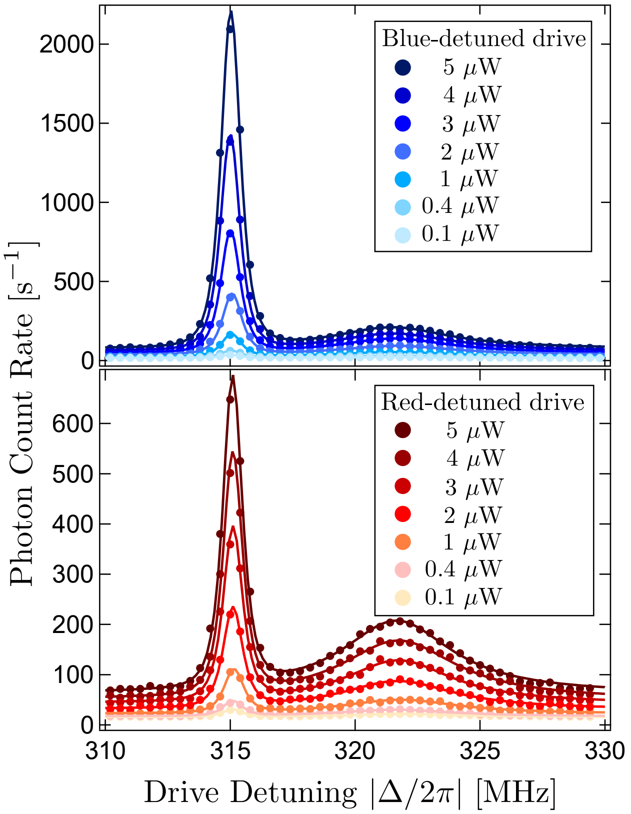

Figure 5.2: **Photon counting spectrum** at various drive power, which are each fit to a sum of a frequency-independent background, a product of two Lorentzians characterizing the signal filters that pass through the sideband photons, and centering around ω_{ac}, as well as a Lorentzian describing the GAWBS feature and centering around $\omega_{\text{G}} \approx 322$ MHz.

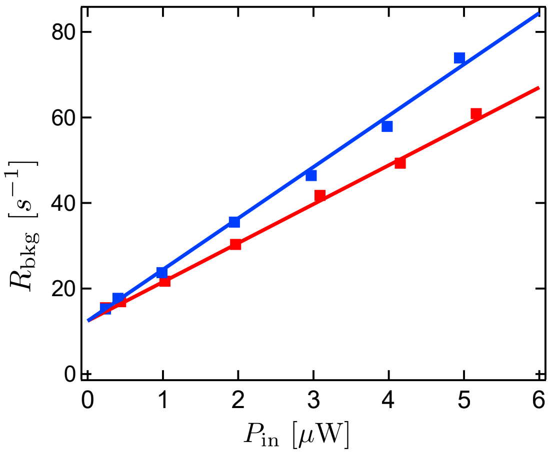

Figure 5.3: **Background photon counts** as a function of drive power for the blue- and red-detuned drive.

transfer function of FC1 and FC2,

$$f_{\text{filter}}(\Delta) = \frac{1}{\left[1+4\left(\frac{|\Delta|-\omega_{\text{ac}}}{\kappa_{\text{FC1}}}\right)^2\right]\left[1+4\left(\frac{|\Delta|-\omega_{\text{ac}}}{\kappa_{\text{FC1}}}\right)^2\right]} \tag{5.2}$$

where $\kappa_{\text{FC1}}/2\pi$ = 1.71 ± 0.02 MHz and $\kappa_{\text{FC2}}/2\pi$ = 1.21 ± 0.05 MHz. Rates of the Stokes and anti-Stokes scattered photons R_{S} and R_{AS} are given by the amplitudes of the sideband signatures and vary with P_{in}, thus the contribution from optomechanical scattering is described by $f_{\text{filter}}(\Delta)R_{\text{S/AS}}(P_{\text{in}})$. Each photon counting spectrum is thus fit to the form,

$$R_{\text{tot}}(\Delta) = R_{\text{bkg}}(P_{\text{in}}) + f_{\text{filter}}(\Delta)R_{\text{S/AS}}(P_{\text{in}}) + f_{\text{G}}(\Delta)R_{\text{G}}(P_{\text{in}}) \tag{5.3}$$

where R_{tot} is the total photon count rate, and R_{bkg} describes the background photon count rate which is independent on Δ but varies with P_{in}. The fitting parameters are $R_{\text{bkg}}(P_{\text{in}})$, $R_{\text{S/AS}}(P_{\text{in}})$, $R_{\text{G}}(P_{\text{in}})$, ω_{ac}, ω_{G}, and κ_{G}.

Resulting fits are shown in Figure 5.2. We notice the acoustic sideband signatures are centered around slightly different frequencies for the blue-detuned and the red-detuned drives ($\omega_{\text{S}}/2\pi$ = 315.04 ± 0.01 MHz, $\omega_{\text{AS}}/2\pi$ = 315.11 ± 0.01 MHz). This can be explained by the signal filters being slightly offset locked from the center of the optical cavity of the device.

Figure 5.3 shows the fit-extracted R_{bkg} as a function of P_{in}, which consists of three sources: (1) the SNSPDs' darks counts, (2) stray photons leaking into the detection chain from the surrounding environment, and (3) unfiltered drive photons leaking around the signal filters, which is linearly proportional to P_{in}. The filter leakage seems to be dependent on the drive photon polarization resulting in different proportionality constants for BL and RL. $R_{\text{bkg}}(P_{\text{in}})$ is thus fit to $R_{\text{bkg,0}}$ + $R_{\text{bkg,blue/red}}P_{\text{in}}$, giving $R_{\text{bkg,red}} = 9.1 \pm 0.2$ s$^{-1}\mu$W^{-1} and $R_{\text{bkg,blue}} = 12.0 \pm 0.4$ s$^{-1}\mu$W^{-1}. $R_{\text{bkg,0}}$ = 12.4 ± 0.8 s^{-1} consists of photons from

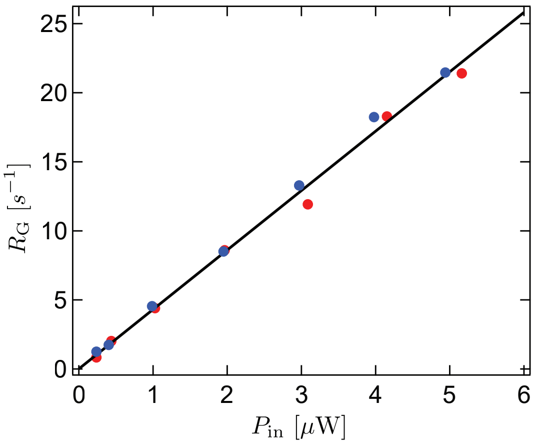

Figure 5.4: **GAWBS-induced photon counts** as a function of drive power for the blue- and red-detuned drive.

sources (1) and (2). We further measure the SNSPDs' dark counts by acquiring the count rate when the input ports directly in front of the detectors are blocked, which is found to be 7 ± 1 s^{-1}. The rate of stray photons detection is thus 5 ± 1 s^{-1}.

The fit-extracted $R_G(P_{\rm in})$ as a function of $P_{\rm in}$ is shown in Figure 5.4. Detection rates of GAWBS-induced photon counts do not differentiate between a blue- and a red-detuned drive. $R_G(P_{\rm in})$ is thus fit simultaneously with both sets of the data to the form linearly increasing with drive power, $R_{G,1}P_{\rm in}$. This gives $R_{G,1}$ = 28.5 ± 0.3 $s^{-1}\mu W^{-1}$.

The fit-extracted optomechanical scattering rate $R_{\rm S/AS}(P_{\rm in})$ as a function of $P_{\rm in}$ is shown in Figure 5.5 (squares). Measurements of $R_{\rm S/AS}(P_{\rm in})$ allow us to to probe important properties of the optomechanical device, such as its temperature, damping rate and optomechanical coupling. A complete model that characterizes its dependence on drive power is given in section 5.2 and 5.3.

To acquire one spectrum as shown in Figure 5.2 and determine the scattering rate $R_{\rm S/AS}$ at low $P_{\rm in}$, it requires an averaging time of $\sim$ 10 minutes. To increase data acquisition efficiency, we show that we can produce the fit and measure $R_{\rm S/AS}$ with high precision via a five-point detuned frequency fit as shown in Figure 5.6, as opposed to the fifty-point detuned frequency fit as shown in Figure 5.2. By picking Δ away from the GAWBS signature, we modify equation 5.3 and fit instead to the form

$$R_{\rm tot}(\Delta) = R_{\rm bkg}(P_{\rm in}) + f_{\rm filter}(\Delta)R_{\rm S/AS}(P_{\rm in}) \tag{5.4}$$

by neglecting the GAWBS contribution. From fits yielded in Figure 5.2, the GAWBS signature has a FWHM of 5.51 ± 0.05 MHz centering 321.5 ± 0.1 MHz. The five data points of $\Delta/2\pi$ used for the simplified fit are 310.2, 311.8, 315.0, 315.4, 315.8 MHz, at least one FWHM away from the GAWBS signature, as shown by hollow circles in Figure 5.6. The simplified fit-extracted $R_{\rm S/AS}$ are shown in Figure 5.5 (circle) in comparison to the results obtained from a full fit (square). The difference is negligible, showing the reliability of the simplified method and the minimal influence of the GAWBS peak on this analysis.

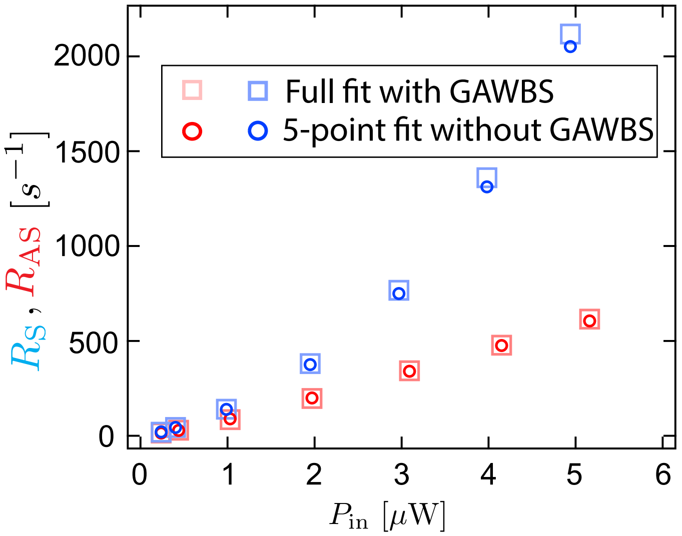

Figure 5.5: **Optomechanically scattered photon counts** as a function of drive power for the blue- and red-detuned drive. The measurements are obtained either with a full fit including the GAWBS signature according to equation 5.3, or with a simplified five-point fit neglecting the GAWBS signature according to equation 5.4.

This method increases the data acquisition efficiency by ten times, and the optomechanical scattering rates results presented in this chapter were acquired using this approach.

5.1.1 Guided acoustic-wave Brillouin scattering

This section gives a detailed characterization of the signature of guided acoustic-wave Brillouin scattering (GAWBS) exhibiting in the photon counting spectrum.

GAWBS is a well-studied interaction between the light propagating in an optical fiber and the thermally populated transverse acoustic modes of the fiber [171] [172]. The thermally excited vibrations produce strain on the fiber core made of fused silica, resulting in a change on its refractive index profile and modulates the transmitted light.

Thermal excitations in a fiber are described by the vibrational eigenmodes of a cylinder, while scattering of the optical field is mainly caused by the transverse displacement of the cylinder in the radial direction. In particular, the dominant source of GAWBS is the radial mode R_{0m} (second index m is the number of vibrational nodes; first index is its dependence on angular coordinates and is 0 for a pure radial mode). It induces pure phase noise on the propagating optical field, as the drive photons and the frequency shifted photons forward scattered by the R_{0m} mode are coupled and shows up as a Stokes or anti-Stokes sideband on the photon counting spectrum.

Resonant frequencies for the R_{0m} mode are determined by boundary conditions corresponding to the fiber,

$$(1-\alpha^2)J_0(y_m) - \alpha^2 J_2(y_m) = 0 \tag{5.5}$$

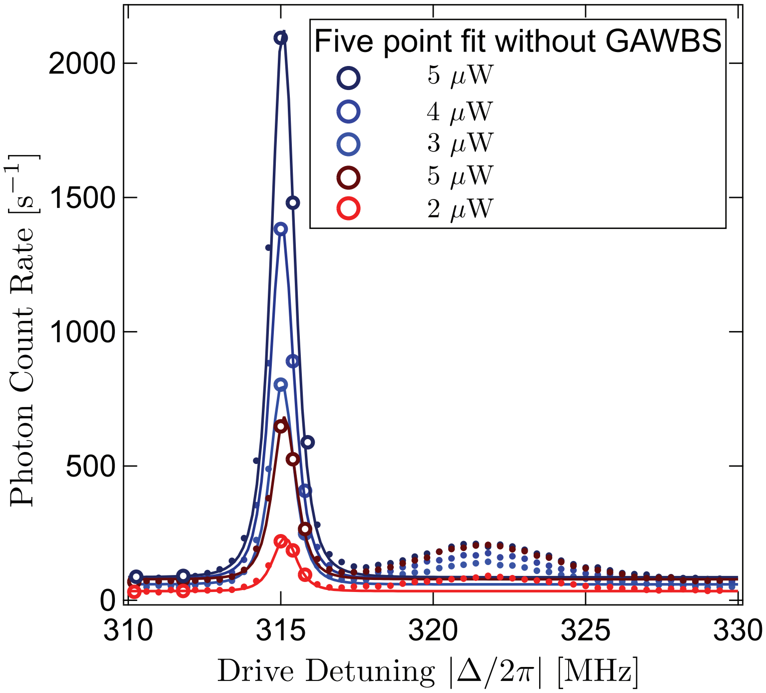

Figure 5.6: **Five-detuning points fits** for a photon counting spectrum, neglecting the GAWBS signature. The fits are done with only the data points shown in hollow circles, away from the GAWBS signature.

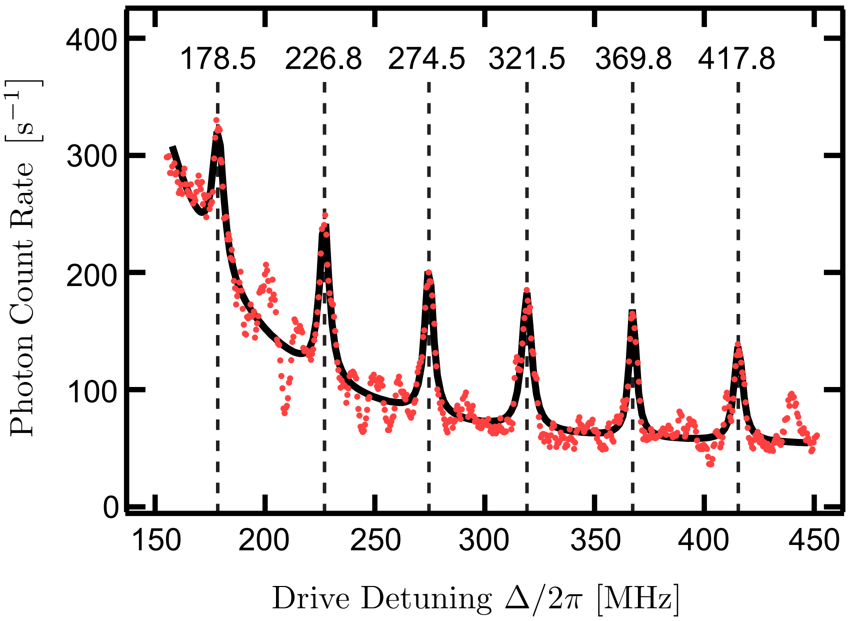

Figure 5.7: A wide detuning range photon counting spectrum showing multiple resonances of the R_{0m} radial GAWBS modes. Dashed lines indicate the fit-extracted resonant frequencies.

where $J_n(y_m)$ is the n^{th} order Bessel function of the first kind and y_m are the m^{th} zero of the equation. Resonant frequency for the m^{th} R_{0m} mode is $f_{\mathrm{G},\,m} = (y_m V_{\mathrm{d}})/a$. For our fibers made of fused silica at room temperature, fiber radius $a = 62.5$ μm, velocity of longituidinal wave V_{d} = 5996 m/s, velocity of transverse wave V_{s} = 3740 m/s, and $\alpha = V_{\mathrm{s}}/V_{\mathrm{d}} = 0.624$.

To verify that the phenomenon agrees with our observation, a spectrum is measured with a frequency detuning $\Delta/2\pi$ varying from 150 MHz to 450 MHz as shown in Figure 5.7. A few Lorentzian-like signatures are exhibited and expected to be arising from the $R_{0\mathrm{m}}$ GAWBS resonance. Due to the large binning in the detuning Δ, the acoustic sideband is not visible in this wide range spectrum. The overall descending background corresponds to the tail of the cascaded signal filter transfer function. We fit it to the form,

$$f_{\text{filter}}(\Delta) = (A_0 + A|\Delta|^{-x_{\text{bkg}}}) + \sum_{m=4}^{m=9} \frac{R_{\mathrm{G},\,m}}{1 + 4\left(\frac{|\Delta| - \omega_{\mathrm{G},\,m}}{\kappa_{\mathrm{G},\,m}}\right)^2} \tag{5.6}$$

where the first term accounts for the overall descending background, decaying with an arbitrary power x_{bkg}, and the summation accounts for the six Lorentzian-like signatures, each individually fit with an amplitude $R_{\mathrm{G},\,m}$, a centered frequency $\omega_{\mathrm{G},\,m}$ and a FWHM $\kappa_{\mathrm{G},\,m}$.

The fit-extracted resonant frequencies $\omega_{\mathrm{G},\,m}/2\pi$ are indicated by the dashed lines in Figure 5.7. They are found to be in close agreement to the theoretically predicted frequencies calculated from equation 5.5 with mode index ranging from m = 4 to m = 9, as shown

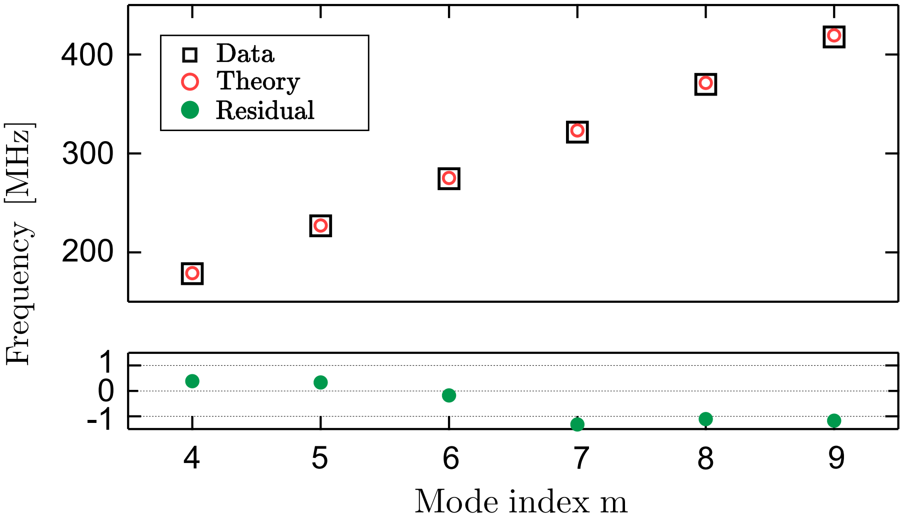

Figure 5.8: **Resonant frequencies of the $R_{\mathbf{0}m}$ radial GAWBS modes.** The fit-extracted peak frequencies shown in black squares are in close agreement to the calculated frequencies shown in red circles. The discrepancies are shown in the bottom panel.

in Figure 5.8 (circle) . This verifies that the broad signature exhibited in the photon counting spectrum is indeed induced by the fiber's transverse acoustic mode R_{0m} vibrating in the radial direction.

5.2 Phonon thermometry

Fundamental asymmetry between the rates of absorption and emission of a phonon in the acoustic mode provides a way to calibrate the mean phonon occupancy of the acoustics. In this section I will describe our characterization of the device temperature by measuring the Stokes and anti-Stokes scattering rates.

Optomechanical interaction imprints the acoustic motion onto the drive optical field, which phase modulates and creates a pair of sidebands $\pm\omega_{\text{ac}}$ away from the drive field. For a Stokes scattering process, one photon is scatterd into the lower energy sideband as one phonon is created into the acoustics. The process is described by $\hat{a}^\dagger\hat{b}^\dagger|0, n_{\text{ac}}\rangle = \sqrt{n_{\text{ac}}+1}|1, n_{\text{ac}}+1\rangle$, at a rate proportional to $|\langle 1, n_{\text{ac}}+1|\hat{a}^\dagger\hat{b}^\dagger|0, n_{\text{ac}}\rangle|^2 = n_{\text{ac}}+1$. Similarly for an anti-Stokes scattering process, one phonon is annihilated in the acoustics as one photon gains the energy and is scattered into the higher energy sideband. This process $\hat{a}^\dagger\hat{b}|0, n_{\text{ac}}\rangle = \sqrt{n_{\text{ac}}}|1, n_{\text{ac}}-1\rangle$, which has a transition rate of n_{ac}. The difference between the two rates of one phonon is known as the quantum sideband asymmetry (QSA).

As formulated in section 2.1.3, in the sideband-resolved regime where $\omega_{\text{ac}} \gg \kappa_{\text{c}}$, for a drive at $\Delta =\sim \pm\omega_{\text{ac}}$, only the Stokes (anti-Stokes) process is enhanced by the optical cavity while the anti-Stokes (Stokes) process is suppressed. Recall that the anti-Stokes process corresponds to $\delta\hat{a}_{\hat{b}} \propto \hat{b}$, and the Stokes process corresponds to $\delta\hat{a}_{\hat{b}^\dagger} \propto \hat{b}^\dagger$. From equation 2.31, we can write

$$\delta\hat{a}_{\hat{b}}[\omega] = -ig_0\bar{a}\chi_\mathrm{c}[\omega+\Delta]\delta\hat{b}[\omega] \tag{5.7}$$

$$\delta\hat{a}_{\hat{b}^\dagger}[\omega] = -ig_0\bar{a}\chi_\mathrm{c}[\omega+\Delta]\delta\hat{b}^\dagger[\omega] \tag{5.8}$$

Assume the mechanical sidebands are on resonance, we have

$$\delta\hat{a}_{\hat{b}}[\omega] = -i2g_0\bar{a}\delta\hat{b}[\omega]/\kappa_\mathrm{c} \tag{5.9}$$

$$\delta\hat{a}_{\hat{b}^\dagger}[\omega] = -i2g_0\bar{a}\delta\hat{b}^\dagger[\omega]/\kappa_\mathrm{c} \tag{5.10}$$

We write the rate of anti-Stokes sideband photon production as

$$\begin{aligned}\dot{n}_{\hat{b}} &= \delta\hat{a}_{\hat{b}}^\dagger\dot{\delta\hat{a}}_{\hat{b}} = (i2g_0\bar{a}^*\delta\hat{b}^\dagger/\kappa_\mathrm{c})(-ig_0\bar{a}\delta\hat{b})\\ &= 2g_0^2n_\mathrm{c}/\kappa_\mathrm{c}\delta\hat{b}^\dagger\delta\hat{b}\end{aligned} \tag{5.11}$$

where the sideband amplitude is given by $\dot{\delta\hat{a}}_{\hat{b}} = -ig_0\bar{a}\delta\hat{b}$ [39]. Similarly, for the rate of Stokes sideband photon production, we have

$$\begin{aligned}\dot{n}_{\hat{b}^\dagger} &= \delta\hat{a}_{\hat{b}^\dagger}^\dagger\dot{\delta\hat{a}}_{\hat{b}^\dagger} = (i2g_0\bar{a}^*\delta\hat{b}/\kappa_\mathrm{c})(-ig_0\bar{a}\delta\hat{b}^\dagger)\\ &= 2g_0^2n_\mathrm{c}/\kappa_\mathrm{c}\delta\hat{b}\delta\hat{b}^\dagger\end{aligned} \tag{5.12}$$

We thus have the difference in their rate as

$$\begin{aligned}\dot{n}_{\hat{b}^\dagger} - \dot{n}_{\hat{b}} &\propto (\delta\hat{b}\delta\hat{b}^\dagger - \delta\hat{b}^\dagger\delta\hat{b})\\ &= [\delta\hat{b}, \delta\hat{b}^\dagger] = 1\end{aligned} \tag{5.13}$$

The difference between the scattering rates of the two sidebands is known as the quantum sideband asymmetry which originates from the commutation relation.

By equation 2.20 and 2.21, we can now model the Stokes sideband scattering rate as $\gamma_\mathrm{ac}C(n_\mathrm{ac,eff}+1)$, where $C = 4g_0^2n_\mathrm{c}/(\kappa_\mathrm{c}\gamma_\mathrm{ac})$ is the multi-photon cooperativity of the optomechanical device, g_0 the single-photon coupling rate, n_c the intracavity photon number and $n_\mathrm{ac,eff}$ the effective phonon occupancy of the acoustics. The rate of Stokes-scattered photons leaking out from the cavity and getting detected by the SNSPDs is thus written as

$$R_\mathrm{S} = \gamma_\mathrm{ac}C(n_\mathrm{ac,eff}+1)\eta_\kappa\eta_\mathrm{det} \tag{5.14}$$

where κ_in is the input coupling rate of the optical cavity, κ_c is the total optical damping rate [1], and $\eta_\kappa = \kappa_\mathrm{in}/\kappa_\mathrm{c}$ [2] is the coupling efficiency of the optical cavity which accounts for the efficiency at which the sideband photons exit the cavity. Finally η_det accounts for the detection efficiency, including losses in optical components, transmittivity through the signal filters and detection efficiency of the SNSPDs. Similarly, the detection rate of anti-

---

[1] $\kappa_\mathrm{c}/2\pi$ = 47.2 ± 0.5 MHz. See appendix B.1 for characterization of the optical cavity.

[2] $\kappa_\mathrm{in}/2\pi$ = 13.6 ± 0.2 MHz, and η_κ = 0.29. See appendix B.1 for characterization of the optical cavity.

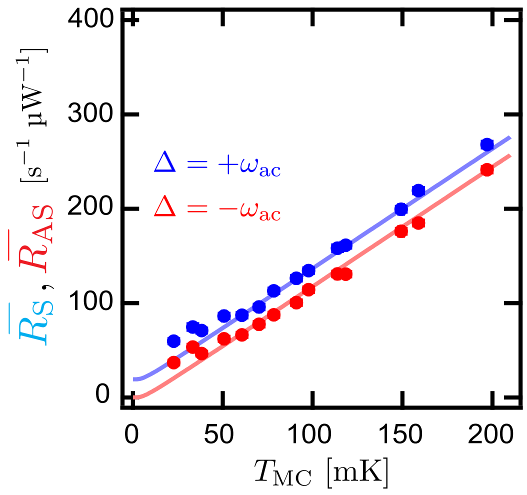

Figure 5.9: Power-normalized sideband scattering rates as a function of bath temperature. Optomechanical backaction is negligible here with low drive power. The constant difference between the Stokes (blue) and the anti-Stokes (red) scattered rate is known as the quantum sideband asymmetry.

Stokes-scattered photons is

$$R_{\mathrm{AS}} = \gamma_{\mathrm{ac}} C n_{\mathrm{ac,eff}} \eta_{\kappa} \eta_{\mathrm{det}} \tag{5.15}$$

To characterize the magnitude of QSA in our system, we measure R_{S} and R_{AS} (extracted from photon counting spectrum via procedure described in section 5.1) as a function of the dilution fridge mixing chamber temperature T_{MC}, as shown in Figure 5.9. We consider the situation where optomechanical backaction is negligible with low drive power $P_{\mathrm{in}} = 250$ nW. The optical heating on the acoustics is also negligible here and the acoustics is in thermal equilibrium with the He bath at mixing chamber (MC) temperature, such that $n_{\mathrm{ac,eff}} = n_{\mathrm{th}} = (e^{\hbar\omega_{\mathrm{ac}}/k_{\mathrm{B}}T_{\mathrm{MC}}} - 1)^{-1}$. As shown in Figure 5.9, we fit the power-normalized sideband counts simultaneously to the form

$$\bar{R_{\mathrm{S}}} = \alpha_{\mathrm{MC}}(n_{\mathrm{th}} + 1) = \alpha_{\mathrm{MC}}((e^{\hbar\omega_{\mathrm{ac}}/k_{\mathrm{B}}T_{\mathrm{MC}}} - 1)^{-1} + 1) \tag{5.16}$$

$$\bar{R_{\mathrm{AS}}} = \alpha_{\mathrm{MC}}(n_{\mathrm{th}} + 1) = \alpha_{\mathrm{MC}}(e^{\hbar\omega_{\mathrm{ac}}/k_{\mathrm{B}}T_{\mathrm{MC}}} - 1)^{-1} \tag{5.17}$$

where T_{MC} is measured independently with a $\mathrm{RuO_2}$ thermometer and is varied with a heater attached to the MC. Since the thermometer is not calibrated for a temperature lower than 50 mK, the fit only uses data points for $T_{\mathrm{MC}} \geqslant 50$ mK. $\alpha_{\mathrm{MC}} = \gamma_{\mathrm{ac}} C \eta_{\kappa} \eta_{\mathrm{det}} / P_{\mathrm{in}} = (\eta_{\kappa} \eta_{\mathrm{det}} / P_{\mathrm{in}}) 4 g_0^2 n_{\mathrm{c}} / \kappa_{\mathrm{c}}$ is the only fitting parameter which characterizes the magnitude of the power-normalized QSA. To determine the value of each individual parameter included in α_{MC}, other experimental settings besides T_{MC} need to be varied. A complete model characterizing detection efficiency, acoustic mode temperature and single photon optomechanical coupling rate is described in section 5.3.

Qualitatively, R_{S} and R_{AS} increases approximately linearly with T_{MC} (except at the lowest T_{MC}) as expected, and the difference between the two rates is relatively constant. This verifies that $n_{\text{ac,eff}}$ under this experimental setting ($P_{\text{in}} \ll 1\ \mu$W) is primarily determined by the bath temperature T_{MC}, where optomechanical backaction and optical heating of the acoustics are negligible, and the splitting between the Stokes and anti-Stokes scattering rates is dominated by the QSA.

5.3 Modeling the phonon occupancy

In this section I will describe our model for determining the acoustic mode temperature, which accounts for the effects of optomechanical backaction and absorption-induced optical heating.

Figure 5.10 shows the power-normalized $\bar{R_{\mathrm{S}}}$ and $\bar{R_{\mathrm{AS}}}$ at a wider range of P_{in}. Qualitatively, the difference between the rates at an effective zero drive power [3] is the power-normalized QSA. While the bath temperature is kept at constant by the dilution fridge cooling ($T_{\mathrm{MC}} \approx 20$ mK) in this measurement, thermal phonon n_{th} increases as the increasing P_{in} induces optical heating. In the absence of backaction, the difference between the two rates remains constant as illustrated by the dashed lines. As P_{in} increases, we also observe that the difference between $\bar{R_{\mathrm{S}}}$ and $\bar{R_{\mathrm{AS}}}$ starts to diverge from the constant QSA, which is due to the dynamical backaction of optomechanics derived in section 2.2.1.

In particular, for a blue-detuned drive at $\Delta \sim +\omega_{\text{ac}}$, the modification to the bare acoustic damping γ_{ac} in equation 2.41, denoted as optomechanical damping rate γ_{opt}, is negative, resulting in a reducing acoustic linewidth. The resulting anti-damping effect or optomechanical amplification is evident from the increase in $\bar{R_{\mathrm{S}}}$ from the blue dashed line, illustrated as blue shade in Figure 5.10. Alternatively for a red-detuned drive at $\Delta \sim -\omega_{\text{ac}}$, $\gamma_{\text{ac,eff}}$ increases which corresponds to an extra damping effect (positive γ_{opt}) and results in optomechanical cooling. It is exhibited as a decrease in $\bar{R_{\mathrm{AS}}}$ from the red dashed line, illustrated in red shade.

The effective phonon occupancy $n_{\text{ac,eff}}$ of the acoustic mode takes into account of the optical heating effect, RPSN and optomechanical backaction in addition to n_{th}. It can be written as

$$n_{\text{ac,eff}} = \langle \hat{\delta b}^{\dagger} \hat{\delta b} \rangle = \frac{g_0^2 n_{\mathrm{c}} \kappa_{\mathrm{c}} |\chi_{\mathrm{c}}[-\omega_{\text{ac,eff}} + \Delta]|^2 + \gamma_{\text{ac}} n_{\text{th}}}{\gamma_{\text{opt}} + \gamma_{\text{ac}}} \tag{5.18}$$

where $\gamma_{\text{opt}} = -2\Im(\Sigma[\omega_{\text{ac,eff}}]) = \mp 4 g_0^2 n_{\mathrm{c}} / \kappa_{\mathrm{c}}$, or equivalent to $\gamma_{\text{ac}} C$ in terms of cooperativity, when the drive is at $\Delta = \pm\omega_{\text{ac}}$. And the intracavity photon number n_{c} is given

---

[3] The data at $P_{\text{in}} = 0$ are measured using pulsed laser excitations and extrapolating the detection rates to zero laser power. See section 5.4.4 for more details on the measurement setup.

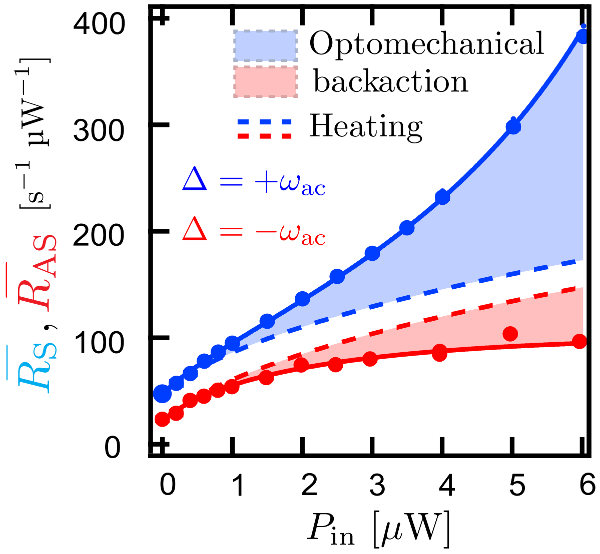

Figure 5.10: **Drive power depedence of the sideband scattering rates** showing the increasing effects of absorption-induced optical heating and optomechanical backaction (ampflication with a blue drive and cooling with a red drive) increasing with P_{in}.

by

$$n_{\text{c}}[\Delta] = \frac{P_{\text{in}}\kappa_{\text{in}}}{\hbar\omega_{\text{c}}}|\chi_{\text{c}}[\Delta]|^2 \tag{5.19}$$

For blue-detuned drive $\Delta = +\omega_{\text{ac}}$, equation 5.18 becomes

$$n_{\text{ac,eff}} = \frac{|\gamma_{\text{opt}}| + \gamma_{\text{ac}}n_{\text{th}}}{\gamma_{\text{opt}} + \gamma_{\text{ac}}} \tag{5.20}$$

And for a red-detuned drive $\Delta = -\omega_{\text{ac}}$, we have

$$n_{\text{ac,eff}} = \frac{|\gamma_{\text{opt}}|(\frac{\kappa_{\text{c}}}{4\omega_{\text{ac,eff}}})^2 + \gamma_{\text{ac}}n_{\text{th}}}{\gamma_{\text{opt}} + \gamma_{\text{ac}}} \tag{5.21}$$

which is a weighted average of its coupling to the thermal bath and the radiation pressure force bath.

Finally we will express n_{th} to account for the heating of the fibers induced by optical absorption of the drive photons. To model the heating effect, we assume that the thermal conductivity of the fiber is a power law in temperature with exponent k such that $\kappa_{\text{fib}}(T) \propto T^k$. By the thermal conductivity law,

$$\dot{Q} = -\kappa_{\text{fib}}\nabla T \propto \int_{T_{\text{fib}}}^{T_{\text{MC}}} T^k dT = T_{\text{MC}}^{k+1} - T_{\text{fib}}^{k+1} \tag{5.22}$$

We then assume a heat load $\dot{Q}$ proportional to P_{in} on the fiber, such that the fiber temperature is given by

$$T_{\text{fib}}^{k+1} = T_{\text{MC}}^{k+1} + \beta^{k+1} P_{\text{in}} \tag{5.23}$$

where β characterizes the amount of heat generated by a given P_{in}. We then assume ballistic transport of heat from the heated fiber via the helium channel inside the cavity to the bath equilibrated to T_{MC}, which is expected to remain at base dilution fridge temeprature independent of P_{in}. The bare mechanical damping rate γ_{ac} can be written as

$$\gamma_{\text{ac}} = \gamma_{\text{ac0}} + \gamma_{\text{ball}} \tag{5.24}$$

where γ_{ac0} is the intrinsic mechanical damping rate at effectively zero temperature originating from only the acoustic loss into the fibers. And γ_{ball} accounts for the three phonon loss rate at some bath temperature, such that $\gamma_{\text{ball}}/2\pi = a_{\text{ball}} T_{\text{MC}}^4$, where $a_{\text{ball}} = 2.7\times10^6$ Hz T^{-4} [38]. $\gamma_{\text{ac}}/2\pi$ is measured to be 3.25×10^3 Hz via independent measurement [4]. We can now express n_{th} as a weighted average of its coupling to the local heating of the fiber and the He bath thermalized to the MC, such that

$$n_{\text{th}} = \frac{n_{\text{fib}}\gamma_{\text{ac0}} + n_{\text{MC}}\gamma_{\text{ball}}}{\gamma_{\text{ac0}} + \gamma_{\text{ball}}} \tag{5.25}$$

where $n_{\text{fib}} = 1/(e^{\hbar\omega_{\text{ac}}/(k_B T_{\text{fib}})}-1)$ and $n_{\text{MC}} = 1/(e^{\hbar\omega_{\text{ac}}/(k_B T_{\text{MC}})}-1)$.

The power-normalized sideband count rates as a function of drive power are thus fit to

$$\bar{R_{\text{S}}} = |\gamma_{\text{opt}}|(n_{\text{ac,eff}} + 1)(\eta_\kappa \eta_{\text{det}}/P_{\text{in}}) = \alpha(n_{\text{ac,eff}} + 1) \tag{5.26}$$

$$\bar{R_{\text{AS}}} = |\gamma_{\text{opt}}| n_{\text{ac,eff}}(\eta_\kappa \eta_{\text{det}}/P_{\text{in}}) = \alpha n_{\text{ac,eff}} \tag{5.27}$$

as shown in 5.11. Multiple iterations of the drive power sweep are simultaneously fit with common fitting parameters T_{MC}, β, k, and optomechanical coupling g_0, which are expected to remain constant under the same experimental setting. We note that detection efficiency varies across different days mainly due to varying transmittivity through the two signal filters, hence each iteration (one set of R_{S} and R_{AS} taken alternatively on the same day) is fit with an individual η_{det}. Solid lines show the best fit to the model described above with data sets combined from seven iterations.

The extracted fitting parameters are shown in Table 5.1. The model determines a bath temperature T_{MC} of 24.4 ± 0.4 mK, equivalent to 1.61 ± 0.03 phonons. The thermal conductivity of the fiber follows a power law in temperature with an exponent k = 1.09 ± 0.03, suggesting a predominantly metallic thermal conductance between the device and MC ($k = 1$ for metals [140]) [5]. The fit also gives a single photon coupling rate of $g_0/2\pi =$

---

[4] See section 5.4 for characterization of the bare mechanical damping rate.

[5] See Appendix B.2 for a detailed characterization of the path of heat transport from the experimental device to the thermal bath of the mixing chamber.

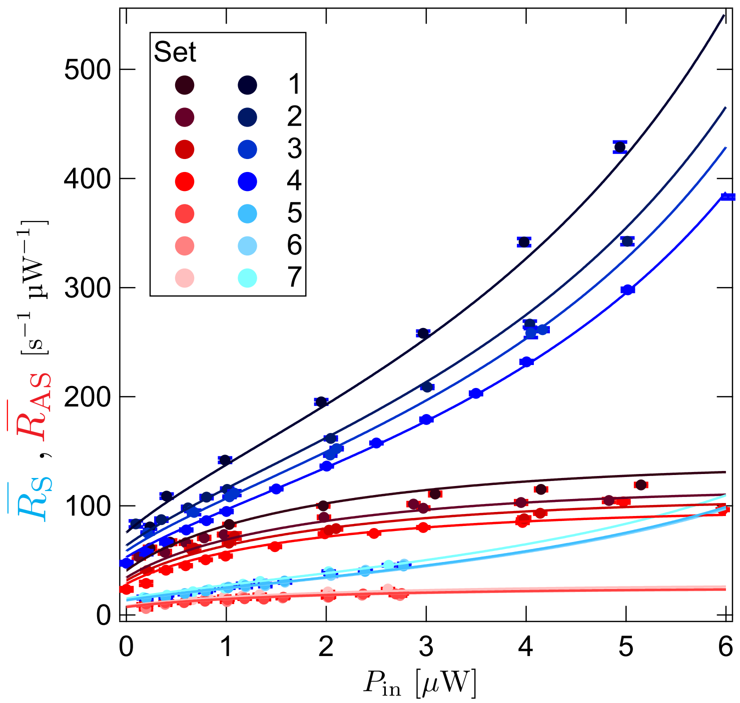

Figure 5.11: **Model for sideband scattering rates** accounting for the effect of optical heating and optomechanical backaction as a function of P_{in}. Solid lines show a global fit to 7 data sets taken on different days, each with an individual detection efficiency.

T_{MC}	24.4 ± 0.4 mK
β	0.54 ± 0.03 K/W$^{1/(k+1)}$
k	1.09 ± 0.03
$g_0/2\pi$	4752 ± 8 Hz

Table 5.1: Fit parameters for the acoustic mode temperature model returned by the best-fit shown in Figure 5.11.

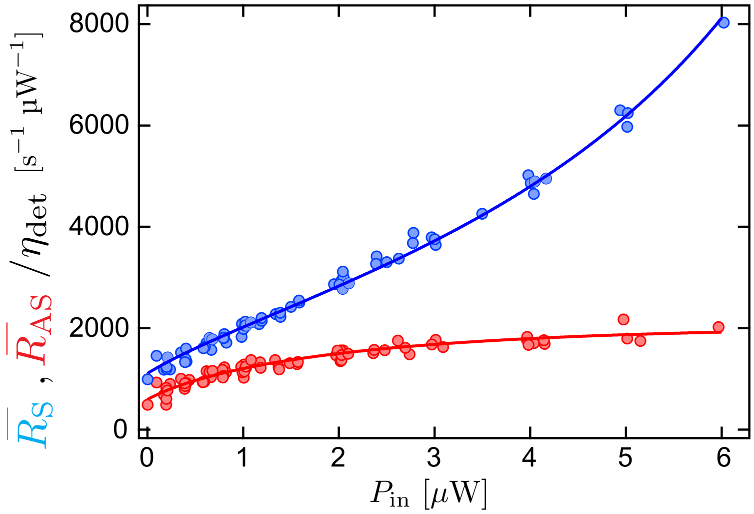

Figure 5.12: Different iterations of data and the sideband scattering rates fit results are normalized from Figure 5.11 to an η_{det} = 1.

4.752 ± 0.008 kHz.

The fitted η_{det} varies from 4% to 22% which is mainly attributed to loss through the signal filters. Different iterations of data and the fit results are normalized to an η_{det} = 1 for display in Figure 5.12. We show that the model presented in this section extracts the effective acoustic mode's temperature under various P_{in} in Figure 5.13, using the fitted parameters and equation 5.18. The acoustic is prepared in an initial state with 1.61 phonons in the absence of optical drive via cooling of the dilution fridge. And as we drive on the red-detuned side, $n_{\text{ac,eff}}$ gradually plateaus with increasing P_{in}, due to a combined effect of the increasing absorptive-induced optical heating and increasing optomechanical cooling.

5.4 Pulsed drive scheme

In this section, I will present further characterization on the acoustics by using a pulsed drive scheme, under which we apply short pulse of drive tone to the device and probe its transient behavior, as opposed to the steady state occupancy discussed in previous sections under a continuous wave (CW) drive scheme.

5.4.1 Optomechanical parametric instability

In this section we will characterize the threshold behavior of the optomechanical amplification interaction, also known as the optomechanical parametric instability [32] [173]. When a tone is placed at $\Delta = +\omega_{\text{ac, eff}}$, an instability occurs under large P_{in} if optomechanical damping $\gamma_{\text{opt}} \geq \gamma_{\text{ac}}$, such that $\gamma_{\text{ac,eff}} = \gamma_{\text{ac}} + \gamma_{\text{opt}} = \gamma_{\text{ac}} - 4g_0^2 n_c/\kappa_c \leq 0$. The effective negative damping rate amplifies the thermal fluctuation and leads to exponentially increasing scattering rates.

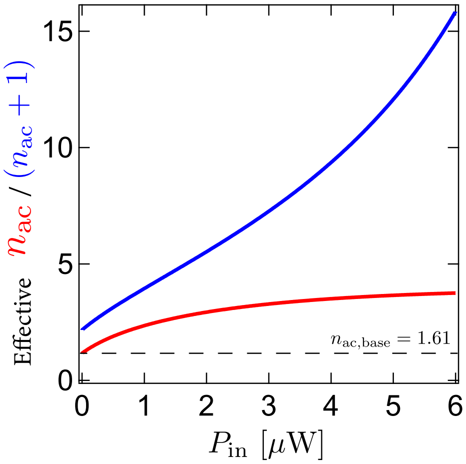

Figure 5.13: Effective phonon occupancy as a function of drive power calculated using the model presented in this section. The acoustic is initiaed with 1.61 phonons in the absence of the optical field.

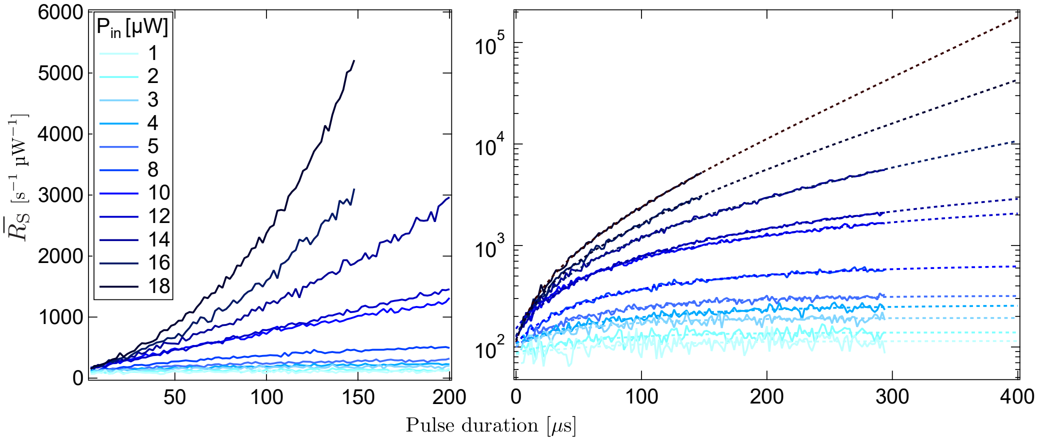

Figure 5.14: **Transient during acoustic ringup** showing count rates as a function of the time during a blue-detuned pulse at various drive power. Data is fit to an exponential form shown by the dashed lines.

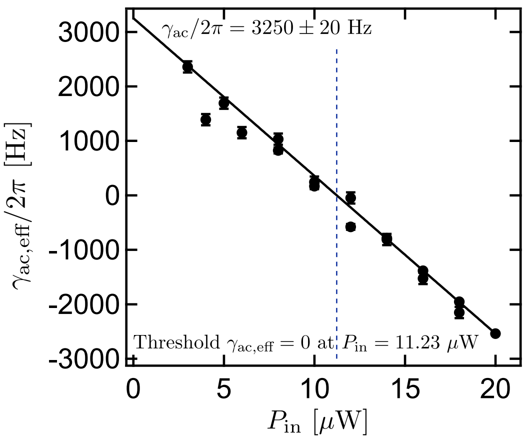

Figure 5.15: **Extracted effective acoustic damping rate from acoustic ringup** showing the acoustic mode transitioning into parametric instability.

To observe the transient behavior, we bin the number of photon detection events by their arrival time as we lock and fix the blue-detuned laser (BL) at $\Delta \sim +\omega_{\text{ac, eff}}$. $\bar{R}_{\text{S}}$ as a function of the time duration after the start of the pulse at various P_{in} is shown in Figure 5.14 (left), where $\bar{R}_{\text{S}}$ is measured by [total number of counts detected in each time bin]/[duration of each bin]. A 2 μs bin is used in the data shown here. A shutter is used to control the pulse sequence (illustrated in Figure 4.1), such that each pulse lasts 150 μs to 200 μs. BL is then turned off (blocked by shutter and attenuator) for 4 ms in between pulses to make sure the acoustic mode has enough time to cool down, and is initiated in the same lowest occupancy state at the beginning of each pulse. Data from the first 4 μs is discarded to account for the switching time of the shutter. Each trace in Figure 5.14 is acquired as the averaging of $\sim 10^5$ of such pulses.

The transient during the acoustic ringup is thus fit to the form $y_0 + Ae^{-2\pi\gamma_{\text{ac,eff}}t}$, where y_0 and A are arbitrary fitting parameters to account for the offset and amplitude. The data and the corresponding best-fits (dashed line) are shown in log scale in Figure 5.14 (right). We sow the extracted $\gamma_{\text{ac,eff}}$ as a function of P_{in} in Figure 5.15. It decreases linearly with increasing P_{in} and is fit to the expected form of $\gamma_{\text{ac,eff}} = \gamma_{\text{bare}} + bP_{\text{in}}$ derived in the linear optomechanics regime (equation 2.41). We thus extract that the bare acoustic damping rate at base bath temperature is $\gamma_{\text{bare}}/2\pi = 3250 \pm 20$ Hz, and the threshold for instability occurs at $P_{\text{threshold}} = 11.23\ \mu$W at $\gamma_{\text{ac,eff}} = 0$. We also extract $g_0/2\pi = 4770$ Hz from slope b which is in agreement with the extracted value from section 5.3.

The optomechanical antidamping amplifies the initial small thermal fluctuation and rings up the acoustics to a dynamically unstable state, which can result in self-induced steady-state amplitude oscillation, analogous to mechanical or phonon lasing [23]. To observe the nonlinear effect and the saturation behavior after the initial exponential growth, the pulse is left on for 45 ms and the corresponding $n_{\text{ac,eff}}$ during the ringup and saturation is shown in Figure 5.16. Note that the data was taken with 30dB attenuation at the SNSPDs to avoid saturating the detectors. As a result, the count rates with a P_{in} below threshold and at the beginning of the pulse have low signal-to-noise ratio after attenuation and are hard

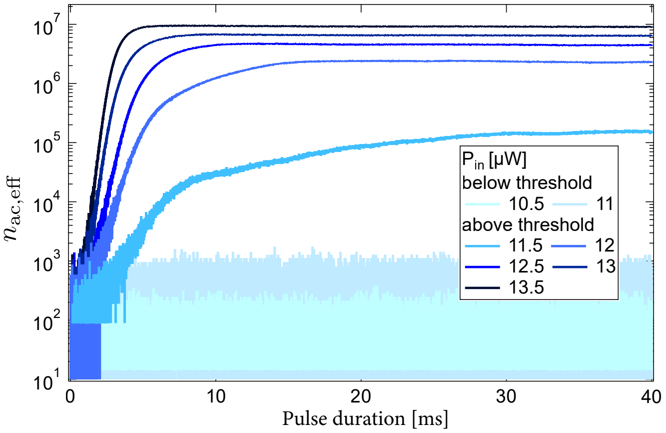

Figure 5.16: Beyond the parametric instability threshold, the effective mean phonon occupancy saturates after the initial exponential growth.

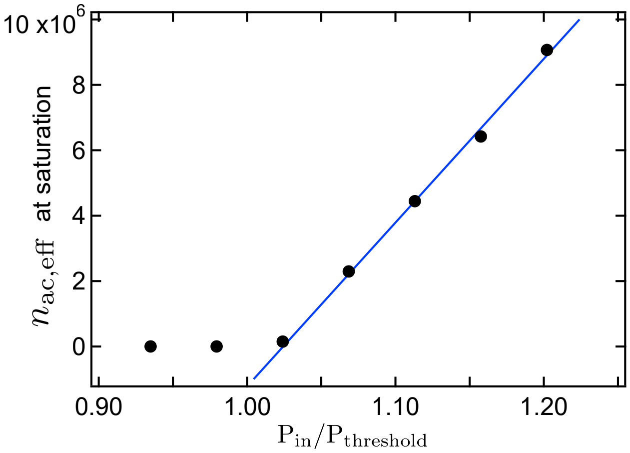

Figure 5.17: Saturation amplitude as a function a drive power in the dynamically unstable state.

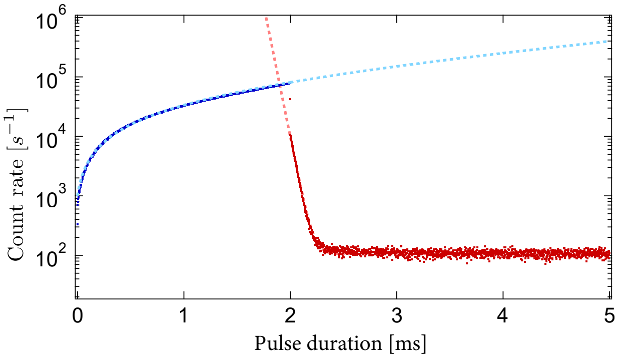

Figure 5.18: A weak red-detuned tone is used to probe the ringdown of the acoustic resonator following its self-oscillation in a dynamically unstable state.

to resolve in this figure. After the initial ringup stage, we observe a relatively fixed large-amplitude motion of the acoustic mode for $P_{\text{in}} > P_{\text{threshold}}$. To focus on the saturation behavior, we show the phonon occupancy at saturation as a function of $P_{\text{in}}/P_{\text{threshold}}$ in Figure 5.17, which is fit to a linear form for $P_{\text{in}}/P_{\text{threshold}} \geq 1$. Since amplitude of the self-induced oscillation is given by $\sqrt{n_{\text{ac,eff}}}$, the amplitude is proportional to the radiation pressure force in this case, and is driven up to $\sqrt{n_{\text{ac,eff}}} \sim 3 \times 10^3$.

5.4.2 Acoustic ringdown

The acoustic ringdown can be directly probed by a red-detuned tone following the ringup stage by a strong blue-detuned tone as discussed in the previous section. Since the acoustic state will be initially driven up to a high motional amplitude, the high sideband count rate during the ringdown is ideal for an accurate extraction of the bare mechanical linewidth with only a weak red-detuned tone that has minimal effect on the acoustic mode.

Figure 5.18 shows the sideband count rate during such a pulse sequence, where a blue-detuned tone of $P_{\text{in}} = 12\ \mu$W is turned on for 2 ms. A red-detuned tone of $P_{\text{in}} = 1\ \mu$W is turned on at $t = 2$ ms. The count rate is binned by 2 μs time window. Count rate during the red pulse from $t_1 = 2.01$ ms to $t_2 = 4$ ms is fit to the form $y_0 + Ae^{-2\pi\gamma_{\text{ac}}t}$. Note that t_1 is chosen such that the data during shutter turning on/off [6] is discarded. It also ensures sufficient time after the blue-detuned tone turned off such that the optomechanical backaction is turned off and the acoustic resonator rings down at its bare damping rate ($\Delta > 1/\omega_{\text{ac}}$). We thus extract a bare acoustic damping rate of $\gamma_{\text{ac}}/2\pi = 3240 \pm 10$ Hz in agreement with the result shown in Figure 5.15.

5.4.3 Pulsed phonon thermometry

We repeat the phonon thermometry measurement under a pulsed scheme. From the transient behavior of the sideband count rates during a pulse, we are able to extrapolate $n_{\text{ac,eff}}$

---

[6] Shutter has a rise or fall time of $\sim 2\ \mu$s.

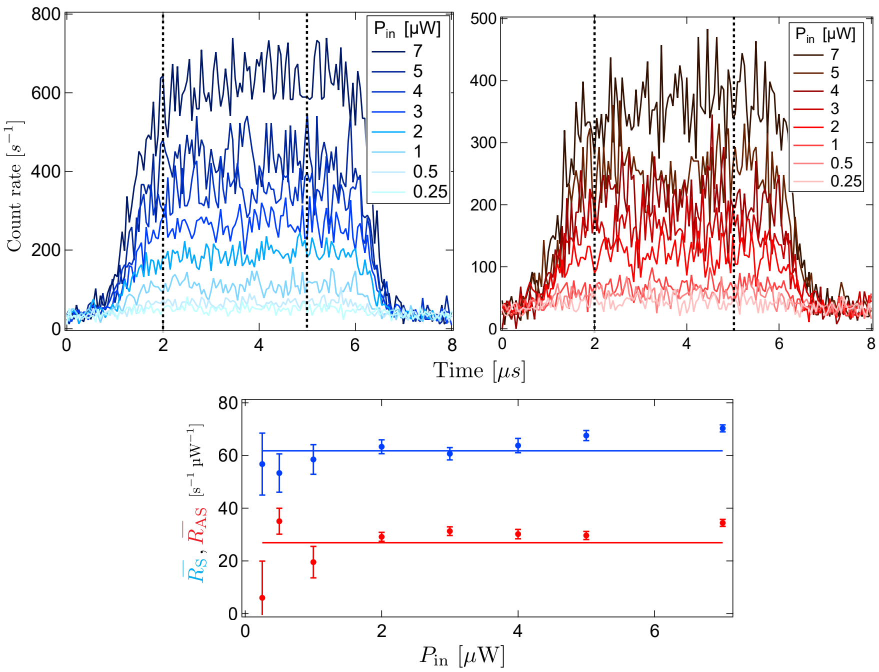

Figure 5.19: **Drive power sweep with a pulsed scheme.** (top:) Sideband count rates during a 5μs pulse at various P_{in}. (bottom:) The average of count rates during the time window shown by the dashed lines in the top figure are plotted and show no effects of optical heating and backaction with increasing P_{in}.

at the beginning of the pulse regardless of the drive power, where the acoustic mode is indeed initiated in its lowest occupancy $n_{\text{ac,eff}} = n_{\text{th}}$ in equilibrium to the He bath at T_{MC}.

Pulsed power sweep

This assumption is first verified by repeating the power sweep shown in Figure 5.10. Sideband count rate is measured as a function of P_{in} with a $t_{\text{d}} = 5$ μs wide pulse. Since $t_{\text{d}} \ll 1/\gamma_{\text{ac}}, 1/\gamma_{\text{opt}}$, $n_{\text{ac,eff}}$ is expected to remain constant during each pulse. Figure 5.19 (top) shows the averaged count rate during a pulse at various P_{in}. The data is binned with 50 ns time window. The rising and falling counting rates during the beginning and after the end of the pulse is mainly attributed to the rise and fall time of the shutters. The average count rates during the time window shown by the dashed lines are plotted as a function of P_{in} in Figure 5.19 (bottom), which remain relatively constant. As compared to Figure 5.10, the effects of optical heating and optomechanical backaction are absent under the pulsed scheme.

Rethermalization time

We determine the rethermalization time required in between pulses such that the acoustic mode is initialized in its lowest occupancy before applying each pulse. This is useful for determining the experimental settings for preparing non-Gaussian quantum states using a

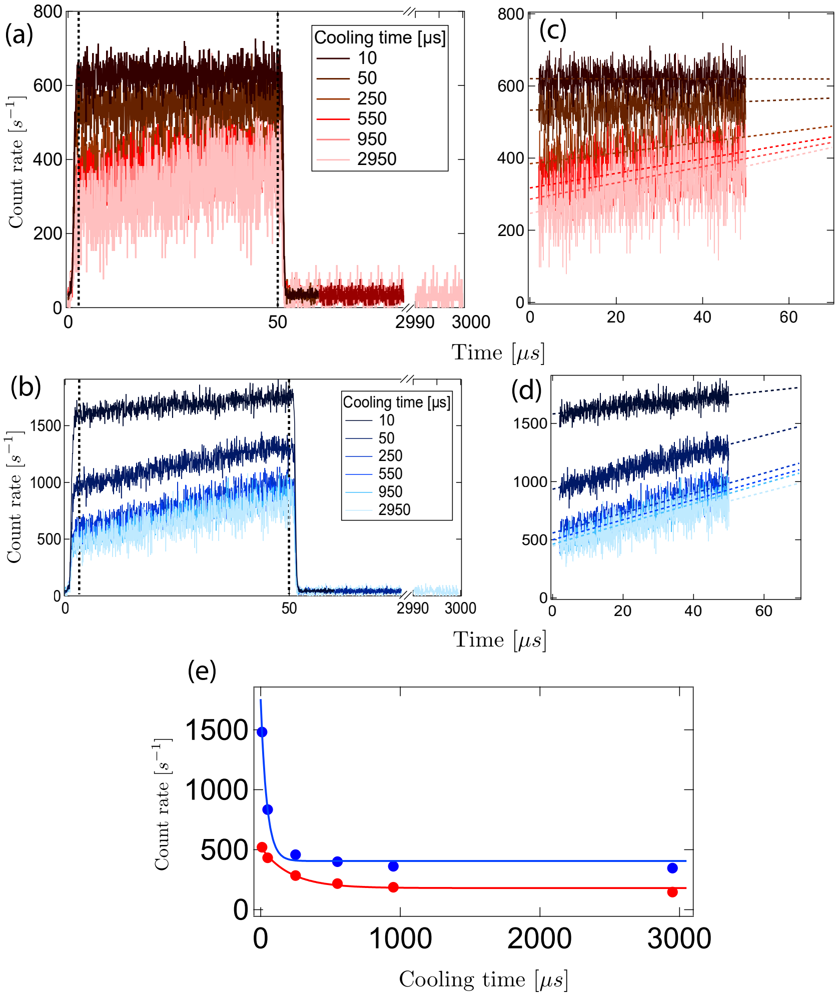

Figure 5.20: **Phonon occupancy as a function of pulse-off time.** Initial phonon occupancy is extracted by linearly extrapolating the count rate during a pulse to zero time, which decreases as cooling time increases.

pulsed scheme, such as generating a photon-phonon entangled state or a single phonon Fock state[24] [25].

Scattering rates are measured during a $t_\mathrm{d} = 50\ \mu$s wide pulse at $P_\mathrm{in} = 5\ \mu$W with various repetition period t_r and shown in Figure 5.20 (a)-(b), where cooling time is the pulse-off time in between pulses $(t_\mathrm{r} - t_\mathrm{d})$. The scattering rates increase approximately linearly during the pulse (marked by the time window in between the dashed lines) excluding the shutter rise time, which allows us to extrapolate the count rate at time zero through a linear fit as shown in Figure 5.20 (c)-(d). Extracting y-intercepts of such fits is equivalent to probing the acoustic state's occupancy with an effective $P_\mathrm{in} = 0$ [7].

The fit-extracted initial count rates are shown as a function of cooling time in Figure 5.20 (e). The acoustic state initiates at a higher mode temperature with lower cooling

---

[7] The 0-power data points in Figure 5.12 are measured via such linear extrapolation.

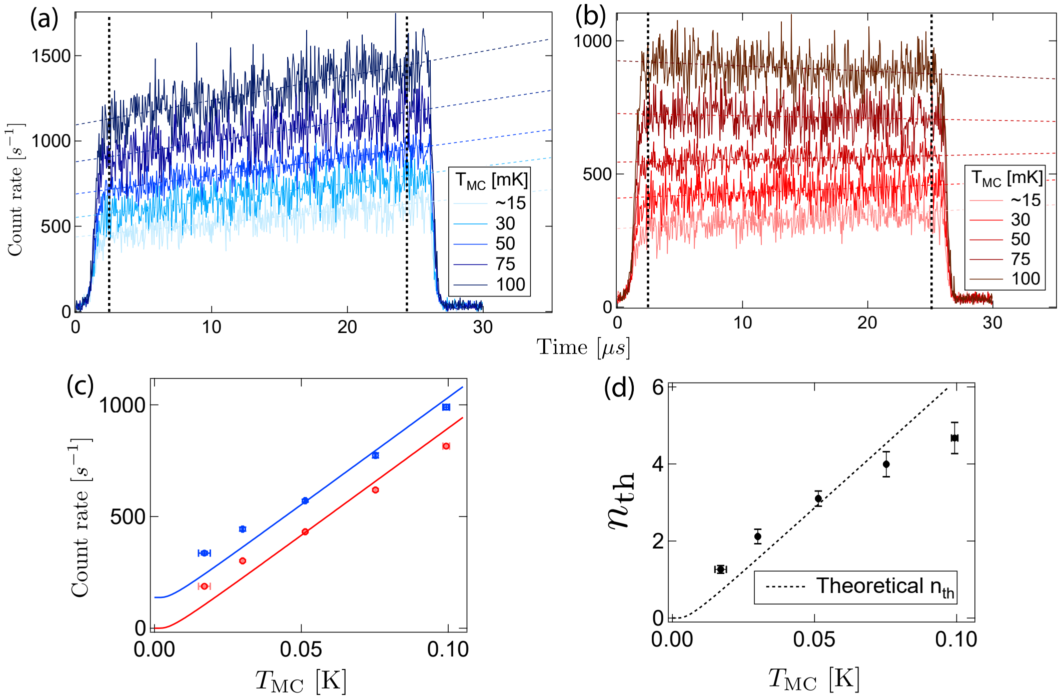

Figure 5.21: **Pulsed phonon thermometry** showing the linearly extrapolated sideband scattering rates at zero pulse time, and the inferred n_{th} calibrated from the QSA, as a function of MC or the He bath temperature.

time, suggesting the time in between pulses is not sufficient for the acoustic mode to rethermalize with the He bath at T_{MC}. The initial occupancy follows approximately an exponential decay with a decay time $\sim 250\ \mu$s (extracted from the red-detuned data).

Phonon thermometry

Based on the characterizations of pulsed measurements from previous sections, we use a $5\ \mu$W, 25 μs pulse with a 400 μs repetition period to extract phonon occupancy via calibration of the QSA. The count rates are measured at various T_{MC} as shown in Figure 5.21.

By linearly extrapolating the count rates to zero time, we obtain the Stokes and anti-Stokes scattering rates, R_{S} and R_{AS}, which correspond to an acoustic mode temperature of $n_{\text{th}} = 1/(e^{\hbar\omega_{\text{ac}}/(k_{\text{B}}T_{\text{MC}})} - 1)$. The extrapolated count rates are simultaneously fit to $\alpha(n_{\text{th}}+1)$ and αn_{th}, where α is the common fitting parameter, as shown in Figure 5.21 (c). We can thus infer n_{th} directly from the QSA, where

$$n_{\text{th}} = \frac{R_{\text{AS}}}{R_{\text{S}} - R_{\text{AS}}} = \frac{\alpha n_{\text{th}}}{\alpha(n_{\text{th}}+1) - \alpha n_{\text{th}}} \tag{5.28}$$

The inferred n_{th} is shown in Figure 5.21 (d), where the dashed line is the n_{th} computed directly from T_{MC}.

In comparison with the measurements shown in section 5.2, drive power used in the pulsed scheme is 20 times as large, resulting in a detection rate ~20 times as large. It allows for more efficienct data acquisition and better signal-to-noise ratio without introducing undesired optical heating and optomechanical backaction in the measurement.

5.4.4 Modeling the evolution of $n_{\text{ac,eff}}$

In this section we model the response of the effective mode occupancy to the thermal bath and the optical bath as we apply an optical tone to the system.

We assume the thermal bath for the acoustics has a linear response to the incident optical power with a damping rate of γ_{th}. Under a pulse train of width t_{d}, repetition period t_{r} and power P_{in}, the response of the thermal bath temperature T_{th} is described by

$$\dot{T}_{\text{th,rise}}(t) = [T_{\text{MC}} + \alpha_{\text{th}} P_{\text{in}} - T_{\text{th,rise}}(t)]\gamma_{\text{th}} \quad \text{for } 0 < t \leq t_{\text{d}} \tag{5.29}$$

$$\dot{T}_{\text{th,fall}}(t) = [T_{\text{MC}} - T_{\text{th,fall}}(t)]\gamma_{\text{th}} \quad \text{for } t_{\text{d}} < t \leq t_{\text{r}} \tag{5.30}$$

where t is the time during a pulse sequence, and α_{th} accounts for the contribution of optical heating due to the incident power P_{in}. We denote $T_{\text{th,rise}}$ as the rising bath temperature during the pulse-on window, and $T_{\text{th,fall}}$ the decreasing bath temperature during the pulse-off window. Since the pulse is periodic, we solve the equations with the boundary conditions that $T_{\text{th,rise}}(t_{\text{d}}) = T_{\text{th,fall}}(t_{\text{d}})$ and $T_{\text{th,rise}}(0) = T_{\text{th,fall}}(t_{\text{r}})$. The solutions are given by

$$T_{\text{th,rise}}(t) = (T_{\text{MC}} + \alpha_{\text{th}} P_{\text{in}}) + e^{-\gamma_{\text{th}} t}[T_{\text{th,eq}} - (T_{\text{MC}} + \alpha_{\text{th}} P_{\text{in}})] \tag{5.31}$$

$$T_{\text{th,fall}}(t) = T_{\text{MC}} + e^{-\gamma_{\text{th}} t}[T_{\text{th,eq}} - (T_{\text{MC}} + \alpha_{\text{th}} P_{\text{in}}(1 - e^{t_{\text{d}}\gamma_{\text{th}}}))] \tag{5.32}$$

where $T_{\text{th,eq}} = T_{\text{th,rise}}(0)$ is the equilibrium temperature of the bath at the beginning of each pulse, given by

$$T_{\text{th,eq}} = \frac{T_{\text{MC}}(e^{t_{\text{r}}\gamma_{\text{th}}} - 1) + \alpha_{\text{th}} P_{\text{in}}(e^{t_{\text{d}}\gamma_{\text{th}}} - 1)}{e^{t_{\text{r}}\gamma_{\text{th}}} - 1} \tag{5.33}$$

The response of the effective acoustic mode temperature can thus be modelled as

$$\dot{n}_{\text{ac,rise}}(t) = \begin{cases} \left[\frac{|\gamma_{\text{opt}}| + n_{\text{th}}(t)\gamma_{\text{ac}}}{\gamma_{\text{ac,eff}}} - n_{\text{ac,rise}}(t)\right]\gamma_{\text{ac,eff}} & \text{for a blue drive} \\ \\ \left[\frac{|\gamma_{\text{opt}}|(\frac{\kappa_{\text{c}}}{4\omega_{\text{ac,eff}}})^2 + n_{\text{th}}(t)\gamma_{\text{ac}}}{\gamma_{\text{ac,eff}}} - n_{\text{ac,rise}}(t)\right]\gamma_{\text{ac,eff}} & \text{for a red drive} \end{cases} \tag{5.34}$$

for $0 < t \leq t_{\text{d}}$. Note that the first term in the bracket is the steady state effective mode occupancy derived in equation 5.20 and 5.21. We calculate $n_{\text{th}}(t) = 1/(e^{\hbar\omega_{\text{ac}}/(k_{\text{B}} T_{\text{th}}(t))} - 1)$

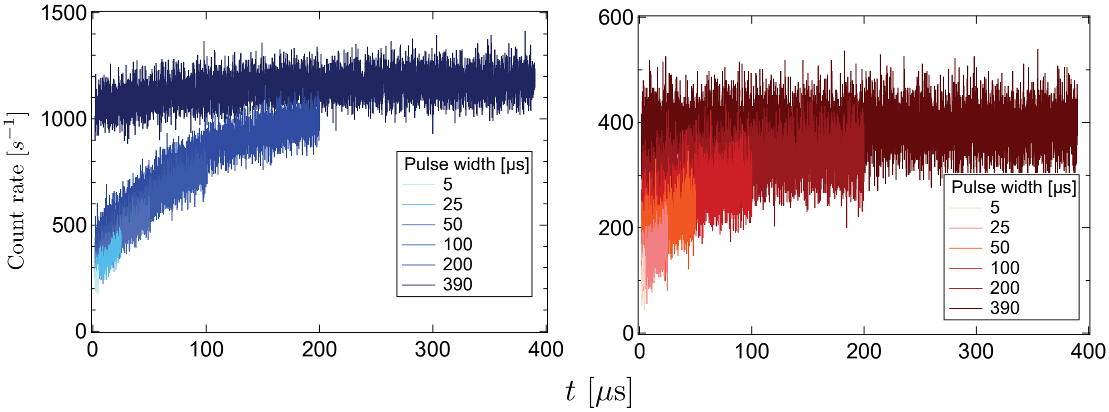

Figure 5.22: **Transient response of the acoustics** as a function of pulse width.

using equation 5.31 and 5.32. During the pulse-off window, we have

$$\dot{n}_{\text{ac,fall}}(t) = (n_{\text{th}}(t) - n_{\text{ac,fall}}(t))\gamma_{\text{ac}} \tag{5.35}$$

for $t_{\text{d}} < t \leq t_{\text{r}}$. The equations of $n_{\text{ac}}(t)$ are analytically solved with the boundary conditions $n_{\text{ac,rise}}(t_{\text{d}}) = n_{\text{ac,fall}}(t_{\text{d}})$ and $n_{\text{ac,rise}}(0) = n_{\text{ac,fall}}(t_{\text{r}})$. Notice that since $\kappa_{\text{c}} \gg \gamma_{\text{th}}, \gamma_{\text{ac}}$, we approximate the response of the optical bath as a step function here, such that the optomechanical backaction turns on and off instantly with the rise and fall of the pulse ($\gamma_{\text{ac,eff}} = \gamma_{\text{ac}} + \gamma_{\text{opt}} \rightarrow \gamma_{\text{ac}}$ when the pulse turns off)[8]. We also assume a constant bare acoustic damping rate γ_{ac}. Although the contribution from the three phonon loss process γ_{ball} (equation 5.24) has a T_{th}^4 dependence, the effect of the variation in T_{th} at low temperature (below 50 mK) is negligible.

We apply a periodic pulse of $P_{\text{in}} = 5\ \mu$W and $t_{\text{r}} = 400\ \mu$sec with a detuning of $\Delta = \pm\omega_{\text{ac}}$ to the cavity. We vary the width of the pulse from $t_{\text{d}} = 5\ \mu$sec to $t_{\text{d}} = 390\ \mu$sec, and measure the count rate during the pulse-on window as shown in Figure 5.22. The count rates are histogrammed with $\Delta t = 50$ ns bin and plotted as a function of t from the beginning of each pulse. Counts where $t < 2\ \mu$s are discarded due to the rising time of the shutters. The count rates are related to the solution of equation 5.34 by $R_{\text{S}}(t) = \alpha(n_{\text{ac,rise}}+1)$ and $R_{\text{AS}}(t) = \alpha n_{\text{ac,rise}}$ for the blue and red tones respectively, where α is a fitting parameter to normalize the phonon occupancy to sideband scattering rates.

The parameters involved in the solution of $n_{\text{ac,rise}}(t)$ include t_{d}, t_{r}, T_{MC}, α_{th}, γ_{th}, γ_{ac} and γ_{opt}. Using $T_{\text{MC}} = 24.4$ mK[9], $\gamma_{\text{ac}}/2\pi = 3250$ Hz[10], and $|\gamma_{\text{opt}}| = 4g_0^2/n_{\text{c}}/\kappa_{\text{c}}$ with $g_0/2\pi = 4750$ Hz[11], we examine the response of the thermal bath as a function of α_{th} and γ_{th}. Based on equation 5.31, α_{th} determines how much T_{th} increases due to optical heating and γ_{th} determines how fast T_{th} equilibrates to the steady state temperature ($T_{\text{MC}} + \alpha_{\text{th}}P_{\text{in}}$)

---

[8] This approximation agrees with the acoustic ringdown measurement shown in section 5.4.2, where we measure the bare acoustic damping rate right after the blue drive tone turns off.

[9] Results from Table 5.1.

[10] Results from Figure 5.15.

[11] Results from Table 5.1

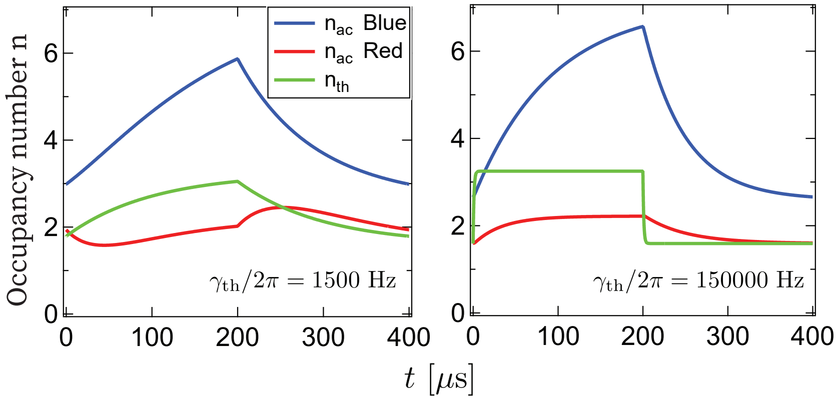

Figure 5.23: Transient resposne of the acoustics and the thermal bath with different thermal bath damping rates γ_{th}.

under a continuous P_{in}. Figure 5.23 shows the computed $n_{\text{ac}}(t)$ and $n_{\text{th}}(t)$ under a $t_{\text{d}} =$ 200 μs wide pulse with the same α_{th} and different values of $\gamma_{\text{th}}(t)$. The solution shows that with relatively slow thermal bath damping (left), n_{th} rises gradually (relative to t_{d}), and there exists an initial cooling of the acoustics due to optomechanical backaction with a red drive before it gets cancelled out by the increasing optical heating. It also arises from not having sufficient cooling time in between the pulses for the thermal bath to rethermalize with the MC.

We fit the count rates data shown in Figure 5.22 for $t_{\text{d}} =$ 50, 100, 200 and 390 μs simultaneously to the analytic expression of $n_{\text{ac,rise}}(t)$, where α (the count rate normalization factor), g_0 (variable in the expression for γ_{opt}), γ_{ac}, α_{th} and γ_{th} are the fitting parameters. The data are smoothed by taking a moving average of 20 and the larger t_{d} data are downsampled such that each data set has the same number of data points as shown in Figure 5.24. The fit captures the overall trend; however it does not quantify the initial temperature of the acoustics very well especially for shorter duration pulse. The fit returns a $\gamma_{\text{ac}}/2\pi =$ 2306 $\pm$ 1 Hz and $g_0/2\pi =$ 4121 $\pm$ 1 Hz which do not accurately describe the properties of the device.

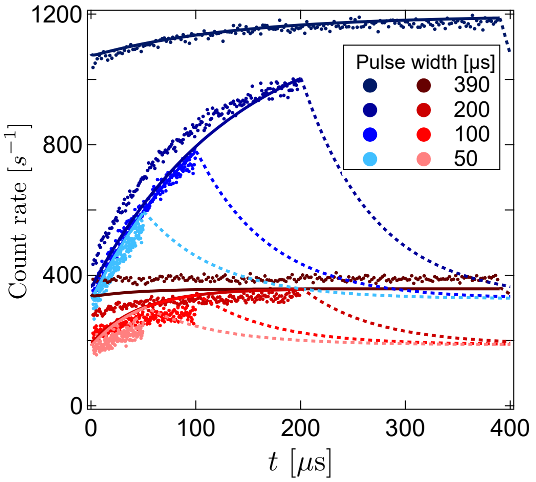

Figure 5.24: **Fit to the solution of** $n_{\textbf{ac,rise}}(t)$ where g_0, γ_{ac}, α_{th} and γ_{th} are the fitting parameters. Solid lines show the fits during the pulse-on window, and the dashed lines show the simulated decay of $n_{\text{ac,fall}}(t)$ during the pulse-off window.

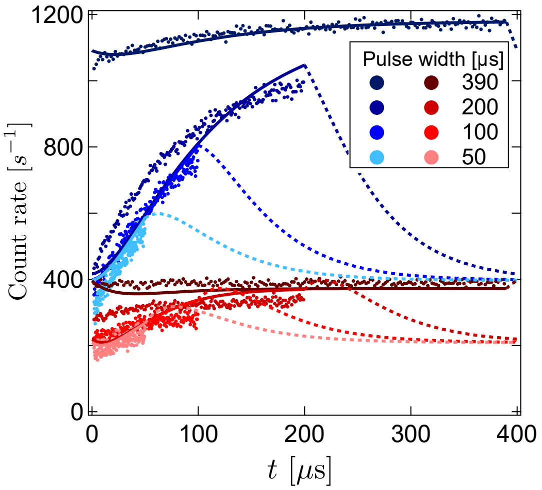

Figure 5.25: **Fit to the solution of** $n_{\textbf{ac,rise}}(t)$ where α_{th} and γ_{th} are the fitting parameters. g_0, γ_{ac} are fixed by using the independently determined values.

An alternative fit done by fixing γ_{ac} and g_0 to their expected values is shown in Figure 5.25, where it returns a thermal bath damping rate of $\gamma_{\text{th}} = 5530 \pm 10$ Hz. The fit does not capture the initial behavior accurately where it shows an initial decaying mode temperature, as the fit-extracted γ_{th} is slow comparing to the pulse duration and the rethermalization time. It suggests that the thermal bath response model we use is an over-simplified approximation and its evolution cannot be completely captured by a single time constant.

Chapter 6

Phonon coherences

In this chapter, I will discuss how we use the statistical properties, in particular, the temporal coherence functions to probe the motional state of the acoustic resonator in thermal equilibrium. Following the formulation of quantum optical coherences motivated in chapter 3, I will first describe the correspondence between photon and phonon coherences, allowing us to access quasi-probability distribution of the acoustic state through the optical field. While in the last chapter, the measurement of the photon counting spectrum (or the mean flux) is effectively a measurement of the first-order coherence of the motional state, I will present in the following our measurements of the phonon coherences of the thermal acoustic state up to the fourth-order. We also prepare and measure the phonon statistics of a phonon-added or -subtracted out-of-equilibrium thermal state via a heralding protocol, where we post-select on photon detection events [174].

6.1 Correspondence between photon and phonon coherences

We probe the thermal acoustic state by measuring the statistical properties of the acoustically scattered photons. In this section, I will derive the correspondence between the detected photon coherence and the phonon coherence of interest.

The bare acoustic oscillator is described by

$$\ddot{x}(t) + \gamma_{\text{ac}}\dot{x}(t) + \omega_{\text{ac}}^2 x(t) = F(t) \tag{6.1}$$

where γ_{ac} is the linewidth of the acoustic oscillator, ω_{ac} the resonant frequency and $F(t)$ the force acting on the oscillator. Correspondingly, in the frequency domain we have

$$-\omega^2 x[\omega] + i\omega\gamma x[\omega] + \omega_0^2 x[\omega] = F[\omega] \tag{6.2}$$

And the PSD of the acoustic oscillator is given by

$$S_{\text{xx}}[\omega] = |x[\omega]|^2 = \frac{S_{\text{FF}}[\omega]}{(\omega_{\text{ac}}^2 - \omega^2)^2 + \omega^2\gamma_{\text{ac}}^2} \tag{6.3}$$

The corresponding creation and annihilation operators where $x = x_{\text{ZPF}}(b+b^\dagger)$[1] is described by the Langevin equation

$$\dot{b} = -\left(\frac{\gamma_{\text{ac}}}{2} - i\omega_{\text{ac}}\right) b + \sqrt{\gamma_{\text{ac}}}\eta_{\text{th}} \tag{6.4}$$

with the corresponding spectrum of the acoustic field described by

$$S_{xx}[\omega] = x_{\text{ZPF}}^2(S_{b^\dagger b}[\omega] + S_{bb^\dagger}[\omega]) \tag{6.5}$$

Note that η_{th} is the thermal noise operator which has the following correlators,

$$\langle \eta_{\text{th}}^\dagger(\tau)\eta_{\text{th}}(0)\rangle = n_{\text{ac}}\delta(\tau) \tag{6.6}$$

$$\langle \eta_{\text{th}}(\tau)\eta_{\text{th}}^\dagger(0)\rangle = (n_{\text{ac}} + 1)\delta(\tau) \tag{6.7}$$

with $n_{\text{ac}} = \langle b^\dagger(t)b(t)\rangle$. It follows that

$$b(\tau) = \sqrt{\gamma_{\text{ac}}} \int_{-\infty}^{\infty} dt' e^{-(\gamma_{\text{ac}}/2 - i\omega_{\text{ac}})(\tau - t')}\eta_{\text{th}}(t') \tag{6.8}$$

Applying the noise operator correlators, we have

$$\langle b^\dagger(\tau)b(0)\rangle = n_{\text{ac}}e^{-(\gamma_{\text{ac}}/2 + i\omega_{\text{ac}})\tau} \tag{6.9}$$

$$\langle b(\tau)b^\dagger(0)\rangle = (n_{\text{ac}} + 1)e^{-(\gamma_{\text{ac}}/2 - i\omega_{\text{ac}})\tau} \tag{6.10}$$

Note that this is slightly different from the expression in equation 3.12, where we now have $\gamma \to \gamma_{\text{ac}}/2$. The exact expressions of phonon coherences of a thermal acoustic state are thus

$$g^{(2)}(\tau) = 1 + e^{-\gamma_{\text{ac}}|\tau|} \tag{6.11}$$

$$g^{(3)}(\tau) = 1 + e^{-\gamma_{\text{ac}}|\tau_1|} + e^{-\gamma_{\text{ac}}|\tau_2|} + 3e^{-\gamma_{\text{ac}}(|\tau_1 + \tau_2|)} \tag{6.12}$$

---

[1] x_{ZPF} is the zero-point fluctuation of the acoustic oscillator.

$$\begin{aligned} g^{(4)}(\tau) = 1 &+ e^{-\gamma_{\text{ac}}|\tau_1|} + e^{-\gamma_{\text{ac}}|\tau_2|} + e^{-\gamma_{\text{ac}}|\tau_3|} + e^{-\gamma_{\text{ac}}(|\tau_1+\tau_3|)} + 3e^{-\gamma_{\text{ac}}(|\tau_1+\tau_2|)} \\ &+ 3e^{-\gamma_{\text{ac}}(|\tau_2+\tau_3|)} + 9e^{-\gamma_{\text{ac}}(|\tau_1+\tau_2+\tau_3|)} + 4e^{-\gamma_{\text{ac}}(|\tau_1+2\tau_2+\tau_3|)} \end{aligned} \tag{6.13}$$

where we simply replace γ by $\gamma_{\text{ac}}/2$ in equation 3.19, 3.23 and 3.24.

We can thus calculate the field spectrum components $S_{b^\dagger b}[\omega]$ and $S_{bb^\dagger}[\omega]$ as

$$\begin{aligned} S_{b^\dagger b}[\omega] = \langle b^\dagger[\omega] b[-\omega] \rangle &= \int_{-\infty}^{\infty} d\tau \, e^{i\omega\tau} \langle b^\dagger(\tau) b(0) \rangle \\ &= \frac{n_{\text{ac}}\gamma_{\text{ac}}}{(\gamma_{\text{ac}}/2)^2 + (\omega + \omega_{\text{ac}})^2} \\ &= n_{\text{ac}}\gamma_{\text{ac}} |\chi_{\text{ac}}[-\omega]|^2 \end{aligned} \tag{6.14}$$

And similarly

$$\begin{aligned} S_{bb^\dagger}[\omega] = \langle b[\omega] b^\dagger[-\omega] \rangle &= \int_{-\infty}^{\infty} d\tau \, e^{i\omega\tau} \langle b(\tau) b^\dagger(0) \rangle \\ &= \frac{(n_{\text{ac}}+1)\gamma_{\text{ac}}}{(\gamma_{\text{ac}}/2)^2 + (\omega - \omega_{\text{ac}})^2} \\ &= (n_{\text{ac}}+1)\gamma_{\text{ac}} |\chi_{\text{ac}}[\omega]|^2 \end{aligned} \tag{6.15}$$

where we write in terms of the acoustic susceptibility

$$\chi_{\text{ac}}[\omega] = 1/(-i(\omega - \omega_{\text{ac}}) + \gamma_{\text{ac}}/2) \tag{6.16}$$

Note that $S_{b^\dagger b}[\omega]$ in equation 6.14 is only nonzero around $\omega \approx -\omega_{\text{ac}}$, hence corresponding to the anti-Stokes scattering events with a red-detuned drive. And $S_{bb^\dagger}[\omega]$ in equation 6.15 is only nonzero around $\omega \approx +\omega_{\text{ac}}$, corresponding to the Stokes scattering events with a blue-detuned drive.

We can now examine the cavity output field from the cavity $o(t)$ and the corresponding field detected by the SNSPDs $p(t)$. We have $o(t)$ related to the cavity field $a(t)$ as such

$$o(t) = \xi_{\text{in}}(t) - \sqrt{\kappa_{\text{in}}} a(t) \tag{6.17}$$

where ξ_{in} and κ_{in} are the fluctuations and coupling rate to the input (output) port. In the rotating frame of optical drive frequency at $\omega_{\text{c}} + \Delta$ (the cavity resonant frequency plus the drive detuning), we can write the cavity field as

$$a[\omega] = \chi_{\text{c}}[\omega + \Delta](-ig_0\bar{a}b[\omega] + \sqrt{\kappa_{\text{in}}}\xi_{\text{in}}[\omega]) \tag{6.18}$$

and the output field as

$$o[\omega] = \xi_{\text{in}}[\omega] + i\sqrt{\kappa_{\text{in}}}\chi_{\text{c}}[\omega + \Delta] g_0 \bar{a} b[\omega] \tag{6.19}$$

where the cavity susceptibility is $\chi_{\text{c}}[\omega] = 1/(\kappa/2 - i\omega)$. We can thus write

$$\begin{aligned} S_{o^\dagger o}[\omega] &= \langle o^\dagger[\omega] o[\omega] \rangle \\ &= \kappa_{\text{in}} g_0^2 n_{\text{c}} |\chi_{\text{c}}[-\omega]|^2 S_{xx}[\omega] \\ &= \kappa_{\text{in}} g_0^2 n_{\text{c}} |\chi_{\text{c}}[-\omega]|^2 (S_{b^\dagger b}[\omega] + S_{bb^\dagger}[\omega]) \end{aligned} \tag{6.20}$$

which is the field induced by optomechanical coupling, and $n_{\text{c}} = \langle a^\dagger a \rangle$ and g_0 are the intracavity photon number and the single photon optomechanical coupling rate respectively.

The output field is detected after passing through a series of filters, where the loss and filter transmission function are described by $f_{filt}[\omega]$, centered around $+\omega_{\text{ac}}$ when a red-detuned drive is used and around $-\omega_{\text{ac}}$ when a blue-detuned drive is used. The detected field $p(t)$ can thus be written as

$$p(t) = \int_{-\infty}^{\infty} \frac{d\omega}{2\pi} e^{-i\omega t} f_{\text{filt}}[\omega] o[\omega] \tag{6.21}$$

Plugging in equation 6.20, we have the correlations of the detected field as

$$\begin{aligned} \langle p^\dagger(t+\tau) p(t) \rangle &= \int_{-\infty}^{\infty} \frac{d\omega}{2\pi}\, e^{-i\omega\tau} |f_{\text{filt}}[-\omega]|^2 S_{o^\dagger o}[\omega] \\ &= \kappa_{\text{in}} g_0^2 n_{\text{c}} \int_{-\infty}^{\infty} \frac{d\omega}{2\pi}\, e^{-i\omega\tau} |f_{\text{filt}}[-\omega]|^2 |\chi_{\text{c}}[-\omega]|^2 (S_{b^\dagger b}[\omega] + S_{bb^\dagger}[\omega]) \end{aligned} \tag{6.22}$$

With a red-detuned drive, we are left with the terms

$$\begin{aligned} \langle p^\dagger(t+\tau) p(t) \rangle &= \kappa_{\text{in}} g_0^2 n_{\text{c}} |\chi_{\text{c}}[\omega_{\text{c}}]|^2 \int_{-\infty}^{\infty} \frac{d\omega}{2\pi}\, e^{-i\omega\tau} S_{b^\dagger b}[\omega] \\ &\propto \langle b^\dagger(t+\tau) b(t) \rangle \end{aligned} \tag{6.23}$$

showing that the normally ordered correlations of the detected anti-Stokes scattered field corresponds to the normally ordered correlations of the acoustic oscillator. We assume a sideband-resolved regime here such that $\gamma_{\text{ac}} \ll \kappa_{\text{c}}$. Also we assume the filter linewidth is larger than the acoustic linewidth, and much smaller than κ_{c}, such that $f_{\text{filt}}[\omega]$ is well-approximated by a constant around detuning $\Delta \approx \pm\omega_{\text{ac}}$. Similarly, we can show that with a blue-detuned drive, we have

$$\begin{aligned} \langle p^\dagger(t+\tau) p(t) \rangle &= \kappa_{\text{in}} g_0^2 n_{\text{c}} |\chi_{\text{c}}[-\omega_{\text{c}}]|^2 \int_{-\infty}^{\infty} \frac{d\omega}{2\pi}\, e^{-i\omega\tau} S_{bb^\dagger}[\omega] \\ &\propto \langle b(t+\tau) b^\dagger(t) \rangle \end{aligned} \tag{6.24}$$

such that the normally ordered correlations of the detected Stokes scattered field corresponds to the anti-normally ordered correlations of the acoustic oscillator. Note that the constants in these correlation functions account for detection efficiency, damping and the parameters of the optomechanical system, and the coupling efficiency, which however gets normalized in the coherence functions by the mean detected flux. The measurement of the statistics is therefore unaffected by system and detection inefficiency.

Thus, there exists a one-to-one correspondence between the coherence functions of the detected optical field and the acoustic oscillator. As the detection of each photon scattered by the acoustics heralds the creation or annihilation of a single phonon, it allows us to directly probe the state of the acoustics through measuring statistics of the detected photon field.

6.2 Measurement of coherence functions

6.2.1 Construction of a delay histogram

In order to measure the phonon coherences $g^{(l)}(\tau_1, \cdots, \tau_{l-1})$ as defined in equation 3.10, we construct a histogram of the delays between the arrivals of l-detected photons, denoted as $C^{(l)}_{\text{AS(S)}}(\tau)$, where AS describes anti-Stokes scattered photons and S describes Stokes-scattered photons.

Consider the most straightforward case for the normally-ordered second-order phonon coherence $g^{(2)}_{\text{ac}}(\tau)$. As shown in section 6.1, it is equivalent to the normally ordered second-order coherence $g^{(2)}_{\text{AS}}(\tau)$ of anti-Stokes scattered photons and its corresponding photon delay histogram $C^{(2)}_{\text{AS}}(\tau)$.

As described in section 4.2, the arrival time of each photon detected by the SNSPDs is tagged by the time-correlated single photon counting (TCSPC) electronics. To gather enough statistics we repeat the lock and drive sequence in a continuous wave measurement that is repeated at a rate of 5 Hz. For a typical measurement of coherences up to the fourth-order, we repeat the 200 ms sequences $\sim 500,000$ times. A gate signal is sent to the SNSPDs at the beginning of each drive period as shown in figure 4.10. To combine the data from each cycle, we thus first obtain the time tag of each photon detection event relative to each gate signal. Figure 6.1 shows a typical relative time tag of photon detection events in one drive period.

To obtain its corresponding delay histogram $C^{(2)}(\tau)$, we compute the list of delays between each pair of photons $\{t_j - t_i\} \forall j > i$. By histogramming the list of delays from figure 6.1, we obtain its corresponding $C^{(2)}(\tau)$ as shown in figure 6.2. Here we use a bin size of 2 μsec and a maximum delay of $\tau = 500$ μs, which is much greater than the coherence time of the acoustic oscillator (~ 500 μs), after which the arrivals of the photons are expected to be uncorrelated.

Individual delay histograms such as the ones shown in figure 6.2 are summed up to obtain a typical cumulative $C^{(2)}_{\text{AS}}(\tau)$ shown in figure 6.3, where we repeat the drive periods by $\sim$ 20,000 times. Here we use a red-detuned drive at a drive power of $P_{\text{in}} \sim 5$ μW. We

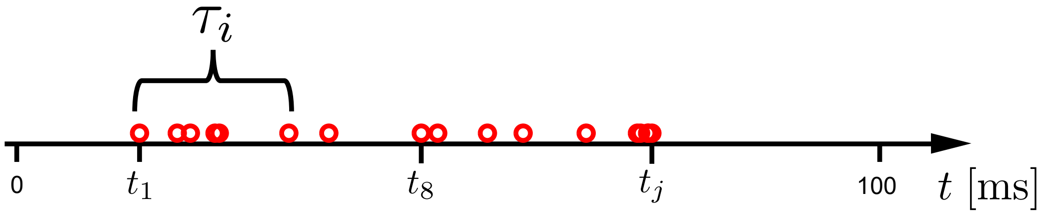

Figure 6.1: Timing of photon detection events in one drive period. Each red dot represents a photon detection event registered by the TCSPC, and t_j is the relative time tag describing the time difference between the time of detection from the gate signal occurring at the beginning of each drive period.

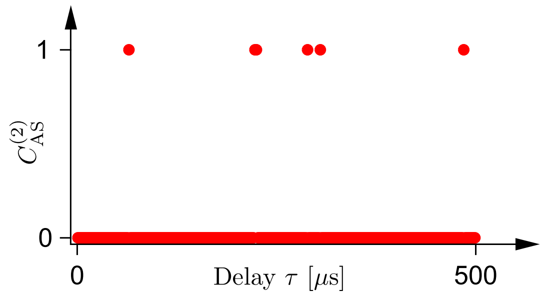

Figure 6.2: A typical delay histogram obtained from one drive period, with a bin size of 2 μsec and a maximum delay of $\tau = 500$ μs.

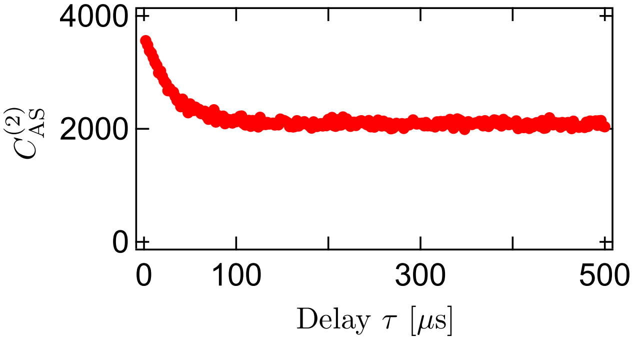

Figure 6.3: A typical second-order cumulative delay histogram, where the drive period is repeated $\sim$ 50,000 times with a red-detuned drive at a drive power of $P_{\text{in}} \sim 5$ μW.

thus effectively measure the second-order time correlation $\langle \hat{a}^\dagger(t)\hat{a}^\dagger(t+\tau)\hat{a}(t+\tau)\hat{a}(t)\rangle$.

6.2.2 Background subtraction

As described in section 5.1, some portion of the detected photons are from background photons, which need to be excluded from the delay histogram of sideband scattered photons of interest. In this section, I will describe our method to correct for the effect of background photon detection on the time correlation of sideband photons.

Note that in a CW measurement, the denominator of $g^{(2)}(\tau)$ is just the square of the mean photon flux $\langle \hat{a}^\dagger \hat{a}\rangle^2$ since $\langle \hat{a}^\dagger(0)\hat{a}(0)\rangle = \langle \hat{a}^\dagger(\tau)\hat{a}(\tau)\rangle$. It follows that in the presence of background photons, the second-order coherence function

$$\begin{aligned} g^{(2)}(\tau) &= \frac{\langle \hat{a}^\dagger(0)\hat{a}^\dagger(\tau)\hat{a}(\tau)\hat{a}(0)\rangle}{\langle \hat{a}^\dagger(0)\hat{a}(0)\rangle\langle \hat{a}^\dagger(\tau)\hat{a}(\tau)\rangle} \\ &= \frac{\langle \hat{a}^\dagger(0)\hat{a}^\dagger(\tau)\hat{a}(\tau)\hat{a}(0)\rangle}{\langle \hat{a}^\dagger \hat{a}\rangle^2} \end{aligned} \tag{6.25}$$

is in fact described by

$$g^{(2)}_{\text{meas}}(\tau) = \frac{\langle [\hat{a}^\dagger(0)+\hat{\xi}^\dagger(0)][\hat{a}^\dagger(\tau)+\hat{\xi}^\dagger(\tau)][\hat{a}(\tau)+\hat{\xi}(\tau)][\hat{a}(0)+\hat{\xi}(0)]\rangle}{\langle [\hat{a}^\dagger(0)+\hat{\xi}^\dagger(0)][\hat{a}(0)+\hat{\xi}(0)]\rangle\langle [\hat{a}^\dagger(\tau)+\hat{\xi}^\dagger(\tau)][\hat{a}(\tau)+\hat{\xi}(\tau)]\rangle} \tag{6.26}$$

where we denote the sideband photon with $\hat{a}$ and the background photon with $\hat{\xi}$. To simplify the expression, we note that the sideband photons and background photons are independent of each other. The cross correlations between them thus vanish such that

$$\langle \hat{a}^\dagger \hat{\xi}\rangle = \langle \hat{\xi}^\dagger \hat{a}\rangle = 0 \tag{6.27}$$

and the background photons are uncorrelated with each other such that

$$\begin{aligned} \langle \hat{\xi}^\dagger(0)\hat{\xi}^\dagger(\tau)\hat{\xi}(\tau)\hat{\xi}(0)\rangle &= \langle \hat{\xi}^\dagger(0)\hat{\xi}(0)\rangle^2 = \langle \hat{\xi}^\dagger(\tau)\hat{\xi}(\tau)\rangle^2 \\ &= \langle \hat{\xi}^\dagger \hat{\xi}\rangle^2 \end{aligned} \tag{6.28}$$

It is useful to define the ratio of mean background photon flux in each measurement, such that

$$\epsilon = \frac{\langle \hat{\xi}^\dagger \hat{\xi}\rangle}{\langle \hat{a}^\dagger \hat{a}\rangle} = \frac{R_{\text{bkg}}}{R_{\text{AS(S)}}} \tag{6.29}$$

where R_{bkg} and R_{bkg} are the rates of detection of background photons and acoustically scattered photons respectively. Note that sources of the background photon counts include stray light from the environment, leakage photons through the filter cavities, and the dark counts of SNSPDs. We assume the total flux of which to remain approximately constant throughout each measurement. Using these relations, the denominator of $g^{(2)}_{\text{meas}}(\tau)$ in equation 6.26 is simplified as

$$
\begin{aligned}
&\langle[\hat{a}^\dagger(0)+\hat{\xi}^\dagger(0)][\hat{a}(0)+\hat{\xi}(0)]\rangle\langle[\hat{a}^\dagger(\tau)+\hat{\xi}^\dagger(\tau)][\hat{a}(\tau)+\hat{\xi}(\tau)]\rangle\\
&=(\langle\hat{a}^\dagger(0)\hat{a}(0)\rangle+\langle\hat{\xi}^\dagger(0)\hat{\xi}(0)\rangle)+(\langle\hat{a}^\dagger(\tau)\hat{a}(\tau)\rangle+\langle\hat{\xi}^\dagger(\tau)\hat{\xi}(\tau)\rangle)\\
&=\langle\hat{a}^\dagger\hat{a}\rangle^2+2\langle\hat{a}^\dagger\hat{a}\rangle\langle\hat{\xi}^\dagger\hat{\xi}\rangle+\langle\hat{\xi}^\dagger\hat{\xi}\rangle^2=\langle\hat{a}^\dagger\hat{a}\rangle^2(1+\epsilon)^2
\end{aligned}
\tag{6.30}
$$

where all the cross correlation terms vanish by equation 6.27. Similarly, we simplify the numerator of $g^{(2)}_{\text{meas}}(\tau)$ as

$$
\begin{aligned}
&\langle[\hat{a}^\dagger(0)+\hat{\xi}^\dagger(0)][\hat{a}^\dagger(\tau)+\hat{\xi}^\dagger(\tau)][\hat{a}(\tau)+\hat{\xi}(\tau)][\hat{a}(0)+\hat{\xi}(0)]\rangle\\
&=\langle\hat{a}^\dagger(0)\hat{a}^\dagger(\tau)\hat{a}(\tau)\hat{a}(0)\rangle+\langle\hat{a}^\dagger(0)\hat{\xi}^\dagger(\tau)\hat{\xi}(\tau)\hat{a}(0)\rangle\\
&\qquad+\langle\hat{\xi}^\dagger(0)\hat{a}^\dagger(\tau)\hat{a}(\tau)\hat{\xi}(0)\rangle+\langle\hat{\xi}^\dagger(0)\hat{\xi}^\dagger(\tau)\hat{\xi}(\tau)\hat{\xi}(0)\rangle\\
&=\langle\hat{a}^\dagger(0)\hat{a}^\dagger(\tau)\hat{a}(\tau)\hat{a}(0)\rangle+2\langle\hat{a}^\dagger\hat{a}\rangle\langle\hat{\xi}^\dagger\hat{\xi}\rangle+\langle\hat{\xi}^\dagger\hat{\xi}\rangle^2
\end{aligned}
\tag{6.31}
$$

We thus have

$$
\begin{aligned}
g^{(2)}_{\text{meas}}(\tau)&=\frac{\langle\hat{a}^\dagger(0)\hat{a}^\dagger(\tau)\hat{a}(\tau)\hat{a}(0)\rangle+2\langle\hat{a}^\dagger\hat{a}\rangle\langle\hat{\xi}^\dagger\hat{\xi}\rangle+\langle\hat{\xi}^\dagger\hat{\xi}\rangle^2}{\langle\hat{a}^\dagger\hat{a}\rangle^2(1+\epsilon)^2}\\
&=\frac{\langle\hat{a}^\dagger(0)\hat{a}^\dagger(\tau)\hat{a}(\tau)\hat{a}(0)\rangle}{\langle\hat{a}^\dagger\hat{a}\rangle^2(1+\epsilon)^2}+\frac{1}{(1+\epsilon)^2}\left(\frac{2\langle\hat{\xi}^\dagger\hat{\xi}\rangle}{\langle\hat{a}^\dagger\hat{a}\rangle}+\frac{\langle\hat{\xi}^\dagger\hat{\xi}\rangle^2}{\langle\hat{a}^\dagger\hat{a}\rangle^2}\right)\\
&=\frac{g^{(2)}(\tau)+2\epsilon+\epsilon^2}{(1+\epsilon)^2}
\end{aligned}
\tag{6.32}
$$

To obtain the actual sideband acoustic photon correlation from the measurement, we thus use the relation

$$
g^{(2)}(\tau)=g^{(2)}_{\text{meas}}(\tau)+2(g^{(2)}_{\text{meas}}(\tau)-1)\epsilon+(g^{(2)}_{\text{meas}}(\tau)-1)\epsilon^2 \tag{6.33}
$$

For the measured cumulative delay histogram shown in figure 6.3, we have

$$
\begin{aligned}
C^{(2)}_{\text{AS, meas}}(\tau)=g^{(2)}_{\text{meas}}(\tau)R_{\text{meas}}&=\frac{g^{(2)}(\tau)R_{\text{AS}}}{1+\epsilon}+\frac{(2\epsilon+\epsilon^2)R_{\text{meas}}}{(1+\epsilon)^2}\\
&=\frac{C^{(2)}_{\text{AS}}(\tau)}{1+\epsilon}+\frac{(2\epsilon+\epsilon^2)R_{\text{meas}}}{(1+\epsilon)^2}
\end{aligned}
\tag{6.34}
$$

where $R_{\text{meas}}=R_{\text{bkg}}+R_{\text{AS(S)}}$.

Note that as discussed in section 5.1 (shown in figure 6.4), the rate of detected background counts is dependent on the drive tone setting, mainly from drive photons leaking through the filters. ϵ thus has to be measured for each experiments with varying drive powers and filter transmission. While a red- or blue-detuned drive ($\Delta=\mp\omega_{\text{ac}}$) is used for generating acoustically scattered photons in the CW phonon coherence experiment discussed in this chapter, we also use a drive tone of the same power as the red or blue drive,

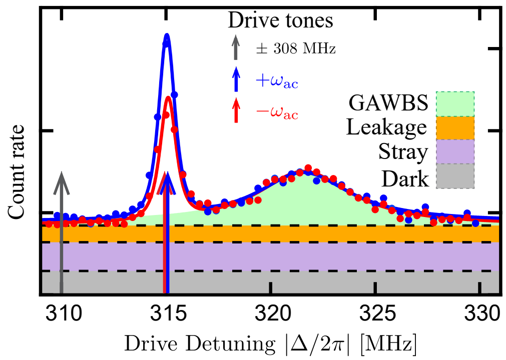

Figure 6.4: A red- or blue-detuned drive ($\Delta = \mp\omega_{\mathrm{ac}}$) is used for generating acoustically scattered photons in the CW phonon coherence experiment discussed in this chapter. Another drive tone of the same power as the red and blue drive is used to calibrate the background photon count rate at a detuning of $\Delta_{\mathrm{bkg}}/2\pi = \mp 308$ MHz.

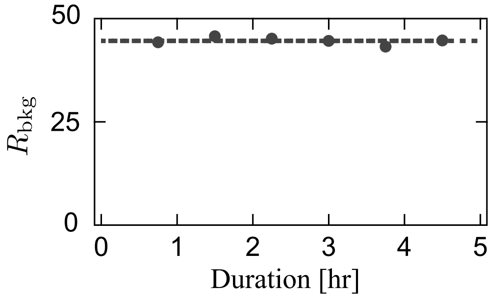

Figure 6.5: A typical background count rate R_{bkg} measurement, which is recorded periodically during a CW phonon coherence measurement.

at a detuning of $\Delta_{\mathrm{bkg}}/2\pi = \mp 308$ MHz, to calibrate the background count rate for each experimental setting of drive tones of various powers.

We find that the GAWBS contribution at ω_{ac} is negligible (section 5.1.1), while the sideband photon contribution at $|\Delta_{\mathrm{bkg}}|$ is also negligible as $|\Delta_{\mathrm{bkg}}| \gg \gamma_{\mathrm{ac}}$. The background count rate is measured periodically during an experiment. Figure 6.4 shows a typical record of background count rate measured over a ~ 5 hour experiment corresponding to the delay histogram (uncorrected for background counts) shown in figure 6.3, where a red-detuned drive of $P_{\mathrm{in}} \sim 5\ \mu$W is used, and we measure a relatively stable mean background photon flux of $R_{\mathrm{bkg}} = 47.0 \pm 0.4\ s^{-1}$. The corresponding ϵ in this measurement is 0.154. For the drive powers used in the results presented in this chapter ($1\mu\mathrm{W} \leq P_{\mathrm{in}} \leq 5\mu\mathrm{W}$), the ratio of the background photon flux ranges from $0.04 \lesssim \epsilon \lesssim 0.2$. We also examine that the statistics of the background photon counts is indeed uncorrelated in time following a Poisson distribution, as we assume in equation 6.28 (see appendix C.1 for more detail).

We apply this correction in equation 6.34 to figure 6.3 to obtain the delay histogram of anti-Stokes scattered photons which is corrected for the contribution from the background photons, as shown in figure 6.6. This background-corrected sideband photon coherence corresponds to the normally ordered phonon coherence of the acoustic oscillator in thermal equilibrium. According to equation 6.11, it follows the functional form $A + Be^{-\gamma_{\mathrm{ac}}\tau}$, where

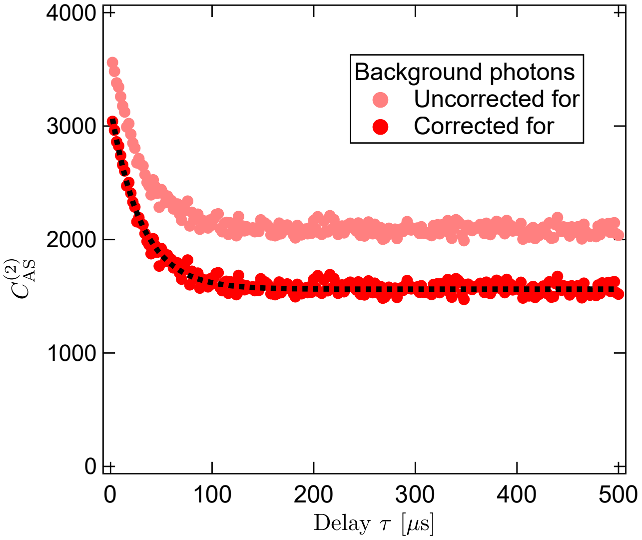

Figure 6.6: Darker red trace shows the delay histogram after background correction according to equation 6.34, which is fit to the functional form of $A + Be^{-\gamma_{\mathrm{ac}}\tau}$ as expected for a thermal acoustic oscillator.

A is a normalization factor accounting for the mean photon flux and $B/A = 1$. The black dashed line shows the best fit of corrected $C^{(2)}_{\mathrm{AS}}$ to this form, where A, B and γ_{ac} are the fitting parameters. It returns an acoustic damping rate of $\gamma_{\mathrm{ac}}/2\pi = 5300 \pm 100$ Hz, which is optomechanically broadened by the red-detuned drive from its bare damping rate of $\gamma_{\mathrm{bare}}/2\pi = 3250 \pm 20$. The time decay of the phonon coherences will be examined in more detail in the next section.

For higher order coherences, we apply similar calculation used for $g^{(2)}_{\mathrm{meas}}$ to correct for the background photon counts. For the third-order coherences, we have

$$g^{(3)}_{\mathrm{meas}}(\tau_1, \tau_2) = \frac{\langle(\hat{a}_0^\dagger + \hat{\xi}_0^\dagger)(\hat{a}_1^\dagger + \hat{\xi}_1^\dagger)(\hat{a}_2^\dagger + \hat{\xi}_2^\dagger)(\hat{a}_0 + \hat{\xi}_0)(\hat{a}_1 + \hat{\xi}_1)(\hat{a}_2 + \hat{\xi}_2)\rangle}{\langle(\hat{a}^\dagger + \hat{\xi}^\dagger)(\hat{a} + \hat{\xi})\rangle^3} \tag{6.35}$$

For the denominator, we have

$$\begin{aligned}\langle(\hat{a}^\dagger + \hat{\xi}^\dagger)(\hat{a} + \hat{\xi})\rangle^3 &= \langle\hat{a}^\dagger\hat{a}\rangle^3 + \langle\hat{\xi}^\dagger\hat{\xi}\rangle^3 + 3\langle\hat{a}^\dagger\hat{a}\rangle^2\langle\hat{\xi}^\dagger\hat{\xi}\rangle + 3\langle\hat{a}^\dagger\hat{a}\rangle\langle\hat{\xi}^\dagger\hat{\xi}\rangle^2 \\ &= (\langle\hat{a}^\dagger\hat{a}\rangle + \langle\hat{\xi}^\dagger\hat{\xi}\rangle)^3\end{aligned} \tag{6.36}$$

Since

$$(1 + \epsilon)^n = \frac{(\langle\hat{a}^\dagger\hat{a}\rangle + \langle\hat{\xi}^\dagger\hat{\xi}\rangle)^n}{\langle\hat{a}^\dagger\hat{a}\rangle^n} \tag{6.37}$$

we have in general that the denominator of $g^{(l)}_{\mathrm{meas}}(\tau_1, \tau_2, \cdots, \tau_l - 1)$ is equivalent to $(1 + \epsilon)^l\langle\hat{a}^\dagger\hat{a}\rangle^l$.

After expanding and eliminating the cross correlation terms, numerator of equation

6.35 becomes

$$\begin{aligned}
&\langle(\hat{a}_0^\dagger+\hat{\xi}_0^\dagger)(\hat{a}_1^\dagger+\hat{\xi}_1^\dagger)(\hat{a}_2^\dagger+\hat{\xi}_2^\dagger)(\hat{a}_0+\hat{\xi}_0)(\hat{a}_1+\hat{\xi}_1)(\hat{a}_2+\hat{\xi}_2)\rangle\\
=&\langle\hat{a}_0^\dagger\hat{a}_1^\dagger\hat{a}_2^\dagger\hat{a}_2\hat{a}_1\hat{a}_0\rangle+\langle\hat{\xi}_0^\dagger\hat{\xi}_1^\dagger\hat{\xi}_2^\dagger\hat{\xi}_2\hat{\xi}_1\hat{\xi}_0\rangle\\
&+\langle\hat{\xi}^\dagger\hat{\xi}\rangle(\langle\hat{a}_0^\dagger\hat{a}_1^\dagger\hat{a}_1\hat{a}_0\rangle+\langle\hat{a}_1^\dagger\hat{a}_2^\dagger\hat{a}_2\hat{a}_1\rangle+\langle\hat{a}_0^\dagger\hat{a}_2^\dagger\hat{a}_2\hat{a}_0\rangle)\\
&+\langle\hat{\xi}^\dagger\hat{\xi}\rangle^2(\langle\hat{a}_0^\dagger\hat{a}_0\rangle+\langle\hat{a}_1^\dagger\hat{a}_2\rangle+\langle\hat{a}_2^\dagger\hat{a}_2\rangle)
\end{aligned}\tag{6.38}$$

We thus have

$$\begin{aligned}
g^{(3)}_{\text{meas}}(\tau_1,\tau_2)=&\frac{\langle\hat{a}_0^\dagger\hat{a}_1^\dagger\hat{a}_2^\dagger\hat{a}_2\hat{a}_1\hat{a}_0\rangle}{(1+\epsilon)^3\langle\hat{a}^\dagger\hat{a}\rangle^3}+\frac{\langle\hat{\xi}^\dagger\hat{\xi}\rangle^3}{(1+\epsilon)^3\langle\hat{a}^\dagger\hat{a}\rangle^3}\\
&+\frac{\epsilon}{(1+\epsilon)^3}\frac{\langle\hat{a}_0^\dagger\hat{a}_1^\dagger\hat{a}_1\hat{a}_0\rangle+\langle\hat{a}_1^\dagger\hat{a}_2^\dagger\hat{a}_2\hat{a}_1\rangle+\langle\hat{a}_0^\dagger\hat{a}_2^\dagger\hat{a}_2\hat{a}_0\rangle}{\langle\hat{a}^\dagger\hat{a}\rangle^2}+\frac{3\epsilon^2}{(1+\epsilon)^3}\\
=&\frac{g^{(3)}(\tau_1,\tau_2)+\epsilon^3+3\epsilon^2+\epsilon(g^{(2)}(\tau_1)+g^{(2)}(\tau_2)+g^{(2)}(\tau_1+\tau_2))}{(1+\epsilon)^3}
\end{aligned}\tag{6.39}$$

where $\hat{a}_0\equiv\hat{a}(0)$, $\hat{a}_1\equiv\hat{a}(\tau_1)$, $\hat{a}_2\equiv\hat{a}(\tau_2)$ respectively. Similarly, we can further write that

$$\begin{aligned}
g^{(4)}_{\text{meas}}(\tau_1,\tau_2,\tau_3)=&\frac{1}{(1+\epsilon)^4}\big(g^{(4)}(\tau_1,\tau_2,\tau_3)+\epsilon^4+4\epsilon^3\\
&+\epsilon^2\sum_{g_j^{(2)}\in\mathbb{G}^{(2)}}g_j^{(2)}+\epsilon\sum_{g_i^{(3)}\in\mathbb{G}^{(3)}}g_i^{(3)}\big)
\end{aligned}\tag{6.40}$$

where $\mathbb{G}^{(2)}$ and $\mathbb{G}^{(3)}$ are sets of coherence functions of the second- and third-order as a function of various time delays, such that

$$\begin{aligned}
\mathbb{G}^{(2)}&=\{g^{(2)}(\tau_1),g^{(2)}(\tau_2),g^{(2)}(\tau_3),g^{(2)}(\tau_1+\tau_2),g^{(2)}(\tau_2+\tau_3),g^{(2)}(\tau_1+\tau_2+\tau_3)\}\\
\mathbb{G}^{(3)}&=\{g^{(3)}(\tau_1,\tau_2),g^{(3)}(\tau_1+\tau_2,\tau_3),g^{(3)}(\tau_1,\tau_2+\tau_3),g^{(3)}(\tau_2,\tau_3)\}
\end{aligned}$$

6.3 High order phonon coherences

In this section, I will show our measurement of phonon coherences up to the fourth-order of our acoustic oscillator in a thermal state, using the result and protocol discussed in previous sections. We use both red and blue drive tones at various drive power to probe the dynamics of the acoustic oscillator.

As discussed in section 6.1, correlations of the anti-Stokes scattered photon from a red drive correspond to the normally ordered phonon coherence, denoted by $g^{(l)}_{\text{ac}}$ such that

$$g^{(l)}_{\text{ac}}\equiv\frac{\langle(\hat{b}^\dagger)^l\hat{b}^l\rangle}{\langle\hat{b}^\dagger\hat{b}\rangle^l}=\frac{\langle(\hat{a}^\dagger)^l\hat{a}^l\rangle}{\langle\hat{a}^\dagger\hat{a}\rangle^l}\equiv g^{(l)}_{\text{AS}}\tag{6.41}$$

And we have the anti-normally ordered phonon coherence,

$$h_{\text{ac}}^{(l)} \equiv \frac{\langle \hat{b}^l (\hat{b}^\dagger)^l \rangle}{\langle \hat{b}^\dagger \hat{b} \rangle^l} = \frac{\langle (\hat{a}^\dagger)^l \hat{a}^l \rangle}{\langle \hat{a}^\dagger \hat{a} \rangle^l} \equiv g_{\text{S}}^{(l)} \tag{6.42}$$

6.3.1 Second-order phonon coherences

The second-order coherences of phonons measured for the acoustic oscillator in thermal equilibrium is shown in figure 6.7.

The measured as well as the background-corrected $C_{\text{AS}}^{(2)}$ and $C_{\text{S}}^{(2)}$ are shown in figure 6.7(a)-(b) for the anti-Stokes and Stokes scattered photons respectively. Delay τ is binned by a 2 μs window, and is histogrammed up to $\tau = 1$ ms to show the time dependence. Total experimental time[2] for collecting both sets of data shown here is ~3.5 hours, during which the anti-Stokes data is collected for 1820 sec with a red-detuned drive of an average power $P_{\text{in}} = 5.24\ \mu$W. The rate of measured photons (including both sideband and background photons) is $R_{\text{meas}} = 756\ s^{-1}$, whereas the background photon rate is $R_{\text{bkg}} = 101\ s^{-1}$, yielding $\epsilon = 0.154$. The Stokes data is collected for 857 sec with a blue-detuned drive of an average power $P_{\text{in}} = 5.09\ \mu$W. The rate of total measured photons is $R_{\text{meas}} = 2334\ s^{-1}$, whereas the background photon rate is $R_{\text{bkg}} = 108\ s^{-1}$, yielding $\epsilon = 0.049$.

The background-corrected $C_{\text{AS}}^{(2)}$ and $C_{\text{S}}^{(2)}$ are fit to the form $A + Be^{-\gamma_{\text{ac}}\tau}$ according to equation 6.11 as shown by the black dashed lines, where A, B, γ_{ac} are the fitting parameters. A is an overall normalization factor used to convert the histogram to phonon coherences $g_{\text{ac}}^{(2)}(\tau)$ and $h_{\text{ac}}^{(2)}(\tau)$, and the corresponding $g^{(2)}(0)$ and $h^{(2)}(0)$ are given by $1 + B/A$. Figure 6.11(c)-(d) shows $g_{\text{ac}}^{(2)}(\tau) = C_{\text{AS}}^{(2)}/A$ and $h_{\text{ac}}^{(2)}(\tau) = C_{\text{S}}^{(2)}/A$ and the corresponding fits $1 + (B/A)e^{-\gamma_{\text{ac}}\tau}$. The fits return

$$g_{\text{ac}}^{(2)}(0) = 2.006 \pm 0.004 \tag{6.43}$$

$$h_{\text{ac}}^{(2)}(0) = 2.03 \pm 0.02 \tag{6.44}$$

with corresponding damping rates of $\gamma_{\text{ac, AS}}/2\pi = 5300 \pm 100$ Hz and $\gamma_{\text{ac, S}}/2\pi = 1780 \pm 10$ Hz, which are increased and decreased respectively due to the optomechanical effects. $g_{\text{ac}}^{(2)}(\tau)$ and $g_{\text{ac}}^{(2)}(\tau)$ are also shown on a logarithmic scale in figure 6.11(e) and (f) to demonstrate their exponential form.

The measurements are repeated for different P_{in}. In general, the amount of detected second-order coincidence counts scale by $\sim\ R_{\text{meas}}^2$. Hence, to achieve the same signal-to-noise ratio to examine the feature of $g_{\text{ac}}^{(2)}(0)$ and $h_{\text{ac}}^{(2)}(0)$ at zero coincidence in particular, the total DAQ time scales inversely with $\sim\ R_{\text{meas}}^2$. The experimental settings and results are summarized in table 6.1. $g_{\text{ac}}^{(2)}(0)$ and $h_{\text{ac}}^{(2)}(0)$ as a function of drive power are plotted in figure 6.8. The stated uncertainty corresponds to one standard deviation of the best-fit parameter to the functional form of coherences of a thermal state. The thermal acoustic

---

[2] This includes the lock period, the drive and DAQ period, the background photon measurement period, and the calibration period that measures filter transmission.

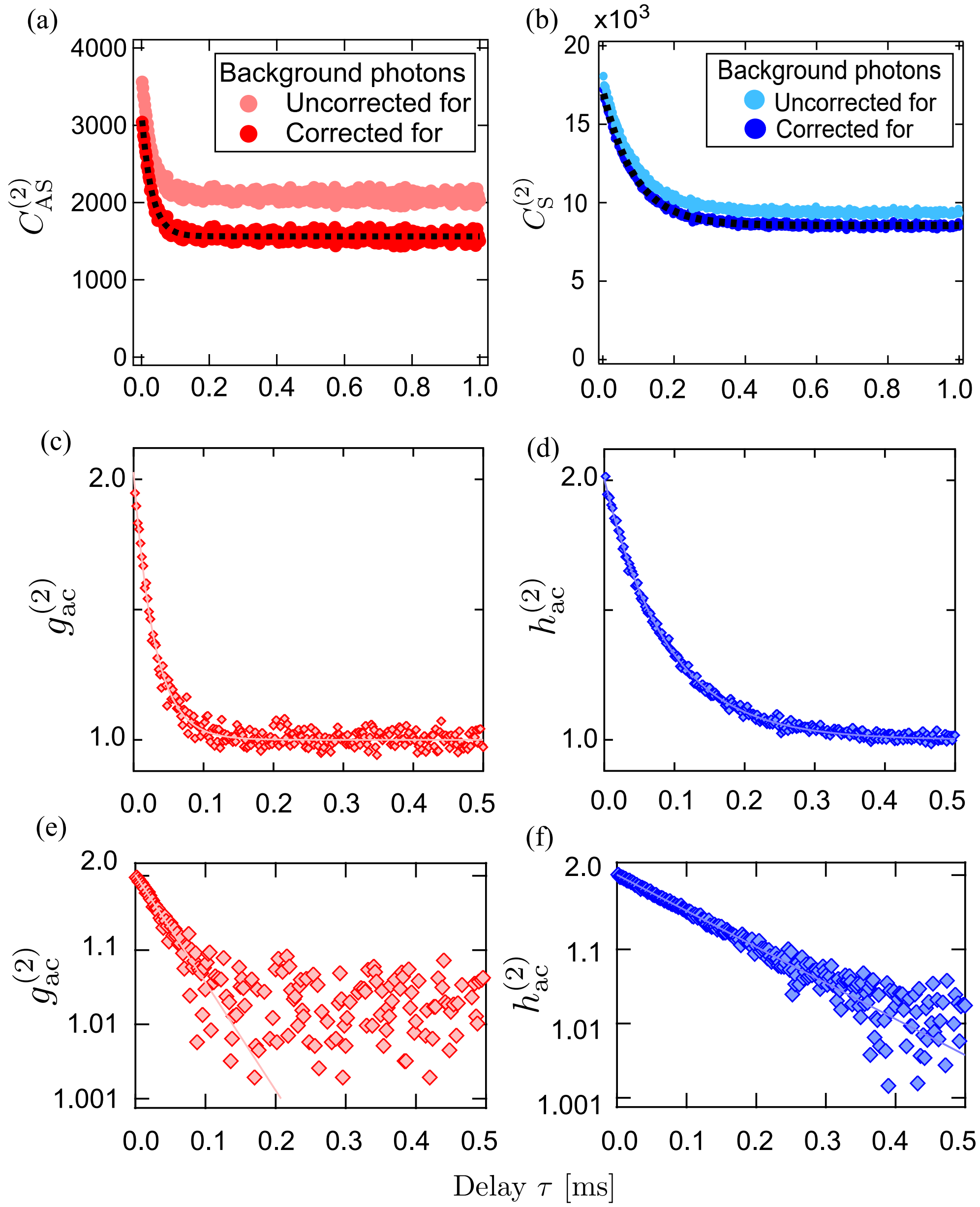

Figure 6.7: (a)-(b): Measured and background-corrected delay histograms, $C^{(2)}_{\rm AS}$ and $C^{(2)}_{\rm S}$; (c)-(d): Phonon coherences of the second-order $g^{(2)}_{\rm ac}$ and $h^{(2)}_{\rm ac}$; (e)-(f): $g^{(2)}_{\rm ac}$ and $h^{(2)}_{\rm ac}$ shown on a logarithmic scale. Time delay τ is histogrammed by 2 μs window. A drive power of $P_{\rm in} = 5.24\,\mu$W and $P_{\rm in} = 5.09\,\mu$W is used on the red- and blue-detuned side respectively. $g^{(2)}_{\rm ac}$ and $h^{(2)}_{\rm ac}$ are fit to the form $1 + B_0 e^{-\gamma_{\rm ac}\tau}$, yielding $g^{(2)}_{\rm ac}(0) = 2.006 \pm 0.004$ and $h^{(2)}_{\rm ac}(0) = 2.03 \pm 0.02$.

Set	Side	P_{in} [μW]	DAQ time [s]	R_{meas} [s^{-1}]	ϵ	$\boldsymbol{g}^{(2)}_{\text{ac}}(\mathbf{0})$ or $\boldsymbol{h}^{(2)}_{\text{ac}}(\mathbf{0})$
1	S	5.75	12520	2245	0.049	2.007 ± 0.001
2	AS	5.26	156570	885	0.120	1.98 ± 0.002
3	AS	5.26	12625	612	0.189	1.967 ± 0.008
4	AS	5.24	1820	756	0.154	2.03 ± 0.02
5	S	5.09	857	2334	0.049	2.006 ± 0.004
6	AS	4.21	4923	597	0.163	1.94 ± 0.01
7	AS	4.16	68517	496	0.203	1.964 ± 0.005
8	S	4.10	2676	1509	0.064	1.995 ± 0.004
9	AS	3.13	7277	432	0.188	1.97 ± 0.01
10	S	3.05	2569	901	0.089	1.983 ± 0.007
11	AS	2.13	19984	285	0.236	1.97 ± 0.01
12	S	2.08	4808	505	0.148	2.03 ± 0.01
13	AS	0.96	40183	127	0.414	1.98 ± 0.02
14	S	0.93	9725	179	0.278	2.01 ± 0.03

Table 6.1: Summary of experimental settings and results for the second-order phonon coherences measurements shown in Figure 6.8.

oscillator indeed exhibits a super-Poissonian distribution showing the bunching effect at zero coincidence and decays in an exponential form.

Note that we can also show the decoherence of the phonon coherences directly via the equation of motion of the acoustic mode, which is given by

$$\dot{\hat{b}} = -(i\omega_{\text{m}} + \frac{\gamma_{\text{m}}}{2})\hat{b} + \sqrt{\gamma_{\text{m}}}\hat{\eta} \tag{6.45}$$

We compute the correlations directly (derived from equations 2.20 and 2.21) and find that

$$\langle \hat{b}^\dagger(t')\hat{b}(t)\rangle = n_{\text{th}} e^{-(\gamma_{\text{ac}}/2 + i\omega_{\text{ac}})(t'-t)} \tag{6.46}$$

$$\langle \hat{b}(t')\hat{b}^\dagger(t)\rangle = (n_{\text{th}} + 1) e^{-(\gamma_{\text{ac}}/2 + i\omega_{\text{ac}})(t'-t)} \tag{6.47}$$

for $t' > t$. The time evolution of the second-order phonon coherence of our acoustic state is directly formulated to be

$$g^{(2)}_{\text{ac}}(\tau) = h^{(2)}_{\text{ac}}(\tau) = 1 + e^{-\gamma_{\text{ac}}\tau} \tag{6.48}$$

Note that this is a direct result of the Langevin equation of motion of the acoustic motional state formulated by the input-output theory, where the noise operators are treated as weakly coupled to a Markovian bath. Our measurements demonstrate that the decoherence of the motional acoustic state does obey that of a state having a Markovian coupling to its thermal bath.

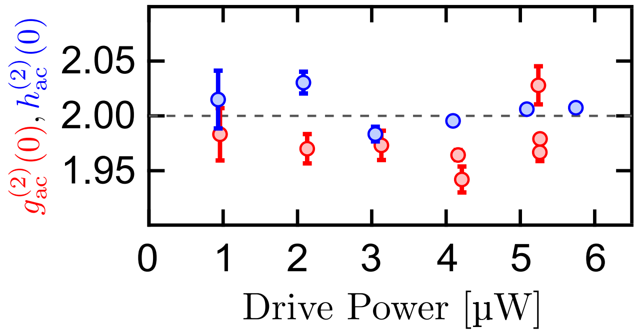

Figure 6.8: $g^{(2)}_{\rm ac}(0)$ and $h^{(2)}_{\rm ac}(0)$ as a function of drive power from $P_{\rm in} \sim 1\ \mu$W to $\sim 6\ \mu$W.

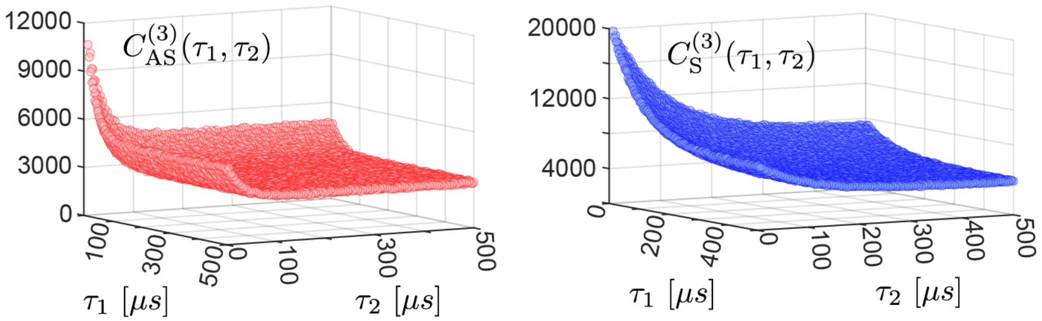

Figure 6.9: Two-time delay histogram $C^{(3)}_{\rm AS(S)}$ as a function of τ_1 and τ_2. The histogram is binned by a 5 μs time window.

6.3.2 Third-order phonon coherences

We can further construct the third-order phonon coherences. Statistics presented in this section are obtained from the same set of experiments discussed in previous sections and summarized in table 6.8.

As described in section 6.2.1, to obtain the third-order phonon coherence we first construct a two-time delay histogram. For $C^{(3)}_{\rm AS(S)}(\tau_1, \tau_2)$, we compute the matrix of delays between the arrival times of each triplet of photons $\{\{t_j - t_i\}\forall j > i, \{t_k - t_j\}\forall k > j\}$. The histogram is then background-corrected following equation 6.39. Figure 6.9 shows an example of $C^{(3)}_{\rm AS}(\tau_1, \tau_2)$ after background photon subtraction, which is histogrammed by a bin size of 5 μs. The example shown here are computed from data sets 2 and 1 in table 6.8, with a drive power of $P_{\rm in} = 5.26\ \mu$W and 5.75 μW for the red and blue side respectively.

The background-corrected $C^{(3)}_{\rm AS(S)}(\tau_1, \tau_2)$ are then fit to the form

$$C^{(3)}_{\rm AS(S)}(\tau_1, \tau_2) = A + B(e^{-\gamma_{\rm ac}\tau_2} + e^{-\gamma_{\rm ac}\tau_1} + 3e^{-\gamma_{\rm ac}(\tau_1+\tau_2)}) \tag{6.49}$$

according to equation 6.12, where A and B are fitting parameters that account for the normalization of flux of photon detection and the behavior at zero delay respectively. $\gamma_{\rm ac}$

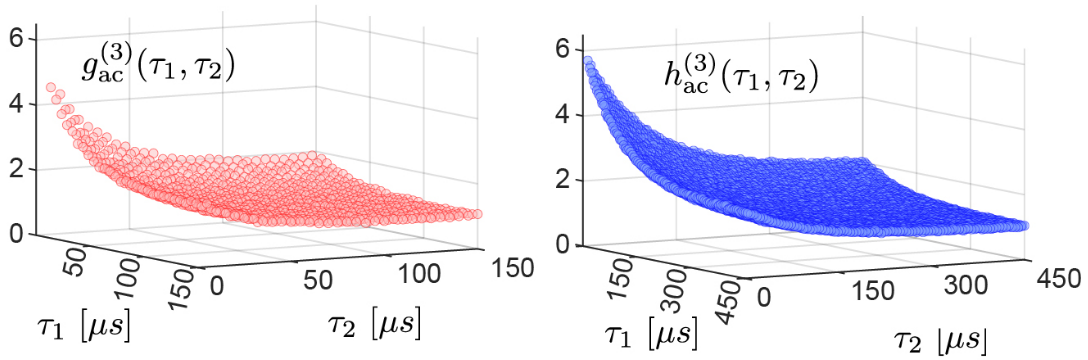

Figure 6.10: $g_{\mathrm{ac}}^{(3)}$ and $h_{\mathrm{ac}}^{(3)}$ plotted as a function of τ_1 and τ_2, obtained by normalizing the histogram shown in figure 6.9.

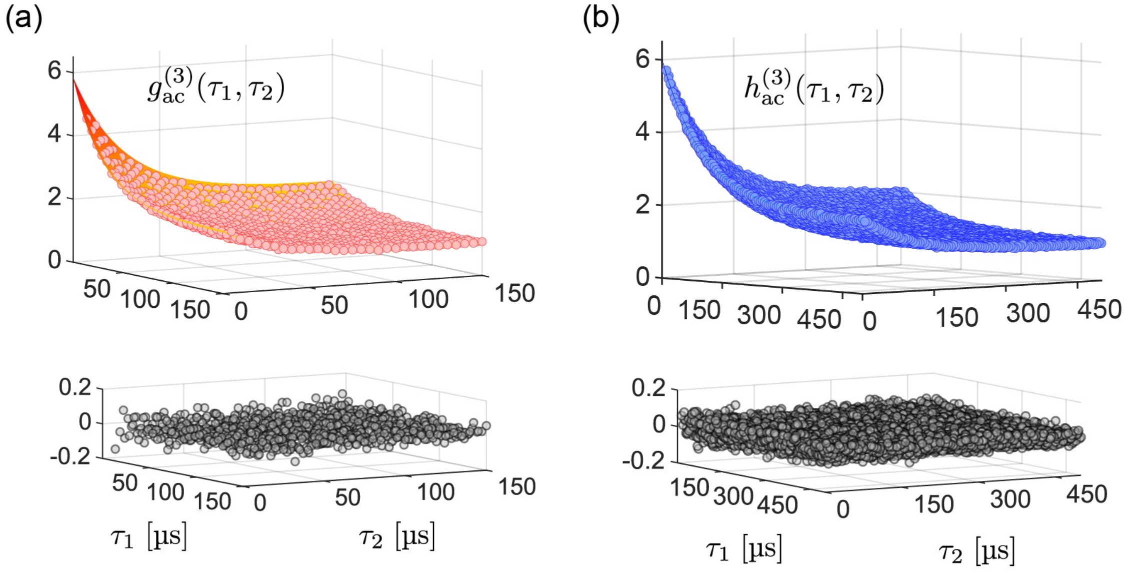

Figure 6.11: $g_{\mathrm{ac}}^{(3)}$ and $h_{\mathrm{ac}}^{(3)}$ shown with the fits in the form of equation 6.49 normalized by the fitting parameter A. It is plotted as a surface on top of the scattered data plot. The corresponding residuals are shown underneath.

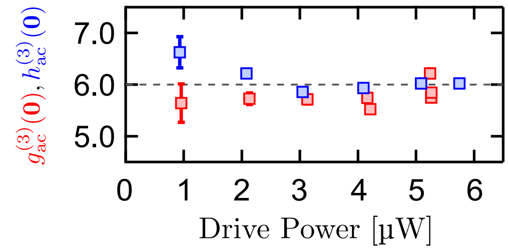

Figure 6.12: $g^{(3)}_{\text{ac}}(0,0)$ and $h^{(3)}_{\text{ac}}(0,0)$ as a function of drive power from $P_{\text{in}} \sim 1\ \mu$W to $\sim 6\ \mu$W, showing the phonon bunching effect of a thermal acoustic state.

is a fitting parameter showing the time decay of the phonon coherences. The third-order phonon coherences (corresponding to the cumulative histograms shown in figure 6.9) are shown in figure 6.10 where the normally ordered $g^{(3)}_{\text{ac}}(\tau_1,\tau_2) = C^{(3)}_{\text{AS}}(\tau_1,\tau_2)/A$ and the anti-normally ordered $h^{(3)}_{\text{ac}}(\tau_1,\tau_2) = C^{(3)}_{\text{S}}(\tau_1,\tau_2)/A$. The resulting fits are plotted on top of the data in figure 6.11 shown as a solid surface. The corresponding residuals are shown underneath in gray.

For the third-order coherence, we have $g^{(3)}_{\text{ac}}(0,0) = h^{(3)}_{\text{ac}}(0,0) \approx 6$ at zero delay as expected for a thermal acoustic state in thermal equilibrium to the bath. More precisely from the fitting function in equation 6.49, we find $g^{(3)}_{\text{ac}}(0,0) = h^{(3)}_{\text{ac}}(0,0) = 1 + 5B/A$. The fitting results for each data set are summarized in table 6.2 and plotted in figure 6.12 to demonstrate the bunching effect of a thermal state at zero delay. $g^{(3)}(0,0)$ indicates that comparing to the uncorrelated arrivals with large delay in between ($\tau \ggg \tau_{\text{ac}}$), triplet of thermal phonons are 6 times more likely to arrive jointly.

Furthermore, by setting one of the delays to $\tau = \infty$, we retrieve the one-dimensional $g^{(2)}_{\text{ac}}$. For the third phonon that arrives with a large delay ($\tau \to \infty$), its arrival becomes uncorrelated to the other pair of phonon. The resulting coherence is thus reduced to the probability of measuring the pair of phonons with a delay τ in between such that $g^{(3)}_{\text{ac}}(\tau_1,\infty) = g^{(3)}_{\text{ac}}(\infty,\tau_2) = g^{(2)}_{\text{ac}}(\tau)$. Mathematically, we can easily see that from the functional form of $g^{(3)}_{\text{ac}}$ as

$$\begin{aligned} g^{(3)}_{\text{ac}}(\tau_1=\infty,\tau_2) = g^{(3)}_{\text{ac}}(\tau_1,\tau_2=\infty) &= 1 + e^{-\gamma_{\text{ac}}\tau_2} + e^{-\gamma_{\text{ac}}\tau_1} + 3e^{-\gamma_{\text{ac}}(\tau_1+\tau_2)} \\ &= 1 + e^{-\gamma_{\text{ac}}\tau} = g^{(2)}(\tau) \end{aligned} \tag{6.50}$$

It follows that $g^{(3)}_{\text{ac}}(\infty,0) = g^{(3)}_{\text{ac}}(0,\infty) = g^{(2)}_{\text{ac}}(0) = 2$.

6.3.3 Damping dynamics

The thermal acoustic oscillator exhibits a super-Poissonian distribution which decays on a timescale set by the damping rate of the acoustic oscillator. From the fits obtained from the second and third-order coherences in previous sections, we show the fit-extracted γ_{ac} as a function of drive power P_{in} in figure 6.13. γ_{ac} extracted from $g^{(2)}_{\text{ac}}$ are shown as circles, and

Set	$\boldsymbol{g_{\text{ac}}^{(3)}(0,0)}$ or $\boldsymbol{h_{\text{ac}}^{(3)}(0,0)}$	$g_{\text{ac}}^{(3)}, h_{\text{ac}}^{(3)}(0,\infty) = g_{\text{ac}}^{(3)}, h_{\text{ac}}^{(3)}(\infty,0)$
1	6.023 ± 0.002	2.023
2	5.843 ± 0.007	1.843
3	5.75 ± 0.05	1.75
4	6.22 ± 0.09	2.22
5	6.024 ± 0.009	2.024
6	5.52 ± 0.07	1.52
7	5.74 ± 0.03	1.74
8	5.93 ± 0.01	1.93
9	5.72 ± 0.09	1.72
10	5.86 ± 0.03	1.86
11	5.7 ± 0.1	1.7
12	6.22 ± 0.06	2.22
13	5.6 ± 0.4	1.6
14	6.6 ± 0.3	2.6

Table 6.2: Summary of experimental settings and results for the third-order phonon coherences measurements shown in Figure 6.12.

those extracted from $g_{\text{ac}}^{(3)}$ are shown as squares, and are consistent with each other within the standard deviation of the best-fit parameter.

As discussed in section 5.3, the effective acoustic damping rate is subjected to the optomechanical backaction. When the optical cavity is driven by a laser at detuning $\Delta = \pm\omega_{\text{ac}}$, we have

$$\begin{aligned}\gamma_{\text{ac,eff}} &= \gamma_{\text{ac}} \mp 4g_0^2 n_{\text{c}}/\kappa_{\text{c}} \\ &= \gamma_{\text{ac}} \mp \{4g_0^2 \frac{\kappa_{\text{in}}}{\kappa_{\text{c}}\hbar\omega_{\text{c}}}|\chi_{\text{c}}[\pm\omega_{\text{ac}}]|^2\} P_{\text{in}}\end{aligned} \tag{6.51}$$

The effective damping rate under optomechanical backaction thus varies linearly with drive power P_{in}. We fit the extracted γ_{ac} from both detuning sides simultaneously to the form $\gamma_{\text{ac,eff}}(P_{\text{in}}) = A \mp BP_{\text{in}}$, where A and B are the fitting parameters, as shown in figure 6.13.

We thus extract the bare acoustic damping rate in absence of optomechanical interaction at approximately the base temperature ($\sim$ 20 mK) to be $\gamma_{\text{ac}}/2\pi = 3307\pm$ 8 Hz [3]. The fit also returns $B = 4g_0^2\kappa_{\text{in}}|\chi_{\text{c}}[\omega_{\text{ac}}]|^2/(\kappa_{\text{c}}\hbar\omega_{\text{c}})$, where all parameters are known or are measured to high precision via independent methods (see section 5.2) except for the single photon optomechanical coupling g_0. We can thus extract g_0 via the time dependence of phonon coherences which yields $g_0/2\pi = 4700 \pm 50$ Hz.

---

[3] The bare acoustic damping rate at fridge base temperature extracted from various methods are summarized in appendix B.4

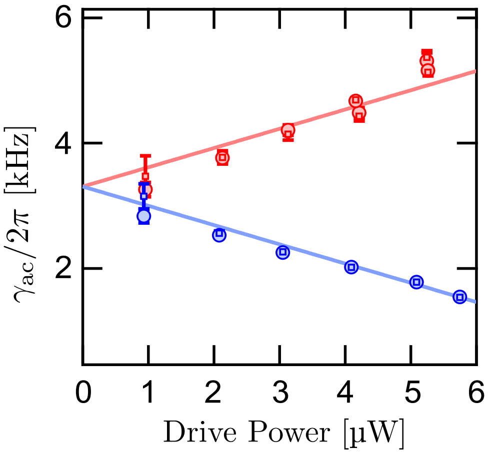

Figure 6.13: $\gamma_{\rm ac}$ extracted from the time decay of the second- and third-order phonon coherences. $\gamma_{\rm ac}$ extracted from $g^{(2)}_{\rm ac}$ are shown as circles, and those extracted from $g^{(3)}_{\rm ac}$ are shown as squares.

6.3.4 Fourth-order phonon coherences

We further construct the fourth-order phonon coherences following the same procedure. Data shown in this section are obtained from data set 2 and 1 in table 6.1 for the anti-Stokes and Stokes side respectively. Note that large DAQ time is needed to construct higher order coherences in order to detect 4-fold joint detection here. We also use a larger time bin of 10 μs to acquire larger number of joint detection (within a time bin).

To construct the three-time delay dependent $g^{(4)}_{\rm ac}(\tau_1,\tau_2,\tau_3)$ and $h^{(4)}_{\rm ac}(\tau_1,\tau_2,\tau_3)$, a three-dimensional matrix is constructed from the time delays between the arrival times of each quadruple of photons $\{\{t_j - t_i\}\forall j > i, \{t_k - t_j\}\forall k > j, \{t_m - t_k\}\forall m > k\}$. In order to display the three-dimensional data sets, we decompose it into sets of two-dimensional slices.

Figure 6.14 shows the 2D slices of $g^{(4)}_{\rm ac}(\tau_1, 0^+, \tau_3)$ and $h^{(4)}_{\rm ac}(\tau_1, 0^+, \tau_3)$. Data are shown in scattered plots in the top row, where we show the subset of data in the bin of 5 μs $< \tau_1 <$ 15 μs, denoted by $\tau_1 = 0^+$. Solid surfaces shown in the middle row are the best-fits to the entire three-dimensional data sets following equation 6.13 with proper normalization factor, such that

$$C^{(4)}_{\rm AS(S)}(\tau_1,\tau_2,\tau_3) = A + B\Big\{e^{-\gamma_{\rm ac}\tau_1} + e^{-\gamma_{\rm ac}\tau_2} + e^{-\gamma_{\rm ac}\tau_3} + e^{-\gamma_{\rm ac}(\tau_1+\tau_3)} + 3e^{-\gamma_{\rm ac}(\tau_1+\tau_2)} + 3e^{-\gamma_{\rm ac}(\tau_2+\tau_3)} + 9e^{-\gamma_{\rm ac}(\tau_1+\tau_2+\tau_3)} + 4e^{-\gamma_{\rm ac}(\tau_1+2\tau_2+\tau_3)}\Big\} \tag{6.52}$$

It follows that $g^{(4)}_{\rm ac}(\tau_1,\tau_2,\tau_3) = C^{(4)}_{\rm AS}/A$ and $h^{(4)}_{\rm ac}(\tau_1,\tau_2,\tau_3) = C^{(4)}_{\rm S}/A$. For a thermal acoustic state, we expect $g^{(4)}_{\rm ac}(0,0,0) = h^{(4)}_{\rm ac}(0,0,0) = 4! = 1 + B/A$. Fits to each three dimensional data set return $g^{(4)}_{\rm ac}(0,0,0) = 1 + B/A =$ 23.01 ± 0.03 and $h^{(4)}_{\rm ac}(0,0,0) =$

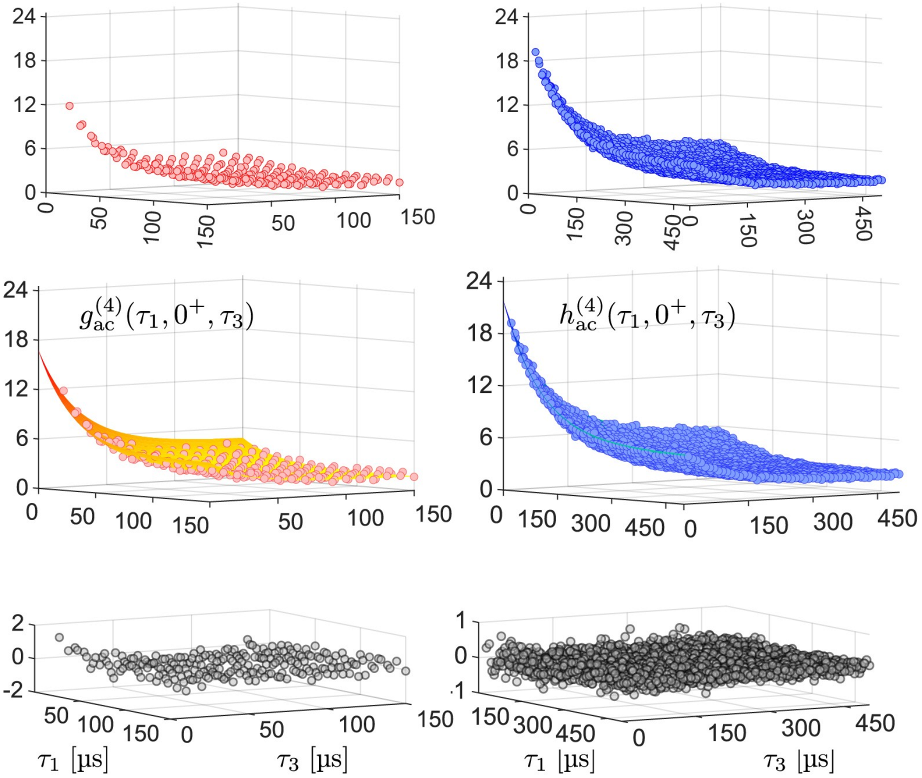

Figure 6.14: 2D slices from the fourth-order phonon coherences, $g_{\mathrm{ac}}^{(4)}(\tau_1, 0^+, \tau_3)$ and $h_{\mathrm{ac}}^{(4)}(\tau_1, 0^+, \tau_3)$, binned by 10 μs window, where $\tau = 0^+$ represents the smallest delay bin with 5 μs $< \tau <$ 15 μs. Fits to the 2D slices are shown in the middle row.

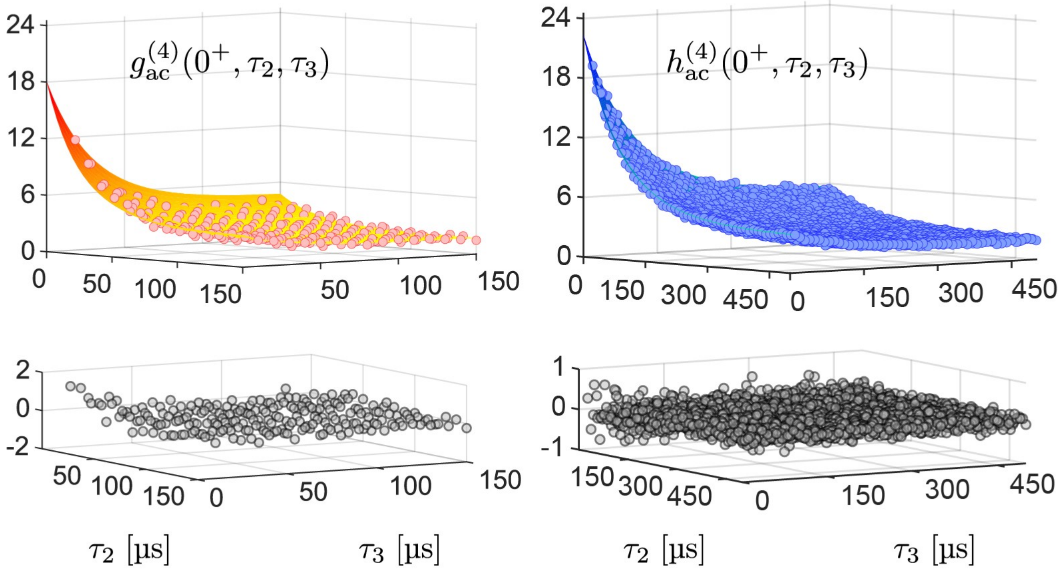

Figure 6.15: 2D slices from the fourth-order phonon coherences, $g_{\mathrm{ac}}^{(4)}(0^+, \tau_2, \tau_3)$ and $h_{\mathrm{ac}}^{(4)}(0^+, \tau_2, \tau_3)$, binned by 10 μs window, and the corresponding fits shown in solid surfaces. $\tau = 0^+$ represents the smallest delay bin with 5 μs $< \tau <$ 15 μs.

$1 + B/A = 23.98 \pm 0.01$ respectively. Note that in figure 6.14, data is shown from a finite delay bin of 5 μs $< \tau_2 <$ 15 μs. Hence, the measured coherence does not reach $g^{(4)}_{\text{ac}}(0,0,0)$ and $h^{(4)}_{\text{ac}}(0,0,0)$ as $(\tau_1, \tau_3) \rightarrow (0,0)$. The solid surface is plotted with $\tau_2 = 10$ μs with the best-fit parameters of A, B and γ_{ac}, such that $g^{(4)}_{\text{ac}}(0,0^+,0) = h^{(4)}_{\text{ac}}(0,0^+,0) = 1 + B/A(5 + 18e^{-\gamma_{\text{ac}}\tau_2})$.

Similarly, we show $g^{(4)}_{\text{ac}}(0^+,\tau_2,\tau_3)$ and $h^{(4)}_{\text{ac}}(0^+,\tau_2,\tau_3)$ in figure 6.15, where the subset of data in the delay bin of 5 μs $< \tau_1 <$ 15 μs is plotted. The solid surface is plotted with the best-fit parameters and $\tau_1 = 10$ μs, where $g^{(4)}_{\text{ac}}(0^+,0,0) = h^{(4)}_{\text{ac}}(0^+,0,0) = 1 + B/A(5 + 18e^{-\gamma_{\text{ac}}\tau_1})$. 2D slices of $g^{(4)}_{\text{ac}}(0^+,\tau_2,\tau_3)$, $h^{(4)}_{\text{ac}}(0^+,\tau_2,\tau_3)$, $g^{(4)}_{\text{ac}}(\tau_1,0^+,\tau_3)$, $h^{(4)}_{\text{ac}}(\tau_1,0^+,\tau_3)$, $g^{(4)}_{\text{ac}}(\tau_1,\tau_3,0^+)$, and $h^{(4)}_{\text{ac}}(\tau_1,\tau_3,0^+)$ all display the same behavior, where

$$\begin{aligned} g^{(4)}_{\text{ac}}, h^{(4)}_{\text{ac}} &\rightarrow 24, \quad \text{as } (\tau_i,\tau_j) \rightarrow (0,0) \\ g^{(4)}_{\text{ac}}, h^{(4)}_{\text{ac}} &\rightarrow 6, \quad \text{as } \tau_i \rightarrow 0 \text{ and } \tau_j \rightarrow \infty \text{ for } i \neq j \\ g^{(4)}_{\text{ac}}, h^{(4)}_{\text{ac}} &\rightarrow 2, \quad \text{as } (\tau_i,\tau_j) \rightarrow \infty \end{aligned} \tag{6.53}$$

As we set one of the delays to zero, these features are consistent with the four-fold, three-fold, two-fold bunching behavior of a thermal state.

Figure 6.16 shows the 2D slices of $g^{(4)}_{\text{ac}}(\tau_1,\infty,\tau_3)$ and $h^{(4)}_{\text{ac}}(\tau_1,\infty,\tau_3)$ on the left, and $g^{(4)}_{\text{ac}}(\tau_1,\tau_2,\infty)$ and $h^{(4)}_{\text{ac}}(\tau_1,\tau_2,\infty)$ on the right, where we plot the subset of data in the large delay bin of $\tau > 10\tau_{\text{ac}}$, denoted by $\tau = \infty$. The solid surfaces are plotted with the best-fit parameters from the three-dimensional fit and the corresponding residuals are shown underneath.

For $g^{(4)}_{\text{ac}}(\tau_1,\infty,\tau_3)$ and $h^{(4)}_{\text{ac}}(\tau_1,\infty,\tau_3)$, as $\tau_2 \rightarrow \infty$, which is the delayed arrival time of the third photon from the second in the quadruple of photons, we have that the arrival times between the pair of the first and second photons, and the pair of the third and forth photons, are thus uncorrelated. $g^{(4)}_{\text{ac}}(\tau_1,\infty,\tau_3)$ and $h^{(4)}_{\text{ac}}(\tau_1,\infty,\tau_3)$ is thus equivalent to the product of the coincidence of one pair of photons arriving with a delay of τ_1, and the coincidence of another pair of photons arriving with a time delay of τ_3. From equation 6.13, it is indeed straightforward to show that

$$\begin{aligned} g^{(4)}_{\text{ac}}(\tau_1,\infty,\tau_3) = h^{(4)}_{\text{ac}}(\tau_1,\infty,\tau_3) &= 1 + e^{-\gamma_{\text{ac}}\tau_1} + e^{-\gamma_{\text{ac}}\tau_3} + e^{-\gamma_{\text{ac}}(\tau_1+\tau_3)} \\ &= g^{(2)}_{\text{ac}}(\tau_1)g^{(2)}_{\text{ac}}(\tau_3) = h^{(2)}_{\text{ac}}(\tau_1)h^{(2)}_{\text{ac}}(\tau_3) \end{aligned} \tag{6.54}$$

Figure 6.16(left) shows

$$\begin{aligned} g^{(4)}_{\text{ac}}, h^{(4)}_{\text{ac}}(\tau_1,\infty,\tau_3) &\rightarrow 4, \quad \text{as } (\tau_1,\tau_3) \rightarrow (0,0) \\ g^{(4)}_{\text{ac}}, h^{(4)}_{\text{ac}}(\tau_1,\infty,\tau_3) &\rightarrow 2, \quad \text{as } (\tau_1,\tau_3) \rightarrow (0,\infty) \text{ or } (\infty,0) \\ g^{(4)}_{\text{ac}}, h^{(4)}_{\text{ac}}(\tau_1,\infty,\tau_3) &\rightarrow 1, \quad \text{as } (\tau_1,\tau_3) \rightarrow (\infty,\infty) \end{aligned} \tag{6.55}$$

as expected.

For $g^{(4)}_{\text{ac}}(\tau_1,\tau_2,\infty)$ and $h^{(4)}_{\text{ac}}(\tau_1,\tau_2,\infty)$ when we set $\tau_3 \rightarrow \infty$, the arrival time of the fourth photon becomes uncorrelated to the first three photons. This is equivalent to the

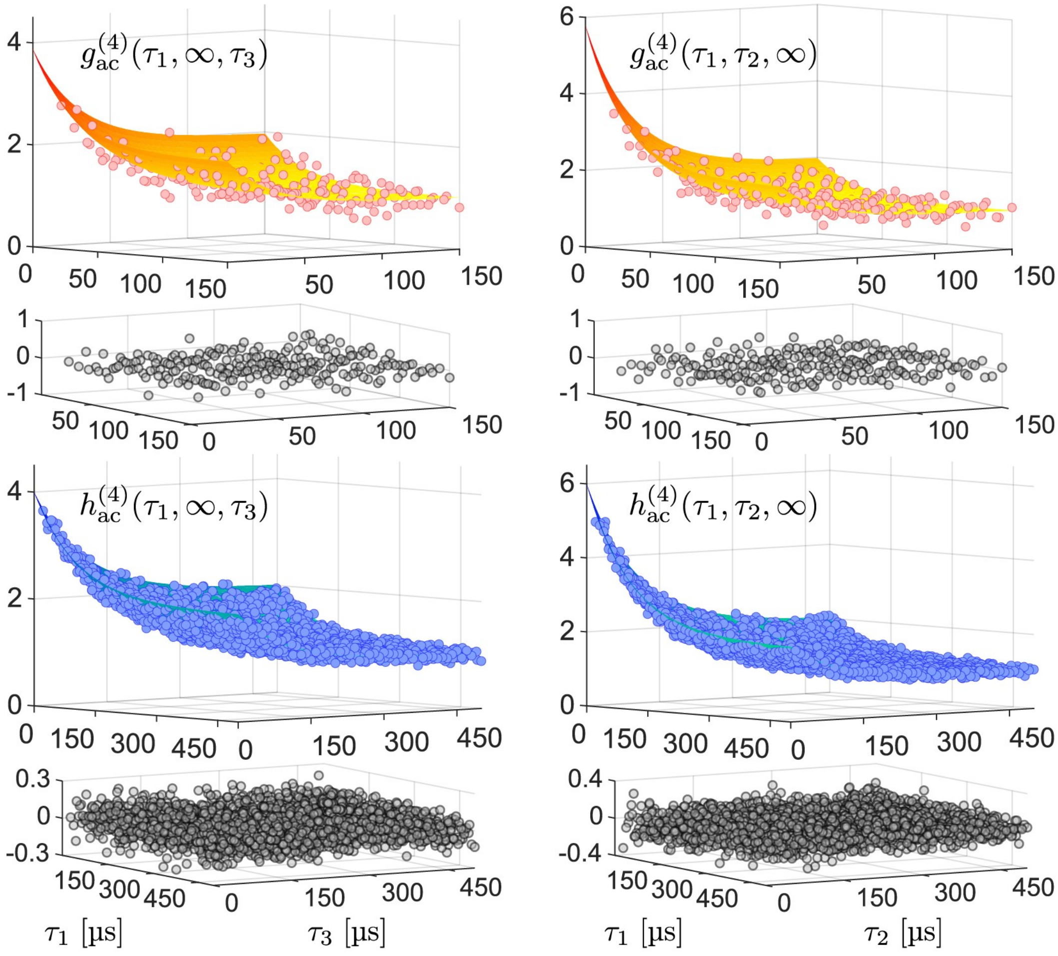

Figure 6.16: 2D slices from the fourth-order phonon coherences, $g^{(4)}_{\mathrm{ac}}(\tau_1,\infty,\tau_3)$, $h^{(4)}_{\mathrm{ac}}(\tau_1,\infty,\tau_3)$, $g^{(4)}_{\mathrm{ac}}(\tau_1,\tau_2,\infty)$, and $h^{(4)}_{\mathrm{ac}}(\tau_1,\tau_2,\infty)$, binned by 10 μs window. Corresponding fits shown in solid surfaces. $\tau=\infty$ represents large delay bin where $\tau > 10\tau_{\mathrm{ac}}$ at least.

third-order coherence for measuring the coincidence of a triplet of photons, where the first two arrive with a time delay of τ_1 and the last two with τ_2. From equation 6.13, we have

$$\begin{aligned} g_{\text{ac}}^{(4)}(\tau_1, \tau_2, \infty) = h_{\text{ac}}^{(4)}(\tau_1, \tau_2, \infty) &= 1 + e^{-\gamma_{\text{ac}}\tau_1} + e^{-\gamma_{\text{ac}}\tau_2} + 3e^{-\gamma_{\text{ac}}(\tau_1+\tau_2)} \\ &= g_{\text{ac}}^{(3)}(\tau_1, \tau_2) = h_{\text{ac}}^{(3)}(\tau_1, \tau_2) \end{aligned} \tag{6.56}$$

as shown in figure 6.16(right).

6.4 Phonon-subtracted and -added thermal state

In the previous section, we demonstrate that phonon coherences of the acoustic state are consistent with those of a state in thermal equilibrium with a bath, such that its energy fluctuations have a Gaussian distribution up to at least the fourth cumulant. One related state of interest is a phonon-subtracted or -added thermal acoustic state, where k-quanta of thermal excitations are subtracted from or added to the state in thermal equilibrium, and the resulting state could acquire an non-Gaussian phase-space distribution depending on the initial state [30]. Such a state could yield richer information that potentially creates quantum advantage in quantum enhanced metrology and sensing[22]. The cooled or heated state is also useful in quantum thermodynamics, as the state is out of equilibrium from its thermal environment, and can be used to perform work and carry information[175].

The optical equivalents of such states have been well studied in the field of nonlinear quantum optics where photon-subtracted and -added optical states are prepared and probed. Interesting results are demonstrated by conditional measurements enabled by the quantum detectors on non-classical as well as classical states, as each single photon detection event heralds the subtraction or addition of exactly one quanta excitation. For instance, weak conditional measurement is used to prepare a Fock state from a coherent state by quantum feedback via cavity quantum electrodynamics[176][177]. In the field of quantum information and thermodynamics, a photonic Maxwell's demon[178] is realized with a highly thermal source, where work is extracted by conditional measurement on thermal light modes leading to a difference in their average energy[179]. With a weak thermal source, quantum-enhanced interferometry have been demonstrated[180]. It has also been shown that a single-photon-added thermal state displays a negative Glauber-Sudarshan P function[181]. Furthermore, highly non-classical states (states with a negative Wigner function) have been prepared and probed via single photon detection and heralded measurement, such as a Schrödinger cat state prepared from a photon-subtracted squeezed optical state[182], or a single photon Fock state via photon addition in a parametric down-conversion[183].

I will show in the following sections that states prepared by heralded single photon detection in our experiment gives the ability to generate and probe the statistics of an acoustic state out of thermal equilibrium, giving potential access to preparing more non-classical states in the mechanical domain [30, 184, 29].

6.4.1 Mean occupancy upon phonon subtraction or addition

One interesting, and perhaps counter intuitive property of these states is that the mean energy of the heralded state increases upon the conditioned operation of phonon subtraction or addition. Consider an acoustic thermal state described by

$$\hat{\rho}_{\text{th}} = \sum_{m=0}^{\infty} p_m |m\rangle\langle m| \tag{6.57}$$

where

$$\begin{aligned} p_m &= \frac{n_{\text{th}}^m}{(n_{\text{th}}+1)^{m+1}}, \\ n_{\text{th}} &= \frac{1}{e^{\beta}-1} \end{aligned} \tag{6.58}$$

and $\beta = \hbar\omega_{\text{ac}}/k_{\text{B}}T$.

Detection of a single anti-Stokes scattered photon corresponds to the subtraction of a single phonon from the acoustic state which transforms the density matrix $\hat{\rho}_{\text{th}}$ to

$$\begin{aligned} \hat{\rho}_{\text{-1}} = \frac{\hat{b}\hat{\rho}_{\text{th}}\hat{b}^{\dagger}}{\text{Tr}\{\hat{b}\hat{\rho}_{\text{th}}\hat{b}^{\dagger}\}} =& \frac{\hat{b}\hat{\rho}_{\text{th}}\hat{b}^{\dagger}}{\text{Tr}\{\hat{\rho}_{\text{th}}\hat{b}^{\dagger}\hat{b}\}} = \frac{\hat{b}\hat{\rho}_{\text{th}}\hat{b}^{\dagger}}{n_{\text{th}}} \\ &= \frac{1}{n_{\text{th}}} \sum_{m=0}^{\infty} p_m m |m-1\rangle\langle m-1| \\ &= \frac{1}{n_{\text{th}}} \sum_{m=0}^{\infty} p_{m+1}(m+1) |m\rangle\langle m| \end{aligned} \tag{6.59}$$

where we have the updated probability distribution

$$p_m|_{-1} = \frac{m+1}{n_{\text{th}}} p_{m+1} \tag{6.60}$$

The unconditioned state has a mean phonon occupancy of $n_{\text{th}} = \langle\hat{b}^{\dagger}\hat{b}\rangle_{\hat{\rho}_{\text{th}}} = \text{Tr}\{\hat{\rho}_{\text{th}}\hat{b}^{\dagger}\hat{b}\}$, whereas the state conditioned on one phonon subtraction has the mean occupancy of

$$\begin{aligned} \langle\hat{b}^{\dagger}\hat{b}\rangle_{\hat{\rho}_{-1}} = \text{Tr}\{\hat{\rho}_{\text{-1}}\hat{b}^{\dagger}\hat{b}\} &= \frac{\text{Tr}\{\hat{b}\hat{\rho}_{\text{th}}\hat{b}^{\dagger}\hat{b}^{\dagger}\hat{b}\}}{n_{\text{th}}} \\ &= \text{Tr}\Big\{\sum_{m=0}^{\infty} p_m|_{-1} |m\rangle\langle m| \sum_{n=0}^{\infty} n|n\rangle\langle n|\Big\} \\ &= \sum_{m=0}^{\infty} p_m|_{-1} m = \frac{1}{n_{\text{th}}} \sum_{m=0}^{\infty} p_m m(m-1) \end{aligned} \tag{6.61}$$

We can solve this directly by defining a factor $q = n_{\text{th}}/(1+n_{\text{th}})$, such that $p_m = (1-q)q^m$.

Equation 6.61 can thus be re-written as

$$\langle\hat{b}^\dagger\hat{b}\rangle_{\hat{\rho}_{-1}} = \frac{(1-q)q^2}{n_{\text{th}}}\frac{d^2}{dq^2}\sum q^m = \frac{(1-q)q^2}{n_{\text{th}}}\frac{d^2}{dq^2}(\frac{1}{1-q})$$
$$= 2n_{\text{th}} = 2\langle\hat{b}^\dagger\hat{b}\rangle_{\hat{\rho}_{\text{th}}} \quad (6.62)$$

where we use $\frac{d^2}{dq^2}q^m = m(m-1)q^{m-2}$. Hence, upon subtraction of a single phonon, the mean phonon occupancy of the conditioned state is twice as that of the unconditioned thermal acoustic state.

Similarly, upon addition of a single phonon, the thermal density matrix is updated to

$$\hat{\rho}_{+1} = \frac{\hat{b}^\dagger\hat{\rho}_{\text{th}}\hat{b}}{\text{Tr}\{\hat{b}^\dagger\hat{\rho}_{\text{th}}\hat{b}\}} = \frac{\hat{b}^\dagger\hat{\rho}_{\text{th}}\hat{b}}{\text{Tr}\{\hat{\rho}_{\text{th}}\hat{b}\hat{b}^\dagger\}} = \frac{\hat{b}^\dagger\hat{\rho}_{\text{th}}\hat{b}}{n_{\text{th}}+1}$$
$$= \frac{1}{n_{\text{th}}+1}\sum_{m=0}^{\infty} p_m(m+1)|m+1\rangle\langle m+1|$$
$$= \frac{1}{n_{\text{th}}+1}\sum_{m=0}^{\infty} p_{m-1}m|m\rangle\langle m| = \sum_{m=0}^{\infty} p_m|_{+1}m \quad (6.63)$$

where we have the updated probability distribution

$$p_m|_{+1} = \frac{m}{n_{\text{th}}+1}p_{m-1} \quad (6.64)$$

It follows that the mean phonon occupancy of the conditioned state becomes

$$\langle\hat{b}^\dagger\hat{b}\rangle_{\hat{\rho}_{+1}} = \frac{1}{n_{\text{th}}+1}\sum_{m=0}^{\infty} p_{m-1}m^2$$
$$= (1-q)\sum_{m=0}^{\infty} q^{m-1}m^2 = \frac{1+q}{(1-q)^2}$$
$$= (1+n_{\text{th}})(2n_{\text{th}}+1) = (2n_{\text{th}}+1)\langle\hat{b}^\dagger\hat{b}\rangle_{\hat{\rho}_{th}} \quad (6.65)$$

From the Bayesian update for the probability distribution of the conditioned states in equation 6.60 and 6.64, we can see that they are biased by a factor of $(m+1)$ and m. The scattered photon is thus much more likely to occur from the Fock components with higher-m, leading to the higher mean energy of the resulting conditional state. The update of the density matrix during a heralding one-phonon-subtracted and -added thermal acoustic state operation is summarized in figure 6.17. Subplot (a) shows the probability distribution for a thermal state p_m, where $n_{\text{th}} = 1$. Figure 6.17(b) shows the distribution of the state immediately following an anti-Stokes scattering event before detection, such that the density matrix is updated as $\sum_{m=0}^{\infty} p_m|_{\text{AS}}|m-1\rangle\langle m-1|$, as shown in equation 6.59. Upon detection, a single-phonon-subtracted thermal state is heralded, which is described by $\sum_{m=0}^{\infty} p_m|_{-1}|m\rangle\langle m|$ in equation 6.60. Similarly, the distribution immediately

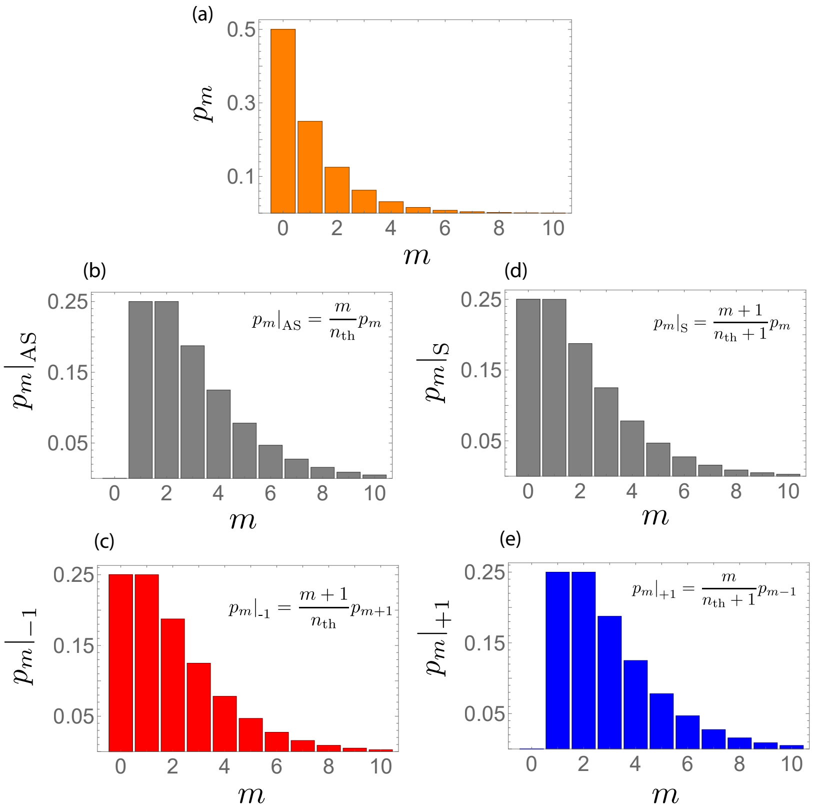

Figure 6.17: Updated probability distribution of a phonon-subtracted and -added thermal acoustic state during a conditional measurement. (a) shows that of a unconditioned thermal state. (b), (d) show the distribution immediately following an anti-Stokes (Stokes) scattering event before detection. (c), (e) show the distribution of a heralded one-phonon-subtracted and -added thermal acoustic state upon a single photon detection.

following a Stokes scattering event and the state heralded by the detection of the Stokes photon are shown in figure 6.17(d) and (e) respectively, corresponding to the density matrix $\sum_{m=0}^{\infty} p_m|_{\mathrm{S}} |m+1\rangle\langle m+1|$ given by equation 6.63, and $\sum_{m=0}^{\infty} p_m|_{+1} |m\rangle\langle m|$ given by equation 6.64.

This result should be evident from the bunching feature in the phonon coherences of a thermal state, such that $g^{(l)}(\mathbf{0}) = l!$. For $g^{(2)}(0) = 2$, it predicts that the probability of detecting another photon upon the detection of one photon doubles. Since the rate of photon scattering events is proportional to n_{ac} for anti-Stokes scattering, and $n_{\mathrm{ac}} + 1$ for Stokes scattering, mean phonon occupancy of the heralded state conditioned on one-photon detection must follow

$$\frac{n_{\mathrm{ac}}^{-1}(0)}{n_{\mathrm{ac}}} = \frac{n_{\mathrm{ac}}^{+1}(0) + 1}{n_{\mathrm{ac}} + 1} = 2 \tag{6.66}$$

Experimentally, by appropriately post-selecting from all the counts registered by the single photon detectors (the full data sets shown in previous section 6.3) to only those

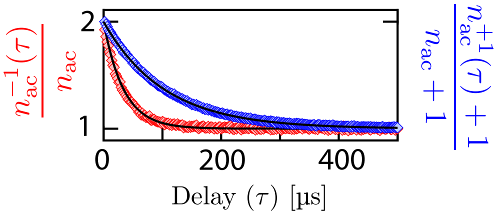

Figure 6.18: Mean phonon occupancy of a one-phonon-subtracted (red) and -added (blue) thermal acoustic state.

that are followed immediately by the detection of one anti-Stokes or Stokes photons, one-phonon-subtracted or -added thermal acoustic states are prepared and probed. Figure 6.18 shows the ratio of the mean phonon occupancy of a one-phonon-subtracted or -added state over that of an unconditioned thermal acoustic state. $n_{\text{ac}}^{-1}(\tau)/n_{\text{ac}}$ for a phonon-subtracted state and $n_{\text{ac}}^{+1}(\tau)+1/(n_{\text{ac}}+1)$ for a phonon-added state are plotted as a function of delay τ.

At time τ, we have

$$n_{\text{ac}}^{-1}(\tau) = \langle \hat{b}^\dagger(\tau)\hat{b}(\tau)\rangle_{\rho_{-1}} = \frac{\hat{b}(0)\hat{\rho}_{\text{th}}(\tau)\hat{b}^\dagger(0)}{\langle \hat{b}^\dagger(0)\hat{b}(0)\rangle_{\hat{\rho}_{\text{th}}}} = \frac{\langle \hat{b}^\dagger(0)\hat{b}^\dagger(\tau)\hat{b}(\tau)\hat{b}(0)\rangle_{\hat{\rho}_{\text{th}}}}{\langle \hat{b}^\dagger(0)\hat{b}(0)\rangle_{\hat{\rho}_{\text{th}}}} \tag{6.67}$$

$$n_{\text{ac}}^{+1}(\tau)+1 = \langle \hat{b}^\dagger(\tau)\hat{b}(\tau)\rangle_{\rho_{+1}} + 1 = \langle \hat{b}(\tau)\hat{b}^\dagger(\tau)\rangle_{\rho_{+1}} = \frac{\langle \hat{b}(0)\hat{b}(\tau)\hat{b}^\dagger(\tau)\hat{b}^\dagger(0)\rangle_{\hat{\rho}_{\text{th}}}}{\langle \hat{b}(0)\hat{b}^\dagger(0)\rangle_{\hat{\rho}_{\text{th}}}} \tag{6.68}$$

It follows that the ratio of the mean phonon occupancy is given by

$$\frac{n_{\text{ac}}^{-1}(\tau)}{n_{\text{ac}}} = \frac{n_{\text{ac}}^{-1}(\tau)}{\langle \hat{b}^\dagger(0)\hat{b}(0)\rangle_{\hat{\rho}_{\text{th}}}} = \frac{g_{\text{ac}}^{(2)}(\tau)}{g_{\text{ac}}^{(1)}(0)} \tag{6.69}$$

$$\frac{n_{\text{ac}}^{+1}(\tau)+1}{n_{\text{ac}}+1} = \frac{n_{\text{ac}}^{+1}(\tau)+1}{\langle \hat{b}(0)\hat{b}^\dagger(0)\rangle_{\hat{\rho}_{\text{th}}}} = \frac{h_{\text{ac}}^{(2)}(\tau)}{h_{\text{ac}}^{(1)}(0)} \tag{6.70}$$

Explicitly, the data is evaluated as

$$\frac{n_{\text{ac}}^{-1}(\tau)}{n_{\text{ac}}} = \frac{g_{\text{ac}}^{(2)}(\tau)}{g_{\text{ac}}^{(2)}(\infty)} = \frac{C_{\text{AS}}^{(2)}(\tau)/C_{\text{AS}}^{(2)}(\infty)}{C_{\text{AS}}^{(2)}(\infty)/C_{\text{AS}}^{(2)}(\infty)} \tag{6.71}$$

$$\frac{n_{\text{ac}}^{+1}(\tau)+1}{n_{\text{ac}}+1} = \frac{h_{\text{ac}}^{(2)}(\tau)}{h_{\text{ac}}^{(2)}(\infty)} = \frac{C_{\text{S}}^{(2)}(\tau)/C_{\text{S}}^{(2)}(\infty)}{C_{\text{S}}^{(2)}(\infty)/C_{\text{S}}^{(2)}(\infty)} \tag{6.72}$$

For the single-phonon subtraction and addition case, it is straightforward to interpret this expression, as the rate of detection at $t=\tau$ after heralding a single phonon subtraction or addition at $t=0$ is simply proportional to $g(h)_{\text{ac}}^{(2)}(\tau)$ or $C_{\text{AS(S)}}^{(2)}(\tau)$, whereas the denominator is proportional to the normalized unconditioned count rate. Solid lines in figure 6.18

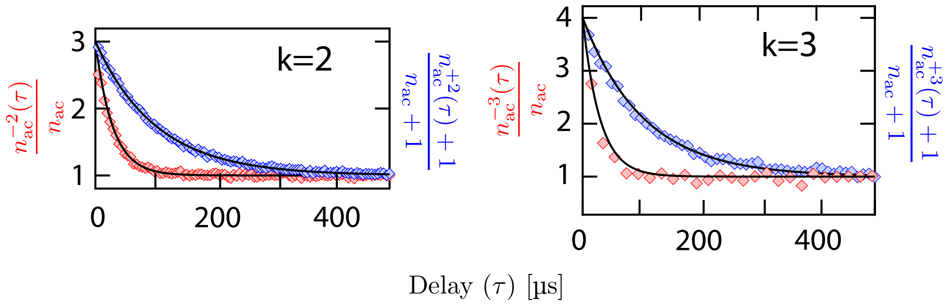

Figure 6.19: Mean phonon occupancy of a two- and three-phonon-subtracted (red) and -added (blue) thermal acoustic state.

show the theoretical predictions

$$\frac{n_{\mathrm{ac}}^{-1}(\tau)}{n_{\mathrm{ac}}} = 1 + e^{-\gamma_{\mathrm{ac,AS}}\tau} \tag{6.73}$$

$$\frac{n_{\mathrm{ac}}^{+1}(\tau)+1}{n_{\mathrm{ac}}+1} = 1 + e^{-\gamma_{\mathrm{ac,S}}\tau} \tag{6.74}$$

which has a value of 2 at zero delay and decays by its acoustic damping rate γ_{ac}.

We also look at the more general cases of k-phonon-subtraction and -addition. Analogous to equation 6.59 and 6.63, upon detection of k anti-Stokes or Stokes photons, $\hat{\rho}_{\mathrm{th}}$ is transformed to

$$\hat{\rho}_{\text{-k}} = \frac{(\hat{b})^k \hat{\rho}_{\mathrm{th}} (\hat{b}^\dagger)^k}{\langle (\hat{b}^\dagger)^k (\hat{b})^k \rangle_{\hat{\rho}_{\mathrm{th}}}} \tag{6.75}$$

$$\hat{\rho}_{\text{+k}} = \frac{(\hat{b}^\dagger)^k \hat{\rho}_{\mathrm{th}} (\hat{b})^k}{\langle (\hat{b})^k (\hat{b}^\dagger)^k \rangle_{\hat{\rho}_{\mathrm{th}}}} \tag{6.76}$$

respectively. Equation 6.68 for the $k = 1$ case can thus be generalized to

$$n_{\mathrm{ac}}^{-k}(\tau) = \langle \hat{b}^\dagger(\tau)\hat{b}(\tau)\rangle_{\rho_{-k}} = \frac{\langle \hat{b}^\dagger(0)^k\ \hat{b}^\dagger(\tau)\hat{b}(\tau)\hat{b}(0)^k\rangle_{\hat{\rho}_{\mathrm{th}}}}{\langle \hat{b}^\dagger(0)^k\ \hat{b}(0)^k\rangle_{\hat{\rho}_{\mathrm{th}}}} \tag{6.77}$$

$$\begin{aligned} n_{\mathrm{ac}}^{+k}(\tau) + 1 = \langle \hat{b}^\dagger(\tau)\hat{b}(\tau)\rangle_{\rho_{+k}} + 1 &= \langle \hat{b}(\tau)\hat{b}^\dagger(\tau)\rangle_{\rho_{+k}} \\ &= \frac{\langle \hat{b}(0)^k\ \hat{b}(\tau)\hat{b}^\dagger(\tau)\hat{b}^\dagger(0)^k\rangle_{\hat{\rho}_{\mathrm{th}}}}{\langle \hat{b}(0)^k\ \hat{b}^\dagger(0)^k\rangle_{\hat{\rho}_{\mathrm{th}}}} \end{aligned} \tag{6.78}$$

It follows that

$$\frac{n_{\text{ac}}^{-k}(\tau)}{n_{\text{ac}}} = \frac{n_{\text{ac}}^{-k}(\tau)}{\langle\hat{b}^\dagger(0)\hat{b}(0)\rangle_{\hat{\rho}_{\text{th}}}} = \frac{g_{\text{ac}}^{(k+1)}(\mathbf{0}^{\otimes(k-1)},\tau)}{g_{\text{ac}}^{(k)}(\mathbf{0})}$$
$$= \frac{g_{\text{ac}}^{(k+1)}(\mathbf{0}^{\otimes(k-1)},\tau)}{g_{\text{ac}}^{(k+1)}(\mathbf{0}^{\otimes(k-1)},\infty)} = \frac{C_{\text{AS}}^{(k+1)}(\mathbf{0}^{\otimes(k-1)},\tau)}{C_{\text{AS}}^{(k+1)}(\mathbf{0}^{\otimes(k-1)},\infty)} \tag{6.79}$$

$$\frac{n_{\text{ac}}^{+k}(\tau)+1}{n_{\text{ac}}+1} = \frac{n_{\text{ac}}^{+k}(\tau)+1}{\langle\hat{b}(0)\hat{b}^\dagger(0)\rangle_{\hat{\rho}_{\text{th}}}} = \frac{h_{\text{ac}}^{(k+1)}(\mathbf{0}^{\otimes(k-1)},\tau)}{h_{\text{ac}}^{(k)}(\mathbf{0})}$$
$$= \frac{h_{\text{ac}}^{(k+1)}(\mathbf{0}^{\otimes(k-1)},\tau)}{h_{\text{ac}}^{(k+1)}(\mathbf{0}^{\otimes(k-1)},\infty)} = \frac{C_{\text{S}}^{(k+1)}(\mathbf{0}^{\otimes(k-1)},\tau)}{C_{\text{S}}^{(k+1)}(\mathbf{0}^{\otimes(k-1)},\infty)} \tag{6.80}$$

where $C_{\text{AS(S)}}^{(k+1)}(\mathbf{0}^{\otimes(k-1)},\tau)$ are the data conditioned on the detection of k photons at time $t=0$. Corresponding post-selected data for $k=2$ and $k=3$ are shown in figure 6.19. The ratio of the mean phonon occupancy of states heralded by the subtraction or addition of k phonons over that of the unconditioned thermal state is shown to to be

$$\frac{n_{\text{ac}}^{-2}(0)}{n_{\text{ac}}} = \frac{n_{\text{ac}}^{+2}(0)+1}{n_{\text{ac}}+1} = 3$$
$$\frac{n_{\text{ac}}^{-3}(0)}{n_{\text{ac}}} = \frac{n_{\text{ac}}^{+3}(0)+1}{n_{\text{ac}}+1} = 4 \tag{6.81}$$

and decays with a timescale set by γ_{ac}.

Mathematically, the derivation for the $k=1$ case given by equation 6.62 and 6.62 can be generalized to arbitrary k, such that

$$\hat{\rho}_{-k} = \frac{\hat{b}^k\,\hat{\rho}_{\text{th}}\hat{b}^{\dagger k}}{\text{Tr}\{\hat{\rho}_{\text{th}}\hat{b}^{\dagger k}\hat{b}^k\}} = \frac{\hat{b}^k\,\hat{\rho}_{\text{th}}\hat{b}^{\dagger k}}{k!n_{\text{ac}}^k} \tag{6.82}$$

It follows that

$$\begin{aligned} n_{\text{ac}}^{-k} &= \langle\hat{b}^\dagger\hat{b}\rangle_{\hat{\rho}_{-k}} = \text{Tr}\{\hat{\rho}_{-k}\hat{b}^\dagger\hat{b}\} \\ &= \frac{1}{k!n_{\text{ac}}^k}\text{Tr}\Big\{\sum_{m=0}^{\infty} p_m m(m-1)\cdots(m-k+1)|m-k\rangle\langle m+k|\sum_{n=0}^{\infty} n|n\rangle\langle n|\Big\} \\ &= \frac{1}{k!n_{\text{ac}}^k}\text{Tr}\Big\{\sum_{m=0}^{\infty} p_{m+k}\frac{(m+k)!}{m!}|m\rangle\langle m|\sum_{n=0}^{\infty} n|n\rangle\langle n|\Big\} \\ &= \sum_{m=0}^{\infty} p_m|_{-k} m = (k+1)n_{\text{ac}} \end{aligned} \tag{6.83}$$

where

$$p_m|_{-k} = \frac{1}{n_{\text{ac}}^k} \frac{(m+k)!}{m!k!} p_{m+k} \tag{6.84}$$

Similarly for a k-phonon-added state, we have

$$\hat{\rho}_{+k} = \frac{\hat{b}^{\dagger k}\ \hat{\rho}_{\text{th}} \hat{b}^k}{k!(n_{\text{ac}}+1)^k} \tag{6.85}$$

It follows that

$$\begin{aligned} n_{\text{ac}}^{+k} &= \langle \hat{b}^\dagger \hat{b} \rangle_{\hat{\rho}_{+k}} = \text{Tr}\{\hat{\rho}_{+k} \hat{b}^\dagger \hat{b}\} \\ &= \frac{1}{k!(n_{\text{ac}}+1)^k} \text{Tr}\Big\{ \sum_{m=0}^{\infty} p_{m-k} \frac{m!}{(m-k)!} |m\rangle\langle m| \sum_{n=0}^{\infty} n|n\rangle\langle n| \Big\} \\ &= \sum_{m=0}^{\infty} p_m|_{+k} m = (k+1)n_{\text{ac}} + k \end{aligned} \tag{6.86}$$

where

$$p_m|_{-k} = \frac{1}{(n_{\text{ac}}+1)^k} \frac{m!}{(m-k)!k!} p_{m+k} \tag{6.87}$$

Therefore, the mean phonon occupancy of a k-phonon-subtracted and -added thermal acoustic state follows the property that

$$\frac{n_{\text{ac}}^{-k}(0)}{n_{\text{ac}}} = \frac{n_{\text{ac}}^{+k}(0)+1}{n_{\text{ac}}+1} = k+1 \tag{6.88}$$

which is consistent with our experimental results shown up to $k = 3$ in figure 6.19. The solid lines are the theoretical prediction derived in this section $1 + ke^{-\gamma_{\text{ac}}\tau}$.

6.4.2 Coherences of a k-phonon-subtracted and -added thermal state

We also construct the coherences of a k-phonon-subtracted and -added thermal acoustic state via proper post-selection. The second-order coherence of a single-phonon-subtracted state is given by

$$g_{\text{ac}}^{(2)}\big|_{-1}(\tau) = \frac{\langle \hat{b}^\dagger(0)\hat{b}^\dagger(\tau)\hat{b}(\tau)\hat{b}(0)\rangle_{\hat{\rho}_{-1}}}{\langle \hat{b}^\dagger(0)\hat{b}(0)\rangle_{\hat{\rho}_{-1}}\ \langle \hat{b}^\dagger(\tau)\hat{b}(\tau)\rangle_{\hat{\rho}_{-1}}} \tag{6.89}$$

Plugging in $\hat{\rho}_{-1}$ from equation 6.59, the numerator becomes

$$\frac{\langle \hat{b}^\dagger(0)\hat{b}^\dagger(0)\hat{b}^\dagger(\tau)\hat{b}(\tau)b(0)b(0)\rangle_{\hat{\rho}_{\text{th}}}}{\langle \hat{b}^\dagger(0)\hat{b}(0)\rangle_{\hat{\rho}_{\text{th}}}} = g_{\text{ac}}^{(3)}(0,\tau)\ \langle \hat{b}^\dagger(0)\hat{b}(0)\rangle_{\hat{\rho}_{\text{th}}}^2 \tag{6.90}$$

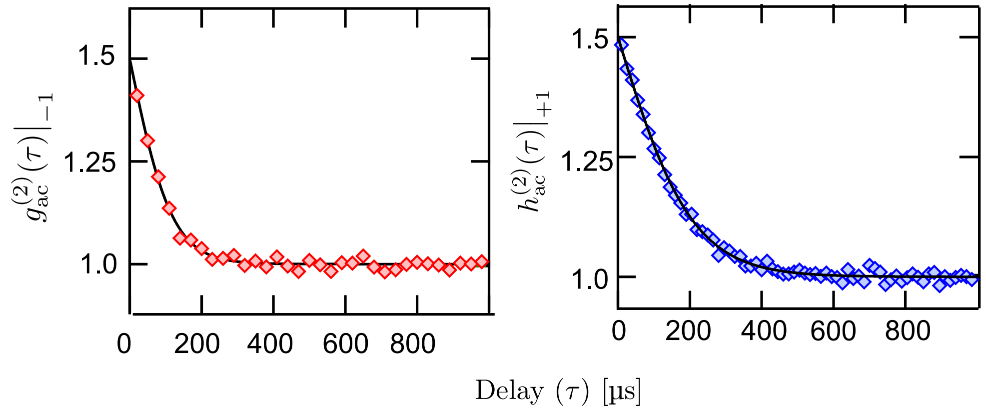

Figure 6.20: Second-order coherences of a single-phonon-subtracted (red) and -added (blue) thermal acoustic state. Data is post-selected following equation 6.94 and 6.94, whereas the solid lines show the theoretical predictions given by equation 6.96.

and the denominator is

$$\frac{\langle \hat{b}^\dagger(0)\hat{b}^\dagger(0)\hat{b}(0)\hat{b}(0)\rangle_{\hat{\rho}_{\mathrm{th}}}\langle \hat{b}^\dagger(0)\hat{b}^\dagger(\tau)\hat{b}(\tau)\hat{b}(0)\rangle_{\hat{\rho}_{\mathrm{th}}}}{\langle \hat{b}^\dagger(0)\hat{b}(0)\rangle^2_{\hat{\rho}_{\mathrm{th}}}} = g_{\mathrm{ac}}^{(2)}(0)\; g_{\mathrm{ac}}^{(2)}(\tau)\; \langle \hat{b}^\dagger(0)\hat{b}(0)\rangle^2_{\hat{\rho}_{\mathrm{th}}} \tag{6.91}$$

We can therefore construct the second-order coherence of a single-phonon-subtracted state by using combinations of the coherences of an unconditioned thermal acoustic state, given by

$$g_{\mathrm{ac}}^{(2)}\big|_{-1}(\tau) = \frac{g_{\mathrm{ac}}^{(3)}(0,\tau)}{g_{\mathrm{ac}}^{(2)}(0)\; g_{\mathrm{ac}}^{(2)}(\tau)} \tag{6.92}$$

Similarly, we compute $h_{\mathrm{ac}}^{(2)}\big|_{+1}(\tau)$ for a single-phonon-added state with $\hat{\rho}_{+1}$ in equation 6.63, such that

$$h_{\mathrm{ac}}^{(2)}\big|_{+1}(\tau) = \frac{h_{\mathrm{ac}}^{(3)}(0,\tau)}{h_{\mathrm{ac}}^{(2)}(0)\; h_{\mathrm{ac}}^{(2)}(\tau)} \tag{6.93}$$

Figure 6.20 shows $g_{\mathrm{ac}}^{(2)}\big|_{+1}(\tau)$ and $h_{\mathrm{ac}}^{(2)}\big|_{+1}(\tau)$ constructed from the post-selected data, which are calculated by

$$g_{\mathrm{ac}}^{(2)}\big|_{-1}(\tau) = \frac{g_{\mathrm{ac}}^{(3)}(0,\tau)}{g_{\mathrm{ac}}^{(2)}(0)\; g_{\mathrm{ac}}^{(2)}(\tau)} = \frac{C_{\mathrm{AS}}^{(3)}(0^+,\tau)/C_{\mathrm{AS}}^{(3)}(\infty,\infty)}{\left[C_{\mathrm{AS}}^{(2)}(0^+)/C_{\mathrm{AS}}^{(2)}(\infty)\right]\left[C_{\mathrm{AS}}^{(2)}(\tau)/C_{\mathrm{AS}}^{(2)}(\infty)\right]} \tag{6.94}$$

$$h_{\mathrm{ac}}^{(2)}\big|_{-1}(\tau) = \frac{h_{\mathrm{ac}}^{(3)}(0,\tau)}{h_{\mathrm{ac}}^{(2)}(0)\; h_{\mathrm{ac}}^{(2)}(\tau)} = \frac{C_{\mathrm{S}}^{(3)}(0^+,\tau)/C_{\mathrm{S}}^{(3)}(\infty,\infty)}{\left[C_{\mathrm{S}}^{(2)}(0^+)/C_{\mathrm{S}}^{(2)}(\infty)\right]\left[C_{\mathrm{S}}^{(2)}(\tau)/C_{\mathrm{S}}^{(2)}(\infty)\right]} \tag{6.95}$$

where $C_{\mathrm{AS(S)}}^{(3)}(0^+,\tau)$ is the post-selected data conditioned on the detection of a pair of photons at time $t = 0^+$, heralding the subtraction or addition of two phonons for example.

Delay $\tau = 0^+$ represents the smallest time bin used (1 μs $\leq \tau \leq$ 3 μs for $g^{(2)}$ and $h^{(2)}$, and 2.5 μs $\leq \tau \leq$ 7.5 μs for $g^{(3)}$ and $h^{(3)}$), and $\tau = \infty$ represents the delay that is much larger than the decoherence time of the oscillator, such that $\tau \gg 10\tau_{\text{ac}}$. The finite time bin at $t = 0^+$ results in a slight shift from the actual theoretical prediction with $t = 0^+$, which is negligible on the scale of figure 6.20.

Solid lines show the theoretical predictions for $g_{\text{ac}}^{(2)}\big|_{+1}(\tau)$ and $h_{\text{ac}}^{(2)}\big|_{+1}(\tau)$, given by

$$g_{\text{ac}}^{(2)}\big|_{-1}(\tau) = h_{\text{ac}}^{(2)}\big|_{+1}(\tau) = \frac{1 + 2e^{-\gamma_{\text{ac}}\tau}}{1 + e^{-\gamma_{\text{ac}}\tau}} \tag{6.96}$$

More generally, we compute the l-th order coherences of a k-phonon-subtracted or -added thermal acoustic state, by using the density matrix $\hat{\rho}_{-k}$ and $\hat{\rho}_{+k}$, given by equation 6.82 and 6.85. Upon detection of k-photons at $t = 0$, we have $g_{\text{ac}}^{(l)}\big|_{-k}(\boldsymbol{\tau})$ (where $\boldsymbol{\tau} = \{\tau_1, \cdots, \tau_{l-1}\}$) is expressed as

$$g_{\text{ac}}^{(l)}\big|_{-k}(\boldsymbol{\tau}) = \frac{\langle \hat{b}^\dagger(0) \cdots \hat{b}^\dagger(\tau_{l-1})\hat{b}(\tau_{l-1}) \cdots \hat{b}(0)\rangle_{\hat{\rho}_{-k}}}{\prod_{i=1}^{l-1}\langle \hat{b}^\dagger(t_i)\hat{b}(t_i)\rangle_{\hat{\rho}_{-k}}} \tag{6.97}$$

where t_i is the cumulative delayed time to the first detected photon at $t = 0$. The numerator can be written as

$$\begin{aligned} &\frac{\langle \hat{b}^\dagger(0)^k \prod_{i=1}^{l-1} \hat{b}^\dagger(\tau_i) \prod_{i=1}^{l-1} \hat{b}(\tau_i)\hat{b}(0)^k\rangle_{\hat{\rho}_{\text{th}}}}{\langle \hat{b}^\dagger(0)^k\hat{b}(0)^k\rangle_{\hat{\rho}_{\text{th}}}} \\ =&\frac{g_{\text{ac}}^{(k+l)}(\mathbf{0}^{\otimes k}, \boldsymbol{\tau})\langle \hat{b}^\dagger(0)\hat{b}(0)\rangle_{\hat{\rho}_{\text{th}}}^{l-1}}{g_{\text{ac}}^{(k+1)}(\mathbf{0})} \end{aligned} \tag{6.98}$$

and the denominator can be written as

$$\frac{\prod_{i=1}^{i=l-1}\langle \hat{b}^\dagger(0)^k\hat{b}^\dagger(t_i)\hat{b}(t_i)\hat{b}(0)^k\rangle_{\hat{\rho}_{\text{th}}}}{\langle \hat{b}^\dagger(0)^k\hat{b}(0)^k\rangle_{\hat{\rho}_{\text{th}}}^{l-1}} \tag{6.99}$$

$$=\frac{\prod_{i=1}^{l-1} g_{\text{ac}}^{(k+1)}(\mathbf{0}^{\otimes k-1}, t_i)}{(g_{\text{ac}}^{(k)}(\mathbf{0}))^{l-1}}\langle \hat{b}^\dagger(0)\hat{b}(0)\rangle_{\hat{\rho}_{\text{th}}}^{l-1} \tag{6.100}$$

Coherences of the k-phonon-added state are derived via the same procedure, where we obtain

$$g_{\text{ac}}^{(l)}\big|_{-k}(\boldsymbol{\tau}) = \frac{g_{\text{ac}}^{(k+l)}(\mathbf{0}^{\otimes k}, \boldsymbol{\tau})\left(g_{\text{ac}}^{(k)}(\mathbf{0})\right)^{l-1}}{g_{\text{ac}}^{(k+1)}(\mathbf{0})\left[\prod_{i=1}^{l-1} g_{\text{ac}}^{(k+1)}\left(\mathbf{0}^{\otimes k-1}, t_i\right)\right]} \tag{6.101}$$

$$h_{\text{ac}}^{(l)}\big|_{+k}(\boldsymbol{\tau}) = \frac{h_{\text{ac}}^{(k+l)}(\mathbf{0}^{\otimes k}, \boldsymbol{\tau})\left(h_{\text{ac}}^{(k)}(\mathbf{0})\right)^{l-1}}{h_{\text{ac}}^{(k+1)}(\mathbf{0})\left[\prod_{i=1}^{l-1} h_{\text{ac}}^{(k+1)}\left(\mathbf{0}^{\otimes k-1}, t_i\right)\right]} \tag{6.102}$$

which are the general expressions for the l-th order coherences of a k-phonon-subtracted and -added thermal acoustic state. Note that to calculate $g_{\text{ac}}^{(l)}\big|_{-k}$ and $h_{\text{ac}}^{(l)}\big|_{+k}$ via post-selection of data, we need the coherences of the unconditioned thermal state of up to the $(k+l)$-th order, where the resulting state is heralded on the joint detection of $k+l$ photons.

These coherences reflect the properties of the distribution of the heralded state which is out of thermal equilibrium, and display distinct behavior at zero delay from that of a thermal state. From equation 6.101 and 6.102, it is easy to show that

$$g_{\text{ac}}^{(2)}|_{-k}(\tau) = \frac{1+(k+1)e^{-\gamma_{\text{ac}}\tau}}{1+ke^{-\gamma_{\text{ac}}\tau}} \tag{6.103}$$

$$h_{\text{ac}}^{(2)}|_{+k}(\tau) = \frac{1+(k+1)e^{-\gamma_{\text{ac}}\tau}}{1+ke^{-\gamma_{\text{ac}}\tau}} \tag{6.104}$$

such that we have in general

$$g_{\text{ac}}^{(2)}|_{-k}(0) = h_{\text{ac}}^{(2)}|_{+k}(0) = 1 + \frac{1}{k+1} \tag{6.105}$$

as shown in figure 6.20.

Chapter 7

Multimode optomechanical coupling

As introduced in section 2.5.1, the simple geometry of the device allows for coupling of one optical mode to exactly one acoustic mode. This is advantageous for correlation measurements in particular, as it distinguish the source of the sideband photons and allows for the generation of a pure state in the acoustic mode of interest. This is because the optomechanical coupling arises from the overlap between the light intensity and the density fluctuation of the helium inside the device, and since the boundary is formed by the mirror-coated fiber ends, it simultaneously constrains both the optical and the acoustic waves. The overlap, and hence the coupling, is thus nonzero only if their half-wavelength wave numbers satisfy the condition, $q^{\text{ac}}_{\lambda/2} = 2q^{\text{opt}}_{\lambda/2}$ given by equation 2.79.

To test the validity of this unique single mode coupling approximation, we measure the response across several acoustic free spectral ranges (FSRs) to characterize the couplings of various acoustic modes to the optical mode with $q^{\text{opt}}_{\lambda/2} = 93$. This mode is mainly coupled to the acoustic mode with $q^{\text{ac}}_{\lambda/2} = 2q^{\text{opt}}_{\lambda/2} = 186$. However, several weakly coupled acoustic modes are also found. I will describe in this chapter the experimental setup and resulting measurements of weakly-coupled paraxial acoustic modes. We attribute these weak couplings to (1) the non-hermiticity of the Hamiltonian arising from the optical and acoustic losses; (2) the penetration of light into the DBR coatings resulting in difference in their boundary conditions; and (3) the three-dimensional overlap of the optical and acoustic modes is not strictly zero.

7.1 Characterization of multimode coupling

7.1.1 Driven acoustics setup

A schematic of the experimental setup is shown in Fig.7.1. It is adapted from the main setup used for correlation measurements as described in figure 4.1. Since the couplings to neighboring acoustic modes are expected to be weak and compared to that of the main acoustic mode, we send an extra drive tone to the optomechanical cavity (OMC) to drive the acoustics at frequency ω_{d} around the main acoustic resonance ω_{ac}.

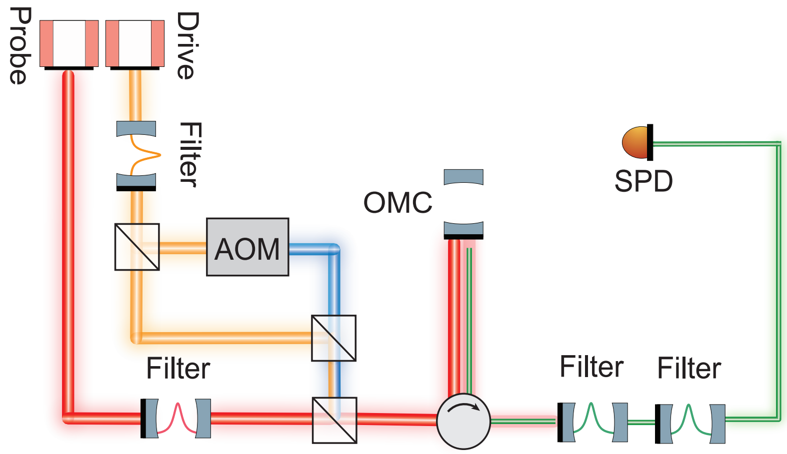

Figure 7.1: Experimental setup for measuring multimode coupling. A beat tone is generated to drive the acoustics directly around ${}_{\text{ac}}$, which is produced by combining the unshifted drive laser tone (yellow) with the tone frequency shifted by an acousto-optic modulator (AOM) shown in blue. Another probe tone (red) is sent to the cavity to read out the driven acoustic response. Sideband photons on resonance with the cavity are collected by the SPD.

The drive tone is generated by a drive laser detuned by $-\omega_{\text{ac}}/2$ from the cavity resonance ω_{c}, as illustrated in the frequency schematic in figure 7.2. It then passes through a drive laser filter to filter the broadband laser noise[1]. It is then split 50/50, where one arm passes through an acousto-optic modulator (AOM)[2], shifting it by frequency ω_{d}[3]. The frequency-shifted arm shown in blue is recombined with the unshifted arm in yellow by a 50/50 beamsplitter. The drive frequency ω_{d} is thus the beat frequency between the two arms, and is set around ω_{ac}. To readout the response from the driven acoustics, a probe laser is sent to the cavity, detuned by $-\omega_{\text{d}}$ from ω_{c} as shown in red. Sideband photons that are anti-Stokes scattered by the driven acoustics are thus on resonance with the optical cavity. The probe tone is combined with the drive tone by another 50/50 beamsplitter. Only acoustically scattered photons are on resonance with the cavity and transmit through the filter cavities centered at ω_{c} shown in green. Sideband photons are finally collected by the SPD.

---

[1] The lasers, filter cavities and other optical components used here are all the same from the standard main setup described in chapter 4, only with the addition of the acousto-optic modulator (AOM).

[2] Brimrose fiber pigtailed acousto-optic frequency shifter. Model: IPF-325-1550-2FP.

[3] An RF signal generator, Vaunix LMS-451D, is sent to the AOM to set the shift frequency.

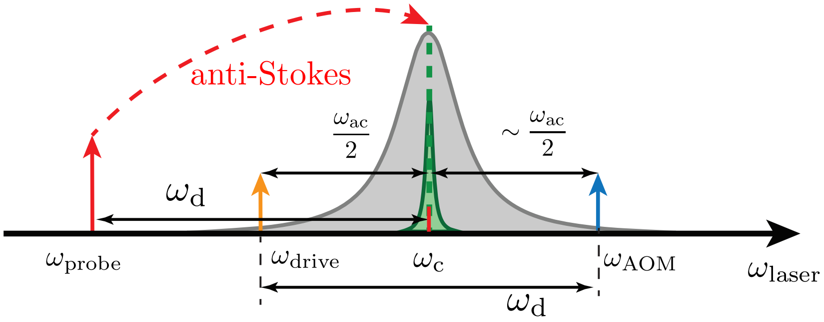

Figure 7.2: Frequency diagram for tones used for multimode coupling measurements. The acoustic is driven by the beat between the drive tone (yellow) and the AOM tone (blue) at frequency ω_d. A probe laser (red) is placed at $-\omega_d$ away from ω_c such that the anti-Stokes scattered photons are on resonance with the optical cavity and the filter cavities (green).

7.1.2 Measurement of weakly-coupled paraxial acoustic modes

Solutions of the optical and acoustic modes inside a Fabry-Perot cavity are given by the paraxial wave equation

$$\nabla_\perp^2 u(\vec{r}) + 2ik\frac{\partial u}{\partial z} = 0 \tag{7.1}$$

under paraxial approximation[4], where $\nabla_\perp^2$ is the transverse Laplacian operator $\frac{\partial^2}{\partial x^2}+\frac{\partial^2}{\partial y^2}$. $u(\vec{r})$ is the transverse profile of the beam propagating in the z direction such that $\psi(\vec{r}) = u(\vec{r})e^{-ikz}$ and $k = \omega/v$ is the wave number. A general solution to equation 7.1 is the orthogonal set of Hermite-Gaussian modes given by [186]

$$\begin{aligned} u_{n,m}(\vec{r}) = u_0\frac{w_0}{w(z)}H_n\Big(\frac{\sqrt{2}x}{w(z)}\Big)H_m\Big(\frac{\sqrt{2}y}{w(z)}\Big) \times \exp\Big(-\frac{r^2}{w(z)^2}\Big) \\ \times \exp\Big(-i\Big[\frac{kr^2}{2R(z)} - \phi_G^{(n,m)}(z) + kz\Big]\Big) \end{aligned} \tag{7.2}$$

in a Fabry-Perot cavity, where $w(z)$ is the beam radius, $w_0 = w(0)$ the beam waist radius where we set the focal point of the beam at $z = 0$, $R(z)$ the radius of curvature of the wavefront, and $r = x^2 + y^2$ the distance from axis of propagation. H_n and H_m are n-th and m-th order Hermite polynomials, and $\phi_G^{(n,m)}$ is the Guoy phase shift[5] given by

$$\phi_G^{(n,m)}(z) = (1 + n + m)\arctan\Big(z\frac{\lambda}{\pi w_0^2}\Big) \tag{7.3}$$

---

[4] Paraxial approximation is assumed when the variation of transverse profile $u_z(\vec{r})$ is much slower than the wavelength (beam waist $w_0 \gg 1/\omega$)[185], such that $\nabla^2 = \nabla_\perp^2$.

[5] Guoy phase is a phase shift acquired during the propagation of a Gaussian beam with respect to a plane wave. [185]

where $z_{\mathrm{R}} = \lambda/\pi w_0^2$ is known as the Rayleigh length. It is related to the beam size by

$$w(z) = w_0\sqrt{1 + (z/z_{\mathrm{R}})^2} \tag{7.4}$$

We thus label each Hermite-Gaussian mode by its mode numbers, (q, n, m) where q is the longituidinal mode number, or the number of half waves, such that $k = \pi q/L_{\mathrm{cav}}$ and L_{cav} is the length of the cavity, and n, m are the transverse mode number describing its transverse mode profile (known as the TEM$_{nm}$ mode).

While the geometry of the cavity ensures that the main optomechanical coupling to the optical tone used here with $q_{\mathrm{opt}} = 93$ is the longituidinal acoustic mode with $q_{\mathrm{ac}} = 186$, we also drive neighboring longituidinal and transverse acoustics modes $(q_{\mathrm{ac}} + q^{'}, n, m)$ to characterize potential (presumably weak) couplings to those modes. To simplify the notation, the neighboring modes are labeled by $(q^{'}, n, m)$ with respect to the main mode in the rest of the work. Resonant frequencies corresponding to neighboring optical and acoustic modes are determined by the optical FSR $\Delta\omega_{\mathrm{opt}}$, the acoustic FSR $\Delta\omega_{\mathrm{ac}}$ and the transverse mode splitting δ_{G}, such that

$$\omega_{\mathrm{opt}}^{(q^{'},n,m)} = \omega_{\mathrm{opt}} + q^{'}\Delta\omega_{\mathrm{opt}} + (n+m)\delta_{\mathrm{G,opt}} \tag{7.5}$$

$$\omega_{\mathrm{ac}}^{(q^{'},n,m)} = \omega_{\mathrm{ac}} + q^{'}\Delta\omega_{\mathrm{ac}} + (n+m)\delta_{\mathrm{G,ac}} \tag{7.6}$$

This is because each longituidinal mode is separated by an optical or acoustic FSR, whereas each transverse mode is separated by $(n + m)$ times of the transverse mode splitting δ_{G} which is a constant proportional to the cumulative Guoy phase shift. Note that the main $(0, 0, 0)$ optical mode is at $\omega_{\mathrm{opt}}/2\pi = 193.63 \pm 0.01$ THz, and its corresponding acoustic mode $(0, 0, 0)$ is at $\omega_{\mathrm{ac}}/2\pi = 315.40 \pm 0.02$ MHz, between which we have measured a single optomechanical coupling of $g_0/2\pi = 4.58$ kHz.

By scanning the laser frequency around ω_{opt}, neighboring optical modes are found via cavity reflection, and their frequencies are summarized in figure 7.3. From the splitting between each longituidinal mode with the same transverse mode number, we measure optical FSR $\Delta\omega_{\mathrm{opt}}/2\pi = 2.08 \pm 0.01$ THz. Since $\Delta\omega_{\mathrm{opt}}/2\pi = c/(2n_{\mathrm{He}}L_{\mathrm{cav}})$, where the index of refraction is $n_{\mathrm{He}} = 1.0261$ for liquid He, we extract cavity length $L_{\mathrm{cav}} = 70.3 \pm 0.3\ \mu$m.

Note that the transverse mode splitting is related to the Guoy phase accumulated as the transverse wave travels through the entire cavity. For a Fabry-Perot cavity with mirrors that have radius of curvature R_1 and R_2, z_{R} in equation 7.3 is related to them by

$$R_1 = z_1\Big(1 + \big(\frac{z_{\mathrm{R}}}{z_1}\big)^2\Big)\ ,\quad R_2 = z_2\Big(1 + \big(\frac{z_{\mathrm{R}}}{z_2}\big)^2\Big) \tag{7.7}$$

where z_1 and z_2 are the distances from the beam waist to each mirror and $L_{\mathrm{cav}} = z_1 + z_2$. We thus write the total Guoy phase shift as

$$\phi_{\mathrm{G}} = \phi_{\mathrm{G}}^{(0,0)}(z_2) - \phi_{\mathrm{G}}^{(0,0)}(-z_1) = \arccos\Bigg(\sqrt{(1 - \frac{n_{\mathrm{He}}L_{\mathrm{cav}}}{R_1})(1 - \frac{n_{\mathrm{He}}L_{\mathrm{cav}}}{R_2})}\Bigg) \tag{7.8}$$

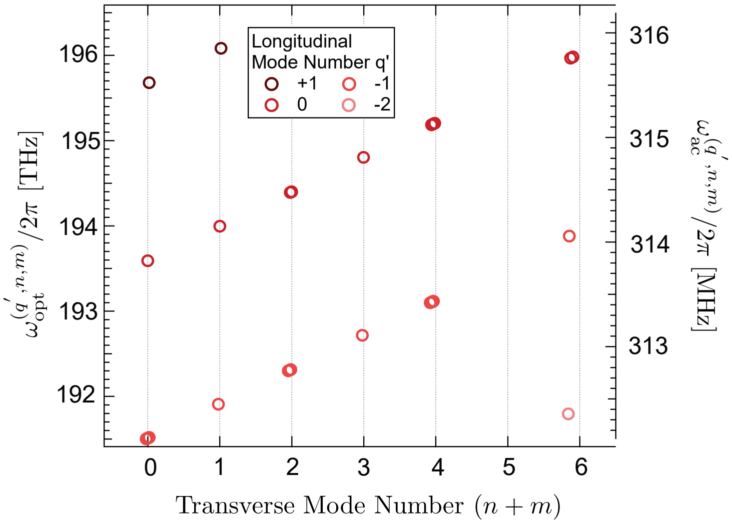

Figure 7.3: Measured frequencies of optical modes around mode (0,0,0) are shown by the data points, which can be mapped to neighboring longituidinal and transverse modes (q',n,m) and agree with the specifications of the Fabry-Perot cavity. Corresponding acoustic mode frequencies inferred from equation 7.6 are indicated by the right axis.

The transverse mode splitting is thus $\delta_{\rm G,opt} = (\phi_{\rm G}/\pi)\Delta\omega_{\rm opt}$. From the measured splitting between each degenerate transverse mode with $(n+m)$, we extract $\phi_{\rm G}/\pi = 0.194 \pm 0.002$ and $\delta_{\rm G,opt}/2\pi = 0.404 \pm 0.004$ THz. For our cavity with $R_1 \approx 324.5$ μm and $R_2 \approx 496.7$ μm, we have an estimated $\phi_{\rm G}/\pi = 0.196$, which agrees with the measurement. From equation 7.6, we estimate the frequencies of neighboring acoustic modes corresponding to each of the measured (q',n,m) optical mode, where we use the acoustic FSR $\Delta\omega_{\rm ac}/2\pi = v_{\rm He}/(2L_{\rm cav}) = 1.695$ MHz and $\delta_{\rm G,ac}/2\pi = 0.194(\Delta\omega_{\rm ac}/2\pi) = 0.33$ MHz. The inferred $\omega_{\rm ac}^{(q',n,m)}$ is indicated by the right axis of figure 7.3.

By sweeping the AOM drive frequency $\omega_{\rm d}$ around $\omega_{\rm ac}^{(q',n,m)}$ for $\{q' | -6 \leqslant q' \leqslant 6, q' \in \mathbb{Z}\}$ and $\{(n,m) | 0 \leqslant n+m \leqslant 6, (n,m) \in \mathbb{Z}\}$, the driven response of each nearby paraxial acoustic mode is probed with a tone placed at a deutning of $-\omega_{\rm ac}^{(\rm q',p)}$. The count rate spectrum of each of these modes is shown in figure 7.4 and 7.5. Each spectrum is acquired under the same drive laser tone power $P_{\rm drive}$ and AOM drive power $P_{\rm AOM}$, and probed with a probe tone at $P_{\rm probe} = 1$ μW. $R_{\rm det}$ is the power-normalized detected count rate, and is plotted against the drive frequency detuned from the acoustic mode frequency, $\omega_{\rm d} - \omega_{\rm ac}^{(q',n,m)}$. $\omega_{\rm d}$ is stepped by 200 Hz around the expected resonant frequency $\omega_{\rm ac}^{(q',n,m)}$, and the count rate at each frequency step bin is acquired by averaging over $>$ 60 sec of DAQ time.

Each spectrum is fit to a Lorentzian form

$$R_{\rm det} = R_{\rm bkg} + \frac{R_{\rm AS}}{1 + \left(\frac{2(\omega_{\rm d} - \omega_{\rm ac}^{(q',n,m)})}{\gamma_{\rm ac}^{(q',n,m)}}\right)^2} \tag{7.9}$$

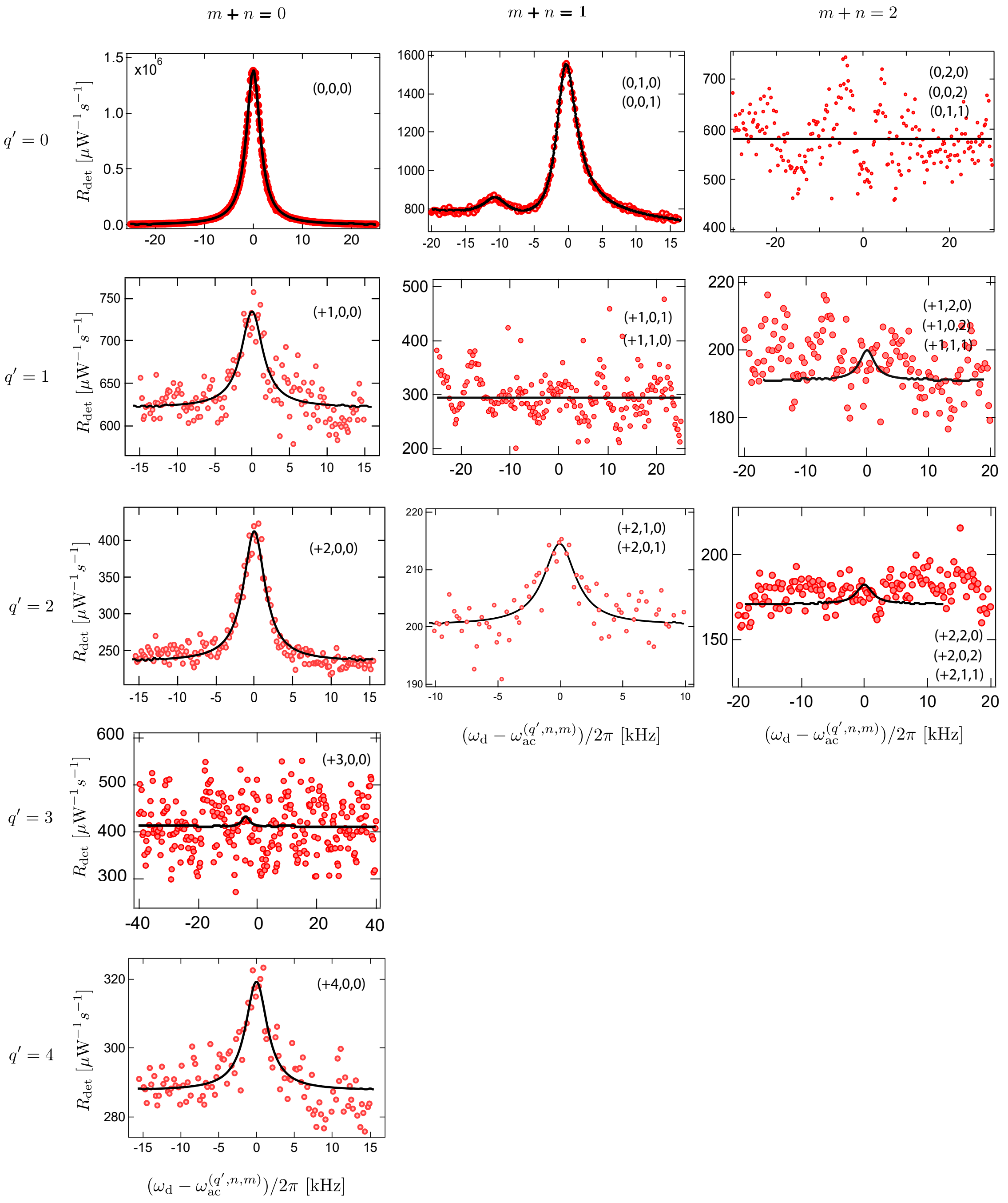

Figure 7.4: Counting spectrum of coupled paraxial acoustic modes (q', n, m), where $q' \geq 0$. All neighboring longituidinal modes are measured up to $q' = +6$, and transverse modes measured up to $n + m = 6$. The spectrum is fit to a Lorentazian form and the amplitude of which characterizes the magnitude of the optomechanical coupling. Some of the modes with negligible response are not all shown here.

where the background detection rate R_{bkg}, sideband count rate R_{AS}, frequency of the (q', n, m) acoustic mode $\omega_{\text{ac}}^{(q',n,m)}$, and linewidth $\gamma_{\text{ac}}^{(q',n,m)}$ are the fitting parameters. Corresponding fits are shown by the black lines. Note that for the spectrum where an acoustic signature is not present or distinguishable from the background counts (such as modes $(0, 2, 0)$, $(1, 0, 1)$, $(2, 0, 2)$ etc.), the fit is done with the parameters R_{bkg} and $\gamma_{\text{ac}}^{(q',n,m)}$ fixed at the average detected count rate and the estimated value of $\gamma_{\text{ac}}^{(q',n,m)}/2\pi = 3500$ Hz. And the fitting parameter $\omega_{\text{ac}}^{(q',n,m)}$ is constrained by $\sim 2\pi$ 20 kHz within the estimated $\omega_{\text{ac}}^{(q',n,m)}$ calculated from equation 7.6 in order to extract an estimate of the corresponding R_{AS}. Examples of such fits are shown in the figure. Some of the other modes with negligible responses are not shown here.

Transverse modes with the same $m + n$ mode number are expected to be degenerate in frequencies. The measured transverse modes appear to be degenerate, with the exception of mode $(0, 1, 0)$ and $(0, 0, 1)$ in figure 7.4, where a split in frequency is observed. The mode is fit to a double Lorentzian form,

$$R_{\text{det}} = R_{\text{bkg}} + \frac{R_{\text{AS1}}}{1 + \left(\frac{2(\omega_{\text{d}} - \omega_{\text{ac}}^{(q',n1,m1)})}{\gamma_{\text{ac}}^{(q',n1,m1)}}\right)^2} + \frac{R_{\text{AS2}}}{1 + \left(\frac{2(\omega_{\text{d}} - \omega_{\text{ac}}^{(q',n2,m2)})}{\gamma_{\text{ac}}^{(q',n2,m2)}}\right)^2} \tag{7.10}$$

with individual fitting sideband count rates, frequencies, and linewidths for each Lorentzian, with $(n1, m1) = (0, 1)$ and $(n2, m2) = (1, 0)$.

Finally in figure 7.5, we measure the $(-1, m+n = 6)$ mode centering at $\omega_{\text{ac}}^{(-1,n+m=6)}/2\pi = 315.624$ MHz. The acoustic mode coincides with the decaying tail of the main acoustic mode $(0, 0, 0)$, and is thus fit to

$$R_{\text{det}} = \frac{R_{\text{bkg}}}{1 + (\frac{\omega_{\text{d}}}{\gamma_{\text{bkg}}})^2} + \frac{R_{\text{AS}}}{1 + \left(\frac{2(\omega_{\text{d}} - \omega_{\text{ac}}^{(q',n,m)})}{\gamma_{\text{ac}}^{(q',n,m)}}\right)^2} \tag{7.11}$$

where R_{bkg} and γ_{bkg} characterizes the background. All the fit-extracted $R_{\text{AS}}^{(q',n,m)}$ and $\gamma_{\text{ac}}^{(q',n,m)}$ corresponding to modes with a distinguishable measured signature (extracted $R_{\text{AS}} > 3\sigma$, where σ is the standard error for a 95% confidence interval) are summarized in table 7.1, and the corresponding modes are plotted in sequence in figure 7.6, where the main acoustic mode (0,0,0) is included as well.

We characterize the single optomechanical coupling $g_0^{(q',n,m)}$ to each of these acoustic modes from its corresponding sideband count rate $R_{\text{AS}}^{(q',n,m)}$. The rate at which the anti-Stokes photons get scattered by the (q', n, m) acoustic mode is proportional to the mean phonon occupancy of the driven acoustic mode $\langle n \rangle_{\text{ac}}^{(q',n,m)}$. The oscillating force generated by the drive and the AOM tone is $\sqrt{P_{\text{drive}} P_{\text{AOM}}}$. The force coupled and applied to the acoustic is thus

$$F_{\text{d}}^{(q',n,m)} = \sqrt{P_{\text{drive}} P_{\text{AOM}} f(g_0^{(q',n,m)})} \tag{7.12}$$

Note that $f(g_0^{(q',n,m)})$ is some function describing the amount of optical drive gets coupled

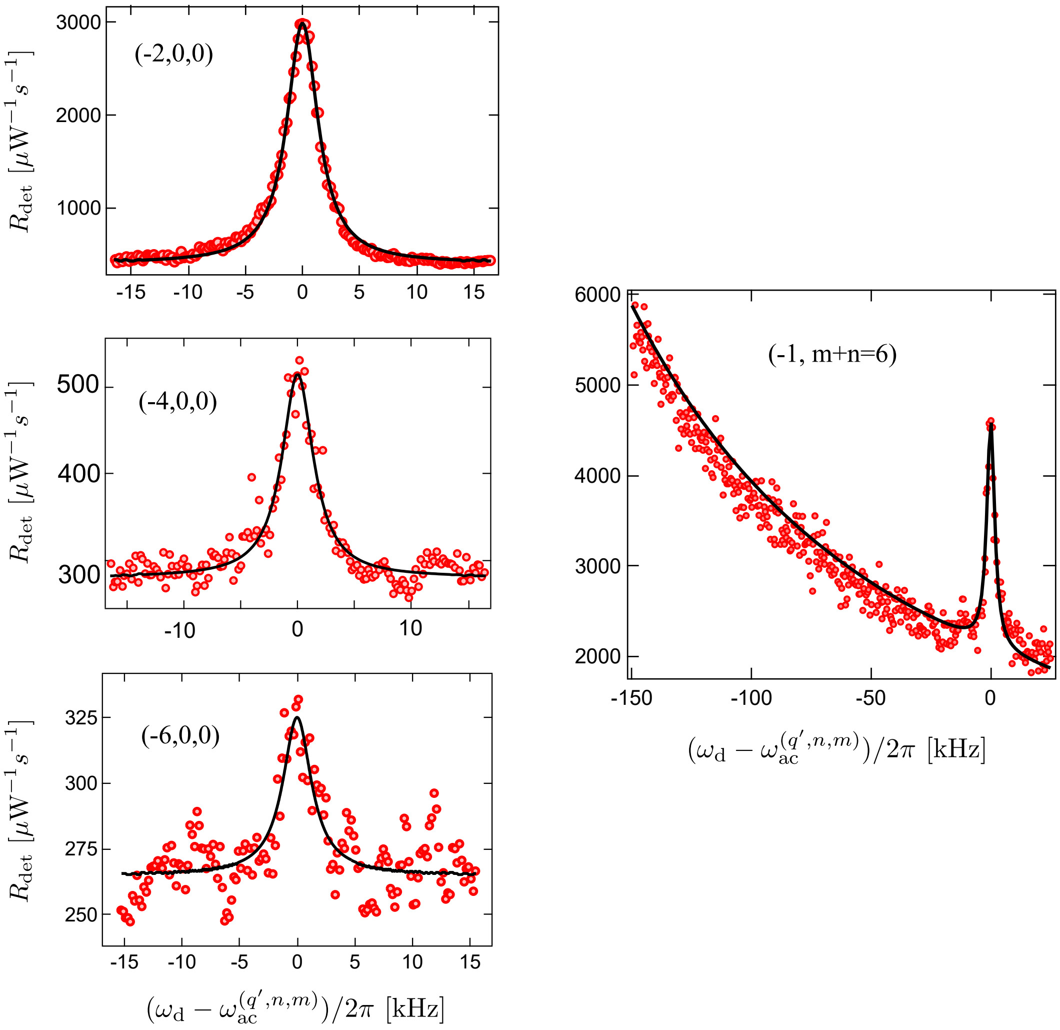

Figure 7.5: Counting spectrum of coupled paraxial acoustic modes (q', n, m), where $q' < 0$. All neighboring longituidinal modes are measured down to $q' = -6$, and transverse modes measured up to $n + m = -6$. The spectrum is fit to a Lorentazian form and the amplitude of which characterizes the magnitude of the optomechanical coupling. Only the modes showing a distinct signature are shown here.

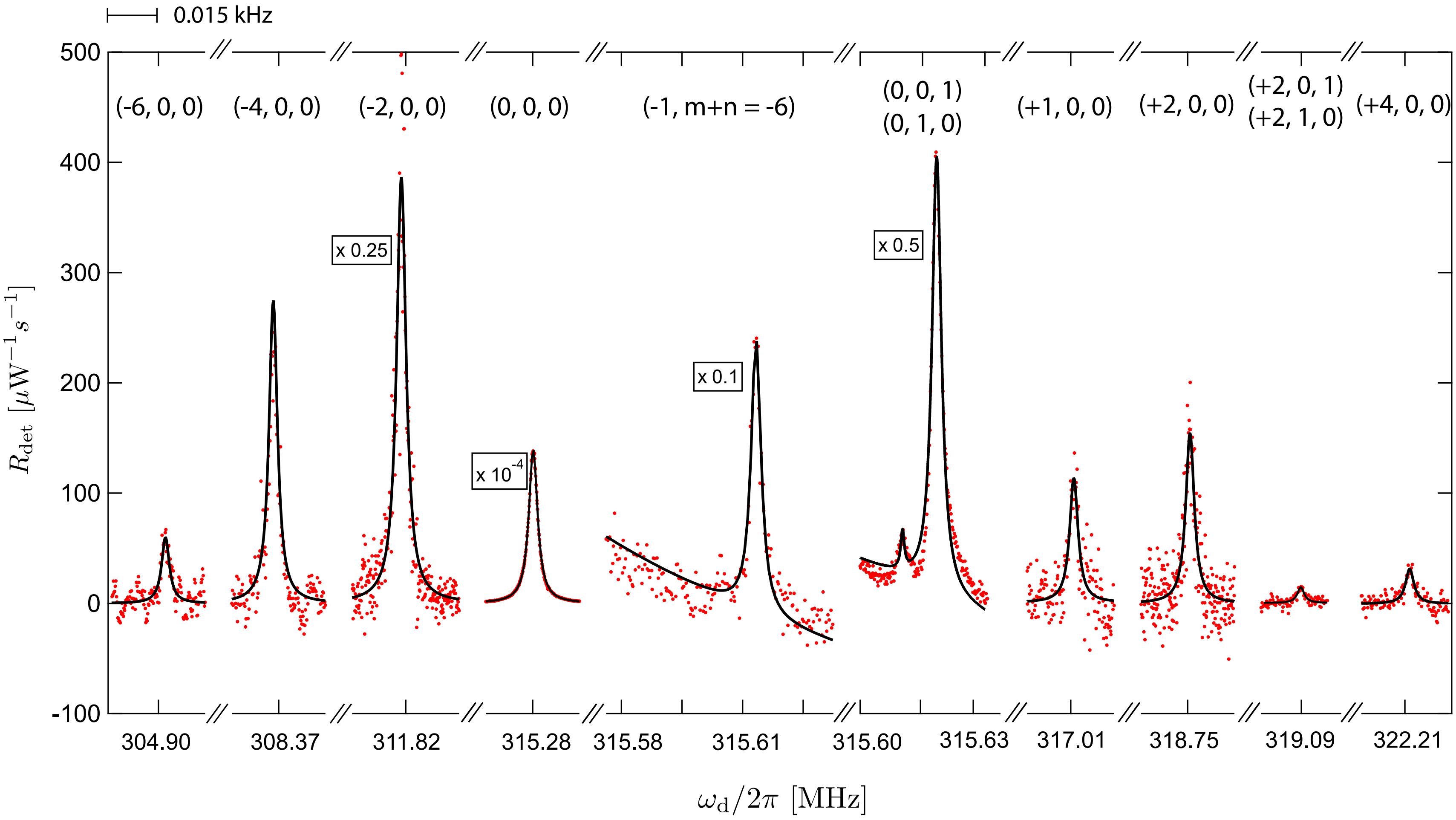

Figure 7.6: Spectrum of the coupled longituidinal and transverse acoustic modes plotted against the AOM drive frequency ω_{d}. Transverse modes are degenerate in frequency with the same $m+n$ mode number except for mode (0,1,0) and (0,0,1). The amplitude R_{det} characterizes the coupling strength, and some modes are plotted with a scaled R_{det} to fit on the same scale.

into the acoustics, which depends on the coupling strength with that mode. The driven phonon number of any acoustic mode $\langle n\rangle_{\text{ac}}^{(q',n,m)}$ is thus given by

$$\langle n\rangle_{\text{ac}}^{(q',n,m)} = \langle b^\dagger b\rangle \propto \frac{F_{\text{d}}^{(q',n,m)^2}}{\left(\omega_{\text{d}} - \omega_{\text{ac}}^{(q',n,m)}\right)^2 + \left(\gamma_{\text{ac}}^{(q',n,m)}/2\right)^2} \tag{7.13}$$

where the driven amplitude is proportional to the square of the drive force. At zero detuning where R_{AS} is measured, we have

$$\langle n\rangle_{\text{ac}}^{(q',n,m)} \propto \frac{F_{\text{d}}^{(q',n,m)^2}}{\left(\gamma_{\text{ac}}^{(q',n,m)}/2\right)^2} \tag{7.14}$$

and the scattering rate is proportional to $\langle n\rangle_{\text{ac}}^{(q',n,m)}$ such that

$$R_{\text{AS}} = \langle a^\dagger a\rangle_{\text{d}} \propto g_0^{(q',n,m)^2}\langle n\rangle_{\text{ac}}^{(q',n,m)} \tag{7.15}$$

Given the same drive tone power, we thus have

$$\frac{R_{\text{AS}}^{(q',n,m)}}{R_{\text{AS}}^{(0,0,0)}} = \left(\frac{g_0^{(q',n,m)}}{g_0}\right)^2 \frac{\langle n\rangle_{\text{ac}}^{(q',n,m)}}{\langle n\rangle_{\text{ac}}} = \left(\frac{g_0^{(q',n,m)}}{g_0}\right)^2 \frac{f(g_0^{(q',n,m)})\gamma_{\text{ac}}}{f(g_0)\gamma_{\text{ac}}^{(q',n,m)}} \tag{7.16}$$

where the sideband count rate is compared to that of the main coupled acoustic mode, such that $g_0^{(q',n,m)}$ can be extracted as a ratio of the coupling to the (0,0,0) mode g_0, which is summarized in table 7.1 and figure 7.7. These results are obtained assuming $f(g_0^{(q',n,m)})$ goes as $(g_0^{(q',n,m)})^2$, which is the amount of optical drive that gets coupled into the acoustic mode. For longituidinal modes, we in general measure a more significant response for even number of q' except for the (1,0,0) mode.

We also obtain the spectrum of a wide frequency scan where the drive frequency ω_{d} is coarsely stepped (by 25 kHz) through six acoustic FSRs to examine the overall background pattern, as shown in figure 7.8. The largest fluctuation centering around 321 MHz is likely induced by the GAWBS signature (see figure 5.8). High variance in the background counts limits our ability to identify existing acoustic mode couplings to higher precision.

7.2 Modeling the multimode coupling

We identify several sources of multimode optomechanical coupling to neighboring paraxial acoustic modes, despite the near-perfect orthogonality condition imposed by the simple geometry of the system.

Mode (q', n, m)	R_{AS} [μW^{-1}s^{-1}]	$\gamma_{\mathrm{ac}}^{(q',n,m)}/2\pi$	$g_0^{(q',n,m)}/2\pi$ [Hz]
(-6,0)	59.8	3019	139 ± 7
(-5,0)	2.2	3400	62 ± 47
(-4,0)	234.3	3349	207 ± 4
(-3,0)	8.4	3400	87 ± 47
(-2,0)	2589.6	3319	375 ± 2
(-2,1)	34.0	3400	123 ± 17
(-1,0)	0.1	3400	32 ± 62
(-1,1)	0.1	3400	28 ± 94
(-1,6)	2504	3888.6	402 ± 16
(0,0)	1.4×10^6	3375.5	4580 ± 10
(0,1)	796.4	3549	289 ± 8
(0,2)	9.7	3400	88 ± 48
(0,3)	21.4	3400	109 ± 43
(+1,0)	113.3	3499	176 ± 8
(+1,1)	17.3	3400	103 ± 45
(+2,0)	177.3	3396	194 ± 4
(+2,1)	14.2	3120	99 ± 7
(+3,0)	4.6	3400	74 ± 49
(+4,0)	31.6	3470	127 ± 7
(+5,0)	0.1	3400	28 ± 52
(+6,0)	11.7	3140	94 ± 19

Table 7.1: Extracted optomechanical coupling to weakly-coupled paraxial acoustic modes.

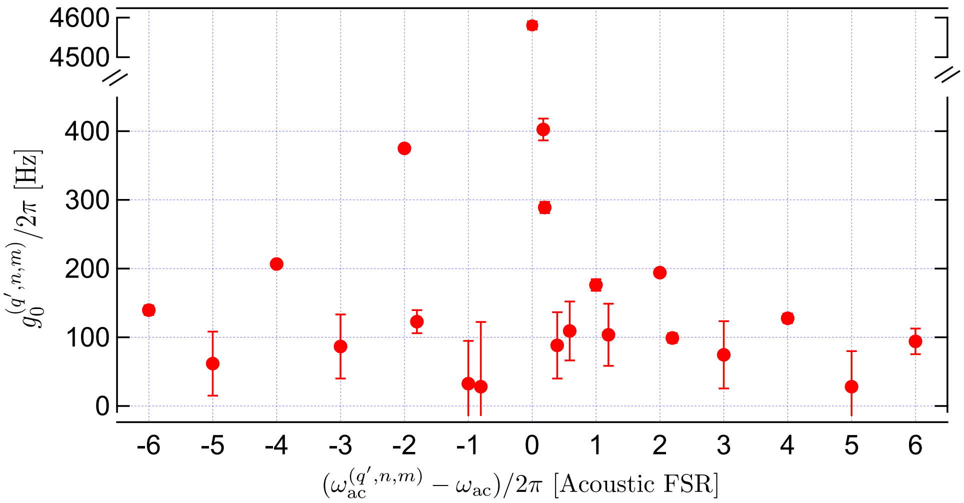

Figure 7.7: Extracted g_0 of neighboring acoustic modes plotted against the neighboring acoustic mode frequency relative to the main ω_{ac} in the unit of the acoustic FSR.

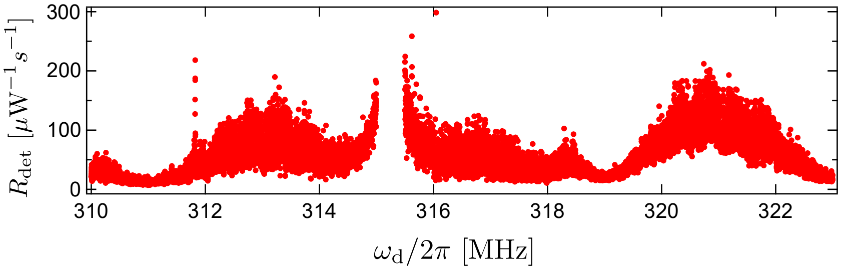

Figure 7.8: Spectrum of a coarse acoustic frequency scan.

7.2.1 Non-Hermiticity

First, the open system is described by a non-Hermitian Hamiltonian for the lossy acoustic mode. This leads to a non-zero overlap between neighboring modes.

The wave equation for the acoustic mode is given by

$$\left(\nabla^2 - \frac{1}{v_{\text{He}}^2}\frac{\partial^2}{\partial t^2} - \frac{2\gamma_{\text{ac}}}{v_{\text{He}}^2}\frac{\partial}{\partial t}\right)\rho = 0 \tag{7.17}$$

where ρ is the density fluctuation of He inside the cavity. The last term accounts for the acoustic loss, which we treat as a perturbation term $\hat{P}$ when solving for the wave equation[187]. We first examine the one dimensional lossless wave equation described by

$$\left(\nabla^2 - \frac{1}{v_{\text{He}}^2}\frac{\partial^2}{\partial t^2}\right)\rho = 0 \tag{7.18}$$

Assume the solution is in the form $\rho = u(\vec{r})\Re[e^{i\omega t}]$, we thus have

$$\nabla^2 u + k^2 u = 0 \tag{7.19}$$

where $k = \omega/v_{\text{He}}$ is the eigenvalue of the hermitian Hamiltonian. Equation 7.17 becomes

$$\left(\nabla^2 + k^2\right)u + \frac{2i\omega\gamma_{\text{ac}}}{v_{\text{He}}^2}u = 0 \tag{7.20}$$

To the first order of the perturbation, the corrected overlap between different modes, $\langle q_{1,\text{corr}}|q_{2,\text{corr}}\rangle$, is given by

$$\begin{aligned}\langle q_{1,\text{corr}}|q_{2,\text{corr}}\rangle &= \frac{1}{k_1-k_2}\langle q_1|(\hat{P}-\hat{P}^\dagger)|q_2\rangle \\ &= \frac{1}{k_1-k_2}\frac{4\omega_2\gamma_{\text{ac}}}{v_{\text{He}}^2}\langle q_1|i|q_2\rangle \\ &\approx \frac{2\gamma_{\text{ac}}}{\omega_2-\omega_1}\langle q_1|i|q_2\rangle \end{aligned} \tag{7.21}$$

Here we assume a one-dimensional Fabry-Perot cavity, such that $|q_1\rangle$, $|q_2\rangle$ represents the

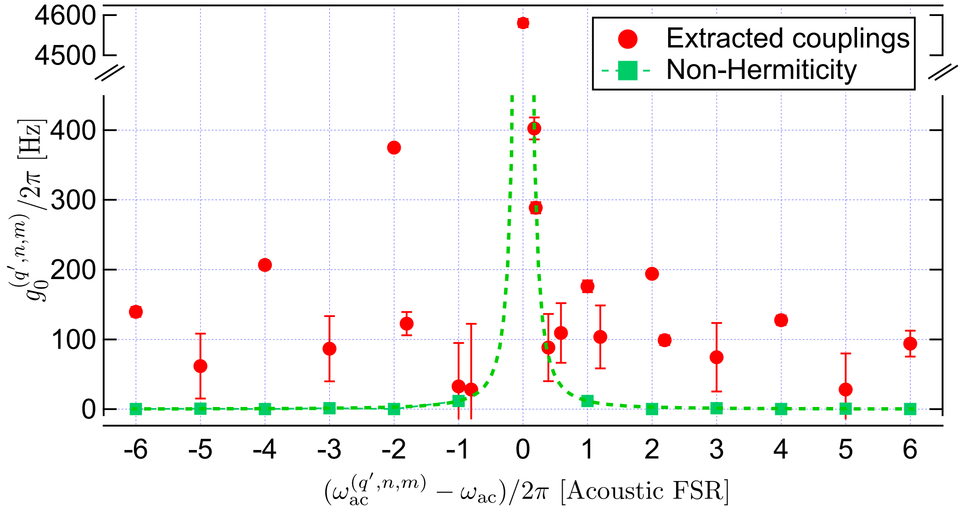

Figure 7.9: Multimode coupling arising from the non-Hermiticity of a lossy system.

mode with eigenvalue $k_{1,2} = \pi q_{1,2}/L_{\rm cav}$ associated with the unperturbed Hamiltonian, and q is the longituidinal mode number used in this chapter or the number of half-waves inside the cavity. In the last step, we assume $\omega_1 \approx \omega_1$. Plugging in the eigenmodes of the unperturbed Hamiltonian, we have

$$\langle q_1|i|q_2\rangle = \int_0^{L_{\rm cav}} \cos\left(\pi q_1 z/L_{\rm cav}\right)\right) \sin\left(\pi q_2 z/L_{\rm cav}\right)\right) \tag{7.22}$$

To compute the overlap with the main acoustic mode where $q_1 = 186$, we have

$$\langle q_1|i|q_2\rangle = \begin{cases} 0 & \text{if } q_2 \text{ is even} \\ \frac{2}{\pi(m-n)} & \text{if } q_2 \text{ is odd} \end{cases} \tag{7.23}$$

Note that with $\omega_2 - \omega_1 = (m-n)\Delta\omega_{\rm ac}$, we have

$$\langle 0|q'\rangle \equiv \langle q_{1,\rm corr}|q_{2,\rm corr}\rangle \approx \frac{4\gamma_{\rm ac}}{\pi q'^2 \Delta\omega_{\rm ac}} \quad \text{if } q' \text{ is odd} \tag{7.24}$$

where $\Delta\omega_{\rm ac}$ and $\gamma_{\rm ac}$ are the known parameters of acoustic FSR and bare linewidth of the main acoustic mode. We thus estimate the coupling arising from non-Hermiticity to be $g_0^{(0,0,0)}\langle 0|q'\rangle$, shown by green squares in figure 7.9. Note that the index of the x-axis is equivalent to q'. The dashed line shows the asymptotic behavior of the estimated contribution from non-hermiticity for a continuous q'.

7.2.2 Three-dimensional overlap integral

In this section I calculate the overlap integral between the three-dimensional cavity modes. Note the coupling is proportional to the overlap integral between the *intensity* of the optical mode and the *amplitude* acoustic mode. The former is not an eigenmode of the paraxial wave equation, which is thus not guaranteed to be orthonormal to the acoustic eigenmode. Equation 7.2 gives the orthogonal sets of Hermite-Gaussian modes in paraxial approximation. It follows that the optical mode inside a Fabry-Perot cavity can be written as [38]

$$u_{q,n,m}(\vec{r}) = u_0 \frac{w_0}{w(z)} H_n\Big(\frac{\sqrt{2}x}{w(z)}\Big) H_m\Big(\frac{\sqrt{2}y}{w(z)}\Big) \times \exp\Big(-\frac{r^2}{w(z)^2}\Big) \\ \times \exp\Big(-i\Big[\frac{kr^2}{2R(z)} - \phi_{\text{G}}^{(n,m)}(z) + kz - \theta_{\text{BC}}^{(n,m)}\Big]\Big) \quad (7.25)$$

where $\theta_{\text{BC}}^{(n,m)}$ is the phase at the boundary to satisfy the boundary condition. For the optical mode with a node at the boundary, we have $\theta_{\text{BC}}^{(n,m)} = -kz_2 + \phi_{\text{G}}^{(n,m)}(z_2)$. Wavenumber k is associated with (q, n, m) by $k = \pi q/L_{\text{cav}} + \phi_{\text{G}}^{(n,m)}(z)$, and the Guoy phase is given by equation 7.3. Beam size $w(z)$ is given by equation 7.4. We thus have the wave equation of the main optical mode (93,0,0) as

$$u_{93,0,0}(\vec{r}) = u_0 \frac{w_0}{w(z)} \exp\Big(-\frac{r^2}{w(z)^2}\Big) \sin\Big(\frac{k(x^2+y^2)}{2R(z)} - \phi_{\text{G}}^{(0,0)}(z) + kz + \theta_{\text{BC}}^{(0,0)}\Big) \quad (7.26)$$

where $k = 93\pi/L_{\text{cav}} + \phi_{\text{G}}^{(0,0)}(z)$. Similarly, for the acoustic mode with an anti-node at boundary, we have

$$\rho_{q,n,m}(\vec{r}) = \rho_0 \frac{w_0}{w(z)} H_n\Big(\frac{\sqrt{2}x}{w(z)}\Big) H_m\Big(\frac{\sqrt{2}y}{w(z)}\Big) \times \exp\Big(-\frac{r^2}{w(z)^2}\Big) \\ \times \cos\Big(\frac{kr^2}{2R(z)} - \phi_{\text{G}}^{(n,m)}(z) + kz + \theta_{\text{BC}}^{(n,m)}\Big) \quad (7.27)$$

We compute the overlap integral between the $(93, 0, 0)$ optical mode and neighboring longituidinal transverse modes $(q', 0, 0)$ by

$$g_0^{(q'0,0)} \propto \int_0^{L_{\text{cav}}} \int_{-5w_0}^{5w_0} \int_{-5w_0}^{5w_0} \big(u_{93,0,0}(x,y,z)\big)^2 \rho_{q',0,0}(x,y,z)\,dxdydz \\ \propto \int_0^{L_{\text{cav}}} \int_{-5w_0}^{5w_0} \int_{-5w_0}^{5w_0} \Big(\frac{w_0}{w_{\text{z}}}\Big)^3 \exp\Big(-\frac{3r^2}{w(z)^2}\Big) \cos\Big(\frac{k^{(q',0,0)}r^2}{2R(z)} - \phi_{\text{G}}^{(0,0)}(z) + k^{(q',0,0)}z + \theta_{\text{BC}}^{(q',0,0)}\Big) \\ \times \sin^2\Big(\frac{k^{(93,0,0)}r^2}{2R(z)} - \phi_{\text{G}}^{(0,0)}(z) + k^{(93,0,0)}z + \theta_{\text{BC}}^{(93,0,0)}\Big) \quad (7.28)$$

where the acoustic mode corresponds to the $q' + 2 \times 93$ longituidinal mode. We numerically compute the integral and scale it by the main optomechanical coupling g_0 to extract $g_0^{(q'0,0)}$ arising from the three-dimensional overlap between the optical and the acoustic modes. For longituidinal acoustic modes, this is only non-zero for even q' as shown in figure 7.10. We further compute the corresponding coupling between the $(0, 0, 0)$ optical mode and

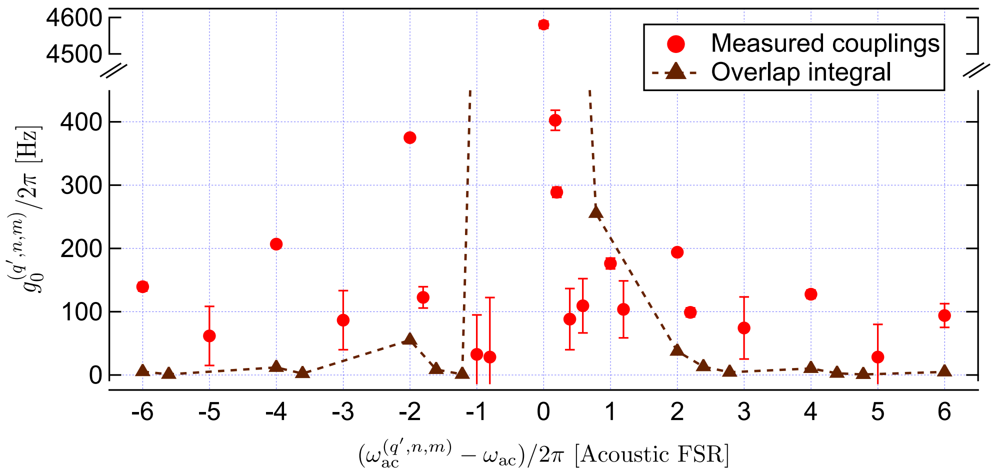

Figure 7.10: Multimode coupling arising from the three-dimensional overlap integral between the intensity of the optical field and the acoustic wave equation.

the transverse acoustic modes described by equation 7.26 and 7.27, which is shown to be non-zero only for even $n + m$.

7.2.3 Asymmetrical boundary condition

In our previous discussions, we have assumed that both the optical and acoustic modes share the exact same boundary conditions; this results in the unique single mode matching condition. While the acoustic mode is strongly confined at the glass and helium interface at the boundary due to the large acoustic impedance mismatch, the optical mode is confined by the optical Distibuted Bragg Reflectors (DBR) coating on the fiber ends. There thus exists some leakage into the DBR coatings, resulting in a different boundary conditions for the optical modes.

When both modes share the same set of boundaries at the helium-glass interface, the simplified one-dimensional waves inside the cavity are shown in figure 7.11 (top), where the optical amplitude is given by $E(z) \propto \sin(\pi q_{\text{opt}} z/L_{\text{cav}})$, the optical intensity given by $I(z) \propto |E(z)|^2 = \sin^2(\pi q_{\text{opt}} z/L_{\text{cav}})$, and the density wave given by $\delta\rho(z) \propto \cos(\pi q_{\text{ac}} z/L_{\text{cav}})$. The waves are plotted with $q_{\text{opt}} = 3$ and $q_{\text{ac}} = 6$. The optical leakage into the DBR coatings is characterized by an additional phase θ_{mod} at the boundary, such that the optical amplitude wave is modified to

$$E(z) \propto \sin\left(\frac{\pi q_{\text{opt}} - \theta_{\text{mod}}}{L_{\text{cav}}} z + \theta_{\text{mod}}/2\right) \tag{7.29}$$

Optical intensity with this modification is plotted in figure 7.11 (bottom) with $\theta_{\text{mod}} = 0.3$ rad.

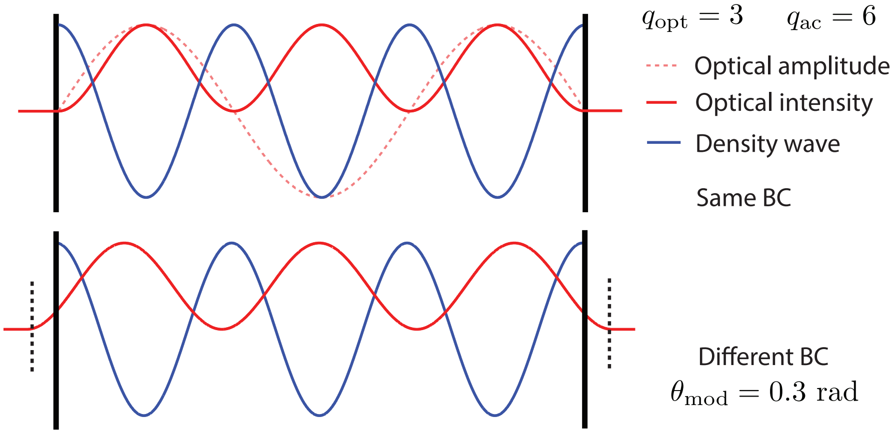

Figure 7.11: A simplified one-dimensional illustration of the Waves inside the cavity with (a) the same boundary conditions (top), and (b) different boundary conditions (bottom). The latter is plotted with a phase difference at the boundary of $\theta_{\rm mod} = 0.3$ rad.

We can thus calculate the mode overlap under different boundary conditions by

$$\begin{aligned}
&\int_0^{L_{\rm cav}} \delta\rho(z) I(z) dz \propto \int_0^{L_{\rm cav}} \cos\left(\frac{\pi q_{\rm ac} z}{L_{\rm cav}}\right) \sin^2\left(\frac{\pi q_{\rm opt} - \theta_{\rm mod}}{L_{\rm cav}} z + \theta_{\rm mod}/2\right) dz \\
&\propto \int_0^{L_{\rm cav}} \cos\left(\frac{\pi q_{\rm ac} z}{L_{\rm cav}}\right) \cos\left(\frac{2\pi q_{\rm opt} - 2\theta_{\rm mod}}{L_{\rm cav}} z + \theta_{\rm mod}\right) dz \\
&= \frac{1}{2}\int_0^{L_{\rm cav}} \cos\left(\frac{(q_{\rm ac} + 2q_{\rm opt})\pi - 2\theta_{\rm mod}}{L_{\rm cav}} z + \theta_{\rm mod}\right) + \cos\left(\frac{(q_{\rm ac} - 2q_{\rm opt})\pi + 2\theta_{\rm mod}}{L_{\rm cav}} z - \theta_{\rm mod}\right) dz \\
&= \frac{1}{2}\Bigg\{ \frac{L_{\rm cav}}{(q_{\rm ac} + 2q_{\rm opt})\pi - 2\theta_{\rm mod}} \sin\left(\frac{(q_{\rm ac} + 2q_{\rm opt})\pi - 2\theta_{\rm mod}}{L_{\rm cav}} z + \theta_{\rm mod}\right)\Big|^z \\
&\qquad + \frac{L_{\rm cav}}{(q_{\rm ac} - 2q_{\rm opt})\pi + 2\theta_{\rm mod}} \sin\left(\frac{(q_{\rm ac} - 2q_{\rm opt})\pi + 2\theta_{\rm mod}}{L_{\rm cav}} z - \theta_{\rm mod}\right)\Big|^z \Bigg\} \qquad (7.30)
\end{aligned}$$

Note that for the same boundary $\theta_{\rm mod} = 0$ case, the expression reduces to

$$\begin{aligned}
\int \delta\rho(z) I(z) dz &\propto \frac{1}{2}\left\{ \frac{L_{\rm cav}}{(q_{\rm ac} + 2q_{\rm opt})\pi} \sin\left((q_{\rm ac} + 2q_{\rm opt})\pi\right) + \frac{L_{\rm cav}}{(q_{\rm ac} - 2q_{\rm opt})\pi} \sin\left((q_{\rm ac} - 2q_{\rm opt})\pi\right) \right\} \\
&= \begin{cases} \frac{1}{2} L_{\rm cav} & \text{if } q_{\rm ac} = 2q_{\rm opt} \\ 0 & \text{if } q_{\rm ac} \neq 2q_{\rm opt} \end{cases} \qquad (7.31)
\end{aligned}$$

where we use $\sin((q_{\rm ac} - 2q_{\rm opt})\pi) \to (q_{\rm ac} - 2q_{\rm opt})\pi$ as $q_{\rm ac} \to 2q_{\rm opt}$ in the first case. This recovers our mode matching condition for modes under the same boundary conditions. In the case where $\theta_{\text{mod}} \neq 0$, we have

$$\begin{aligned} g_{0,\text{mod}}/g_0 &= \frac{1}{(q_{\text{ac}} + 2q_{\text{opt}})\pi - 2\theta_{\text{mod}}} \sin\left((q_{\text{ac}} + 2q_{\text{opt}})\pi - \theta_{\text{mod}}\right) \\ &\qquad + \frac{1}{(q_{\text{ac}} - 2q_{\text{opt}})\pi + 2\theta_{\text{mod}}} \sin\left((q_{\text{ac}} - 2q_{\text{opt}})\pi + \theta_{\text{mod}}\right) \\ &= \frac{1}{(q_{\text{ac}} + 2q_{\text{opt}})\pi - 2\theta_{\text{mod}}} \sin\left(-\theta_{\text{mod}}\right) \cos\left((q_{\text{ac}} + 2q_{\text{opt}})\pi\right) \\ &\qquad + \frac{1}{(q_{\text{ac}} - 2q_{\text{opt}})\pi + 2\theta_{\text{mod}}} \sin\left(\theta_{\text{mod}}\right) \cos\left((q_{\text{ac}} - 2q_{\text{opt}})\pi\right) \end{aligned} \tag{7.32}$$

For odd $q_{\text{ac}} - 2q_{\text{opt}}$, it follows that

$$\begin{aligned} g_{0,\text{mod}}/g_0 &= \sin\left(\theta_{\text{mod}}\right)\left(\frac{1}{(q_{\text{ac}} + 2q_{\text{opt}})\pi - 2\theta_{\text{mod}}} - \frac{1}{(q_{\text{ac}} - 2q_{\text{opt}})\pi + 2\theta_{\text{mod}}}\right) \\ &\to \sin\left(-\theta_{\text{mod}}\right)\frac{1}{(q_{\text{ac}} - 2q_{\text{opt}})\pi + 2\theta_{\text{mod}}} \end{aligned} \tag{7.33}$$

And for even $q_{\text{ac}} - 2q_{\text{opt}}$, we have the same form

$$g_{0,\text{mod}}/g_0 \to \sin\left(\theta_{\text{mod}}\right)\frac{1}{(q_{\text{ac}} - 2q_{\text{opt}})\pi + 2\theta_{\text{mod}}} \tag{7.34}$$

where we assume large q_{ac} and q_{opt} such that $1/(q_{\text{ac}} + 2q_{\text{opt}}) \to 0$.

In figure 7.12, we show the combined coupling contribution modeled in section 7.2.1 and 7.2.2 arising from non-hermiticity and three-dimensional overlap integral by the black hollow circles, which we denote as $g_{\text{fit0}}^{(q',n,m)}$. We then fit the unaccounted for contribution $g_{\text{meas}}^{(q',0,0)} - g_{\text{fit},0}^{(q',0,0)}$ for all even q' to the boundary condition model in the form of equation 7.33, where θ_{mod} is the fitting parameter. The fit-extracted contribution from asymmetric boundary condition is shown by the orange curve in figure 7.12. The model returns a best-fit boundary phase of $\theta_{\text{mod}} = 0.1211 \pm 0.0006$ rad. And the total contributions to the couplings from all sources modeled in this chapter are shown by the blue data points labeled as $g_{\text{fit}}^{(q',n,m)}$.

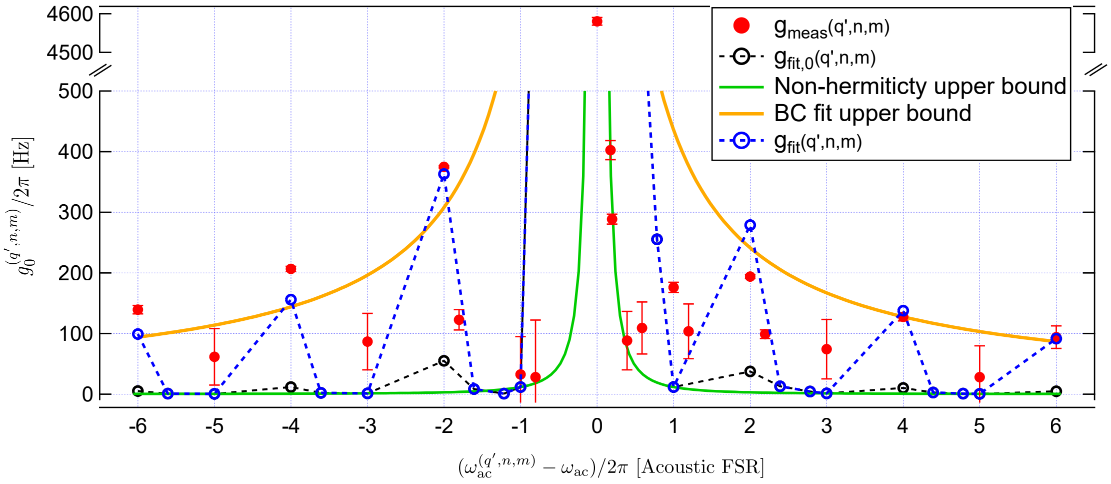

Figure 7.12: Measured couplings are fit to the asymmetric boundary condition model, whose contribution is shown by the asymptotic yellow upper bound with a fit-extracted boundary phase $\theta_{\mathrm{mod}} = 0.1211 \pm 0.0006$ rad. The non-hermiticity bound is shown by the green line, while the black points show the combined contribution from non-hermiticty and the 3D overlap integral. Blue points show the combined contribution from all the sources modeled in this chapter.

Chapter 8

Summary and outlook

8.1 Summary

Appendices

Appendix A

Measurement setup

A.1 Pound-Drever-Hall locking

In this section I will talk about the implementation of the Pound-Drever-Hall (PDH) technique for laser frequency locking in our setup; in particular, it is used for locking the TL to the LFC, the lock tone to the OMC, and the FC1 and FC2 to the lock tone, as discussed in section 4.1. Schematic of generating the error signal of a PDH lock is shown in Figure A.1, where the locking of the lock tone to the OMC via feedback to the MIQM is used as an example.

The lock tone is modulated by the EOM, reflected off the OMC and detected at the OMC PD. The EOM is driven by a local oscillator (LO) at ω_{LO} = 43.7 MHz generated by an arbitrary waveform generator (AWG)[1]. The reflected tone detected at the OMC PD is separated via a bias-tee into a DC part, which is the DC reflected intensity from the OMC, and a RF part. The latter is mixed down with the LO via a mixer, equivalent to comparing the variation in cavity reflection to the variation in lock tone frequency, thus giving information on which side of the cavity resonance the lock tone frequency is at in order to apply correction. Prior to mixing, the RF signal is amplified and passes a phase shifter[2] manually tuned via a control voltage, in order to compensate for the phase difference between the LO and the RF paths due to difference in their path lengths. The mixed-down signal then passes a 10 kHz LPF such that only the small frequency mixed-down signal of interest is preserved as the error signal.

A derivation of the error signal is given in reference [188]. In particular, the DC reflection signal is given by

$$P_{\mathrm{DC}}(\Delta) \propto |\chi_{\mathrm{cav}}(\Delta)|^2 = 1 - \frac{4\eta_\kappa(1-\eta_\kappa)}{1+(2\Delta/\kappa_{\mathrm{cav}})^2} \tag{A.1}$$

as shown by the dashed lines in Figure A.2, where $\chi_{\mathrm{cav}} = 1 - 2\eta_\kappa/(1-2i\Delta/\kappa_{\mathrm{cav}})$ is the cavity susceptibility, κ_{cav} the cavity linewidth, η_κ the cavity input coupling efficiency, and

---

[1] Kooletron signal generator counter; Model: CJDS66.

[2] Mini-Circuits voltage variable phase shifter; Model: TB-122B.

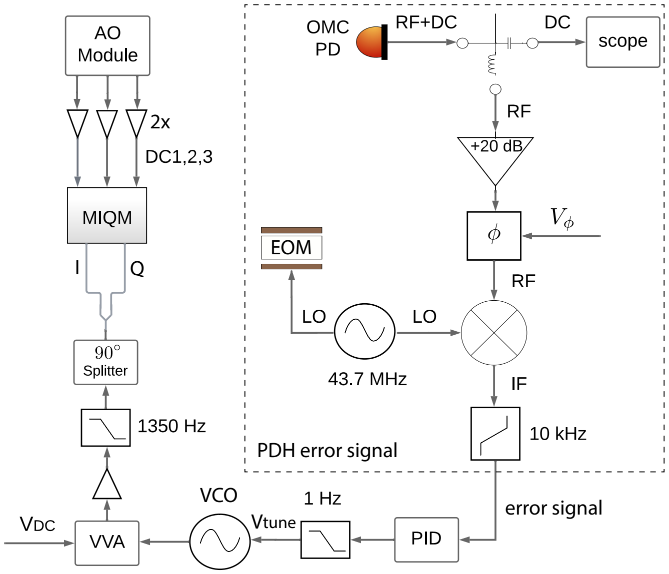

Figure A.1: **Electronic connections for implementing the PDH lock** The error signal is generated by comparing the frequency modulation on the lock tone (via the EOM) and the resulted variation in the reflected intensity from the cavity as detected by the PD.

Δ the lock tone detuning from the cavity resonance.

In the case where the modulation on the lock tone is slow (i.e. locking of the lock tone to the OMC), such that $\kappa_{\text{cav}} \approx \omega_{\text{LO}}$, the modulation can be treated as a small perturbation and expanded to the first order such that the error signal is described by

$$P_{\text{err, slow}}(\Delta) \propto \frac{\partial P_{\text{DC}}}{\partial \Delta} = \frac{\Delta/\kappa_{\text{cav}}}{\left(1+(2\Delta/\kappa_{\text{cav}})^2\right)^2} \tag{A.2}$$

as shown by the solid line in Figure A.2 (left). Finally, in the case where the modulation is fast (i.e. locking of the TL to the refernce cavity LFC, and of the signal filters FC1, FC2 to the lock tone), such that $\kappa_{\text{cav}} \ll \omega_{\text{LO}}$, the error signal is described by

$$P_{\text{err, fast}}(\Delta) \propto \Im|\chi_{\text{cav}}[\Delta]\chi^*_{\text{cav}}[\Delta+\omega_{\text{LO}}] - \chi^*_{\text{cav}}[\Delta]\chi_{\text{cav}}[\Delta-\omega_{\text{LO}}]| \tag{A.3}$$

as shown by the solid line in Figure A.2 (right).

The error signal is sent to a commercial PID controller [3], and the feedback is either sent to the VCO to drive the IQM, or directly to the piezo of the FCs. Note that for the OMC lock, the feedback signal is filtered by a 1 Hz low-pass filter[4], as we observe a ~ 60 Hz self-sustaining oscillation in the OMC locking feedback. The oscillation is most likely caused by a gas column confined in some long cryogenic "tube" subjected to a large temperature gradient in the dilution fridge, which is a thermoacoustic phenomenon known as the Taconis oscillation [189][190]. By adjusting the configuration of various vent ports

---

[3] New Focus PI controller; Model: LB1005.

[4] Stanford Research System low-pass filter; Model: SIM 965.

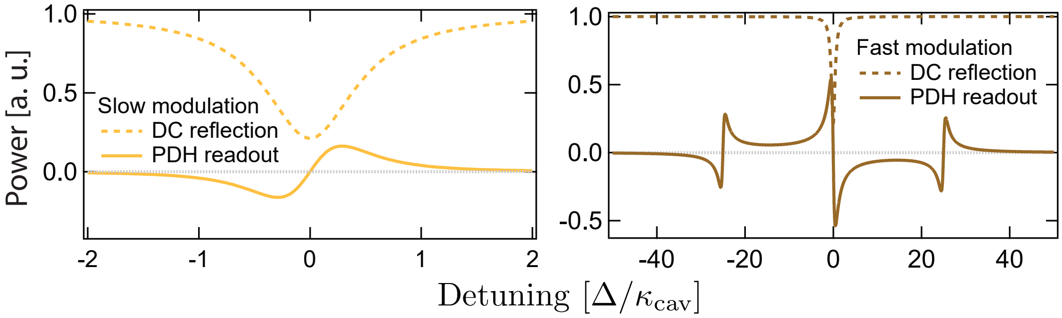

Figure A.2: **Error signal from a standard PDH lock** where the modulation is slow (left) compared to cavity linewidth, and fast (right). The linear steep region in the PDH readout around cavity resonance allows for efficient correction to lock the beam to the zero-crossing.

of the dilution fridge dewar to the atmosphere, the oscillation could be damped to some extent but never completely vanishes. The lock feedback is thus low-pass filtered such that the laser frequency is stably locked to the OMC center frequency without tracking the Taconis oscillation.

A.2 Thermal stabilization and tuning

Main optical components described in section 4.1 are either temperature stabilized to minimize drift in their resonant frequency and phase change, or thermally tuned with active locking feedback.

The FCs (FC1, FC2, LFC) are temperature controlled via thermoelectric cooler elements which are driven by the current produced by a temperature controller (TC)[5]. The temperature is stabilized to within 0.1 Celsius. The reference cavity LFC, which is used to stabilize the TL output frequency, is frequency stabilized to within 15 MHz via temperature control.

The IQMs are temperature stabilized by the same method. Phase shift set in the IQM's interferometric arms could drift over a phase of π on the scale of a day, without temperature stabilization or feedback to its control voltages. Such deviation from operating the IQMs in the SSBCS regime hinders our ability to lock the system for long period of time.

Finally, the broadband noise filter cavities for the drive lasers (BFC, RFC) are thermally tuned. Thermally-controlled FCs consist of a positive temperature coefficient thermistor, whose temperature is tuned by the current source flowing through, thus tuning the cavity length. The temperature controller receives the voltage error correction from a PID module implemented digitally, and converts it into a current to thermally tune the BFC and the RFC[6].

---

[5] Stanford Research System programmable temperautre controller; Model: PTC 10.

[6] BFC and RFC have a temperature response of $\sim$ 10 pm per Celsius. One full FSR of 12.5 GHz corresponds to a temperature change of $\sim$ 10 Celsius.

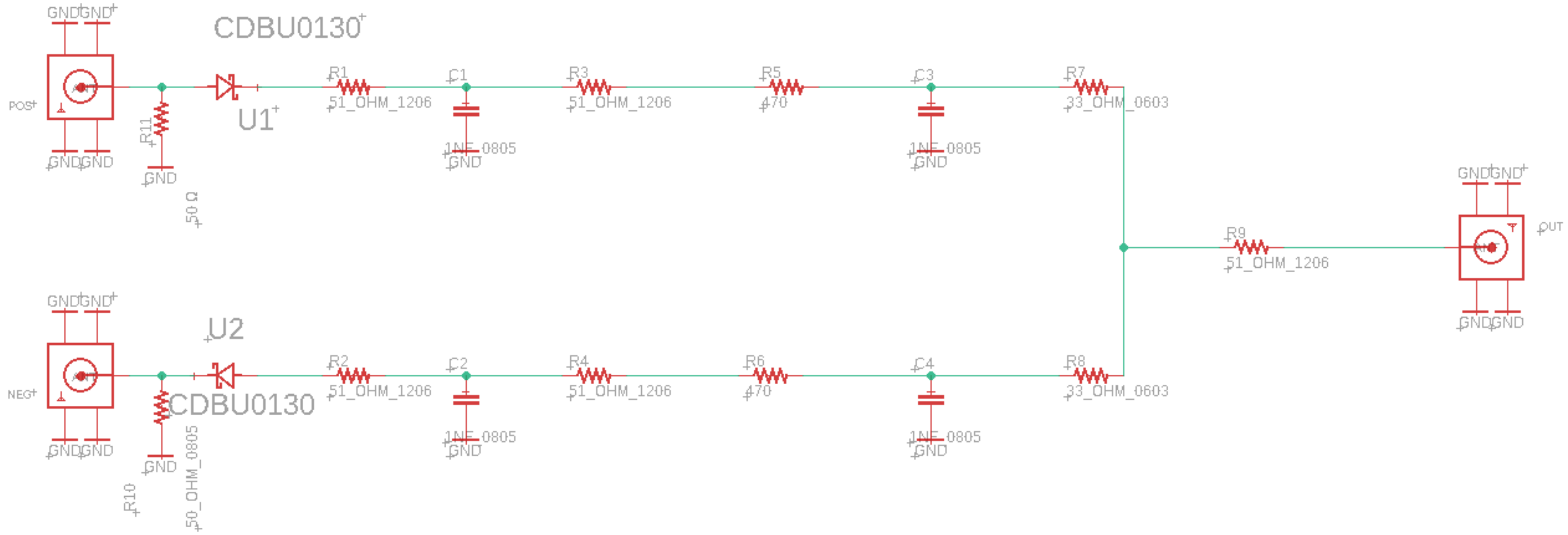

Figure A.3: **FTV circuit design**, which generates the error signal for the drive laser beat lock.

A.3 FTV circuit

The electronic circuit of the frequency-to-voltage (FTV) converter used in the drive laser beat lock setup (section 4.1.2) is shown in Figure A.3. The circuit is manufactured on a printed circuit board and generates a frequency dependent error signal for the beat lock. The design is derived from references [170]. The positive branch takes in the high-pass filtered signal which follows the amplitude response of a HPF with steep cut-off frequency. The negative branch takes in the unfiltered signal, as the circuit converts the AC signal into a negative DC signal with the inverted diode. The combined output from the two branches thus generates an error signal which follows the response of the HPF while having a zero-crossing around the middle of the steep slope, that is, the cut-off frequency of the HPF.

Appendix B

Optomechanical device properties

B.1 Extract optical cavity linewidth

To extract the linewidth and the input coupling efficiency to the optical cavity, we sweep the laser across cavity resonance and fit to its reflection. The reflection is shown in Figure B.1 in dashed line, which is acquired by using the setup described in section 4.1. The laser frequency is modulated with an IQM with a 5 Hz triangular sweep. The normalized reflection is acquired by measuring $P_{\text{DC}} = P_{\text{res}}/P_{\text{bkg}}$, where the background is the off-resonance reflection signal detected. The cavity susceptibility with an input coupling efficiency of η_κ in reflection can be written as

$$\chi_{\text{cav, reflc}}[\Delta] = 1 - \frac{\kappa_{\text{in}}}{\kappa_{\text{c}}/2 - i\Delta} = 1 - \frac{\eta_\kappa \kappa_{\text{c}}}{\kappa_{\text{c}}/2 - i\Delta} \tag{B.1}$$

where $\eta_\kappa = \kappa_{\text{in}}/\kappa_{\text{c}}$ and κ_{in} characterizes the loss through the cavity input port. The normalized DC reflection of the optical cavity is thus

$$P_{\text{DC}}[\Delta] = |\chi_{\text{cav, reflc}}|^2 = 1 - \frac{\eta_\kappa(1-\eta_\kappa)\kappa_{\text{c}^2}}{(\kappa_{\text{c}}/2)^2 + \Delta^2} \tag{B.2}$$

As shown in Figure B.1, we also see an asymmetric Fano signature exhibited in the reflection signal. The asymmetric lineshape arises from the interference between the back reflection and the resonant scattering [191]. Equation B.2 is thus modified to

$$P_{\text{DC}}[\Delta] = 1 - \frac{\eta_\kappa[(\cos\phi + 2\sin\phi(\Delta/\kappa_{\text{c}})) - \eta_\kappa]\kappa_{\text{c}^2}}{(\kappa_{\text{c}}/2)^2 + \Delta^2} \tag{B.3}$$

where an arbitrary phase ϕ is introduced as a fitting parameter to account for the asymmetric lineshape.

Figure B.2 shows the best-fit of the normalized cavity reflection to equation B.2. The fit returns a total damping rate of κ_{c} = 0.00807 ± 0.00002 second. To convert the time sweep as shown in Figure B.2 to a frequency sweep to extract the linewidth in frequency, we calibrate the sweep by using the pair of sidebands created by the EOM used for PDH

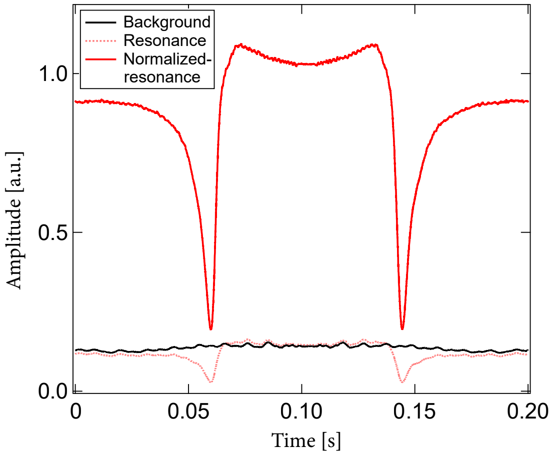

Figure B.1: **Sweep over the optical cavity reflection** used to extract the cavity linewidth.

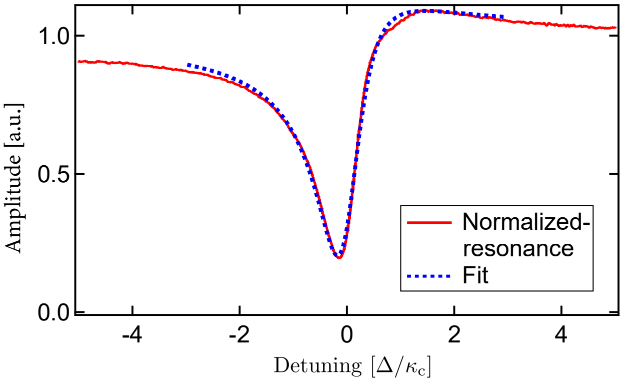

Figure B.2: **Fit to optical cavity reflection,** accounting for the input coupling efficiency and the asymmetric Fano shape. The fit-extracted total cavity damping rate is thus $\kappa_c/2\pi$ = 47.2 ± 0.5 MHz, with an input coupling efficiency η_κ = 0.29 ($\kappa_{in}/2\pi$ = 13.6 ± 0.2 MHz).

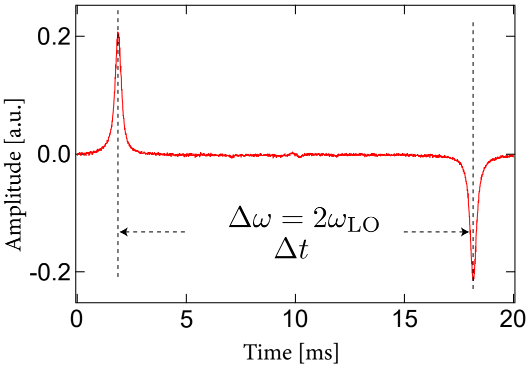

Figure B.3: **Calibration of frequency sweep** using the PDH error signal of the signal filter cavity, where the sidebands created by the EOM show up as two peaks and separated by a frequency of exactly $2\omega_{LO}$.

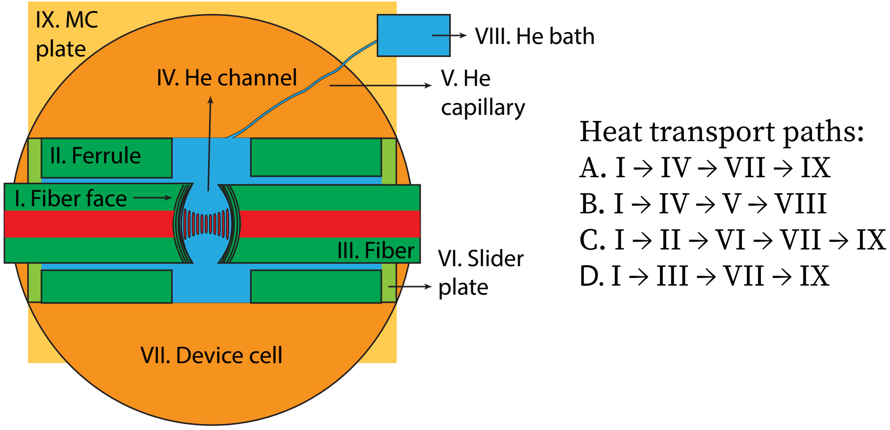

Figure B.4: **Device schematics** showing the various paths through which heat could be transported from the fiber faces to the MC.

locking as described in section A.1. The error signal of the signal filters is used for the calibration, which has the general shape shown in Figure A.2 (right) under the condition $\kappa_{\mathrm{FC}} \ll \omega_{LO}$. We change the phase of the LO until the error signal shows the sidebands as two peaks, which are separated by a time of Δt and a frequency of exactly $2\omega_{LO}$. We thus obtain the time-to-frequency conversion factor of $2\omega_{LO}/\Delta t = 5.854 \times 10^9$ Hz/s here. The fit-extracted total cavity damping rate is thus $\kappa_{\mathrm{c}}/2\pi = 47.2 \pm 0.5$ MHz, with an input coupling efficiency $\eta_\kappa = 0.29$ ($\kappa_{\mathrm{in}}/2\pi = 13.6 \pm 0.2$ MHz).

B.2 Heat transport path of the device

In this section we model the heat transport path from the heated fiber in the optomechanical device to the cold thermal bath of the mixing chamber (MC) of the dilution fridge. By the law of thermal conduction, we model the heat transport by $\dot{Q} = T_{\mathrm{MC}}^{k+1} - T_{\mathrm{fib}}^{k+1}$, where $\kappa_{\mathrm{fib}}(T) \propto T^k$ describes the effective thermal conductivity over the heat transfer path from the fiber face to the large thermal bath cooled to and kept constant at T_{MC}. We show in section 5.3 that the effective temperature at the fiber face is consistent with such a model where $k_{\mathrm{mod}} = 1.09 \pm 0.03$. Since $k = 1$ for metal [140], the model suggests a predominantly metallic conductance between the fiber and the MC. We will further examine the various heat transport paths based on the geometry and setup of our device and compare their thermal conductance with this fit-extracted value.

A simplified top view of the device schematic is shown in Figure B.4. A pair of fibers (III) are inserted through the ferrules (II) to form the Fabry-Perot cavity. The ferrules are epoxied on top of a slider plate (VI), while the slider is epoxied onto the larger device cell (VII). Helium is filled through a thin capillary line (V) from a liquid He bath(VIII). The device cell is then attached to the MC plate (IX) via a gold-plated OFHC copper[1] mount.

---

[1] Oxygen-free high thermal conductivity (OFHC) copper, which is used for the device cell and the cell

The He bath (VIII) is in a sliver sintered chamber. The chamber is in good thermal contact with the MC and acts as a heat exchanger for the He inflow, such that we can assume the He bath is at a constant T_{MC}[38].

We examine the heat transport from the fiber face (I) at T_{fib} to either the MC (IX) or the He bath (VIII) (both at a constant T_{MC}), through the following paths: (A) via the He channel in between the fiber faces (IV) to the device cell (VII) then to the MC; (B) via the He channel (IV) then through the narrow He capillary line (VIII) to the bath (VIII); (C) via the ferrules to the slider, then to the cell; and (D) from the fiber faces through the fibers (III), which are epoxied onto the device cell directly at their far ends (not shown in the figure here).

Heat flow via path A

The heat flow via path A is illustrated in Figure B.5(a), where $T_{\text{He/Cu}}$ is the temperature at the boundary between IV and VII. The device cell (VII) is made of OFHC copper (Cu) as illustrated. In general, the rate of heat flow $\dot{q}$ (per unit area) in a material of cross-section A is given by

$$\dot{q} = \dot{Q}/A = -\kappa \nabla T \tag{B.4}$$

where ∇T is the temperature gradient, and κ the thermal conductivity coefficient. Phonon conductivity dominates the thermal conduction in insulators like helium, which is given by [192]

$$\kappa_{\text{He}} = \frac{1}{3} C_{\text{He}} v_{\text{He}} d_{\text{He}} \frac{2-f}{f} \tag{B.5}$$

in a narrow channel of diameter d_{He}. The specific heat per unit volume $C_{\text{He}} = \frac{2\pi^2 k_{\text{B}}^4}{15\hbar^3 v_{\text{He}}^3} T_{\text{He}}^3$, and helium sound velocity $v_{\text{He}} = 238.25$ m/s [193]. In low temperature, phonons are predominantly scattered by channel boundaries in ^{4}He and we thus assume the fraction of phonons undergoing scattering from the channel walls to be $f = 1$. We then have

$$\kappa_{\text{He}} = \frac{2\pi^2 k_{\text{B}}^4 d_{\text{He}}}{45\hbar^3 v_{\text{He}}^2} T_{\text{He}}^3 = \kappa_{\text{He},0} d_{\text{He}} T_{\text{He}}^3 \tag{B.6}$$

as a function of d_{He} and T_{He}. The heat flow equation in section IV in Figure B.5(a) is thus given by

$$\int_0^{l_{\text{IV}}} \frac{\dot{Q}}{A_{\text{IV}}} dx = \int_{T_{\text{He/Cu}}}^{T_{\text{fib}}} \kappa_{\text{He},0} d_{\text{IV}} T^3 dT \tag{B.7}$$

$$\dot{Q} \frac{l_{\text{IV}}}{d_{\text{IV}} A_{\text{IV}}} = \frac{\kappa_{\text{He},0}}{4} (T_{\text{fib}}^4 - T_{\text{He/Cu}}^4) \tag{B.8}$$

---

mount to the MC [38].

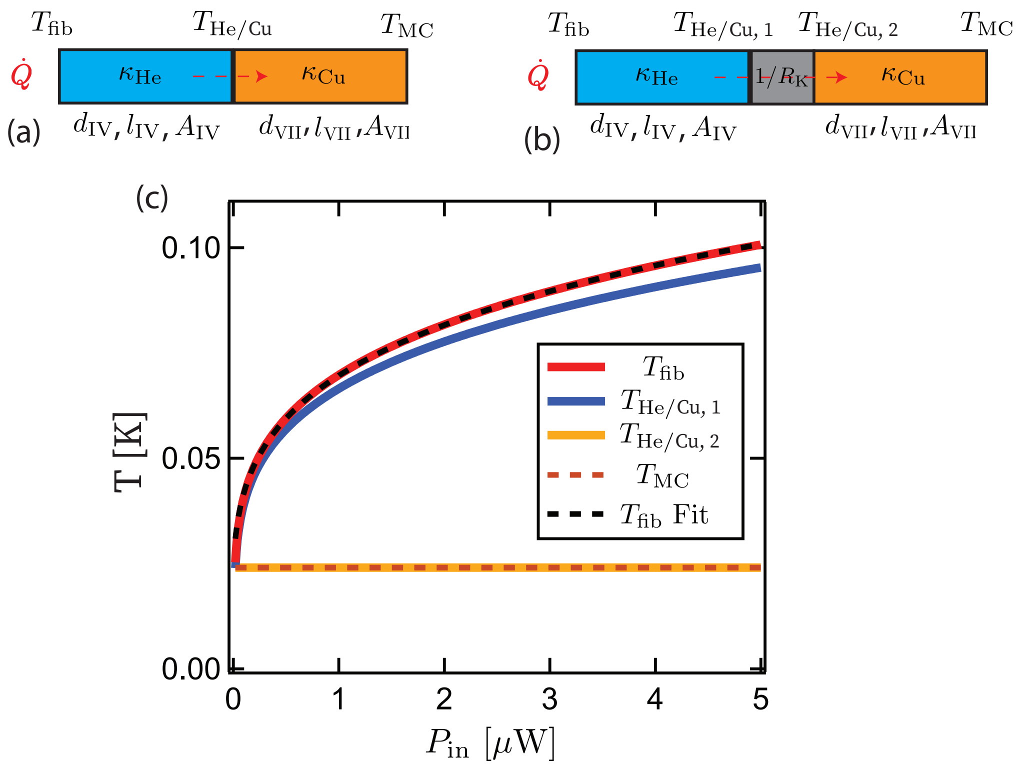

Figure B.5: **Heat path A** (a) Diagram of the heat flow from the fiber to the MC; (b) Heat flow including the Kapitza resistance at He/Cu boundary; (c) Numerically solved temperatures across heat transport path A.

where we have $d_{\text{IV}} = 0.5$ mm, $A_{\text{IV}} = \pi\ (d_{\text{IV}}/2)^2$ and $l_{\text{IV}} = 2.5$ cm.

Similarly we find the heat flow equation in the other section (VII) in Figure B.5(a) where the path goes through the device cell made of Cu. In metal, the electronic thermal conductivity due to conduction electrons is dominant. Specifically for Cu at low temperature, we have $\kappa_{\text{Cu}} = (\text{RRR}/0.76)\ T = \kappa_{\text{Cu,0}}T$, where we take the residual resistivity ratio (RRR) of the cell to be 50 [140]. We thus have

$$\dot{Q}\frac{l_{\text{VII}}}{A_{\text{VII}}} = \frac{\kappa_{\text{Cu,0}}}{2}(T^2_{\text{He/Cu}} - T^2_{\text{MC}}) \tag{B.9}$$

where the device cell geometry is characterized by $d_{\text{VII}} = 10$ mm, $A_{\text{VII}} = \pi\ (d_{\text{VII}}/2)^2$ and $l_{\text{VII}} = 10$ mm.

Note that there also exists a resistance to heat flow across the boundary between different materials, known as the thermal boundary or Kapitza resistance R_{K} [194]. In particular, between a liquid helium and solid interface, a temperature step ΔT_{K} occurs due to the acoustic mismatch of the two materials, impeding the transmission of phonons, and is given by $\Delta T_{\text{K}} = R_{\text{K}}\dot{Q}$. We thus modify the heat flow diagram as shown in Figure B.5(b).

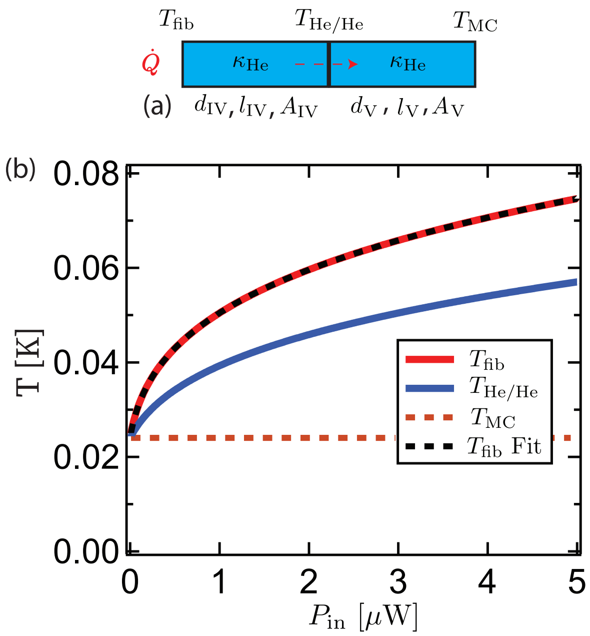

Figure B.6: **Heat path B** (a) Diagram of the heat flow from the fiber to the MC; (b) Numerically solved temperatures across heat transport path B.

Since $R_{\mathrm{K}} = R_{\mathrm{K},0}T^{-3.5}$ for T < 1 K [192], such that

$$\dot{Q} = \frac{1}{R_{\mathrm{K},0}} \int_{T_{\mathrm{He/Cu,2}}}^{T_{\mathrm{He/Cu,1}}} T^{3.5} dT \tag{B.10}$$

$$\dot{Q}\frac{1}{A_{\mathrm{IV}}} = \frac{1}{4.5 \cdot 10^{-3}}(T^{4.5}_{\mathrm{He/Cu,1}} - T^{4.5}_{\mathrm{He/Cu,2}}) \tag{B.11}$$

where we use the empirically determined value $A_{\mathrm{IV}}R_{\mathrm{K}}T^{3.5} \approx 10^{-3}$ $[\mathrm{m^2K^{4.5}W^{-1}}]$ [140]. Combining equation B.8, B.9, B.11, we numerically solve for temperatures T_{fib}, $T_{\mathrm{He/Cu,1}}$, $T_{\mathrm{He/Cu,2}}$ as a function of $\dot{Q}$ (P_{in} from 0 to 5 μW) using $T_{\mathrm{MC}} = 24$ mK determined in section 5.3, as shown in Figure B.5(c) (red, blue yellow respectively). Most of the temperature drops occurs across the He/Cu boundary.

To compare to the fiber temperature and the effective thermal conductivity coefficient k_{mod} extracted from the model presented in section 5.3, we fit the numerically solved T_{fib} to equation 5.23, such that

$$T_{\mathrm{fib}} = (T^{k_{\mathrm{A}}+1}_{\mathrm{MC}} + \beta^{k_{\mathrm{A}}+1}P_{\mathrm{in}})^{1/(k_{\mathrm{A}}+1)} \tag{B.12}$$

where β and k_{A} are the fitting parameters. β accounts for the amount of optical power contributing to the absorptive heating of the fibers. The fit returns k_{A} = 3.320 ± 0.005, describing the overall temperature dependence of the thermal conduction over path A, and is in between $k_{\mathrm{He}} = 3$ and $k_{\mathrm{Kapitza}} = 3.5$. This is distinct from $k_{\mathrm{mod}} = 1.09 \pm 0.03$, and

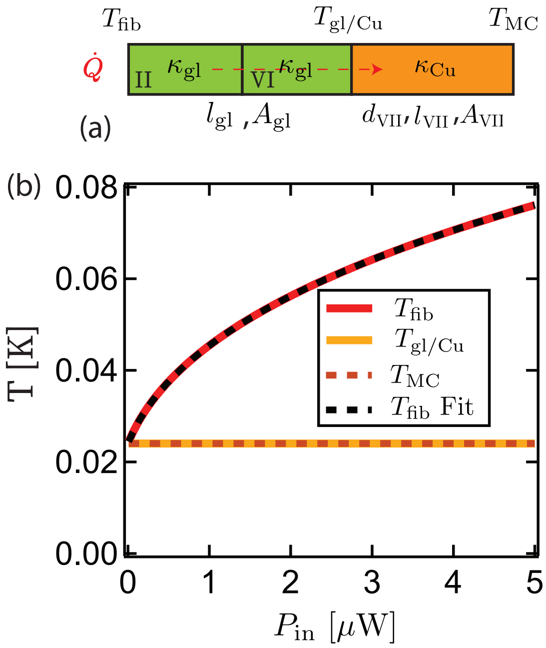

Figure B.7: **Heat path C** (a) Diagram of the heat flow from the fiber to the MC; (b) Numerically solved temperatures across heat transport path C.

indicates that path A is not the main path through which heat is transported.

Heat flow via path B

The heat flow via path B is illustrated in Figure B.6(a), where $T_{\mathrm{He/He}}$ is the temperature at the boundary between the He channel and the capillary (IV and V). Modifying equation B.7, we numerically solve for the temperatures along path B via the following equations

$$\dot{Q}\frac{l_{\mathrm{IV}}}{d_{\mathrm{IV}}A_{\mathrm{IV}}} = \frac{\kappa_{\mathrm{He},0}}{4}(T_{\mathrm{fib}}^4 - T_{\mathrm{He/He}}^4) \tag{B.13}$$

$$\dot{Q}\frac{l_{\mathrm{V}}}{d_{\mathrm{V}}A_{\mathrm{V}}} = \frac{\kappa_{\mathrm{He},0}}{4}(T_{\mathrm{He/He}}^4 - T_{\mathrm{MC}}^4) \tag{B.14}$$

where we estimate the geometry of the capillary line with $d_{\mathrm{V}} = 1$ mm, $A_{\mathrm{V}} = \pi\ (d_{\mathrm{V}}/2)^2$ and $l_{\mathrm{V}} = 10$ cm. The results are shown in Figure B.6(b). And by fitting the numerically solved T_{fib} from path B to equation B.12 we obtain $k_{\mathrm{B}} = 3.00014 \pm 7\times10^{-6}$, agreeing with the temperature dependence of He conductivity at low temperature as expected.

Heat flow via path C

The heat flow via path C is illustrated in Figure B.7(a), where the heat flows from the fiber face to the ferrule (II) and slider (VI), then to the Cu cell (VII), and finally to the MC.

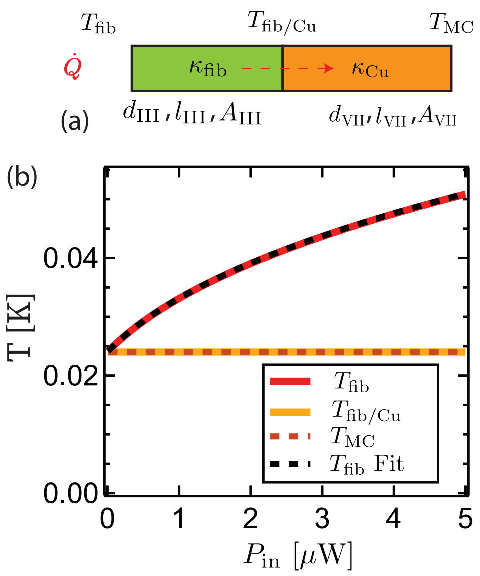

Figure B.8: **Heat path D** (a) Diagram of the heat flow from the fiber to the MC; (b) Numerically solved temperatures across heat transport path D.

Here we assume the ferrule and slider as a single piece made of glass with conductivity coefficient κ_{gl}, and $T_{\text{gl/Cu}}$ is the temperature at the boundary between VI and VII.

For the first portion of path C, we use the thermal conductivity of glass BK7 which has a temperature dependence of $\kappa_{\text{gl}} = \kappa_{\text{gl},0} T^{1.85}$, where $\kappa_{\text{gl},0} = 0.02$ [Wm^{-1}K$^{-2.85}$] below 1 Kelvin [140]. The heat flow equation is thus given by

$$\dot{Q}\frac{l_{\text{gl}}}{A_{\text{gl}}} = \frac{\kappa_{\text{gl},0}}{2.85}(T_{\text{fib}}^{2.85} - T_{\text{gl/Cu}}^{2.85}) \tag{B.15}$$

where we take $l_{\text{gl}} = 3.5$ mm and $A_{\text{gl}} = 2$ mm $\cdot$ 2 mm. The heat flow equation in the second portion has the same form as equation B.9, such that

$$\dot{Q}\frac{l_{\text{VII}}}{A_{\text{VII}}} = \frac{\kappa_{\text{Cu},0}}{2}(T_{\text{gl/Cu}}^{2} - T_{\text{MC}}^{2}) \tag{B.16}$$

We thus numerically solve for the temperatures along path C as shown in Figure B.7(b). The temperature drop mostly occurs in the glass portion of the path, and a fitting to equation B.12 yields a conductivity coefficient $k_{\text{c}} = 1.61 \pm 0.01$, close to the value of BK7 glass (1.85).

Heat flow via path D

Finally for path D, we show the heat flow diagram in Figure B.8(a), where the heat is transported via the fiber (III) directly to the Cu cell (VII). We use the thermal conductivity of fused silica for the optical fiber which has a temperature dependence of $\kappa_{\text{fib}} = \kappa_{\text{fib},0} T^{1.91}$, where $\kappa_{\text{fib},0} = 0.0248$ [Wm^{-1}K$^{-2.91}$] below 1 Kelvin [140]. The heat flow equation is thus

k_A via heat path A	3.320 ± 0.005
k_B via heat path B	$3.00014 \pm 7\times10^{-6}$
k_C via heat path C	1.61 ± 0.01
k_D via heat path D	1.8482 ± 0.0001
k_mod from section 5.3 model	1.09 ± 0.03
k_He	3
k_Cu	1
k_Kapitza	3.5
k_fib	1.91
k_glass	1.85

Table B.1: k-values of the temperature dependence of the thermal conductivity of the device, transporting heat from the fiber faces to the cold thermal bath.

given by

$$\dot{Q}\frac{l_\text{III}}{A_\text{III}} = \frac{\kappa_\text{fib,0}}{2.91}(T_\text{fib}^{2.91} - T_\text{fib/Cu}^{2.91}) \tag{B.17}$$

where we take $l_\text{III} = 5$ cm and $A_\text{III} = \pi(d_\text{III}/2)^2$ with the core of fiber having $d_\text{III} = 125$ μm. Combining with equation B.16, we show the numerically solved temperature along path D in Figure B.8(b). The temperature drop mostly occurs along the fiber and the thermal conduction is dominant by the fiber conductivity. A fit to equation B.12 yields $k_\text{D} = 1.8482 \pm 0.0001$.

The k-values determined through various models are summarized in Table B.1. We do not identify an exact path where the thermal conduction is dominant by metal as predicted by the section 5.3 model with k_mod. Path C going through a combination of glass and metal is the closest approximation.

B.3 Optomechanically induced transparency/amplification

In this section, we characterize the acoustic mode and the optomechanical coupling with the well-known technique called optomechanically induced transparency or amplification (OMIT/A) [195]. As illustrated in Figure B.9, two optical tones (a strong control tone and a weak probe) are sent into the cavity which produce a beat note at frequency ω_ac, hence effectively driving it. The driven acoustics imprints a pair of sidebands around the control tone, where one of them is coherent with the probe beam. As they interfere either constructively or destructively, the amplitude of the probe tone is modified. The tones are set up such that the probe tone is around the optical cavity resonance which can be treated as a perturbation to the optical mode. The change in the probe tone amplitude depends on the acoustic susceptibility and is imprinted onto the optical readout of the cavity. We thus directly measure the spectrum of the optical response via a heterodyne detection, which provides a characterization of the acoustics independent of the single photon counting measurement.

It can be shown that the optical readout with the probe beam can be described with a modified effective cavity susceptibility [2]

$$\chi_{\mathrm{c,eff}}[\Delta_\mathrm{p}] = \chi_\mathrm{c}[\Delta_\mathrm{c}+\Delta_\mathrm{p}]\left(1-|g_0|^2 n_\mathrm{c}\chi_\mathrm{c}[\Delta_\mathrm{c}+\Delta_\mathrm{p}](\chi_{\mathrm{ac,eff}}[\Delta_\mathrm{p}]-\chi^*_{\mathrm{ac,eff}}[-\Delta_\mathrm{p}])\right) \tag{B.18}$$

where Δ_c is the detuning from the control tone to the cavity at ω_c, Δ_p the detuning from the probe tone to the control tone and $\chi_{\mathrm{ac,eff}}$ the effective acoustic susceptibility derived in equation 2.38. Note that since $\chi_\mathrm{c}[\omega]$ centers at zero, only the situations where Δ_c and Δ_p are of opposite signs are relevant as shown in Figure B.9. And since $\chi_{\mathrm{ac,eff}}$ centers at $\omega_{\mathrm{ac,eff}}$, we have

$$\chi_{\mathrm{c,eff}}[\Delta_\mathrm{p}] = \chi_\mathrm{c}[\Delta_\mathrm{c}+\Delta_\mathrm{p}]\left(1-\frac{|g_0|^2 n_\mathrm{c}\chi_\mathrm{c}[\Delta_\mathrm{c}+\Delta_\mathrm{p}]}{\gamma_{\mathrm{ac,eff}}/2-i(\Delta_\mathrm{p}-\omega_{\mathrm{ac,eff}})}\right) \tag{B.19}$$

for a positive Δ_p (lower control tone), and

$$\chi_{\mathrm{c,eff}}[\Delta_\mathrm{p}] = \chi_\mathrm{c}[\Delta_\mathrm{c}+\Delta_\mathrm{p}]\left(1+\frac{|g_0|^2 n_\mathrm{c}\chi_\mathrm{c}[\Delta_\mathrm{c}+\Delta_\mathrm{p}]}{\gamma_{\mathrm{ac,eff}}/2+i(\Delta_\mathrm{p}+\omega_{\mathrm{ac,eff}})}\right) \tag{B.20}$$

for a negative Δ_p (upper control tone) respectively. The former results in an induced transparency or a reduced amplitude, while the latter results in an induced amplification or an increased amplitude. The change in the cavity susceptibility feature is described by the narrow Lorentzian of the acoustic mode characterized by $\gamma_{\mathrm{ac,eff}}$ and $\omega_{\mathrm{ac,eff}}$, and the change in its amplitude is proportional to the optomechanical coupling.

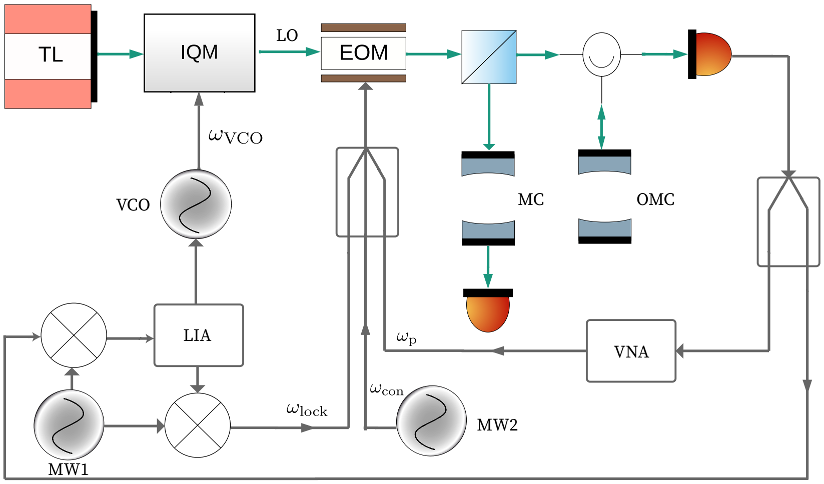

Figure B.10: Schematic for the OMIT/A measurement setup.

---

[2] A detailed derivation of the OMIT/A feature is given in [39] and [195].

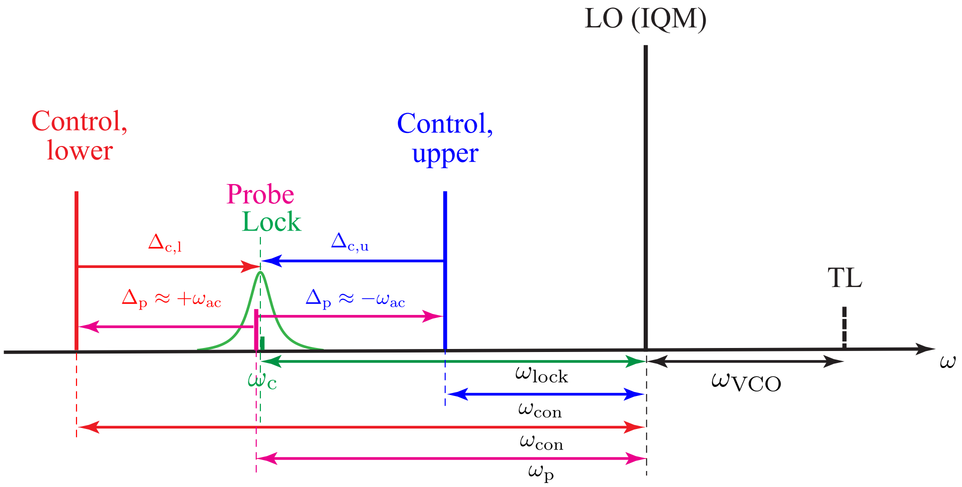

Figure B.9: **Schematic for an OMIT/A measurement** showing the frequencies of the optical tones required, including a lock tone, a probe tone and a control tone, which are produced by a phase modulator as the sidebands of the LO.

The setup for the OMIT/A measurement is shown in Figure B.10. The laser (TL) output is modulated by an IQM operating in the SSBCS regime, and the downshifted tone is used as the LO. The lock, control and probe tones are then generated by the EOM by sending a microwave signal to the EOM for each tone. The lock tone ($\omega_{\text{lock}}/2\pi = 2100$ MHz) is created by mixing up a 1900 MHz signal output by a signal generator (MW1[3]) with a 200 MHz signal output by a lock-in amplifier (LIA[4]). The LO is then locked with respect to the cavity via the PDH technique. The cavity reflection is down-mixed with the MW1 signal and sent to the LIA, which generates the feedback signal to the VCO that outputs ω_{VCO}. The control tone is generated by MW2[5] and is detuned from the cavity by Δ_c. For an OMIT measurement, we use a lower control tone and varies $\Delta_{c,l}$ from $-\omega_{ac} - 2\kappa_c$ to $-\omega_{ac} + 2\kappa_c$ ($\omega_{\text{con}}/2\pi \sim 1785$ MHz). For an OMIA measurement, we use an upper control tone and varies $\Delta_{c,u}$ from $+\omega_{ac} - 2\kappa_c$ to $+\omega_{ac} + 2\kappa_c$ ($\omega_{\text{con}}/2\pi \sim 2415$ MHz). Finally the probe tone is generated by a vector network analyzer (VNA)[6] at frequency ω_p such that Δ_p is around $\pm\omega_{ac}$. The PD output is then sent to the VNA to detect the reflected signal at frequency ω_p, which is the beatnote between the prompt-reflected LO and the probe tone subject to optomechanical interaction. At each control tone detuning, we capture a VNA sweep that is $2\pi{\cdot}50$ kHz around $\omega_{\text{con}} \mp \omega_{ac}$ to acquire the amplitude and the phase information from the complex amplitude of the reflected probe tone around the OMIT/A feature. The optical power of these tones are calibrated by monitoring the transmission of the EOM output through the monitor cavity (MC).

An example of a VNA sweep of the reflected beatnote in an OMIT measurement is shown in Figure B.11, where the horizontal axis is the detuning from the optical cavity

---

[3] Vaunix digital RF signal gerator LMS-402.

[4] Zurich UHFLI lock-in amplifier; Power: -34 dBm output.

[5] Vaunix digital RF signal gerator LMS-402.

[6] Vector network analyzer; Model: HP 8722D; Power: -23 dBm

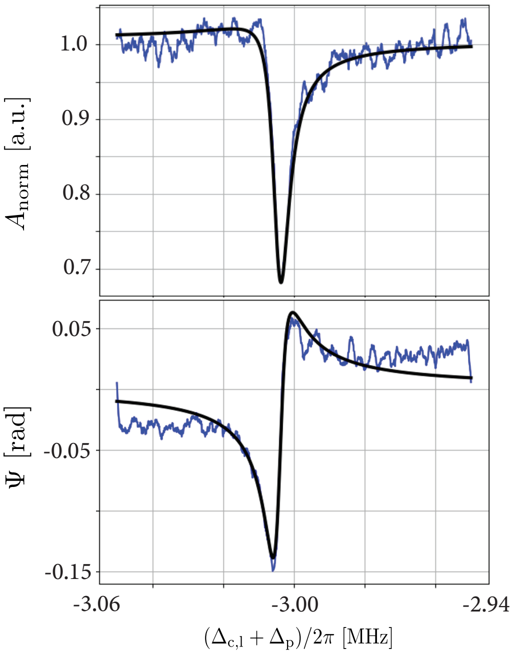

Figure B.11: An example of a VNA sweep in an OMIT measurement and the corresponding complex Lorentzian fit.

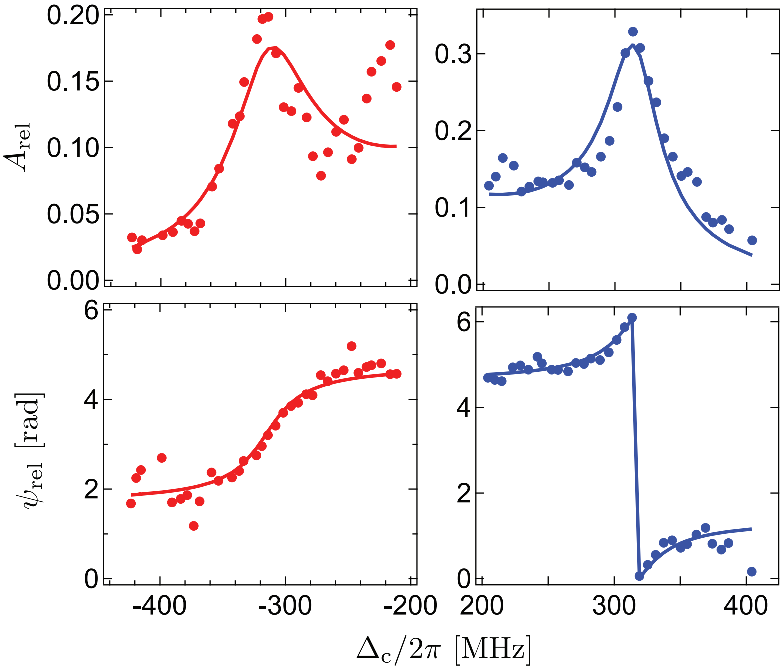

Figure B.12: Fit to the OMIT/A signature at various control detunings which extracts the optomechanical coupling.

$\Delta_c + \Delta_p$. Based on equation B.19 and B.20, the sweep is fit to a complex Lorentzian

$$a_{\text{p,reflc}}[\omega] = a_{\text{bkg}} + \frac{a_{\text{OMIT}}}{\gamma_{\text{ac,eff}}/2 - i(\omega - \omega_{\text{ac,eff}})}) \tag{B.21}$$

where $\gamma_{\text{ac,eff}}$, $\omega_{\text{ac,eff}}$, a complex background $a_{\text{bkg}} = A_{\text{bkg}} e^{i\phi_{\text{bkg}}}$ and a complex amplitude characterizing the OMIT/A feature $a_{\text{OMIT}} = A_{\text{OMIT}} e^{i\phi_{\text{OMIT}}}$ are the fitting parameters. Fits shown in Figure B.11 are normalized with respect to the background .

By acquiring such sweeps at different Δ_c on both sides and the corresponding fit-extracted parameters, we obtain Figure B.12 where the left (right) panel corresponds to the OMIT (OMIA) measurement. Relative amplitudes ($A_{\text{rel}} = |2A_{\text{OMIT}}/A_{\text{bkg}}\gamma_{\text{ac,eff}}|$) and phases ($\psi_{\text{rel}} = \phi_{\text{OMIT}} - \phi_{\text{bkg}}$) obtained from equation B.22 are shown as a function of Δ_c. They are fit to

$$a_{\text{rel}}(\Delta_c) = \frac{-n_c(g_0 + ig_{\text{th}})}{\gamma_{\text{ac,eff}}/2} \frac{1}{\kappa_c - i(\Delta_c + \omega_{\text{ac,eff}})} \tag{B.22}$$

where $a_{\text{rel}} = A_{\text{rel}} e^{i\psi_{\text{rel}}}$. And the photothermal coupling g_{th} is a term to account for an additional driving force on the acoustic mode due to the absorptive heating on the fiber mirror coatings, which creates fluctuation in the fiber and helium boundary [7]. The fit returns $g_0/2\pi = 4700 \pm 30$ Hz. The corresponding damping and spring effects are shown in Figure B.13 with a $\gamma_{\text{ac}}/2\pi = 4460$ Hz and $\omega_{\text{ac}}/2\pi = 315.375$ MHz.

B.4 Extracted bare acoustic linewidth

The bare acoustic linewidth γ_{ac} at base fridge temperature ($\sim$ 20 mK) is extracted via several methods presented in this work.

In section 5.4.1, γ_{ac} is extracted via optemechanical parametric instability where the acoustic rings up beyond the threshold of optomechanical amplification. We measure $\gamma_{\text{ac}}/2\pi = 3250 \pm 20$ Hz as summarized in table B.2. During the ringdown following the ringup stage, we measure $\gamma_{\text{ac}}/2\pi = 3240 \pm 10$ Hz in section 5.4.2. From the time decay of high-order phonon coherences measurements, we extract $\gamma_{\text{ac}}/2\pi = 3307 \pm 8$ Hz as shown in figure 6.13.

Similarly to the acoustic ringdown measurement following parametric amplification in section 5.4.2, we use the AOM and the setup in figure 7.1 to drive the acoustic directly via a beat tone at ω_{ac} and measure the mechanical decay rate during its ringdown. The RF drive applied to the AOM is switched on and off to control the drive on the acoustics. For each pulse cycle, the AOM drive is turned on for 2 ms for the driven acoustics to reach its steady state. It is then turned off for 6 ms during which the acoustic mode rings down. A

---

[7] See section 5.5 of [38] and section 7.3 of [39] for a full description and derivation of the photothermal coupling. It is characterized as a purely imaginary component in the optomechanical coupling and only exhibits in the phase information of the optical readout as shown in Figure B.12. The force modifies the acoustic mode equations of motion only, resulting in a very small change in its self-energy and effective mode number. It is negligible for the single photon counting experiment discussed in this work.

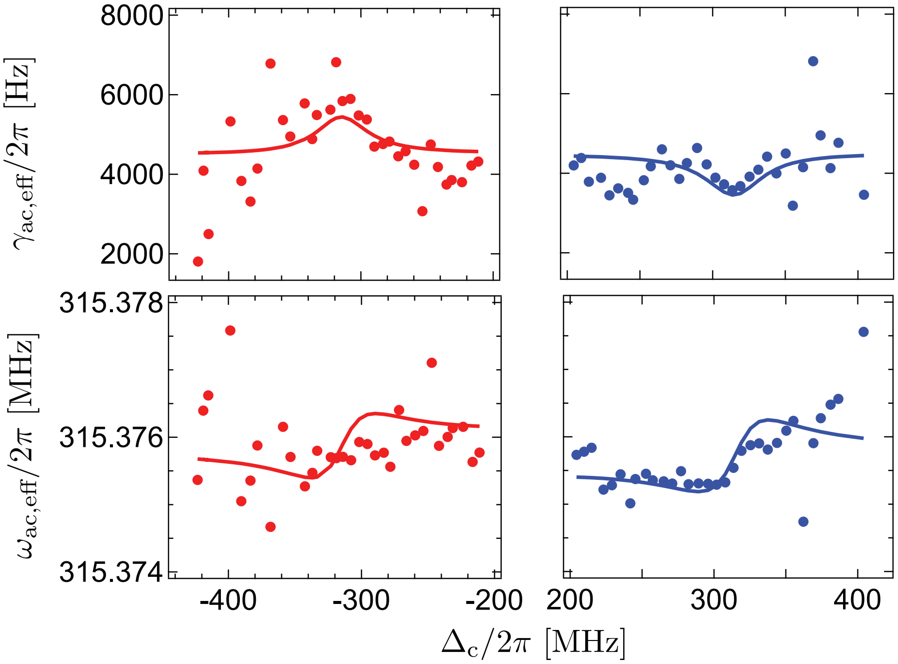

Figure B.13: Dynamical backaction in the OMIT/A measurements showing the optical damping and spring effects.

Measurement	$\gamma_{\mathrm{ac}}/2\pi$ [Hz]
Parametric instability ringup (5.4.1)	3250 ± 20
Acoustic ringdown (5.4.2)	3240 ± 10
Phonon coherences (6.3.3)	3307 ± 8
AOM sweep of the acoustics (B.4)	3504 ± 15
AOM ringdown (B.4)	3490 ± 10

Table B.2: Bare acoustic linewidth at base dilution fridge temperature γ_{ac} extracted via various methods.

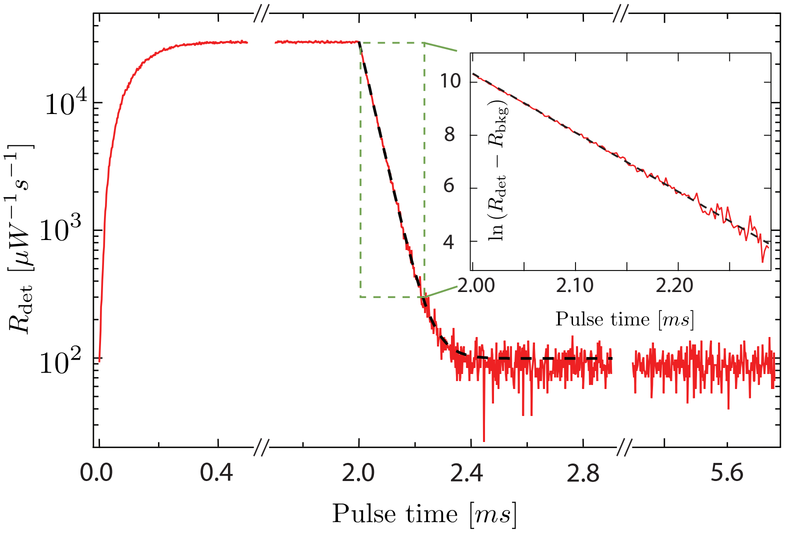

Figure B.14: Detected sideband count rates scattered by the acoustic state as it rings up and rings down controlled by an AOM drive. γ_{ac} is extracted from the transient during ringdown, and fit to equation B.24 is shown in black.

1 μW probe tone is constantly sent to the cavity to measure the sideband count rate and its dynamics during the acoustic ringup and ringdown (the measurement tone setup is the same as shown in figure 7.2). A typical measurement averaged over $> 10^4$ cycles is shown in figure B.14. During ring down, we have

$$R_{\text{det}} = R_{\text{bkg}} + R_{\text{AS}}e^{-(t-t_0)\gamma_{\text{ac}}} \tag{B.23}$$

where R_{bkg} is the steady-state count rate measured when the acoustic returns to the undriven thermal state, taken as the average count rate detected from pulse time $t = 4$ ms to $t = 6$ ms, $t_0 = 2$ ms at which the ringdown begins, and γ_{ac} is a fitting parameter. The log of the background-subtracted sideband counting rate is shown in the inset, which follows the linear form of

$$\ln(R_{\text{det}} - R_{\text{bkg}}) = \ln(R_{\text{AS}}) - (t - t_0)\gamma_{\text{ac}} \tag{B.24}$$

The fit to equation B.24 is shown as the dotted black line.

We repeat the ringdown measurements for various AOM drive powers. The extracted γ_{ac} are shown in figure B.15 (black), where we characterize the drive power by the parameter $\langle n_{\text{d}}\rangle/\langle n_{\text{th}}\rangle$. $\langle n_{\text{d}}\rangle$ is the mean phonon number of the driven state, and $\langle n_{\text{th}}\rangle$ is the mean phonon number of the thermal state, which are proportional to the detected sideband count rate at steady state of the driven state.

With the AOM drive, we also directly acquire the count rate spectrum of the driven acoustic mode. As the AOM drive is swept around ω_{ac}, an example of the count rate spectrum is shown in figure B.16, where the AOM drive frequency ω_{d} is stepped in 100 Hz intervals, and a 0.1 μW probe at a constant detuning of $-\omega_{\text{ac}}$ (from the cavity resonance)

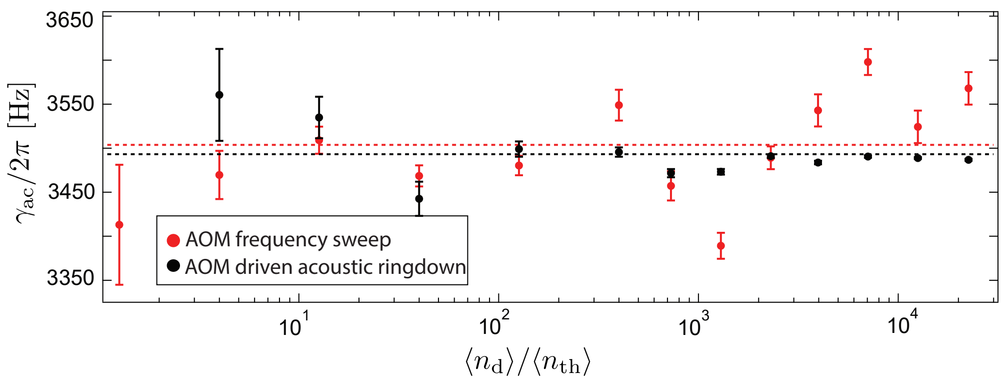

Figure B.15: Fit-extracted bare γ_{ac} at various AOM drive powers from (1) the counting spectrum (red) given by equation B.25 and (2) the ringdown (black) given by equation B.24 of an AOM driven acoustic state.

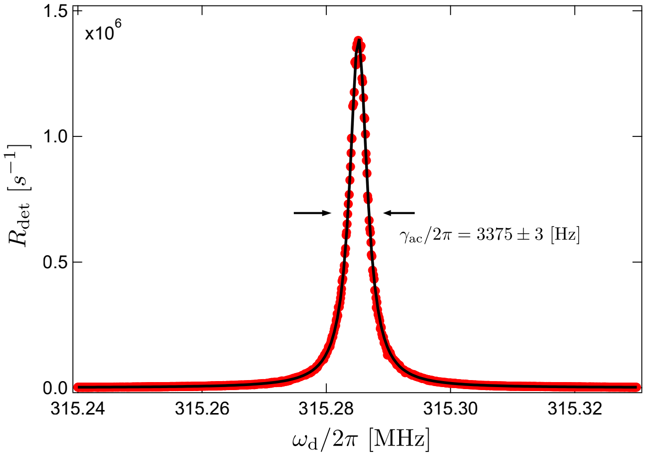

Figure B.16: Counting spectrum of an AOM driven acoustic state. Black line shows the fit to a Lorenztian where γ_{ac} is the fitting parameter.

is used to read out the cavity response. Since the cavity damping rate $\kappa_{\mathrm{c}} \gg \gamma_{\mathrm{ac}}$, the change in cavity susceptibility is negligible across the linewidth of the acoustics and the spectrum of the acoustic mode can be fit to the simple Lorentzian form

$$R_{\mathrm{det}} = R_{\mathrm{bkg}} + \frac{R_{\mathrm{AS}}}{1 + 2((\omega_{\mathrm{AOM}} - \omega_{\mathrm{ac}})/\gamma_{\mathrm{ac}})^2} \tag{B.25}$$

where R_{bkg}, R_{bkg} and γ_{ac} are the fitting parameters. The AOM frequency sweep is repeated at various AOM drive powers, and the corresponding extracted γ_{ac} are summarized in figure B.15 (red).

Appendix C

Phonon coherence

C.1 Poisson distributed background photons

We derive and demonstrate in chapter 6 that for a thermal state, the coherence functions show the anti-bunching signature at zero time delay such that $g^{(l)}(\mathbf{0}) = l!$. On the other hand, for a coherent state, a Poisson photon distribution is expected such that the photon arrivals are uncorrelated with a stable average rate of arrival as discussed in chapter 2.3. We show here that the laser source indeed has a $g^{(2)}(0) = 1$ corresponding to a Poissonian distribution, as opposed to that of a thermal state. We use this conclusion in section 6.2.2 for subtracting background counts from the measurement of phonon coherences of a thermal state, where we assume the background photons are uncorrelated with each other and $\langle \hat{\xi}^\dagger(0)\hat{\xi}^\dagger(\tau)\hat{\xi}(\tau)\hat{\xi}(0)\rangle = \langle \hat{\xi}^\dagger\hat{\xi}\rangle^2$.

In figure C.1, we show the measurement of the photon coherences of our drive laser source $g^{(2)}_{\text{laser}}$. The time delay histogram is fit to the $A + Be^{-\gamma\tau}$ form, which returns a $g^{(2)}(0) = 1 + B/A = 1.011 \pm 0.006$. This is in agreement with the expected form for a coherent source. In comparison, the coherence of a thermal acoustic state is shown, where the background subtraction is done with the premise that the arrivals of background photon counts are uncorrelated with each other. For a coherent source, we thus have random photons where $g^{(2)}(\tau_1) = g^{(2)}(\tau_2)$ for any τ_1 and τ_2. The photon counts are Poisson distributed such that $g^{(2)}(0) = 1$. For a thermal state, we have anti-bunching photons where $g^{(2)}(\tau_1) > g^{(2)}(\tau_2)$ for any $\tau_1 < \tau_2$. The counts are super-Poisson distributed such that $g^{(2)}(0) > 1$.

C.2 Sources of false counts

The sideband photon correlations are computed with proper background subtraction as introduced in section 6.2.2, where the presence of a stable flux of uncorrelated background photons is corrected for, including SPD dark counts, leakage from the environment, and photon leakage through the filter cavities. In this section, I will briefly discuss the additional filtering done on the detected photon counts during the analysis, which we recognize

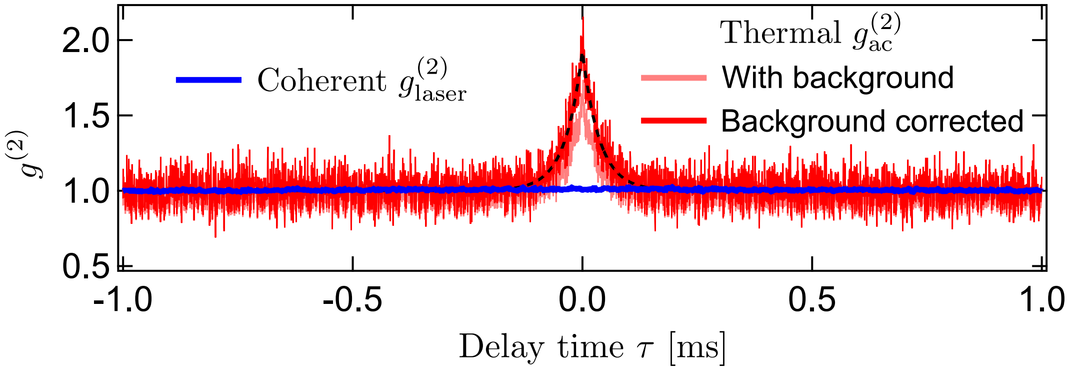

Figure C.1: $g^{(2)}$ of a coherent laser source is shown with $g^{(2)}(0) = 1.011 \pm 0.006$, agreeing with that of a Poisson distribution. The coherence of a thermal acoustic state is shown in comparison with $g^{(2)} = 2$, where the background subtraction is done with the premise that the arrivals of background photon counts are uncorrelated with each other.

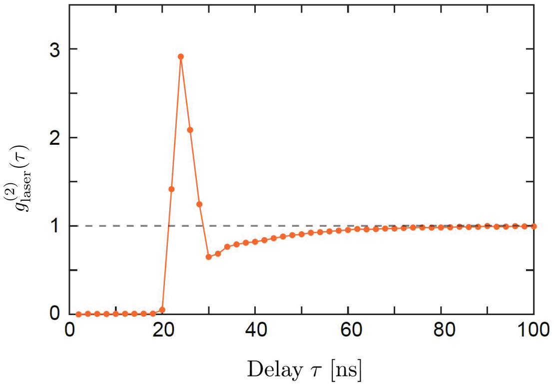

Figure C.2: Afterpulsing in $g^{(2)}_{\text{laser}}$, where a sharp feature is detected at $\tau_{\text{ap}} \approx 24$ ns. The delay histogram is binned by 2 ns step. $g^{(\tau)}_{\text{laser}}$ decays back to 1 for $\tau > 50$ ns.

as the false counts registered by the SNSPDs arising from SNSPD afterpulses and rapid bursts.

Afterpulsing is a well-known source of false counts registered by a SNSPD. It is the reflection of the electrical signal generated by real photon counts or dark photon counts (random and independent detection events registered falsely with no photon source). When a single photon is absorbed and breaks superconductivity of the nanowire, a voltage pulse is generated and then amplified in the readout circuit to be detected. An afterpulse is generated by the reflection of the amplified voltage from the circuit, and is likely to occur at some fixed time ($\sim$ 100 ns) following a detection event [196] [197].

We observe the phenomenon of afterpulsing from the measurement of coherence function of a coherent laser source. $g^{(2)}_{\text{laser}}(\tau)$ is shown with a fine bin size of 2 ns to examine its behavior at small time delay on the $\sim$ 100 ns scale in figure C.2. A sharp feature is observed at around $\tau_{\text{ap}} \approx 24$ ns, which decays back to $g^{(2)}_{\text{laser}}(\tau) = 1$ for $\tau > 50$ ns as expected for a coherent source. We speculate this feature is mostly likely due to the afterpulsing effect, which occurs at τ_{ap} after a real or dark photon detection event for our SNSPDs and readout circuit.

To filter out such afterpulsing events, we simply remove any photon detection events 50 ns within each other. This does not compromise our measurement result as the smallest time delay used in this work is $\tau = 0^+ \rightarrow\ 1\mu$s.

We observe another main source of false counts which are the rapid bursts of photon detection that occur at abnormally high rate for short duration (10-100 μs). We develop a criteria to determine whether the count rate is abnormal. We measure the mean count rate during an experiment to be R. The probability of detecting k photons in some time interval Δt can be described by some model $P(k, \lambda = R\Delta t)$. Suppose there are N number of Δt intervals in an experiment, the expected number of intervals during which k photons are detected is thus $NP(k, \lambda)$. We thus determine the counts detected in one time interval to be abnormal if $k > k_{\text{threshold}}$ where $NP(k_{\text{threshold}}, \lambda) < 10^{-1}$. The threshold means that we expect to get fewer than 0.1 such time intervals during which we detect more than $k_{\text{threshold}}$ of photons.

For a thermal acoustic state, we assume the statistical model of photon detection to be $P_{\text{th]}}(k, \lambda = R\Delta t) = \lambda^k/(1+\lambda)^{k+1}$. We discard the entire 90 ms hold period if during which there exists any time intervals that receive more than $k_{\text{threshold}}$ of photons which we consider as an abonormal rapid burst. A more detailed description of the choice of the statistical model and the filtering process is presented in the work [198].

Bibliography

[1] A. B. Shkarin, A. D. Kashkanova, C. D. Brown, S. Garcia, K. Ott, J. Reichel, and J. G. E. Harris. Quantum optomechanics in a liquid. *Physical Review Letters*, 122:153601, Apr 2019.

[2] A. D. Kashkanova, A. B. Shkarin, C. D. Brown, N. E. Flowers-Jacobs, L. Childress, S. W. Hoch, L. Hohmann, K. Ott, J. Reichel, and J. G. E. Harris. Superfluid brillouin optomechanics. *Nature Physics*, 13:74, Oct 2017.

[3] H. J. Kimble. The quantum internet. *Nature*, 452:1023, Jun 2008.

[4] M. Arndt, A. Ekers, W. Klitzing, and H. Ulbricht. Focus on modern frontiers of matter wave optics and interferometry. *New Journal of Physics*, 14:125006, Dec 2012.

[5] O. Romero-Isart, A. C. Pflanzer, F. Blaser, R. Kaltenbaek, N. Kiesel, M. Aspelmeyer, and J. I. Cirac. Large quantum superpositions and interference of massive nanometer-sized objects. *Physical Review Letters*, 107:020405, Jul 2011.

[6] A. Bassi, K. Lochan, S. Satin, T. P. Singh, and H. Ulbricht. Models of wave-function collapse, underlying theories, and experimental tests. *Review Modern Physics*, 85:471–527, Apr 2013.

[7] D. Carney et. al. Mechanical quantum sensing in the search for dark matter. *Quantum Science and Technology*, 6:024002, Jan 2021.

[8] D. Brooks, T. Botter, S. Schreppler, T. P. Purdy, N. Brahms, and D. M. Stamper-Kurn. Non-classical light generated by quantum-noise-driven cavity optomechanics. *Nature*, 488:476, Aug 2012.

[9] A. A. Clerk, K. W. Lehnert, P. Bertet, J. R. Petta, and Y. Nakamura. Hybrid quantum systems with circuit quantum electrodynamics. *Nature Physics*, 16:257, Mar 2020.

[10] K. C. Lee, M. R. Sprague, B. J. Sussman, J. Nunn, N. K. Langford, X. M. Jin, T. Champion, P. Michelberger, K. F. Reim, D. England, D. Jaksch, and I. A. Walmsley. Entangling macroscopic diamonds at room temperature. *Science*, 334(6060):1253–1256, 2011.

[11] D. A. Golter, T. Oo, M. Amezcua, K. A. Stewart, and H. Wang. Optomechanical quantum control of a nitrogen-vacancy center in diamond. *Physical Review Letters*, 116:143602, Apr 2016.

[12] A. N. Cleland and M. R. Geller. Superconducting qubit storage and entanglement with nanomechanical resonators. *Physical Review Letters*, 93:070501, Aug 2004.

[13] J. D. Teufel, T. Donner, D. Li, J. W. Harlow, M. S. Allman, K. Cicak, A. J. Sirois, J. D. Whittaker, K. W. Lehnert, and R. W. Simmonds. Sideband cooling of micromechanical motion to the quantum ground state. *Nature*, 475:359, Jul 2011.

[14] J Chan, T. P. M. Alegre, A. H. Safavi-Naeini, J. T. Hill, A. Krause, S. Gröblacher, M. Aspelmeyer, and O. Painter. Laser cooling of a nanomechanical oscillator into its quantum ground state. *Nature*, 478:89, Oct 2011.

[15] J. D. Teufel, T. Donner, M. A. Castellanos-Beltran, J. W. Harlow, and K. W. Lehnert. Nanomechanical motion measured with an imprecision below that at the standard quantum limit. *Nature Nanotechnology*, 4:820, Nov 2009.

[16] G. Anetsberger, E. Gavartin, O. Arcizet, Q. P. Unterreithmeier, E. M. Weig, M. L. Gorodetsky, J. P. Kotthaus, and T. J. Kippenberg. Measuring nanomechanical motion with an imprecision below the standard quantum limit. *Physical Review A*, 82:061804, Dec 2010.

[17] A. H. Safavi-Naeini, S. Gröblacher, J. T. Hill, J. Chan, M. Aspelmeyer, and O. Painter. Squeezed light from a silicon micromechanical resonator. *Nature*, 500:185, Aug 2013.

[18] T. P. Purdy, P.-L. Yu, R. W. Peterson, N. S. Kampel, and C. A. Regal. Strong optomechanical squeezing of light. *Physical Review X*, 3:031012, Sep 2013.

[19] A. Mari and J. Eisert. Positive wigner functions render classical simulation of quantum computation efficient. *Physical Review Letters*, 109:230503, Dec 2012.

[20] E. Knill, R. Laflamme, and G. J. Milburn. A scheme for efficient quantum computation with linear optics. *Nature*, 409:46, Jan 2001.

[21] L.-M. Duan, M. D. Lukin, J. I. Cirac, and P. Zoller. Long-distance quantum communication with atomic ensembles and linear optics. *Nature*, 414:413, Nov 2001.

[22] D. R. M. Arvidsson-Shukur, Y. Halpern, H. V. Lepage, A. L. Aleksander, H. W. B. Crispin, and S. Lloyd. Quantum advantage in ostselected metrology. *Nature Communications*, 11, Nov 2020.

[23] J. D. Cohen, S. M. Meenehan, G. S. MacCabe, S. Gröblacher, A. H. Safavi-Naeini, F. Marsili, M. D. Shaw, and O. Painter. Phonon counting and intensity interferometry of a nanomechanical resonator. *Nature*, 520:522–525, Apr 2015.

[24] R. Riedinger, S. Hong, R. A. Norte, J. A. Slater, J. Shang, A. G. Krause, V. Anant, M. Aspelmeyer, and S. Gröblacher. Non-classical correlations between single photons and phonons from a mechanical oscillator. *Nature*, 530:313–316, Jan 2016.

[25] S. Hong, R. Riedinger, I. Marinkovic, A. Wallucks, S. G. Hofer, R. A. Norte, M. Aspelmeyer, and S. Gröblacher. Hanbury brown and twiss interferometry of single phonons from an optomechanical resonator. *Science*, 358:203–206, Sep 2017.

[26] R. Riedinger, A. Wallucks, I. Marinkovic, C. Löschnauer, M. Aspelmeyer, S. Hong, and S. Gröblacher. Remote quantum entanglement between two micromechanical oscillators. *Nature*, 556:473, Apr 2018.

[27] T. A. Palomaki, J. D. Teufel, R. W. Simmonds, N. Lehnert, K. W.Fiaschi, B. Hensen, A. Wallucks, R. Benevides, J. Li, T. P. M. Alegre, and S. Gröblacher. Optomechanical quantum teleportation. *Nature Photonics*, 15:817, Oct 2021.

[28] I. Galinskiy, Y. Tsaturyan, Parniak M., and E. S. Polzik. Phonon counting thermometry of an ultracoherent membrane resonator near its motional ground state. *Optica*, 7(6):718–725, Jun 2020.

[29] G. Enzian, L. Freisem, J. J. Price, A. $\emptyset$. Svela, J. Clarke, B. Shajilal, J. Janousek, B. C. Buchler, P. K. Lam, and M. R. Vanner. Non-gaussian mechanical motion via single and multiphonon subtraction from a thermal state. *Physical Review Letters*, 127:243601, Dec 2021.

[30] G. Enzian, J. J. Price, L. Freisem, J. Nunn, J. Janousek, B. C. Buchler, P. K. Lam, and M. R. Vanner. Single-phonon addition and subtraction to a mechanical thermal state. *Physical Review Letters*, 126:033601, Jan 2021.

[31] P. Lebedw. Untersuchungen $\ddot{u}$ber die druckkr$\ddot{a}$fte des lichtes. *Annalen der Physik*, 311:433, 1901.

[32] F. Marquardt, J. G. E. Harris, and S. M. Girvin. Dynamical multistability induced by radiation pressure in high-finesse micromechanical optical cavities. *Physical Review Letters*, 96:103901, Mar 2006.

[33] A. Ashkin. Acceleration and trapping of particles by radiation pressure. *Physical Review Letters*, 24:156–159, Jan 1970.

[34] A. Schliesser, P. Del'Haye, N. Nooshi, K. J. Vahala, and T. J. Kippenberg. Radiation pressure cooling of a micromechanical oscillator using dynamical backaction. *Physical Review Letters*, 97:243905, Dec 2006.

[35] C. D. Brown, Y. Wang, M. Namazi, G. I. Harris, M. T. Uysal, and J. G. E. Harris. Superfluid helium drops levitated in high vacuum. *Physical Review Letters*, 130:216001, May 2023.

[36] H. Xu, D. Mason, L. Jiang, and J. G. E. Harris. Topological energy transfer in an optomechanical system with exceptional points. *Nature*, 537:80, Sep 2016.

[37] B. Abbott et. al. Observation of a kilogram-scale oscillator near its quantum ground state. *New Journal of Physics*, 11(7):073032, Jul 2009.

[38] A. D. Kashkanova. *Optomechanics with superfluid helium*. PhD thesis, Yale University, 2017.

[39] A. B. Shkarin. *Quantum optomechanics with superfluid helium*. PhD thesis, Yale University, 2017.

[40] M. J. Collett and C. W. Gardiner. Squeezing of intracavity and traveling-wave light fields produced in parametric amplification. *Physical Review A*, 30:1386–1391, Sept 1984.

[41] C. Gardiner and P. Zoller. *Quantum noise: a handbook of Markovian and non-markovian quantum stochastic methods with applications to quantum optics*. Springer Berlin, Heidelberg, 2005.

[42] M. Aspelmeyer, Kippenberg T. J., and Marquardt F. Cavity optomechanics. *Reviews of Modern Physics*, 86:1391–1452, Dec 2014.

[43] F. Marquardt, J. P. Chen, A. A. Clerk, and S. M. Girvin. Quantum theory of cavity-assisted sideband cooling of mechanical motion. *Physical Review Letters*, 99:093902, Aug 2007.

[44] M. Yuan, V. Singh, Y. M. Blanter, and G. A. Steele. Large cooperativity and microkelvin cooling with a three-dimensioanl optomechanical cavity. *Nature Communications*, 6:8491, Oct 2015.

[45] J. Zhang, K. Peng, and S. L. Braunstein. Quantum-state transfer from light to macroscopic oscillators. *Physical Review A*, 68:013808, Jul 2003.

[46] T. A. Palomaki, J. W. Harlow, J. D. Teufel, R. W. Simmonds, and K. W. Lehnert. Coherent state transfer between itinerant microwave fields and a mechanical oscillator. *Nature*, 495:210–214, Mar 2013.

[47] R. W. Andrews, R. W. Peterson, T. P. Purdy, R. W. Simmonds, K. Cicak, C. A. Regal, and K. W. Lehnert. Bidirectional and efficient conversion between microwave and optical light. *Nature Physics*, 10:321–326, Mar 2014.

[48] D. V. Strekalov, A. A. Savchenkov, A. B. Matsko, and N. Yu. Efficient upconversion of subterahertz radiation in a high-q whispering gallery resonator. *Optical Letters*, 34(6):713–715, Mar 2009.

[49] M. Tsang. Optomechanics sets the beat. *Nature Physics*, 10:245, Mar 2014.

[50] J. Ye, J. Peng, R. J. Jones, K. W. Holman, J. L. Hall, D. J. Jones, S. A. Diddams, J. Kitching, S. Bize, J. C. Bergquist, L. W. Hollberg, L. Robertsson, and L. Ma. Delivery of high-stability optical and microwave frequency standards over an optical fiber network. *Journal of the Optical Society of America B*, 20:1459–1467, Jul 2003.

[51] Z. Xiang, S. Ashhab, J. Q. You, and F. Nori. Hybrid quantum circuits: Superconducting circuits interacting with other quantum systems. *Reviews of Modern Physics*, 85:623, Apr 2013.

[52] C. M. Caves, K. S. Thorne, R. W. P. Drever, V. D. Sandberg, and M. Zimmermann. On the measurement of a weak classical force coupled to a quantum-mechanical oscillator. i. issues of principle. *Reviews of Modern Physics*, 52:341, Apr 1980.

[53] K. Jähne, C. Genes, K. Hammerer, M. Wallquist, E. S. Polzik, and P. Zoller. Cavity-assisted squeezing of a mechanical oscillator. *Physical Review A*, 79:063819, Jun 2009.

[54] J. Liao and C. K. Law. Parametric generation of quadrature squeezing of mirrors in cavity optomechanics. *Physical Review A*, 83:033820, Mar 2011.

[55] C. Fabre, M. Pinard, S. Bourzeix, A. Heidmann, E. Giacobino, and S. Reynaud. Quantum-noise reduction using a cavity with a movable mirror. *Physical Review A*, 49:1337, Feb 1994.

[56] A. Heidmann and S. Reynaud. Photon noise reduction by reflection from a movable mirror. *Physical Review A*, 50:4237, Nov 1994.

[57] A. A. Clerk, M. H. Devoret, S. M. Girvin, F. Marquardt, and R. J. Schoelkopf. Introduction to quantum noise, measurement, and amplification. *Reviews of Modern Physics*, 82:1155, Apr 2010.

[58] M. J. Holland, D. F. Walls, and P. Zoller. Quantum nondemolition measurements of photon number by atomic beam deflection. *Physical Review Letters*, 67:1716, Sep 1991.

[59] M. Pinard, C. Fabre, and A. Heidmann. Quantum-nondemolition measurement of light by a piezoelectric crystal. *Physical Review A*, 51:2443, Mar 1995.

[60] V. B. Braginsky, Y. I. Vorontsov, and K. S. Thorne. Quantum nondemolition measurements. *Science*, 209:547, Aug 1980.

[61] V. B. Braginsky and F. Y. A. Khalili. *Quantum Measurements*. Cambridge University Press, Cambridge, England, 1995.

[62] K. Jacobs, P. Tombesi, M. J. Collett, and D. F. Walls. Quantum-nondemolition measurement of photon number using radiation pressure. *Physical Review A*, 49:1961, Mar 1994.

[63] M. R. Vanner, M. Aspelmeyer, and M. S. Kim. Quantum state orthogonalization and a toolset for quantum optomechanical phonon control. *Physical Review Letters*, 110:010504, Jan 2013.

[64] M. R. Vanner, J. Hofer, G. D. Cole, and M. Aspelmeyer. Cooling-by-measurement and mechanical state tomography via pulsed optomechanics. *Nature Communications*, 4:2295, Jul 2013.

[65] V. B. Braginsky, Y. I. Vorontsov, and F. Y. Khalili. Optimal quantum measurements in detectors of gravitation radiation. *JETP Letter (USSR) (Engl. Transl.); (United States)*, 27:276, Mar 1978.

[66] M. D. LaHaye, O. Buu, B. Camarota, and K. C. Schwab. Approaching the quantum limit of a nanomechanical resonator. *Science*, 304(5667):74, 2004.

[67] S. Mancini, V. I. Man'ko, and P. Tombesi. Ponderomotive control of quantum macroscopic coherence. *Physical Review A*, 55:3042, Apr 1997.

[68] S. Bose, K. Jacobs, and P. L. Knight. Preparation of nonclassical states in cavities with a moving mirror. *Physical Review A*, 56:4175, Nov 1997.

[69] A. Einstein, B. Podolsky, and N. Rosen. Can quantum-mechanical description of physical reality be considered complete? *Physical Review*, 47:777, May 1935.

[70] S. L. Braunstein and P. Van Loock. Quantun information with continuous variables. *Reviews of Modern Physics*, 77:513, Jun 2005.

[71] C. P. Weedbrook, S. Pirandola, R. Garcia-Patron, N. J. Cerf, T. C. Ralph, J. H. Shapiro, and S. Lloyd. Gaussian quantum information. *Review of Modern Physics*, 84:621, Jun 2012.

[72] M. J. Woolley and A. A. Clerk. Two-mode back-action-evading measurements in cavity optomechanics. *Physical Review A*, 87:063846, Jun 2013.

[73] W. Wasilewski, K. Jensen, H. Krauter, J. J. Renema, M. V. Balabas, and E. S. Polzik. Quantum noise limited and entanglement-assisted magnetometry. *Physical Review Letters*, 104:133601, Mar 2010.

[74] S. Mancini, V. Giovannetti, D. Vitali, and P. Tombesi. Entangling macroscopic oscillators exploiting radiation pressure. *Physical Review Letters*, 88:120401, Mar 2002.

[75] D. Vitali, S. Gigan, A. Ferreira, H. R. Böhm, P. Tombesi, A. Guerreiro, V. Vedral, A. Zeilinger, and M. Aspelmeyer. Optomechanical entanglement between a movable mirror and a cavity field. *Physical Review Letters*, 98:030405, Jan 2007.

[76] S. Pirandola, D. Vitali, P. Tombesi, and S. Lloyd. Macroscopic entanglement by entanglement swapping. *Physical Review Letters*, 97:150403, Oct 2006.

[77] S. Huang and G. S. Agarwal. Entangling nanomechanical oscillators in a ring cavity by feeding squeezed light. *New Journal of Physics*, 11:103044, Oct 2009.

[78] T. S. Cubitt, F. Verstraete, W. Dür, and J. I. Cirac. Separable states can be used to distribute entanglement. *Physical Review Letters*, 91:037902, Jul 2003.

[79] S. G. Hofer, W. Wieczorek, M. Aspelmeyer, and K. Hammerer. Quantum entanglement and teleportation in pulsed cavity optomechanics. *Physical Review A*, 84:052327, Nov 2011.

[80] K. Hammerer, E. S. Polzik, and J. I. Cirac. Teleportation and spin squeezing utilizing multimode entanglement of light with atoms. *Physical Review A*, 72:052313, Nov 2005.

[81] T. A. Palomaki, J. D. Teufel, R. W. Simmonds, and K. W. Lehnert. Entangling mechanical motion with microwave fields. *Science*, 342:710, Oct 2013.

[82] S. Mancini, D. Vitali, and P. Tombesi. Scheme for teleportation of quantum states onto a mechanical resonator. *Physical Review Letters*, 90:137901, Apr 2003.

[83] R. Raussendorf and H. J. Briegel. A one-way quantum computer. *Physical Review Letters*, 86:5188, May 2001.

[84] X. Han, C. Zou, and H. X. Tang. Multimode strong coupling in superconducting cavity piezoelectromechanics. *Physical Review Letters*, 117:123603, Sep 2016.

[85] Y. Chu, P. Kharel, W. H. Renninger, L. D. Burkhart, L. Frunzio, P. T. Rakich, and R. J. Schoelkopf. Quantum acoustics with superconducting qubits. *Science*, 358(6360):199, Sep 2017.

[86] L. Mercier de Lépinay, C. F. Ockeloen-Korppi, M. J. Woolley, and M. A. Sillanpää. Quantum mechanics-free subsystem with mechanical oscillators. *Science*, 372(6542):625, 2021.

[87] D. Zoepfl, M. L. Juan, C. M. F. Schneider, and G. Kirchmair. Single-photon cooling in microwave magnetomechanics. *Physical Review Letters*, 125:023601, Jul 2020.

[88] J. Guo, R. Norte, and S. Gröblacher. Feedback cooling of a room temperature mechanical oscillator close to its motional ground state. *Physical Review Letters*, 123:223602, Nov 2019.

[89] T. Richter and W. Vogel. Nonclassicality of quantum states: a hierarchy of observable conditions. *Physical Review Letters*, 89:283601, Dec 2002.

[90] F. Damanet, J. Kübler, J. Martin, and D. Braun. Nonclassical states of light with a smooth p-function. *Physical Review A*, 97:023832, Feb 2018.

[91] A. A. Clerk, F. Marquardt, and K. Jacobs. Back-action evasion and squeezing of a mechanical resonator using a cavity detector. *New Journal of Physics*, 10, Sep 2008.

[92] D. H. Santamore, A. C. Doherty, and M. C. Cross. Quantum nondemolition measurement of fock states of mesoscopic mechanical oscillators. *Phys. Rev. B*, 70:144301, Oct 2004.

[93] J. D. Thompson, B. M. Zwickl, A. M. Jayich, F. Marquardt, S. M. Girvin, and J. G. E. Harris. Strong dispersive coupling of a high-finesse cavity to a micromechanical membrane. *Nature*, 452:72, Mar 2008.

[94] A. M. Jayich, J. C. Sankey, B. M. Zeickl, C. Yang, J. D. Thompson, S. M. Girvin, and A. A. Clerk. Dispersive optomechanics: a membrane inside a cavity. *New Journal of Physics*, 10, Sep 2008.

[95] J. C. Sankey, C. Yang, B. M. Zwickl, A. M. Hayich, and J. G. E. Harris. Strong and tunable nonlinear optomechanical coupling in a low-loss system. *Nature Physics*, 6:707, Sep 2010.

[96] T. P. Purdy, D. W. C. Brooks, T. Botter, N. Brahms, Z. Y. Ma, and D. M. Stamper-Kurn. Tunable cavity optomechanics with ultracold atoms. *Physical Review Letters*, 105:133602, Sep 2010.

[97] P. Meystre, E. M. Wright, J. D. McCullen, and E. Vignes. Theory of radiation-pressure-driven interferometers. *Journal of the Optical Society of America B*, 2:1830–1840, Jun 1985.

[98] M. Bhattacharya, H. Uys, and P. Meystre. Optomechanical trapping and cooling of partially reflective mirrors. *Physical Review A*, 77:033819, Mar 2008.

[99] M. Bhattacharya, P. L. Giscard, and P. Meystre. Optical squeezing of a mechanical oscillator by dispersive interaction. *arXiv*, 0803.1219, 2008.

[100] S. Gupta, K. L. Moore, K. W. Murch, and D. M. Stamper-Kurn. Cavity nonlinear optics at low photon numbers from collective atomic motion. *Physical Review Letters*, 99:213601, Nov 2007.

[101] A. D. O'Connell, M. Hofheinz, M. Ansmann, R. C. Bialczak, M. Lenander, E. Lucero, M. Neeley, D. Sank, H. Wang, M. Weides, J. Wenner, J. M. Martinis, and A. N. Cleland. Quantum ground state and single-phonon control of a mechanical resonator. *Nature*, 464:697, Mar 2010.

[102] Q. A. Turchette, C. J. Hood, W. Lange, H. Mabuchi, and H. J. Kimble. Measurement of conditional phase shifts for quantum logic. *Physical Review Letters*, 75:4710–4713, Dec 1995.

[103] A. A. Clerk and D. Wahyu Utami. Using a qubit to measure photon-number statistics of a driven thermal oscillator. *Phys. Rev. A*, 75:042302, Apr 2007.

[104] J. C. Howell and J. A. Yeazell. Reducing the complexity of linear optics quantum circuits. *Physical Review A*, 61:052303, Apr 2000.

[105] J. Liao, H. K. Cheung, and C. K. Law. Spectrum of single-photon emission and scattering in cavity optomechanics. *Physical Review A*, 85:025803, Feb 2012.

[106] W. Marshall, C. Simon, R. Penrose, and D. Bouwmeester. Towards quantum superpositions of a mirror. *Physical Review Letters*, 91:130401, Sep 2003.

[107] D. Kleckner, I. Pikovski, E. Jeffrey, L. Ament, E. Eliel, J. Brink, and D. Bouwmeester. Creating and verifying a quantum superposition in a micro-optomehcanical system. *New Journal of Physics*, 10(9):095020, Sep 2008.

[108] F. Khalili, S. Danilishin, H. Miao, H. Müller-Ebhardt, H. Yang, and Y. Chen. Preparing a mechanical oscillator in non-gaussian quantum states. *Physical Review Letters*, 105:070403, Aug 2010.

[109] S. Bose, K. Jacobs, and P. L. Knight. Scheme to probe the decoherence of a macroscopic object. *Physical Review A*, 59:3204–3210, May 1999.

[110] T. Hong, H. Yang, H. Miao, and Y. Chen. Open quantum dynamics of single-photon optomechanical devices. *Physical Review A*, 88:023812, Aug 2013.

[111] A. Bienfait, Y. P. Zhong, H. S. Chang, M. H. Chou, C. R. Conner, E. Dumur, J. Grebel, G. A. Peairs, R. G. Povey, K. J. Satzinger, and A. N. Cleland. Quantum erasure using entangled surface acoustic phonons. *Physical Review X*, 10:021055, Jun 2020.

[112] L. R. Sletten, B. A. Moores, J. J. Viennot, and K. W. Lehnert. Resolving phonon fock states in a multimode cavity with a double-slit qubit. *Physical Review X*, 9:021056, Jun 2019.

[113] S. Scheel, K. Nemoto, W. J. Munro, and P. L. Knight. Measurement-induced nonlinearity in linear optics. *Physical Review A*, 68:032310, Sep 2003.

[114] C. Cabrillo, J. I. Cirac, P. García-Fernández, and P. Zoller. Creation of entangled states of distant atoms by interference. *Physical Review A*, 59:1025–1033, Feb 1999.

[115] T. Wong, S. M. Tan, M. J. Collett, and D. F. Walls. Interference of resonance fluorescence from two four-level atoms. *Physical Review A*, 55:1288–1299, Feb 1997.

[116] W. M. Itano, J. C. Bergquist, J. J. Bollinger, D. J. Wineland, U. Eichmann, and M. G. Raizen. Complementarity and young's interference fringes from two atoms. *Physical Review A*, 57:4176–4187, Jun 1998.

[117] M. D. Eisaman, J. Fan, A. Migdall, and S. V. Polyakov. Single-photon sources and detectors. *Review of Scientific Instruments*, 82(7):071101, Jul 2011.

[118] C. M. Natarajan, M. G. Tanner, and R. H. Hadfield. Superconducting nanowire single-photon detectors: physics and applications. *Superconductor Science and Technology*, 25(6):063001, Apr 2012.

[119] E. A. Dauler, A. J. Kerman, B. S. Robinson, J. K. W. Yang, B. Voronov, G. Goltsman, S. A. Hamilton, and K. K. Berggren. Photon-number-resolution with sub-30-ps timing using multi-element superconducting nanowire single photon detectors. *Journal of Modern Optics*, 56(2):364–373, Oct 2010.

[120] G. N. Gol'tsman, O. Okunev, G. Chulkova, A. Lipatov, A. Semenov, K. Smirnov, B. Voronov, A. Dzardanov, C. Williams, and R. Sobolewski. Picosecond superconducting single-photon optical detector. *Applied Physics Letters*, 79(6):705–707, 08 2001.

[121] H. Takesue, S. W. Nam, Q. Zhang, R. H. Hadfield, T. Honjo, K. Tamaki, and Y. Yamamoto. Quantum key distribution over a 40-db channel loss using superconducting single-photon detectors. *Nature Photonics*, 1:343, Jun 2007.

[122] F. Marsili, V. B. Verma, J. A. Stern, S. Harrington, A. E. Lita, T. Gerrits, I. Vayshenker, B. Baek, M. D. Shaw, R. P. Mirin, and S. W. Nam. Detecting single infrared photons with 93% system efficiency. *Nature Photonics*, 7:210, Mar 2013.

[123] L. Duan, J. I. Cirac, P. Zoller, and E. S. Polzik. Quantum communication between atomic ensembles using coherent light. *Physical Review Letters*, 85:5643–5646, Dec 2000.

[124]

[125] C. W. Chou, H. Riedmatten, D. Felinto, S. V. Polyakov, S. J. Enk, and H. J. Kimble. Measurement-induced entanglement for excitation stored in remote atomic ensembles. *Nature*, 438:828, Dec 2005.

[126] C. Chou, J. Laurat, H. Deng, K. S. Choi, H. Riedmatten, D. Felinto, and H. J. Kimble. Functional quantum nodes for entanglement distribution over scalable quantum networks. *Science*, 316(5829):1316–1320, 2007.

[127] K. S. Choi, H. Deng, J. Laurat, and H. J. Kimble. Mapping photonic entanglement into and out of a quantum memory. *Nature*, 452:67, Mar 2008.

[128] I. Marinković, A. Wallucks, R. Riedinger, S. Hong, M. Aspelmeyer, and Simon Gröblacher. Optomechanical bell test. *Physical Review Letters*, 121:220404, Nov 2018.

[129] D. Hunger, C. Deutsch, R. J. Barbour, R. J. Warburton, and J. Reichel. Laser micro-fabrication of concave, low-roughness features in silica. *AIP Advances*, 2(1):012119, 01 2012.

[130] Hunger. D., T. Steinmetz, Y. Colombe, C. Deutsch, T. W. Hänsch, and J. Reichel. A fiber fabry-perot cavity with high finesse. *New Journal of Physics*, 12(6):065038, jun 2010.

[131] B. M. Abraham, Y. Eckstein, J. B. Ketterson, M. Kuchnir, and P. R. Roach. Velocity of sound density, and gruneisen constant in liquid $^4\mathrm{He}$. *Physical Review A*, 2:550–550, Aug 1970.

[132] C. Metzger, M. Ludwig, C. Neuenhahn, A. Ortlieb, I. Favero, K. Karrai, and F. Marquardt. Self-induced oscillations in an optomechanical system driven by bolometric backaction. *Physical Review Letters*, 101:133903, Sep 2008.

[133] M. Ludwig, A. H. Safavi-Naeini, O. Painter, and F. Marquardt. Enhanced quantum nonlinearities in a two-mode optomechanical system. *Physical Review Letters*, 109:063601, Aug 2012.

[134] K. Stannigel, P. Komar, S. J. M. Habraken, S. D. Bennett, M. D. Lukin, P. Zoller, and P. Rabl. Optomechanical quantum information processing with photons and phonons. *Physical Review Letters*, 109:013603, Jul 2012.

[135] I. S. Grudinin, H. Lee, O. Painter, and K. J. Vahala. Phonon laser action in a tunable two-level system. *Physical Review Letters*, 104:083901, Feb 2010.

[136] H. Xu, L. Jiang, A. A. Clerk, and J. G. E. Harris. Nonreciprocal control and cooling of phonon modes in an optomechanical system. *Nature*, 568:65, Apr 2019.

[137] P. Kapitza. Viscosity of liquid helium below the λ-point. *Nature*, 141:74, Jan 1938.

[138] L. London. The λ-phenomenon of liquid helium and the bose-einstein degeneracy. *Nature*, 141:643, Apr 1938.

[139] L. Landau. Theory of the superfluidity of helium ii. *Physical Review Letters*, 60:356–358, Aug 1941.

[140] F. Pobell. *Matter and methods at low temperatures*. Springer, 2007.

[141] H. W. Jackson. Erratum: foundations of a comprehensive theory of liquid $^4\mathrm{He}$. *Physical Review B*, 20:4762–4762, Dec 1979.

[142] C. M. Surko, G. J. Dick, F. Reif, and W. C. Walker. Spectroscopic study of liquid helium in the vacuum ultraviolet. *Physical Review Letters*, 23:842–846, Oct 1969.

[143] H. J. Maris and W. E. Massey. Phonon dispersion and the propagation of sound in liquid helium-4 below 0.6 k. *Physical Review Letters*, 25:220–222, Jul 1970.

[144] L. A. De Lorenzo and K. C. Schwab. Superfluid optomechanics: coupling of a superfluid to a superconducting condensate. *New Journal of Physics*, 16(11):113020, Nov 2014.

[145] L. A. De Lorenzo and K. C. Schwab. Ultra-high q acoustic resonance in superfluid ^{4}he. *Journal of Low Temperature Physics*, 186:233, Feb 2017.

[146] G. I. Harris, D. L. McAuslan, E. Sheridan, Y. Sachkou, C. Baker, and W. P. Bowen. Laser cooling and control of excitations in superfluid helium. *Nature Physics*, 12:788, Aug 2016.

[147] G. Koolstra, D. McKay, G. Yang, D. Czaplewski, and D. Schuster. Optomechanics with ripplons on superfluid helium. *Bulletin of the American Physical Society*, 60, 2015.

[148] C. D. Brown, G. Harris, and J. G. E. Harris. Optomechanics in a levitated droplet of superfluid helium. *Bulletin of the American Physical Society*, 62, 2017.

[149] A. A. Michelson. On the application of interference methods to astronomical measurements. *The Astrophysical Journal*, 51:257–263, Jun 1920.

[150] R. Hanbury Brown and R. Q. Twiss. A test of a new type of stellar interferometer on sirius. *Nature*, 178:1046–1048, Nov 1956.

[151] E. M. Purcell. The question of correlation between photons in coherent light rays. *Nature*, 178:1449–1450, Dec 1956.

[152] I. Silva and O. Freire Jr. The concept of the photon in question: the controversy surrounding the hbt effect circa 1956-1958. *Historical Studies in the Natural Sciences*, 43:453–491, Sep 2013.

[153] R. Loudon. *The quantum theory of light*. Oxford Science Publications, 2000.

[154] R. Hanbury Brown and R. Q. Twiss. Correlation between photons in two coherent beams of light. *Nature*, 177:27–29, Jan 1956.

[155] P. A. M. Dirac. The quantum theory of the emission and absorption of radiation. *Proceedings of the Royal Society of London Series A*, 114:243–265, Mar 1927.

[156] L. Mandel and E. Wolf. *Optical coherence and quantum optics*. Cambridge University press, 1995.

[157] R. J. Glauber. The quantum theory of optical coherence. *Physical Review*, 130:2529–2539, Jun 1963.

[158] G. C. Wick. The evaluation of the collision matrix. *Physical Review*, 80:268–272, Oct 1950.

[159] S. M. Barnett and P. M. Radmore. *Methods in Theoretical Quantum Optics*. Cambridge Oxford Academic press, 2002.

[160] X. T. Zou and L. Mandel. Photon-antibunching and sub-poissonian photon statistics. *Physical Review A*, 41:475–476, Jan 1990.

[161] E. C. G. Sudarshan. Equivalence of semiclassical and quantum mechanical descriptions of statistical light beams. *Physical Review Letters*, 10:277–279, Apr 1963.

[162] R. J. Glauber. Coherent and incoherent states of the radiation field. *Physical Review*, 131:2766–2788, Sep 1963.

[163] R. Filip and L. Lachman. Hierarchy of feasible nonclassicality criteria for sources of photons. *Physical Review A*, 88:043827, Oct 2013.

[164] L. Lachman, I. Straka, J. Hlousek, M. Jezek, and R. Filip. Faithful hierarchy of genuine n-photon quantum non-gaussian light. *Physical Review Letter*, 123:043601, Jul 2019.

[165] R. Filip. Hierarchy of quantum non-gaussian states: theory and experiment. page W2B.1. Optica Publishing Group, 2021.

[166] M. A. Lemonde, N. Didier, and A. A. Clerk. Antibunching and unconventional photon blockade with gaussian squeezed states. *Physical Review A*, 90:063824, Dec 2014.

[167] I. Straka, A. Predojević, T. Huber, L. Lachman, L. Butschek, M. Mikov*á*, M. Micuda, G. S. Solomon, G. Weihs, M. Jezek, and R. Filip. Quantum non-gaussian depth of single-photon states. *Physical Review Letters*, 113:223603, Nov 2014.

[168] L. Lachman and R. Filip. Robustness of quantum nonclassicality and non-gaussianity of single-photon states in attenuating channels. *Physical Review A*, 88:063841, Dec 2013.

[169] T. Stace, A. N. Luiten, and R. P. Kovacich. Laser offset-frequency locking using a frequency-to-voltage converter. *Meas. Sci. Technol.*, 9:1635–1637, Feb 1998.

[170] G. Ritt, G. Cennini, C. Geckeler, and M. Weitz. Laser frequency offset locking using a side of filter technique. *Appl. Phys. B*, 79:363–365, Aug 2004.

[171] R. M. Shelby, M. D. Levenson, and P. W. Bayer. Guided acoustic-wave brillouin scattering. *Phys. Rev. B*, 31:5244–5252, Apr 1985.

[172] N. Takefushi, M. Yoshida, K. Kasai, T. Hirooka, and M. Nakazawa. Gawbs noise characteristics in digital coherent transmission in various optical fibers. In *2019 24th OptoElectronics and Communications Conference (OECC) and 2019 International Conference on Photonics in Switching and Computing (PSC)*, Fukuoka, Japan, Jul 2019. IEEE.

[173] M. Ludwig, B Kubala, and F. Marquardt. The optomechanical instability in the quantum regime. *New Journal of Physics*, 10, Sep 2008.

[174] Y. S. S. Patil, J. Yu, S. Frazier, Y. Wang, K. Johnson, J. Fox, J. Reichel, and J. G. E. Harris. Measuring high-order phonon correlations in an optomechanical resonator. *Physical Reivew Letters*, 128, May 2022.

[175] J. Hloušek, M. Ježek, and R. Filip. Work and information from thermal states after subtraction of energy quanta. *Scientific Reports*, 7:13046, Oct 2017.

[176] C. Sayrin, I. Dotsenko, X. Zhou, B. Peaudecerf, T. Rybarczyk, S. Gleyzes, P. Rouchon, M. Mirrahimi, H. Amini, M. Brune, J Raimond., and S. Haroche. Real-time quantum feedback prepares and stabilizes photon number states. *Nature*, 477:73–77, Aug 2011.

[177] C. Guerlin, J. Bernu, S. Deléglise, C. Sayrin, S. Gleyzes, S. Kuhr, M. Brune, J Raimond., and S. Haroche. Progressive field-state collapse and quantum non-demolition photon counting. *Nature*, 448:889–893, Aug 2007.

[178] J. C. Maxwell. *Theory of Heat*. Longman, 1871.

[179] M. D. Vidrighin, O. Dahlsten, M. Barbieri, M. S. Kim, V. Vedral, and I. A. Walmsley. Photonic maxwell's demon. *Physical Review Letters*, 116:050401, Feb 2016.

[180] S. M. H. Rafsanjani, M. Mirhosseini, O. S. Magaña Loaiza, B. T. Gard, R. Birrittella, B. E. Koltenbah, C. G. Parazzoli, B. A. Capron, C. C. Gerry, J. P. Dowling, and R. W. Boyd. Quantum-enhanced interferometry with weak thermal light. *Optica*, 4:487–491, Apr 2017.

[181] T. Kiesel, W. Vogel, V. Parigi, A. Zavatta, and M. Bellini. Experimental determination of a nonclassical glauber-sudarshan p function. *Phys. Rev. A*, 78:021804, Aug 2008.

[182] Ourjoumtsev A., Tualle-Brouri R., Laurat J., and Grangier P. Generating optical schrödinger kittens for quantum information processing. *Science*, 312(5770):83–86, 2006.

[183] A. I. Lvovsky, H. Hansen, T. Aichele, O. Benson, J. Mlynek, and S. Schiller. Quantum state reconstruction of the single-photon fock state. *Physical Review Letters*, 87:050402, Jul 2001.

[184] R. N. Patel, T. P. McKenna, Z. Wang, J. D. Witmer, W. Jiang, R. Van Laer, C. J. Sarabalis, and A. H. Safavi-Naeini. Room-temperature mechanical resonator with a single added or subtracted phonon. *Physical Review Letters*, 127:133602, Sept 2021.

[185] J. W. Goodman. *Introduction to Fourier optics*. Englewood, CO: Roberts Co. Publishers, 2005.

[186] F. Pampaloni and J. Enderlein. Gaussian, hermite-gaussian, and laguerre-gaussian beams: A primer. *arXiv.physics*, 0410021, 2004.

[187] Ingrid Rotter. Non-hermitian quantum physics of open systems. *arXiv*, 1707.03298, Sept 2017.

[188] E. D. Black. An introduction to pound-drever-hall laser frequency stabilization. *Am. J. Phys.*, 69:79–87, 2001.

[189] T. Yazaki. Experimental observation of thermoacoustic turbulence and universal properties at the quasiperiodic transition to chaos. *Phys. Rev. E*, 48:1806–1819, 1993.

[190] A. Tominaga, Y. Narahara, and T. Yazaki. Thermoacoustic effects of inviscid fluids. *Journal of Low Temperature Physics*, 54:233–245, 1984.

[191] U. Fano. Effects of configuration interaction on intensities and phase shifts. *Physical Review*, 124:1866, Dec 1961.

[192] B. Bertman and T. A. Kitchens. Heat transport in superfluid filled capillaries. *Cryogenics*, 8:36–41, Feb 1968.

[193] W. M. Whitney. Velocity of sound in liquid helium at low temperatures. *Physical Review Letters*, 9, Sep 1962.

[194] G. L. Pollack. Kapitza resistance. *Rev. Mod. Phys.*, 41, Jan 1969.

[195] S. Weis, R. Rivière, S. Deléglise, E. Gavartin, O. Arcizer, A. Schliesser, and T. J. Kippenberg. Optomechanically induced transparency. *Science*, 330:1520–1523, Nov 2010.

[196] V. Burenkov, H. Xu, B. Qi, R. H. Hadfield, and H-K. Lo. Investigations of afterpulsing and detection efficiency recovery in superconducting nanowire single-photon detectors. *Journal of Applied Physics*, 113:213102, Jun 2013.

[197] M. Fujiwara, A. Tanaka, S. Takahashi, K. Yoshino, Y. Nambu, A. Tajima, S. Miki, T. Yamashita, Z. Wang, A. Tomita, and M. Sasaki. Afterpulse-like phenomenon of superconducting single photon detector in high speed quantum key distribution system. *Optics Express*, 19:19562–19571, Sept 2011.

[198] Y. Wang. *Manipulating and measuring states of a superfluid optomechanical resonator in the quantum regime*. PhD thesis, Yale University, 2023.